MAPS Calorimetry for a Future Linear Collider

O. D. Miller

School of Physics and Astronomy

University of Birmingham

"Science my lad, has been built upon many errors; but they are errors which it is good to fall into, for they led to the truth"

Jules Verne, Journey to the Centre of the Earth.

Abstract

The International Linear Collider (ILC) is intended to be a new high precision electron-positron collider operating at the TeV scale. The studies detailed within this thesis deal primarily with the development of Monolithic Active Pixel Sensors (MAPS) which could be used as the sensitive component of an ILC Electromagnetic Calorimeter (ECAL). These include simulations of a MAPS ECAL to investigate pixel saturation as a function of reset time, and energy resolution for single electrons. The energy resolution $\frac{\sigma(E)}{E}$ was found to be $\frac{(0.1147 \pm 0.0004)}{\sqrt{E(\text{GeV})}}$. The remaining studies describe part of the calibration process for prototype MAPS sensors and how those sensors were used to characterise the response of MAPS pixels to a 120 GeV pion beam. This resulted in a measurement of the MIP (Minimum Ionising Particle) efficiency of MAPS pixels of 75% to 95% with some variation due to the properties of the epitaxial layer.

Author's Contribution

The studies detailed within this thesis were performed as part of the CALICE UK/SPiDeR collaboration working to develop new calorimeter sensors for a future linear collider. As part of this collaboration I have constructed and analysed simulations to predict the single particle energy resolution of an innovative electromagnetic calorimeter (ECAL) which would use digital calorimetry. In order to accomplish this I modified a pre-existing simulation model of the ILD detector so that it included an ECAL consistent with the characteristics of the new calorimeter.

I have also run and analysed simulations of a similar digital ECAL to examine how that calorimeter would deal with pixel saturation (where a pixel is rendered useless through part of data taking due to its inability to record more than one hit before readout). These simulations dealt with pixel saturation due to beam-beam interactions and this resulted in two stages of analysis. In the first stage of analysis I established whether or not there was a risk of beam-beam interactions causing pixel saturation in the ECAL. Having established that beam-beam interactions could cause pixel saturation, in the second stage of analysis I quantified the extent of pixel saturation due to beam-beam interaction in far forward regions of the ECAL as a function of time between readouts.

Additionally I investigated the uniformity of hit thresholds of pixels in prototype TPAC 1.0 sensors based on noise runs with a range of thresholds set. Based on this investigation I then developed and implemented techniques for improving pixel uniformity by fine tuning the threshold set for each individual pixel.

I also participated in tests of the TPAC 1.2 those sensors using a 120 GeV pion beam to characterise their efficiency. Specifically I ran the analysis of results from the test beam both to measure efficiency, and to check for problems during the tests. Pixel efficiency was measured using three different analysis techniques referred to as the 2D method, the 1D method and the counting method. I developed the 2D and 1D methods to replicate the analysis performed by Prof. Paul Dauncey and measured the lower limit of pixel efficiency, and the lower limit of pixel for idealised

pixel respectively. I developed the counting method independently to measure the upper limit of TPAC 1.2 pixel efficiency.

Aknowledgements

I would like to thank my family and friends for their support. I would also like to thank my colleagues both within the Birmingham HEP group and the CALICE UK/SPiDeR collaboration for their advice, and for tolerating my many, many, mistakes. In particular I would like to thank Dr. Nigel Watson who has been my teacher and mentor for the past four years, without whom this would not have been possible. O. Miller, Birmingham 2010

This thesis is dedicated to all those lost along the way, still with us through the spaces they leave behind.

Contents

List of Tables

List of Figures

17

Chapter 1

Particle Physics and the Standard Model

While the majority of this thesis will deal with practical research and development of high energy physics detectors, it is necessary to first cover some of the motivations for the creation of those sensors. The natural point at which to begin this process is a brief summary of the theoretical framework which describes high energy particle physics; the Standard Model.

1.1 Components of the Standard Model

While the full derivation of the Standard Model is not within the scope of this document, it is necessary to begin by introducing some of the key components which were combined to construct this theory.

1.1.1 Quarks and Leptons

Since the Standard Model deals primarily with the interactions of fundamental particles, it is important to first establish which particles are fundamental and what their characteristics are. With the exception of the gauge bosons, covered in section 1.2.2, all known fundamental particles are either quarks or leptons. The principal distinction between quarks and leptons is that quarks are affected by the strong

	Symbol			Mass(MeV)			q($\lvert e \rvert$)
Generation:	1st	2nd	3rd	1st	2nd	3rd	
Quarks:	u	c	t	1.5→3.3	$(1.16{\to}1.34){\times}10^3$	$(171.3 \pm 1.6) \times 10^3$	$+\frac{2}{3}$
	d	s	b	3.5→6.0	70→130	$(4.13{\to}4.37){\times}10^3$	$-\frac{1}{3}$
Leptons:	e	μ	τ	0.51	105.66	$(1776.84{\pm}0.17)$	-1
	ν_e	ν_μ	ν_τ	$<2{\times}10^{-6}$	<0.19	<18.2	0

Table 1.1: Known quarks and leptons[2][3][4].

interaction (discussed in section 1.2.2) and are therefore always bound in hadrons, while leptons are not subject to the strong interaction and therefore can be found as free particles[1].

In addition to these distinctions, all known quarks and leptons are grouped into three 'generations' with each particle sharing characteristics with lighter and/or heavier counterparts in the other generations[1]. These particle generations, along with the characteristics of the quarks and leptons within them are described in table 1.1.

1.1.2 Gauge Invariance

One of the first requirements in the formulation of the Standard Model is that the resulting theory be gauge invariant (i.e. there should be no change in measurable values) under any transformation of the form $\psi(x) \rightarrow e^{i\alpha}\psi(x)$ (which changes the phase of the wave function ψ). As long as α remains constant this requirement has no consequences since the absolute phase of wave function at any point cannot be measured. However it is possible that α is a function of position, meaning that the wave function undergoes a different transformation at every point in space. This is a problem because undergoing a different transformation at every point in space would result in changes to the relative phase of the wave function between different points, which is measurable. In order to compensate for this it is necessary to introduce new 'gauge fields' which would be affected by the same transformations and which would cancel out any apparent effect those transformations would otherwise have on predictions. This would be no more than an interesting mathematical trick, except

the new fields required for local gauge invariance correspond to measurable physical phenomena, namely the interactions and accompanying gauge bosons discussed in section 1.2.2[1][5][6].

1.2 The Standard Model Lagrangian

Using the principles of gauge invariance and applying them to models of observed particles and phenomena results in the derivation of a preliminary Lagrangian for all fermion electroweak interactions shown below[7].

$$\mathcal{L}_F = \sum_i \overline{\psi_i}(i\partial\!\!\!/ - m_i)\psi_i$$

$$-\frac{g}{2\sqrt{2}}\sum_i \overline{\psi_i}\gamma^\mu(1-\gamma^5)(T^+W_\mu^+ + T^-W_\mu^-)\psi_i$$

$$-e\sum_i q_i\overline{\psi_i}\gamma^\mu\psi_i A_\mu$$

$$-\frac{g}{2cos\theta_W}\sum_i \overline{\psi_i}\gamma^\mu(g_V^i - g_A^i\gamma^5)\psi_i Z_\mu \tag{1.1}$$

Where: θ_W is the weak mixing angle, e is the positron electric charge, A is the massless photon field, $W^\pm$ and Z are the massive weak boson fields, T^+ and T^- are the weak isospin raising and lowering operators, ψ_i is the ith fermion, m_i is the mass of the ith fermion, q_i is the charge of the ith fermion, and g is the gauge coupling constant, H is the physical neutral Higgs scalar and M_W is the mass of the W boson[7]

However this preliminary Lagrangian does not accurately describe the observed behaviour of particles. In order to bring the predictions of this Lagrangian in line with observed interactions two corrections were required, the first of these corrections is renormalisation. Renormalisation does not explicitly alter the Standard Model Lagrangian, instead renomalisation alters the definitions of mass(m_i) and the gauge coupling constant(g) in that Lagrangian such that they represent the apparent val-
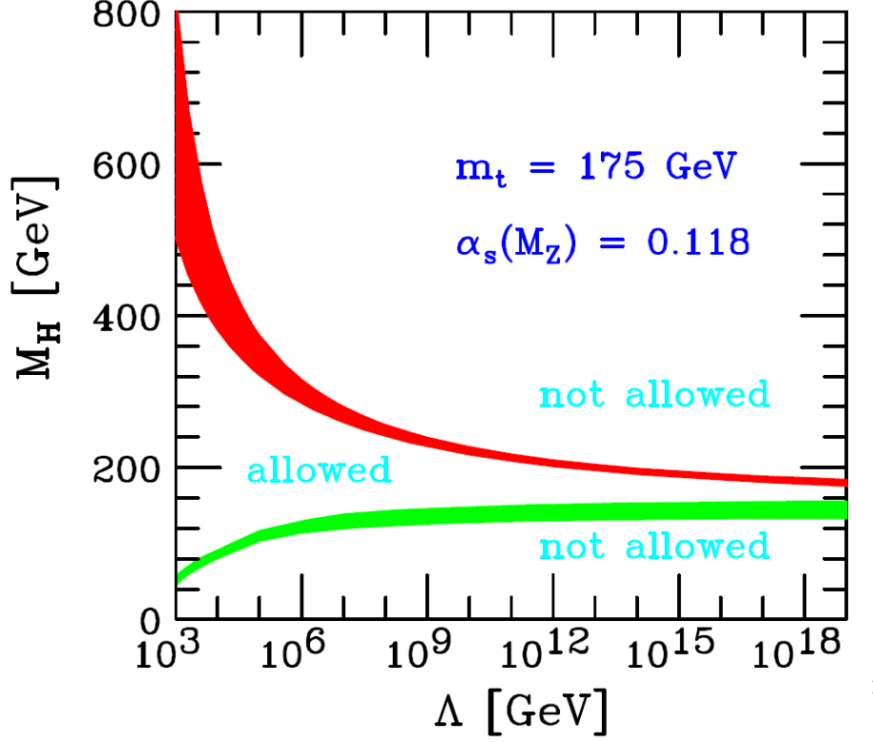
Figure 1.1: Theoretical range of the Higgs mass assuming the Standard Model remains valid up to cut-off scale Λ[8].

ues of these constants rather than absolute values[1]. The second correction was the introduction of the Higgs mechanism as described in section 1.2.1. Unlike renormalisation, introducing the Higgs mechanism adds a new term to the Standard Model Lagrangian which would alter the form of the Lagrangian shown in equation 1.1.

1.2.1   The Higgs Mechanism

A notable feature of the weak interaction is that it is extremely short ranged, only affecting particles within approximately 10^{-18}m of each other. This is explained by the fact that the gauge bosons associated with the weak interaction (the W^+, W^- and Z^0 bosons) are extremely massive, meaning that as virtual particles they can neither last long or travel far. However massive gauge bosons create a problem in that giving them explicit masses would make the Standard Model no longer gauge invariant. The solution to this problem was to introduce a new scalar field into the Lagrangian called the Higgs field which not only makes the W and Z bosons massive,

but also introduces a new boson to the Standard Model: the Higgs boson[1]. The resulting modified Lagrangian is shown previously as equation 1.1.

While the above reasoning makes the Higgs field and the Higgs boson interesting on its own, there are thought to be other implications of introducing a new field and particle. Perhaps the most interesting of these implications is the idea that massive fermions couple to the Higgs field, and this coupling acts to interfere with changes in the particles motion hence creating the inertial mass of all massive fermions[9]. Additionally, the unmodified Standard Model would predict that the cross section of several interactions would exceed unity at higher energy scales, this is demonstrated in the case of longitudinal WW scattering in figure 1.2 (note how the cross section without the Higgs increases at high energy). Adding the Higgs boson to the Standard Model model would introduce new interactions mediated by the Higgs boson, modifying higher order corrections when calculating cross sections. This ensures that predicted cross sections do not exceed unitarity (figure 1.2 demonstrates this for longitudinal WW scattering, showing a decreasing cross section at high energies)[10].

Having established the importance of the Higgs field and its associated boson, the obvious question becomes: is there any way to confirm or refute their existence. Like most particles the easiest way to establish (or disprove) the existence of Higgs bosons is to attempt to produce them, and this requires some knowledge of the mass of the Higgs (M_H). Currently it is predicted that M_H is given by[11]:

$$M_H^2 = 2\lambda v^2 \tag{1.2}$$

Where: λ is the self coupling strength of the Higgs, v is the electroweak scale

Unfortunately λ cannot be derived from any currently observed phenomena leaving both λ and M_H unknown. Despite this it is possible to place some limits on M_H through the following reasoning: for any given value of M_H the Standard Model will start to produce unphysical predictions at some energy scale. Therefore if the Standard Model is assumed to be valid up to a given energy scale Λ then there is a

range of Higgs masses which would match that assumption. In practice this means that the upper and lower limits of the Higgs mass are given by[11]:

Due to the vacuum stability condition (which means that the minima of the Higgs potential cannot be at a Higgs vacuum expectation value of zero), the upper limit of the Higgs mass is given by[11]:

$$M_H^2 > \frac{3 G_F \sqrt{2}}{8\pi^2} (2M_W^4 + M_Z^4 - 4m_t^4) log \frac{\Lambda^2}{\upsilon^2} \tag{1.3}$$

where: G_F is the Fermi constant, M_W is the mass of the W boson, M_Z is the mass of the Z boson, m_t is the mass of the top quark, and Λ is the energy scale at which new phenomena are expected to emerge.

Similarly, since vacuum energy must not tend to infinity/negative infinity at high interaction energies, the upper limit of the Higgs mass is given by[11]:

$$M_H^2 \log(\frac{\Lambda}{M_H}) \leq \frac{4\pi^2 \upsilon^2}{3} \tag{1.4}$$

Substituting currently known values into these equations produces the graph shown in figure 1.1[11].

1.2.2 Interactions

From the Standard Model Lagrangian it is possible to derive accurate models for all currently observed fundamental particle interactions. All of these interactions can be divided into two categories; electroweak interactions, and strong interactions[5].

Electroweak Interactions: According to theories formulated by Glashow, Weinberg and Salam (GWS) the weak interaction and the electromagnetic interaction are actually two facets of the same phenomena, an idea supported by the fact that the coupling strengths of the two interactions start to match at higher energies. Despite their high energy unification, on a practical level it is simpler to describe the phenomenology of the weak and electromagnetic interactions separately[5].

The electromagnetic interaction is long ranged, affects only charged particles, and is mediated via the massless photon[5]. In contrast, the weak interaction is
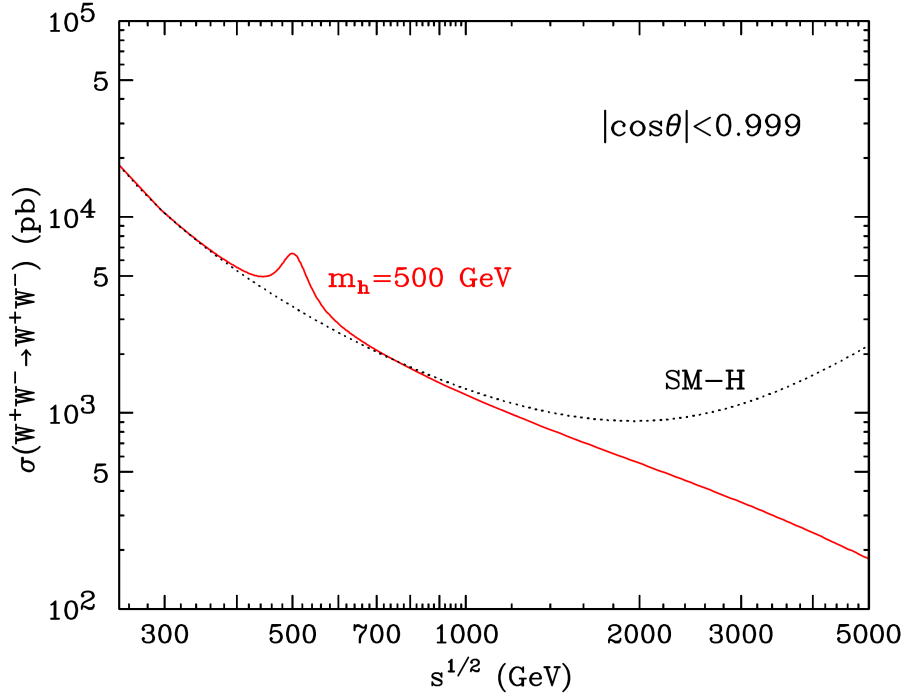
Figure 1.2: The predicted cross section of WW scattering in the Standard Model without a Higgs boson (black), and with a 500 GeV Higgs boson (red), adapted from [12].

short ranged, affects all particles, and is mediated by the massive W and Z bosons. Because W bosons are charged, weak interactions can include processes which change the charge of particles. Most notably this includes beta decays which could not occur without the weak interaction[1]. Additionally, unlike electromagnetic interactions, weak force interactions are affected by the 'handedness' of the interacting particles. Specifically, W bosons can only couple to left handed particles meaning that weak interactions involving one or more right handed particles can only be mediated by Z bosons, making such interactions less likely and rendering some processes impossible for right handed particles[9].

Strong Interactions: The strong interaction is governed by Quantum Chromodynamics (QCD), and only affects particles which possess 'colour charge', i.e. quarks, and the gauge bosons of QCD, gluons. The fact that gluons are therefore capable of self coupling leads to the force between two particles with colour charge increasing as their separation increases, and quickly becoming negligible at small separations

(this self coupling makes QCD a non-Abelian gauge theory). Because of this phenomena quarks are always found in composite particles which have no net colour. This is either due to the particle containing three quarks (one with each of the three colour charges) in the case of baryons, or containing one quark carrying one colour charge, and one anti-quark carrying the equivalent 'anti-colour charge' in the case of mesons. Collectively baryons and mesons are referred to as hadrons[5].

1.3   The Need for the ILC

The ILC is intended to be a new electron positron collider operating at the 1TeV scale in order to observe and measure new high energy phenomena. Because the ILC will not be the first machine to explore the TeV energy scale the justification for its construction is not primarily based on the dicovery of new phenomena at this scale, but rather on the new detailed observations that the ILC would make possible[13].

The ILC is often presented as a high precision counterpart to the LHC (with the LHC acting as a 'discovery' machine) and the comparison between these two machines can act as a good starting point for describing the advantages (and hence justification) of the ILC. Compared to the LHC the ILC has a relatively low centre of mass energy (1TeV after upgrades compared to 14TeV after upgrades), however the use of leptons instead of hadrons means that the centre of mass energy in the ILC is not shared amongst component particles, resulting in a comparable effective centre of mass energy. Additionally, lepton-lepton collisions should result in relatively clean events in ILC detectors with almost all particles observed in the detector being the result of hard processes (in contrast the final states of hadron-hadron collisions are complicated by debris from the incoming beam particles and initial state QCD radiation). Another implication of using leptons rather than hadrons is that while the phenomena observed at the ILC will be the same as those observed at the LHC, many of the exact couplings observed will be different, potentially providing new data[13].

Another significant feature of the ILC is the level of control that its operators
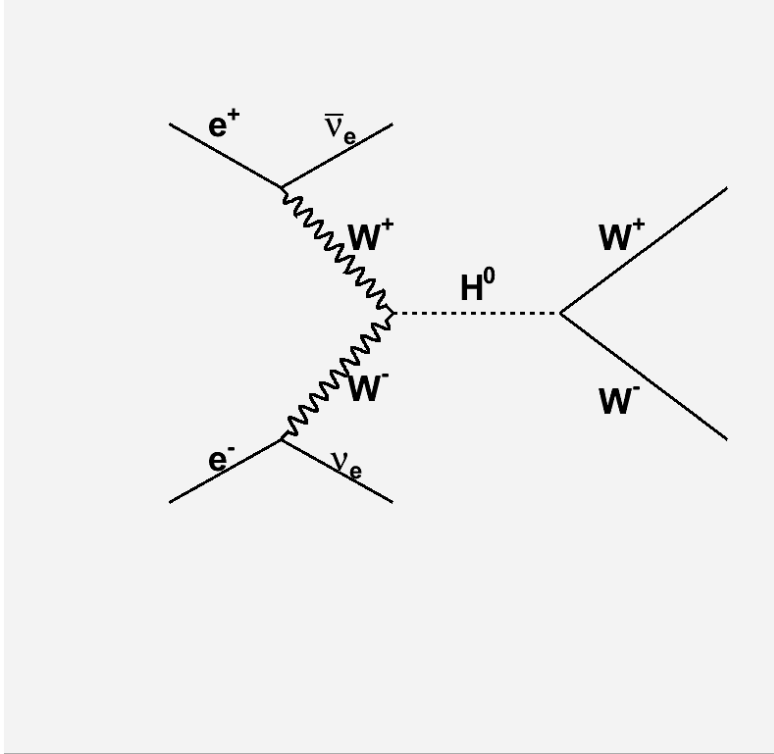
Figure 1.3: A Feynmann diagram for WW Scattering at the ILC.

will have over the interacting beams; the centre of mass energy at the ILC interaction point should be simultaneously extremely precise and highly tuneable. When combined these two characteristics should produce a machine which can scan an energy range for interesting phenomena and then reproduce any points of interest with high precision. Additionally the ILC should produce highly polarised beams (80% polarisation in electron beams, 50% polarization in the positron beams), allowing greater control over the ILC interaction point[14][8]. More information on the ILC design can be found in chapter 2.

1.3.1 WW Scattering

One of the channels which will be studied at the ILC is WW scattering (shown in figure 1.3). This interaction is of interest because as shown in figure 1.2 the cross-section of this interaction varies significantly depending on whether or not the Higgs boson exists. Therefore, if the Higgs boson is discovered this interaction is a good test to see whether or not it behaves as predicted. If the Higgs boson

is not discovered this interaction is still of interest because the behaviour of its cross-section at higher energies could provide valuable information about possible Higgsless standard models[8][15].

In order to study the cross-section of WW scattering, and in particular its centre-of-mass energy dependence, it is necessary to distinguish the its final states from the final states of other interactions which present similar topologies in the detector. The most difficult of these, accounting for 4/9 of all WW decays, will be events in which both Ws decay to hadronic jets. The separation between WW candidates and background can be achieved using methods based on measuring the invariant mass of pairs of hadronic jets, however this will require excellent measurement of the energy of jets. Using Particle Flow analysis (discussed further in section 2.3.2) a good jet energy resolution would require good energy resolution in the calorimeters (to deal with neutral particles), good momentum resolution in the momentum trackers (to deal with charged particles), and a high degree of granularity in both systems to ensure that particles appearing in the calorimeters and the momentum trackers are not counted twice[8][15].

Chapter 2

Hardware

2.1 The ILC Project

The overarching purpose of the studies described in later chapters was to develop Monolithic Active Pixel Sensors (MAPS) for use in future high energy physics projects. The most prominent future project with which MAPS is currently associated is the ILC introduced in section 1.3.

The ILC is currently in its technical design phase with a Technical Design Report (TDR) expected in 2012, at which time the basic design for the ILC, referred to as the ILC minimal machine, will be finalized. Once the TDR has been completed the process determining the site of the machine will begin (assuming adequate funding has been procured at that point). Just as the final site of the ILC is currently unknown, the dates for the construction, completion, start-up and upgrade of the ILC are all unclear at this point. It is hoped that construction of the ILC will begin some time in the next decade[13].

Although the design of the ILC has not yet been finalised it is already possible to state its basic characteristics with a reasonable degree of certainty. The ILC will consist of an accelerator system based on superconducting radio frequency (SCRF) cavities which will initially collide electrons with positrons at collision energies ranging from 200 GeV to 500 GeV, later upgrades will push the maximum collision energy to 1TeV. These accelerators (described in section 2.2 below) will
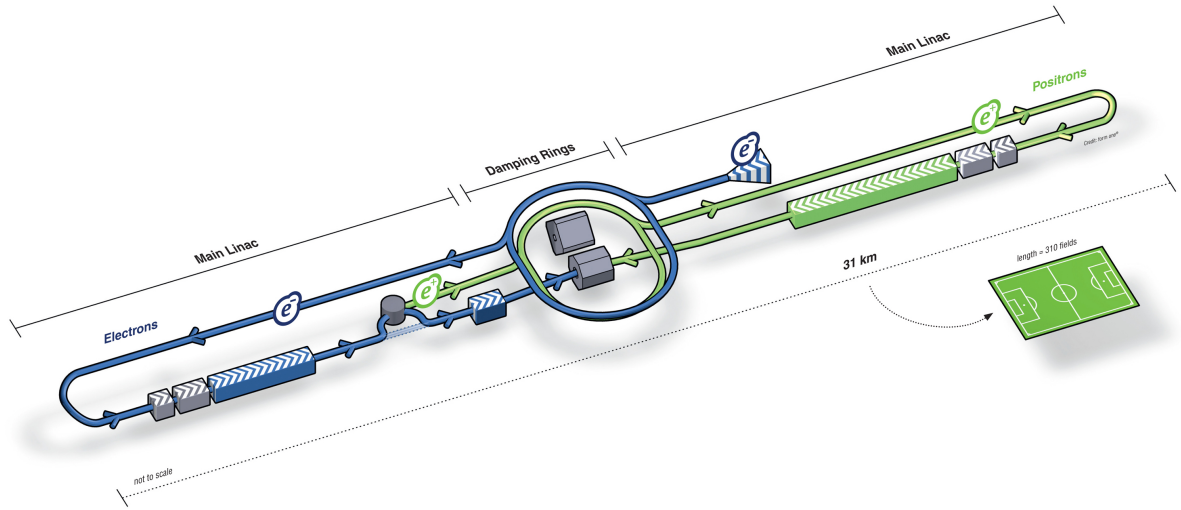
Figure 2.1: Basic Layout of the ILC[16].

feed in to two general purpose, high precision detectors which can be moved in and out of the beam interaction point as needed[13]. These two detectors are likely to be selected from the three currently proposed detector designs; the International Large Detector(ILD), the Silicon Detector(SiD), and the 4th detector, all of which are described in section 2.3[13][17].

2.2 The ILC accelerator

Like any electron positron collider the ILC accelerator must contain the following components: a mechanism for producing electrons, a mechanism for producing positrons, one or more systems for shaping these electrons and positrons into highly compact beams (in this case this task is primarily performed by the damping rings described in section 2.2.3 and focusing quadrupoles built in to the experimental detectors described in section 2.2.5), a main accelerator for accelerating the two beams up to their target centre of mass energy and finally a beam delivery system which will ensure that the beams meet at the interaction point. Additionally the ILC design includes systems for monitoring the beam in the accelerator, and since it is a linear collider, beam dumps which allow the spent beams to leave the interaction

Parameters	Nominal	High Lum	Large γ	Low P	Low Q
Particles per bunch	2.00×10^{10}	2.00×10^{10}	2.00×10^{10}	2.00×10^{10}	1.00×10^{10}
C.o.M. Energy (GeV)	500	500	500	500	500
Bunch Length,σ_z(m)	3.00E-04	1.50E-04	5.00E-04	2.00E-04	1.50E-04
Bunch Width,σ_x(m)	6.55E-07	4.52E-07	4.95E-07	4.52E-07	4.95E-07
Bunch Height,σ_y(m)	5.7E-09	3.5E-09	8.1E-09	3.8E-09	3.5E-09
Bunch Separation(ns)	307.7	307.7	307.7	461.5	153.8
Bunches Per Train	2820	2820	2820	1330	5640
Luminosity($m^{-2}s^{-1}$)	2.03×10^{38}	4.92×10^{38}	2.00×10^{38}	2.05×10^{38}	2.01×10^{38}

Table 2.1: ILC beam parameters for 500 GeV centre of mass energy. The beam parameter sets described above are the Nominal parameter set (similar to the beam parameters stated for TESLA), the High Luminosity (High Lum) set optimised for luminosity, the Large Spot (Large γ) set allowing larger beam emmitances, the Low Beam Power (Low P) set which permits operation at lower average beam power, and the Low Charge (Low Q) set which halves the charge carried per bunch while doubling the number of bunches per train[20].

point without damaging the accelerator[14].

Naturally these components must be designed and manufactured in such a way that they produce a beam that meets the ILC beam parameters given in tables 2.1 and 2.2. These parameters are considered particularly difficult to meet as they require beams that are extremely dense and precisely shaped while also producing an extremely high centre of mass energy[13][14][18][19]. Specifically the ribbonlike shape of the beams is a notable feature of the ILC, this feature is intended to maximize the luminosity of the machine relative to the background produced, but it also increases the difficulty of producing the beam[14][19].

2.2.1 Electron Source

The source of the electron beam (and indirectly the positron beam) for the ILC will be a photocathode DC gun. Once the photocathode DC gun has produced the beam electrons, normal-conducting (i.e. non superconducting) structures are used to form these electrons into bunches and accelerate them up to 76 MeV. The beam then passes into a relatively short superconducting linac which will accelerate the beam up to an energy of 5 GeV. Before being injected into the damping rings (see figure 2.1) the beam is passed through a series of superconducting solenoids which

Parameters	Nominal	High Lum	Large Y	Low P	Low Q
Particles per bunch	2.00×10^{10}	2.00×10^{10}	2.00×10^{10}	2.00×10^{10}	1.00×10^{10}
C.o.M. Energy (GeV)	1000	1000	1000	1000	1000
Bunch Length,σ_z(m)	3.00E-04	1.50E-04	6.00E-04	2.00E-04	1.50E-04
Bunch Width,σ_x(m)	5.54E-07	3.20E-07	3.67E-07	3.50E-07	3.92E-07
Bunch Height,σ_y(m)	3.5E-09	2.5E-09	7.0E-09	2.7E-09	2.5E-09
Bunch Separation(ns)	307.7	307.7	307.7	461.5	153.8
Bunches Per Train	2820	2820	2820	1330	5640
Luminosity($\mathrm{m^{-2}s^{-1}}$)	2.82×10^{38}	7.88×10^{38}	2.81×10^{38}	2.92×10^{38}	2.84×10^{38}

Table 2.2: ILC beam parameters for 1TeV centre of mass energy. The beam parameter sets described above are the Nominal parameter set (similar to the beam parameters stated for TESLA), the High Luminosity (High Lum) set optimised for luminosity, the Large Spot (Large γ) set allowing larger beam emmitances, the Low Beam Power (Low P) set which permits operation at lower average beam power, and the Low Charge (Low Q) set which halves the charge carried per bunch while doubling the number of bunches per train[20].

rotate the spin vector of the beam electrons into the vertical thus polarising the beam. Finally the beam is passed through a superconducting RF structure which compresses the energies of the beam electrons (i.e. this structure ensures that all the beam particles have roughly the same energy when they are injected into the damping ring)[14].

2.2.2   Positron Source

Unlike the electrons used to make the electron beam, the positrons used in the positron beam do not already exist and therefore need to be produced via the apparatus shown in figure 2.2. The production of the positron beam begins with extracting a fraction of the particles in the electron beam during their passage through the main linac. At the point they are extracted the electrons in the beam have an energy of around 150 GeV. These electrons are passed through a 150 metre helical undulator in order to produce 10 MeV photons before being returned to the main linac. These high energy photons collide with a rotating titanium alloy target producing electron positron pairs. At this point the particles do not form a cohesive beam and are all travelling in different directions. An Optical Matching Device (OMD) is used to re-direct these particles so that they are all travelling in (roughly) the same direc-
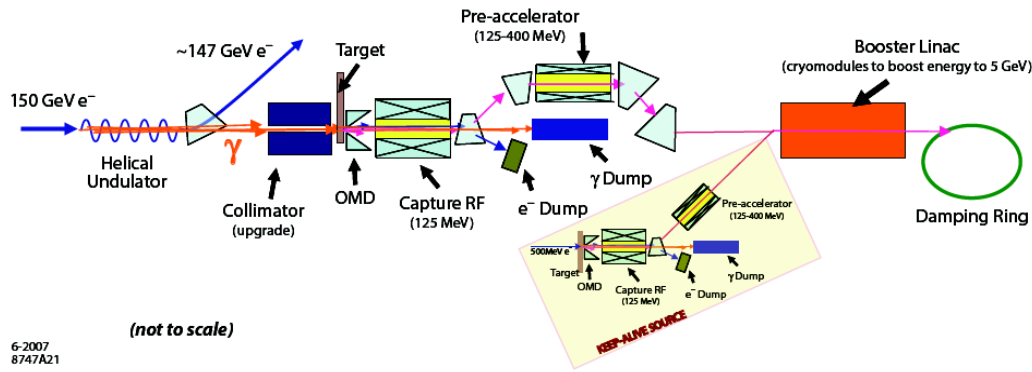
Figure 2.2: The proposed layout of the ILC positron source[14].

tion and can be passed into other components of the positron source. The resulting beam is then fed into a capture L-band RF. The capture RF accelerates the beam up to 125 MeV before the beam is split into its three components; electrons, positrons and remaining photons. The electrons and photons are discarded by bending the beam with a magnetic field and the resulting positron beam is further focused and accelerated up to 400 MeV. Finally the beam is accelerated up to 5 GeV with a linac and inserted into the positron damping ring. At present the ILC baseline design does not require the positron beam to be polarised, however upgrades may require up to 60% polarisation. This set up already produces a beam that is 30% polarised and it would be relatively easy to upgrade this to a 60% polarised beam as needed. If necessary this increase in polarisation would be achieved in the ring to main linac (RTML) system using structures analagous to those used in the electron RTML system[13][14].

2.2.3   Damping Rings and Ring To Main Linacs

The ILC baseline design includes two 6.7km circumference damping rings designed to accept 5 GeV beams from the electron and positron sources. The damping rings are designed to reduce the transverse and longitudinal emittances (the spread of beam particles both in 3D space and momentum phase space) of these beams down to the emittances required by the beam parameters described in tables 2.1 and 2.2. During normal operation each bunch train is stored in the damping rings for

36
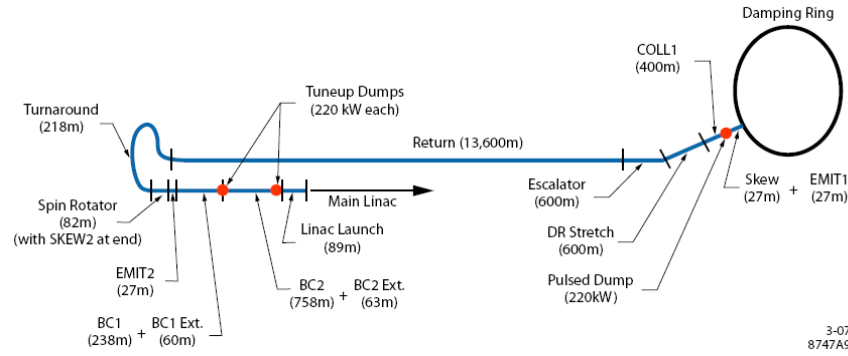
Figure 2.3: A diagram showing the layout of the proposed ILC ring to main linac system (RTML)[14].

approximately 200ms and in that time the emittance of the beam will be damped by up to five orders of magnitude. This is achieved by alternating RF accelerating cavities with 'wigglers' within the damping ring. A wiggler is essentially a series of dipole magnets with alternating polarities which rapidly change the beam trajectory causing the beam particles to emit synchrotron radiation and therefore lose energy and momentum, hence reducing emittance at the expense of reducing the overall energy of the beam. After passing through each set of wigglers the beam particles pass through an RF cavity which accelerates the particle along the beam line. This alternation between accelerators and wigglers acts to reduce the emittance of the beam without reducing its overall energy[21][14].

Once 200ms have passed the beams are injected into the Ring to Main Linac (RTML) system, a 15km beam line which takes the 5 GeV beams from the damping rings to the main linacs, the basic layout of this system is shown in figure 2.3. In addition to taking the beams from their damping rings to the main linacs the RTML also removes the 'beam halo' aquired in the damping rings, reduces the length of the bunches in the beams (the bunches produced by the damping ring are around 30 to 45 times the length finally needed at the interaction point), and rotates the polarisation of the beams as needed[14].

2.2.4 Main Linacs

The core of the ILC accelerator will be the main linear accelerators (or Linacs) which will accelerate the electron and positron beams up to their target centre of mass energy (initially 500 GeV, later this will be increased to 1TeV after an upgrade). The Linacs will have an initial combined length of around 23km, when the ILC is upgraded to increase its centre of mass energy to 1TeV the linacs will be extended by 11km each giving a total length of 45km. The main linac will be based around 1.3GHz SCRF accelerating cavities. The smallest separate unit of such technology planned for the ILC is a nine cell 1.3GHz niobium cavity roughly 1m long, approximately 17000 such cavities will be required to construct the ILC. The production of these cavities alone is a daunting task considering that so far only around 160 such cavities have been constructed. Additionally in order to function optimally these cavities must be kept at a temperature of 2K. To maintain this low temperature the SCRF cavities will operate inside dedicated cryostats referred to as *cryomodules*. At present it is assumed that each cryomodule will contain eight or nine 1m long SCRF cavities. This design is based on the SCRF cavities and cryomodules already constructed for XFEL. The cryomodules being used for the XFEL are from the third generation of their type, the fourth generation is currently under development for use at the ILC. These fourth generation cryomodules will contain a saturated helium II bath, surrounded by helium gas cooled shields to block out thermal radiation and conduction. At present the main linac will have to accelerate electrons and positrons from 15 GeV to the target beam energy of 250 GeV. This will require an average accelerating gradient of at least 31.5MV/m within the linacs. To put this requirement in context; the highest average accelerating gradient currently produced by the SCRF technology on a large scale is 25MV/m. However individual cavities producing up to 50MV/m have been manufactured implying that this technology is capable of producing the required high performance cavities. Therefore in order to meet this goal the main focus of research and development for the ILC main linac is improving the manufacturing techniques used to produce the SCRF cavities.

Present research implies that the key to producing high gradient SCRF cavities is ensuring that the inner surface of the cavity is ultra-clean and defect free. The best method found for producing these results is a process called electropolishing which has been developed specifically for the manufacture of superconducting cavities by researchers at KEK and CERN. Since this is the most promising technique for producing high performance SCRF cavities research and development on the ILC main linac is likely to focus on optimising this process[14] [13] [22].

Once constructed the whole linac will be contained in two tunnels which will be between 25m and 600m underground depending on the local topography. Due to the large amount of radiation produced by the main linac there will be a service tunnel running parallel to each beam tunnel shielded from the radiation found in the beam tunnels. The service tunnel will house equipment which might be damaged by the high levels of ionizing radiation, and/or equipment that will require regular maintenance and monitoring. This includes the RF sources which will power the SCRF cavities, typically one source will power a total of 26 cavities contained in three crymodules[14].

2.2.5 Beam Delivery System

The last component of the ILC accelerator that the beams will pass through will be the beam delivery system (BDS). The BDS is designed to take the electron and positron beams from the main linacs to the beam interaction point. The most important part of this process is ensuring that the two beams actually cross at the interaction point (very much a non-trivial achievement considering that the BDS tunnels alone are each 4.5km long and the cross section of the beams is only $3.65 \times 10^{-15} \text{m}^2$). This is largely achieved by taking precise measurements of the beam as it leaves the main linac and using these measurements to guide 'matching' mechanisms which tweak the beam trajectory based on the exact state of the beam leaving the main linac. Final focusing of the beam at the interaction point is performed by superconducting quadrupoles integrated into the experimental detectors themselves. The
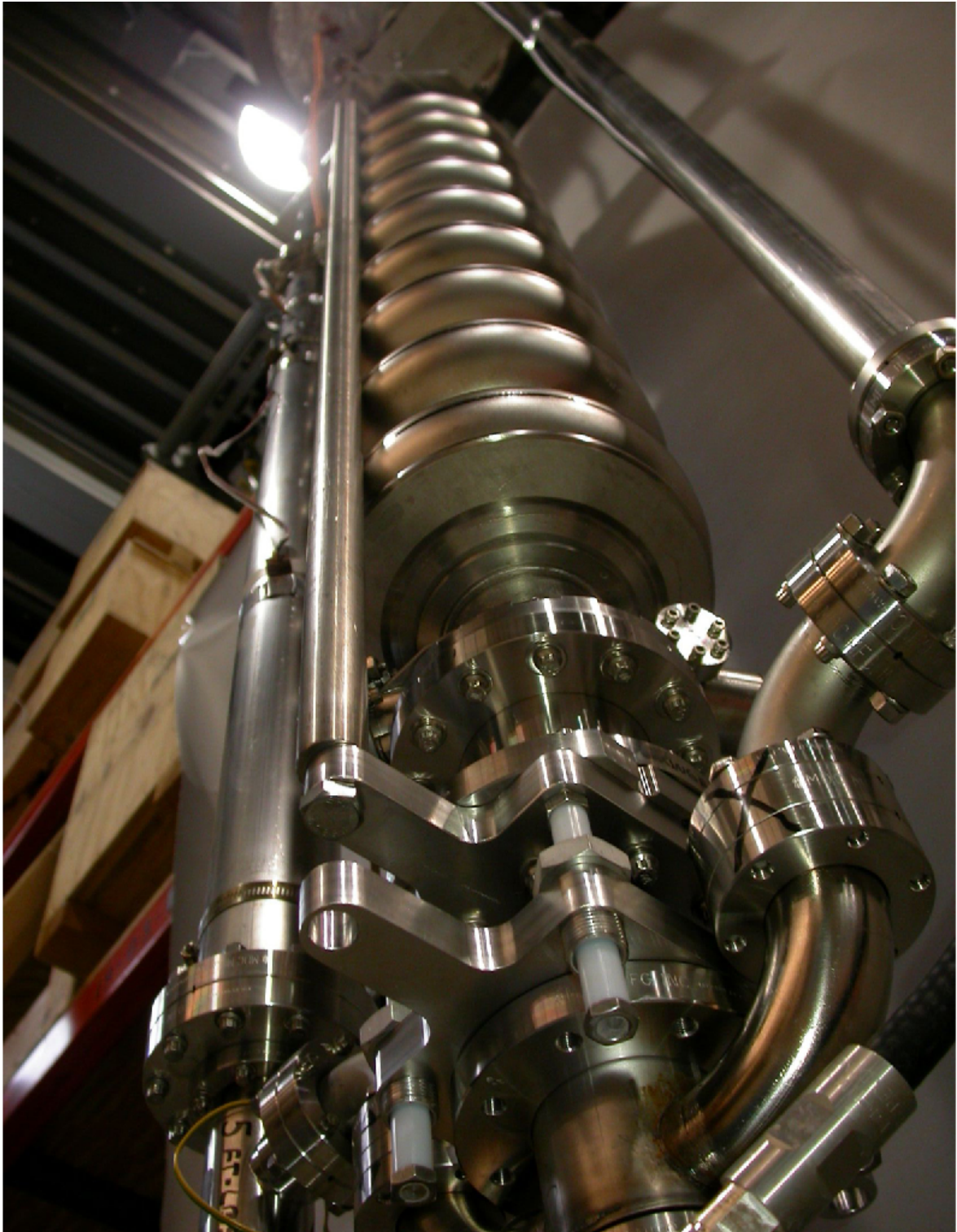
Figure 2.4: ILC SCRF cavity undergoing testing at Cornell[16].

BDS does however do more than just steering the beam into the interaction point: the key physics parameters (such as energy and polarization) are measured before and after the beams enter the experimental detectors. Additionally high amplitude (or 'halo') particles appearing after the passage of the beam down the main linac are removed via collimation in the BDS, preventing these halo particles from causing background hits in the detector. Also the BDS acts as a safety mechanism for the ILC; if there is a fault (or the beam is simply unneeded) then the BDS includes an extraction system which will redirect the beam to an auxiliary beam dump without allowing the beam to damage the accelerator or the experimental detectors. Finally after the collision of the two beams the BDS takes the badly disrupted beams from the interaction point to a pair of water cooled beam dumps [13][14].

2.3   Detectors

2.3.1   Overview

Initially there were four detector designs proposed for the ILC: LDC, GLD, SiD and 4th. The LDC and GLD concepts have since been merged into the ILD concept and this section should provided an overview of all these concepts. At present the ILC design calls for two detectors and a single interaction region, this apparent discrepancy is solved via a push-pull mechanism which will switch the detector connected to the accelerators during down time. This push-pull mechanism adds a requirement to the ILC detectors; that the detector can be regularly moved in and out of the beam-line without risking alterations in the internal alignment of the detector and without requiring regular recalibrations of the detector[15].

ILD

The ILD (International Large Detector) collaboration was created from the merging of the LDC and GLD collaborations, making the ILD the newest current ILC detector design as of Spring 2010. The main sensitive components of the ILD are the
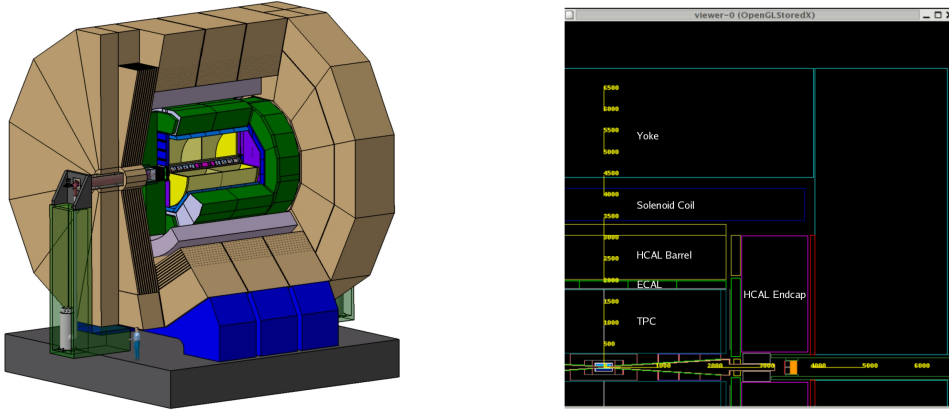
Figure 2.5: The overall intended structure of the ILD(left)[17] and a $\frac{1}{4}$ diagram showing the relative locations of major components(right)[23].

TPC, silicon based tracking detectors (together these first two components perform the momentum tracking for the ILD), silicon pixel vertex detectors, a main ECAL, a HCAL, a system of radiation hard far forward calorimeters, and either scintillator strips or RPCs integrated into an iron yoke to act as a muon detector/tail catcher. Other major components include a solenoid providing a 3.5T uniform magnetic field within the detector, and an integrated platform to allow the detector to be moved in and out of the beam[17]. These components are discussed in more detail in later sections and the relative arrangements of these components are shown in figure 2.5.

The ILD design calls for both high energy resolution for calorimeter components and high spatial resolution for all detector components to optimize event reconstruction. The mechanical design of the ILD has a high emphasis on detector stability while the detector is moved in and out of the ILC beam. Specifically the ILD is being designed to minimize the recalibration necessary when the detector is moved into the beam.[17]

GLD

The GLD detector concept was one of the four concepts which were proposed for the ILC detectors its Reference Design Report (RDR) published in 2007. Since that time the GLD collaboration has merged with the LDC collaboration to form the ILD collaboration. This means that while the GLD detector is no longer under
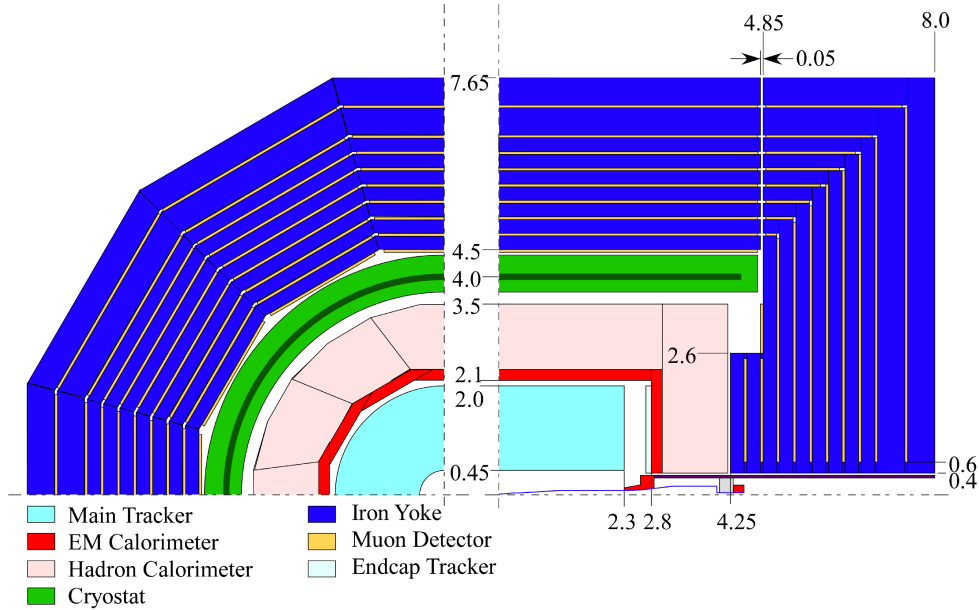
Figure 2.6: Diagram of the GLD detector[24]

consideration for use in the ILC, it is a direct forebear of the ILD concept and it is a major influence on that detector design[17]. For this reason a summary of the proposed GLD concept has been included in this chapter.

Like most ILC detector concepts the GLD detector has been designed to have both an extremely high energy resolution and an extremely high particle momentum resolution. The GLD detector would have been built around a large gaseous tracker (specifically a time projection chamber, TPC). This large chamber combined with a strong (3 Tesla) magnetic field produced by a solenoid magnet, would have given the GLD detector a sufficiently high momentum resolution[15]. The components of the GLD detector are described in more detail in later sections, and its overall structure is shown in figure 2.6.

LDC

The Large Detector Concept (LDC) was one of the four initial detector concepts proposed in the ILC Reference Design Report (RDR) published in August 2007. Since that time the LDC collaboration has been merged with the GLD collaboration (the GLD concept is discussed above) to form the ILD collaboration[17]. Even though the LDC is no longer being considered as an ILC detector design, information
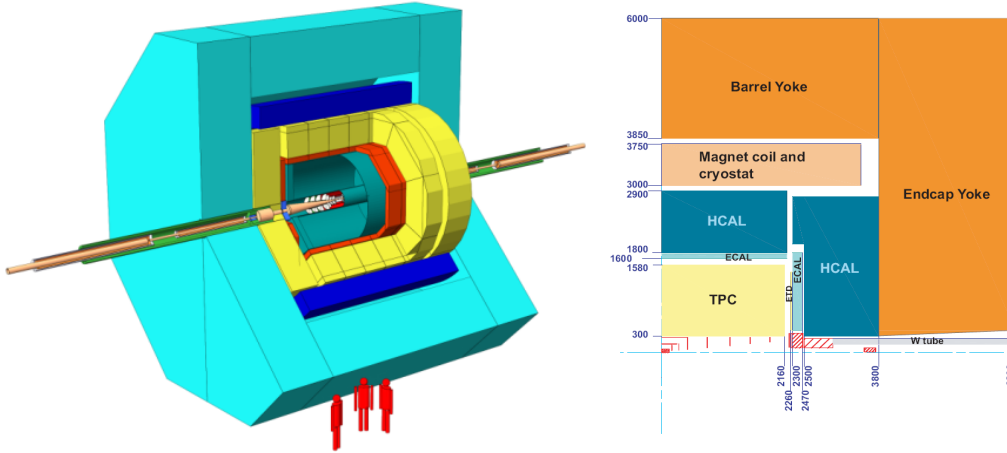
Figure 2.7: 3D diagram of the Large Detector Concept(LDC)(left) and a $\frac{1}{4}$ diagram showing the relative locations of components[15].

on the LDC is included here for two reasons; first, the relatively new ILD concept described above is a direct descendent of the LDC, and therefore information on the LDC provides useful background material. The second reason for the inclusion of the LDC in this chapter is that the study described in chapter 4 was conducted before detector models for the ILD existed, and therefore used LDC detector models as a substitute.

The LDC detector was designed with the intention of creating an extremely high momentum resolution and a high jet energy resolution in a detector. To this end the core of the LDC was intended to be a large volume time projection chamber (TPC) supplemented by a Silicon tracker and surrounded by high granularity electromagnetic and hadronic calorimeters. The calorimeters will in turn be surrounded by a coil producing a strong magnetic field (roughly 4T). Surrounding these components there would have been an iron return yoke which would also serve as a muon tracker. Each of these components is described in more detail in later subsections. The arrangement of all the LDC components at the time when the ILC RDR was published and the basic structure of the LDC at that point are shown in figure 2.7[15].

SiD

One of the remaining detector concepts currently proposed for the ILC is simply known as the Silicon Detector or SiD. The SiD concept is designed to be robust

44
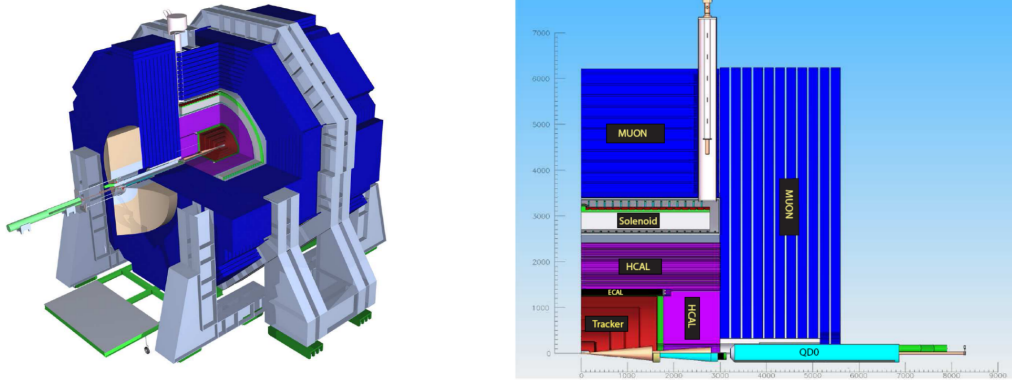
Figure 2.8: 3D diagram of the SiD concept (left), and a $\frac{1}{4}$ diagram showing the structure of the SiD concept(right). Note: on this diagram the iron return yoke of the solenoid has been labelled as the muon system because the muon system uses the return yoke for its absorber layers, meaning both systems occupy the same space.[25]

general purpose solution to the detector requirements of the ILC based on well established technologies.

One of the central themes of the SiD design is that it will be a fully integrated detector. All the relevant particle tracker components should act as a single detector; ideally the tracking of a particle from one component to another should be seamless without any data loss. The primary appeal of this design is the robustness of the detector components, the vertex detector, momentum tracker and calorimeters of the SiD concept should be able to absorb large amounts of radiation without experiencing significant problems[15][25].

4th

The 4th Concept aims to combine high detector performance with a simple versatile design. While the 4th Concept does share several detector components with other detector designs, overall it diverges considerably from the other detector concepts described in this chapter. The 4th concept detector will have just four main sensitive components unlike most detectors which typically have a large number of sub- and support components. These components are; the Pixel Vertex chamber, the time projection chamber (TPC), the Multiple Readout Calorimeters, and the Muon Dual-
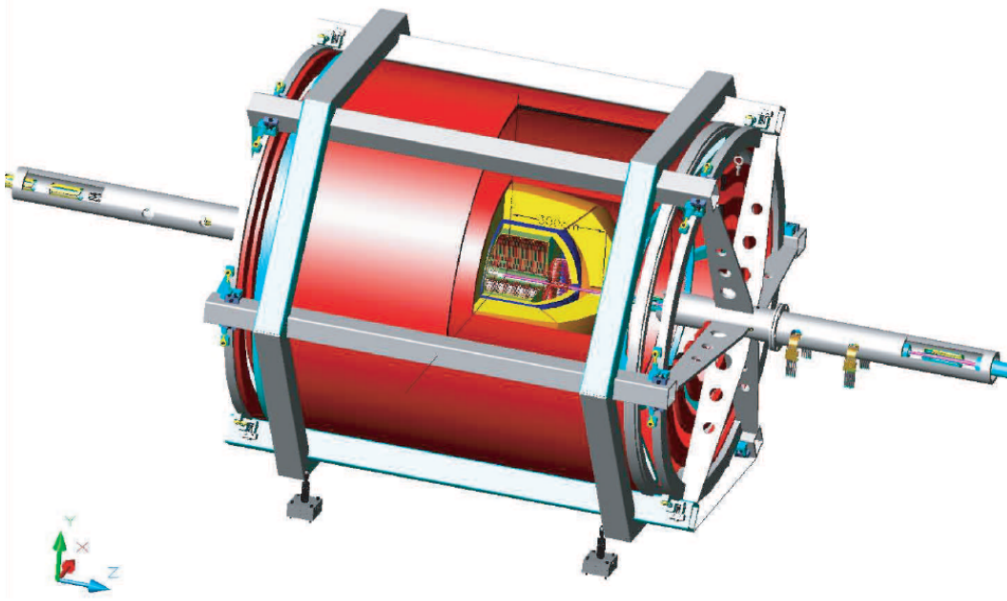
Figure 2.9: A diagram of the 4th concept detector[15]. On this diagram the Pixel Vertex Chamber is shown in blue, the TPC is shown in green, the Multiple Readout Calorimeters are shown in yellow, and the Dual-Solenoid is shown in red.

Solenoid, the relative positions of these components are shown in figure 2.9[15][26].

2.3.2 Physics Requirements

Although there is considerable variation in detector designs for the ILC, the physics goals of the experiment enforce a common set of performance requirements. These requirements can be roughly divided into the requirements for each detector subsystem, which are; the main calorimeter systems, the forward calorimeter systems, the particle tracking systems, and the vertex detectors[15].

Calorimetry Requirements

The primary characteristic which the calorimetry of an ILC detector will be based on is its jet energy resolution. Ideally the jet energy resolution of an ILC detector should be comparable to the natural decay widths of the parent particles of the jets. In the ILC this gives a target jet energy resolution of the order of 1 GeV, or in more

general terms $\sigma_E/E < 3 \sim 4\%$ (($30/\sqrt{E}$)% for jets below 100 GeV). Achieving this jet energy resolution will require significant improvements in detector performance relative to the current state of the art. This performance could be achieved through Particle Flow Analysis (PFA), where the four-vectors of all visible particles in an event are reconstructed in order to measure the energy of each particle within a jet individually, the energy of the jet is then equal to the sum of those particle energies. This provides better performance than a purely calorimetric measurement because the energies of charged particles could be measured in high resolution tracking detectors without risking double counting of their energies (neutral particles would still be measured directly by the calorimeters). While PFA could improve the jet energy resolution of a detector, the need to associate showers in the calorimeters with tracks in momentum trackers, and the need to distinguish between nearby particle showers in high energy jets would add in a new requirement for ILC calorimeters: high granularity. ILC calorimeters must have cell sizes 1cm^2 at the largest to provide the required spatial resolution. If this granularity can be achieved then the target energy resolution should be possible provided the electromagnetic optimised regions of the calorimeters have an energy resolution of ($15/\sqrt{E}$)% and the hadronic optimised regions have a resolution $> (40/\sqrt{E})$%[15].

In addition to the requirements on jet energy resolution ILC calorimeters will need to provide highly efficient lepton identification for a variety of processes. Efficient electron and muon identification will be required for studies of W and Z decays. Electron and muon identification within jets will be used to establish the presence of neutrinos produced in heavy quark decays and will contribute to flavour tagging of quark jets to identify the original quark. Efficient tau lepton identification will be more difficult to achieve than the electron or muon counterparts, however it is important because measurements of tau decays are useful for analysing tau polarization states[15].

Lepton ID with an acceptable efficiency will require the calorimeters to be highly hermetic and sensitive to Minimum Ionising Particles (MIPs). Additionally, in order to achieve acceptable lepton ID efficiencies, ILC calorimeters will need to feature

compact electromagnetic shower development in addition to the good granularity and electromagnetic energy resolution requirements already mentioned[15].

Very Forward Calorimeter Requirements

Calorimeters in the forward regions of the ILC detectors fall into three distinct categories each with its own role in the detector, these categories are referred to as the Lumical, the Beamcal and the Gamcal. The Beamcal is located close to the beam axis and exists primarily to monitor the ILC beams as they enter the detector. It is intended that the Beamcal and the Gamcal will be used together to measure the luminosity of the beams on a per bunch basis. The Beamcal contributes to this measurement by recording the amount of energy deposited on the Beamcal by electron positron pairs generated by beam-beam interactions. At the same time the Gamcal measures how much energy is deposited by the photons created in the same beam-beam interactions. These two measurements are then combined to produce the final 'bunch-by-bunch' luminosity measurement[15].

Other beam parameters are measured by analysing the distribution of energy deposited in the Beamcal and Gamcal. In order for the Gamcal and the Beamcal to be used in this way they must be read out after each bunch crossing which will require new developments in fast readout electronics. Additionally the Beamcal can be used (in conjunction with other detector components) to search for new particles where the final state has considerable missing energy and/or momentum, or where energetic particles are created with low transverse momentum. To be useful in this capacity the Beamcal must to be able to pick out high energy electrons from the large quantity of background e^+e^- pairs produced by beam-beam interactions, this will require a physically dense and finely segmented Beamcal. In addition to these requirements the Beamcal and Gamcal both need to be able to operate very close to the ILC beam axis. Therefore both systems must be able to withstand the large numbers of e^+e^- pairs and photons created by beam-beam interactions. In total it is estimated that these sensors will absorb up to 10MGy per year, this means that a significant aim for far forward calorimeter development is to develop sensors which

can maintain uniform performance regardless of the dose absorbed[15].

The role of the Lumical is to improve the hermiticity of its detector by increasing the detectors angular coverage, and to provide fast luminosity measurements. The Lumical should be located further from the beam axis than the Beamcal and Gamcal to avoid the e^+e^- pairs and photons created by beam-beam interactions and will measure the luminosity of the beams ILC by counting Bhabha events[15].

Tracking Requirements

As with any experiment, high resolution measurements are desirable because they allow the experiment to produce high precision results for fewer measurements than would otherwise be required. Translated into particle physics terms, high resolution measurements give the experiment a boost to effective luminosity. The target for charged particle momentum resolution is $\Delta p_t/p_t^2 = 2 \times 10^{-5} \text{GeV}^{-1}$, a value that is well beyond the current state of the art[15].

Vertex Detector Requirements

The principle role of vertex detectors used in any ILC detector will be to reconstruct vertices and assist in characterising tracks. In order to provide adequate performance in these areas the vertex detectors used in any ILC detector will require an impact parameter resolution of $5\mu m \oplus 10\mu m/p(\text{GeV/c})\sin^{2/3}\theta$. Additionally, in order to properly reconstruct all the vertices involved in heavy particle production any ILC vertex detector will need to be highly efficient and will need to have good angular coverage of the interaction region[15].

In addition the need to operate in the environment close to the ILC interaction region represents a significant technical challenge for ILC vertex detector design. While the expected data rate and radiation load for a detector in this region should not be a problem for current detector technology, the amount of background hits created by e^+e^- pair production could be problematic. Specifically, the number of hits created in this way could easily overwhelm any attempts to reconstruct vertices if they are not properly managed. In order to deal with this problem the

vertex detector will be designed to eliminate background hits by having a very high time resolution. This high time resolution should ensure that only background hits which occur almost simultaneously with interesting events need to be analysed while the rest can be safely discarded. This high time resolution will require readout technology significantly faster than the readouts used in traditional pixel vertex detectors[15].

Whole Detector Requirements

In addition to the requirements previously listed there are some requirements which apply to the detector as a whole (although these requirements often motivate requirements for individual detector systems). Most notably, ILC detectors will require a high degree of hermeticity in order to be used for particle flow calorimetry. Since particle flow calorimetry is thought to be necessary to achieve the high energy resolution needed by the ILC, hermeticity has become a requirement for all detector designs. Another overall requirement is that any detector components inside the calorimeters of an ILC detector must be constructed using minimal amounts of material to ensure that they do not interfere with the performance of those calorimeters[15].

2.3.3 Calorimetry

ILD

The calorimeter of the ILD concept is divided into an inner ECAL (elecromagnetic calorimeter) and an outer HCAL (hadronic calorimeter). Both calorimters are further subdivided into a cylindrical barrel and a pair of flat endcaps. In the ECAL these sections are comprised of large modules (one for each endcap and eight in the barrel) all maintaining large regions of overlap with their adjacent modules when viewed from the centre of the detector to maximize the hermeticity of the detector. The positioning of these modules is shown in figure 2.10. The ECAL used will either be a scintillator-tungsten design or an analogue silicon-tungsten design which could potentially be swapped with a digital MAPS silicon-tungsten design. In all cases the
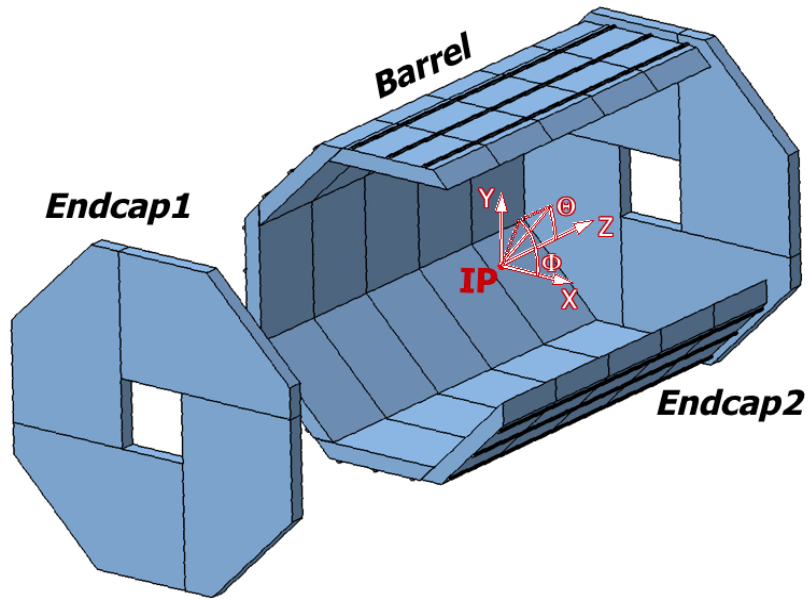
Figure 2.10: One potential arrangement of detector modules in the ILD ECAL[17].

ECAL is expected to have 30 layers of sensitive material interleaved with tungsten absorbers for a total depth of 24 radiation lengths. In both the scintillator-tungsten design and the analogue silicon-tungsten design the sensitive layers of the ECAL are expected to be segmented into 5mm to 10mm wide pixels[17], if they are used, MAPS pixels are likely to be significantly smaller at $50\mu m$ wide[27].

The HCAL for the ILD is intended to be based on layers of steel absorbers interleaved with either scintillator tiles or gaseous detectors as the sensitive components. This gives a total detector depth of 5.5 to 6 interaction lengths in the HCAL preceded by one interaction length in the ECAL[23]. Like the ECAL, the HCAL components can be separated into the barrel and the endcaps and like the ECAL, the barrel and endcaps of the HCAL are both subdivided into a number of modules. Although the exact number and arrangement of the HCAL modules had not been finalized when the ILD letter of intent was published, the two leading possibilities are shown in figure 2.11[17].
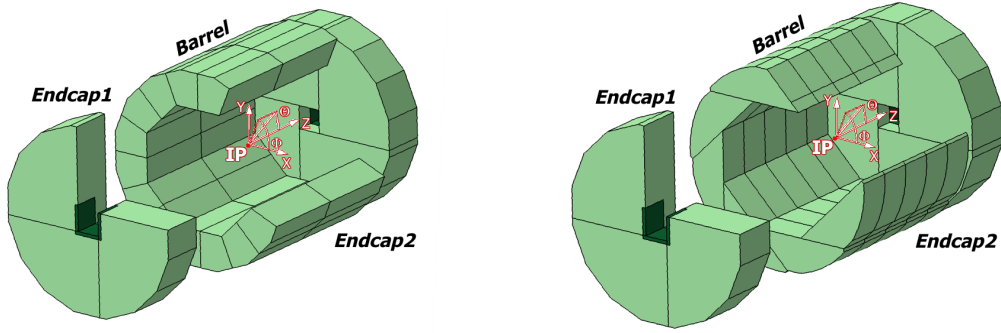
Figure 2.11: The two potential arrangement of detector modules in the ILD HCAL[17].

GLD

The calorimetry in the GLD concept was to be handled by two systems; the ECAL and the HCAL. The ECAL of the GLD detector would be positioned outside the main momentum trackers and inside the HCAL. The ECAL was to be composed of 30 alternating layers of absorber plates and scintillator detectors separated into barrel and endcap regions. The absorbers would have been composed of either tungsten or lead and the scintillator layers were to be composed of $1 \times 4cm^2$ scintillators with each layer positioned at a right angle compared to the previous layer to give an effective $1 \times 1cm^2$ cell size. The total depth of the GLD ECAL would have been 27 radiation lengths[15].

The GLD hadron calorimeter followed a similar design, it was to be composed of 46 alternating layers of lead absorber and scintillators for a total detector thickness of 5.8 interaction lengths in the HCAL (in addition to approximately one interaction length in the ECAL). In the standard GLD design the scintillator layers would have been composed of $1 \times 20cm^2$ scintillator strips interleaved with $4 \times 4cm^2$ tiles. A potential alternative to this design would have been a digital hadron calorimeter, this would have replaced the previously mentioned scintillator structure with a structure entirely based of scintillator strips. This design could have reduced the cost of readout electronics, but at the point when the ILC RDR was published it was still

unknown what scintillator strip length and width would have been needed to make the digital HCAL viable[15].

LDC

The LDC calorimeters can be divided into two categories; the ECAL and the HCAL. The ECAL for the LDC was the innermost calorimeter and was to be constructed from alternating layers of sensitive silicon and tungsten absorber plates. The whole ECAL was to consist of thirty layers of sensors and absorbers arranged into a cylindrical barrel region and endcap plates in each forward region. There would have been 29 absorber plates composed of either tungsten or lead, the first 20 absorber layers would each be $0.6X_0$ thick and the last 9 absorber layers would have each been $1.2X_0$ thick, the whole ECAL would have been 23 radiation lengths thick. Prior to the merging of the LDC and GLD concepts a MAPS was developed as a possible alternative to analogue silicon sensors for the LDC ECAL[15].

The HCAL proposed for the LDC would have been based on alternating layers of iron absorbers and sensitive layers, with the sensitive layers either being composed of scintillators or gaseous detectors. The total depth of the LDC HCAL would have been 4.6 interaction lengths with an additional interaction length within the ECAL. The barrel region of the HCAL would have been composed of two half barrels and the barrel would have been closed by a flat endcap in each forward region. The HCAL would be outside the ECAL, occupying the space between the ECAL and the solenoid cryostat[15].

SiD

The SiD calorimeters are divided into three systems; the ECAL, the HCAL and the forward calorimeters (the LumCal and BeamCal) described in section 2.3.4. The SiD ECAL will be made from 30 alternating layers of tungsten absorbers and large area silicon diode detectors for a total detector depth of 29 radiation lengths (approximately one hadronic interaction length). This kind of high granularity Silicon-Tungsten ECAL is likely to produce an exceptionally high performance calorimeter,

however this kind of calorimeter can also be expensive to produce due to the large quantity of high quality silicon required. The SiD HCAL will be composed of 40 alternating layers of steel absorbers and resistive plate chambers (RPCs) for a total detector depth of four interaction lengths[15][25]. The arrangement of both these systems can be seen in figure 2.8.

4th

The multiple readout calorimeters of the 4th Concept detector will be sampling calorimeters using fine grained dual readout quartz fibres as the sensitive components. These fibres will use both cherenkov light and relatively conventional scintillators to make energy measurements of particle showers, and should be able to disentangle hadronic showers into electromagnetic and hadronic components through this dual readout system. While the dual readout calorimeters are intended to function as a single device, it is expected that the inner regions of this calorimeter will be optimised as an electromagnetic calorimeter, while outer regions will be optimised as a hadron calorimeter. The effective depth if the calorimeter will be 27 radiation lengths (one interaction length) in the (inner) electromagnetic section, and 9 interaction lengths in the (outer) hadronic section[15][26].

2.3.4 Far Forward Calorimeters

ILD

The role of the ILD forward detectors (specifically the forward calorimeters) is to monitor the beam, establishing the exact interaction energy at any given moment. The calorimeters used for this role are referred to as the BeamCal, the LumiCal, and the GamCal, the arrangement of these components is shown in figure 2.12. The BeamCal is designed to produce a relative luminosity measurement while the LumiCal produces an absolute normalised luminosity measurement. The GamCal detector is intended to be positioned 100m 'downstream' from the detector to assist with beam tuning. Additionally the LHcal extends the HCAL to angles very close
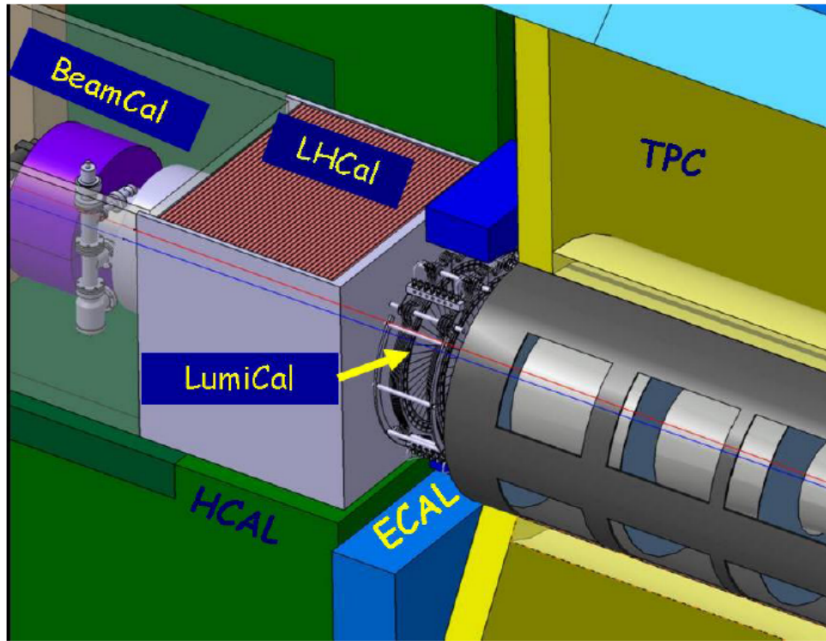
Figure 2.12: The arrangement of detector components in the far forward region of the ILD[17]. In the region shown in this diagram is such that the nearest point where a particle beam enters the detector is somewhere to the left of the region shown, and the interaction point is to the right of the region shown.

to the test beam also improving the hermeticity of the detector.[17]

GLD

The forward calorimeters of the GLD detector would be divided into the FCAL and BCAL as shown in figure 2.13. The FCAL would be positioned so that it would avoid most of the background caused by the electron positron pairs created by beam-beam interactions, and would be composed of 55 layers of sensitive silicon interleaved with tungsten absorbers. The BCAL would have been positioned closer to the beam axis next to the beam focusing magnets, and it is probable that the BCAL would have used the same technology and basic design as the FCAL, although the number of sensitive layers would be reduced to 33. However it was possible that the BCAL might require greater radiation resistance than would be possible with this technology, this problem could potentially have been solved by replacing the silicon sensors with more radiation hard counterparts such as diamond sensors[15].
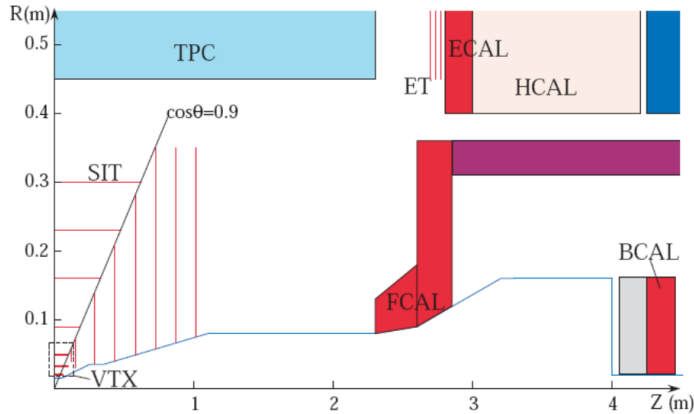
Figure 2.13: Diagram of the GLD detector near to the beam axis. Note: the R and Z axes of this diagram use different scales[15].

LDC

The LDC forward calorimeters were to consist of three separate systems; the LumCal, the BeamCal and the LHCAL. The BeamCal and the LumCal were both intended to be electromagnetic calorimeters with the BeamCal closest to the beam pipe and the LumCal covering larger angles. The LHCAL was to be a hadronic calorimeter covering the same range of angles as the LumCal. Together these calorimeters were to increase the hermeticity of the detector, shield the rest if the detector from backscattered particles, and monitor the electron positron pairs produced by beam-beam interactions. Additionally, as its name suggests the LumCal was intended to monitor the luminosity of the beams via small angle Bhabha scattering[15].

SiD

Calorimetry in the forward region of the SiD detector is handled by the LumCal, and BeamCal systems. In addition to extending calorimeter coverage to very small angles relative to the beam axis these calorimeters also serve to measure the luminosity of the beam. Instantaneous measurements of beam luminosity are made using the BeamCal system by recording the numbers and characteristics of electron positron

56
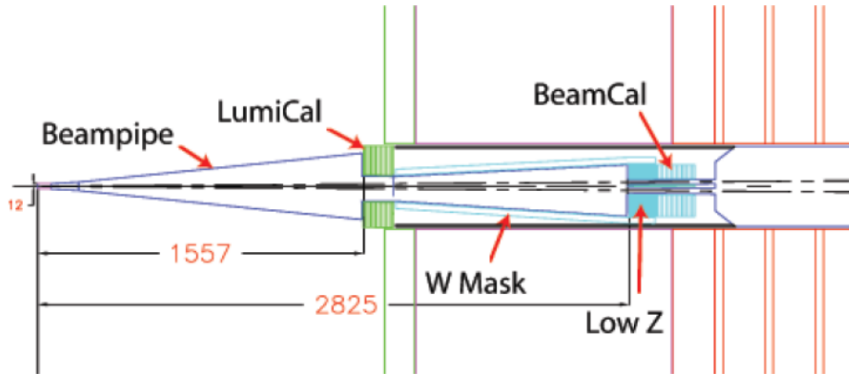
Figure 2.14: A diagram showing the placement of the forward calorimeters of the SiD detector relative to the beam line[25].

pairs created by beam-beam interactions. Precision measurements of the integrated luminosity are made by monitoring Bhabha events using the LumiCal system[25][15]. The arrangement of the forward calorimeters is shown in figure 2.14.

4ᵗʰ

As of its most recent LOI (March 2009), the 4th concept detector will use the same forward calorimeters as the ILD concept.

2.3.5 Momentum Tracking

ILD

The momentum of particles passing through the ILD will be primarily measured by three detector systems; the TPC, and two silicon based tracking detectors. Of these components, the system is primarily based around the TPC with the silicon trackers serving to extend the depth of the tracking system (both inwards and outwards) and

to extend the tracker into forward regions of the detector to cover small angles away from the beam line. The arrangement of these systems is shown in figure 2.15[17].

The TPC was selected as the centerpiece of the momentum tracking system due its high momentum resolution (created by the large number of points recorded per track in the TPC), and the minimal impact the TPC has on the energies of particles passing through. In the barrel region the TPC is bracketed by two silicon tracking detectors; the Silicon Internal Tracker (SIT) and the Silicon External Tracker (SET). The SIT system is positioned between the vertex detector and the TPC, similarly the SET system is located outside the TPC and provides the interface between the TPC and the ECAL. In addition to providing connections between other detector components, both the SIT and SET improve the momentum resolution of the detector by providing additional measurement points, and both provide time stamping information to tag each event. Both systems are based on three layers of silicon strips[17].

Momentum tracking in the forward regions of the detector is handled by two silicon tracker systems; the Forward Tracking Detector (FTD) and the Endcap Tracking Detector (ETD). The FTD system will consist of seven sensor disks positioned along the beam line, inside the the TPC as shown in figure 2.16. The primary role of the FTD system is to extend the coverage of the momentum tracker to very small angles away from the beam. Conversely the function of the ETD system is, like SET system mentioned previously, to provide an interface between the TPC and the ECAL whilst simultaneously providing additional data points for momentum tracking. To this end the ETD is positioned between the TPC and the ECAL endcap as shown in figure 2.15[17].

GLD

Momentum tracking in a GLD detector would be primarily handled by a large TPC supplemented by a silicon strip particle tracker. The TPC was expected to have an inner radius of 40cm and an outer radius of 200cm. Non-spiralling tracks detected in the TPC were expected to be defined by at least 200 points, and the spatial
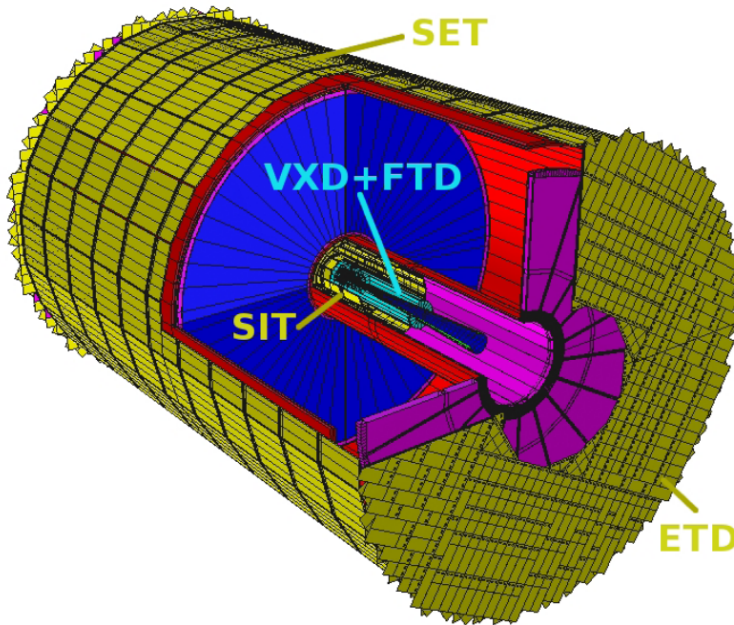
Figure 2.15: The proposed arrangement of the momentum tracking systems in the ILD concept, the blue section is the TPC[17].

resolution of the TPC in the $r - \phi$ plane was expected to be between 50μm and 150μm[15].

The silicon tracker was to be located inside the inner radius of the TPC and outside the vertex detector. This system would consist of two components; the Barrel Inner Detector (BIT) and the Forward Inner Detector (FIT). The BIT was intended to act as an interface between the TPC and the vertex detector in the barrel region, and would consist of four layers of silicon strip detectors with an innermost radius of 9cm and an outermost radius of 30cm. Like the BIT, the FIT was intended to act as an interface between the TPC and the vertex detector in the forward region, additionally parts of the FIT would be positioned close to the beam axis to extend the angular coverage of the momentum tracker systems. The FIT would consist of seven layers of disks, the technologies used for this detector had not been determined at the point when the ILC RDR was published, but were assumed to be a mixture of pixel sensors and strip sensors[15].
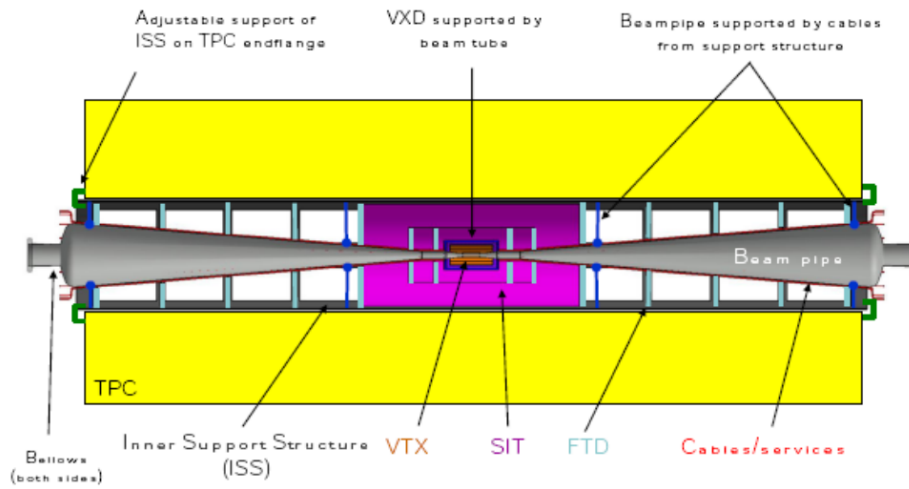
Figure 2.16: The proposed arrangement of the inner subsystems of the momentum tracking systems in the ILD concept[17].

Additionally, the design called for several layers of silicon strip detectors between the TPC and the ECAL endcap to act as an interface between the two systems. This Endcap silicon Tracker (ET) would also be used to improve momentum resolution for particles which registered relatively few hits in the TPC[15].

LDC

Momentum tracking in an LDC detector would be handled by three systems; the silicon trackers, the TPC, and a forward tracker system. The momentum tracking system closest to the beam axis (surrounding the vertex detector would be the silicon tracker. This system would consist of two layers of concentric silicon strip detectors surrounding the vertex detector in the barrel region, and six silicon disks (at least two of which would be pixel detectors) covering the forward region. This system would serve as an interface between the vertex detector and the TPC as well as providing tracking close to the beam axis due to the small inner radius of the

forward silicon disks[15].

The next furthest system from the beam line, and the system which would provide the largest amount of tracking data, was the TPC. This system was designed to provide both robust pattern recognition and high momentum resolution. To this end the TPC was expected to record over two hundred points per track, with a spatial resolution in the $r - \phi$ plane in the 100μm range[15].

The final component of an LDC detectors momentum tracking system would be an additional chamber behind the TPC endplate. At the point when the ILC RDR was published the technology to be use for this component had not been decided. This system would have served as an interface between the TPC and the ECAL endcaps, and would have improved the polar angle definition of forward going tracks[15].

SiD

The most notable difference between the SiD concept and the concepts previously discussed is that the SiD detector will not include a TPC for momentum tracking. Instead of the combined silicon tracker/TPC systems found in most other detector concepts, the SiD concept will use an integrated momentum tracker based around a large silicon tracking sensor[25][15].

This integrated tracker will be composed of two systems; the main tracker, and the ECAL. The main tracker will system surround the vertex detector with five layers of silicon microstrip sensors, these sensors will collect the majority of the information used to measure particle momentum. The arrangement of the vertex detector and the main tracker is shown in figure 2.17. Because the vertex detector is not expected to identify all particle tracks, information from the ECAL would be used to identify some particle tracks (as of 2007 it was estimated that approximately 5% of tracks are missed by the vertex detector because they come from neutral particle decays)[25][15]. Since it will be primarily used for calorimetry, the ECAL is described in more detail in section 2.3.3.

4ᵗʰ

The TPC of the 4th concept detector will (aside from the vertex detector) be the only momentum tracker in the detector. The 4th concept TPC design is intended to be similar to the TPCs developed for the LDC and GLD designs, described in this section. This TPC should provide a high level of precision while having little impact on particles passing through, and it is hoped that a sufficiently high precision machine should negate the need for any auxiliary detectors[15][26].

2.3.6 Muon Trackers

ILD

Like the LDC and GLD designs that preceded it, the ILD muon tracker is designed to use the iron of the solenoid yoke as an absorber for the system, interleaving the iron of the yoke with sensitive layers. This system is likely to include ten sensitive layers, each layer separated from the next by 10cm of absorber. Since the iron yoke being used as the absorber is intended to be 275cm thick, only the innermost part of the yoke will be instrumented in this way. The design also includes smaller numbers of sensitive layers interleaved with the iron yoke at greater radii, potential arrangements of the ILD muon tracker layers can be seen in figure 2.18[17].

The technology to be used for the sensitive layers of the muon system has not yet been determined. The sensitive layers will require a spatial resolution in the 1cm range and a temporal resolution in the 1ns range. Additionally, due to the large area covered by the muon tracker layers, the sensors used must be reliable and reasonably inexpensive. Designs currently under consideration will either use extruded scintillator strips or gas detectors, the gas detectors in question are likely be either resistive plate chambers (RPCs) or plastic streamer tubes (PSTs)[17].

GLD

The muon trackers of the GLD detector were to be based on scintillator strips interleaved with the iron of the solenoid return yoke as shown in figure 2.6. This

system would have had a total of nine scintillator layers spaced evenly throughout the 2.5m thick return yoke[15].

LDC

The LDC muon trackers were intended to use the iron of the solenoid yoke as absorbers as shown in figure 2.7. In order to detect muons these iron layers would be interleaved with some sort of sensitive detectors, however as of August 2007 no single technology had been selected for this purpose (although resistive plate chambers were a strong candidate). The sensor technology used for this purpose would need to be reliable, sturdy, and due to the large area covered, inexpensive[15].

SiD

The SiD muon tracker is intended to use the iron of the solenoid return yoke as an absorber, interleaving the steel plates with sensitive layers. Since there are 11 steel layers in the solenoid return yoke, this should result in $10 - 12$ sensitive layers in the muon system. These sensitive layers will either use scintillator strips or double layered Resistive Plate Chambers (for a total of 20 to 24 RPC layers) to detect particles with a spatial resolution of at least $1 - 2$cm per layer[25][15]. The location of this system relative to other components is shown in figure 2.8.

4$^{\text{th}}$

In the 4th detector concept particle tracks within the muon tracker will be recorded by high spatial precision drift tubes. It is hoped that combined with the magnetic field in this muon tracker (-1.5T), this system should be able to produce a second momentum measurement independent of the TPC[15][26].

2.3.7 Vertex Detectors

ILD

The technology to be used for the vertex detector (or VTX) of the ILD concept has, at the point when the ILD letter of intent was published, not yet been identified. Whatever technology is finally used will need to produce a detector which is highly granular and radiation resistant, while simultaneously having a negligible impact on the energy of particles passing through, and not being susceptible to saturation by background[17].

GLD

The GLD vertex detector would be situated inside the TPC and the silicon tracker systems, and would have consisted of three 'doublet' layers, each doublet consisting of two sensor layers separated radially by 2mm. These sensor layers would have used fine pixel CCDs with a per pixel area of roughly $5 \times 5 \mu m^2$. This system was to have an inner radius of 20mm and an outer radius of 50mm[15].

LDC

The LDC vertex detector would be situated inside the innermost silicon trackers, and would surround the interaction point with gaps for the beams to enter and leave. This detector would be arranged in five concentric layers with radii varying from 1.55cm for the innermost layer, to 6cm for the outermost layer. When the ILC RDR was published the technology to be used in this detector had not been determined, any detector used would have needed to provide high precision whilst minimising material (to reduce interference with other detector systems)[15].

SiD

The SiD vertex detector is primarily intended to identify tracks which can be picked up by the main tracker, and is composed of several layers of pixel detectors (five layers in the barrel region, four in each endcap as shown in figure 2.17)[15][25].
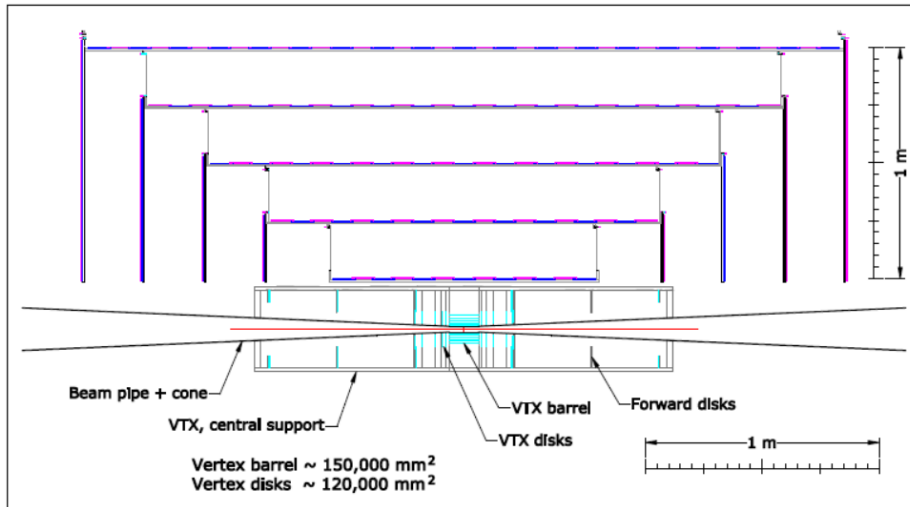
Figure 2.17: A diagram showing the inner components of the SiD detector[15].

4th

4th

The pixel vertex chamber will be a silicon pixel detector sharing a design with the vertex detector used in the SiD concept shown in figure 2.17 (note: the silicon tracking detector shown in the same diagram is unique to the SiD concept). This detector will be composed of thin silicon wafers each of which is composed of $15\mu m \times 15\mu m$ pixels and is used for particle tagging and vertex reconstruction[15].

2.3.8 Solenoid

ILD

As noted previously the ILD design calls for a uniform 3.5T field within the detector. This field will be produced by a superconducting solenoid shown in figure 2.18. As shown in the aforementioned figure the iron yoke of the solenoid is divided into the barrel yoke and the endcap yokes. The barrel yoke will be constructed in three separate sections while the endcap yokes will consist of two sections each. The
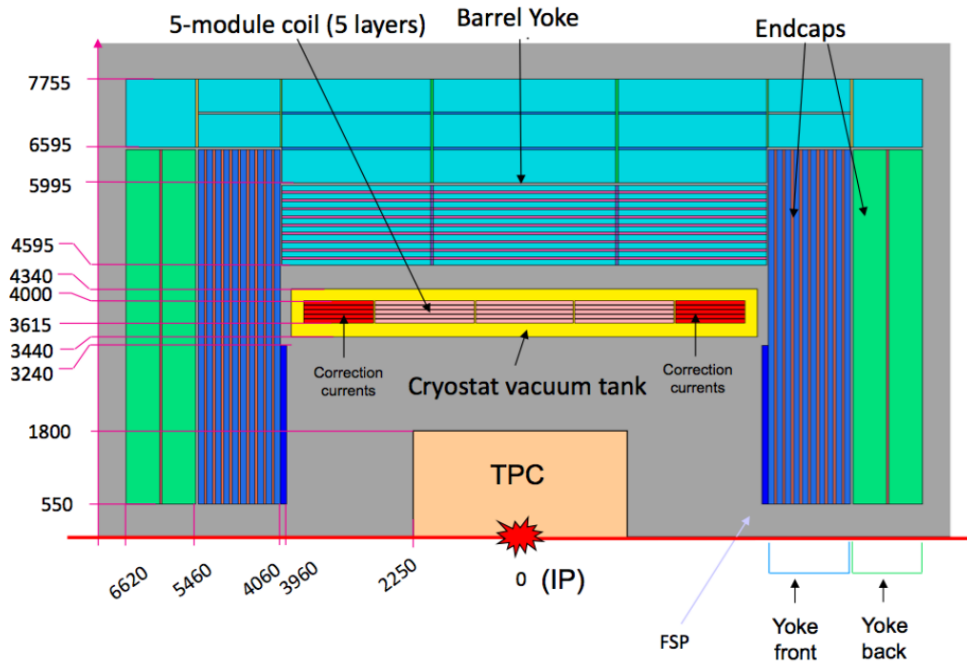
Figure 2.18: The proposed layout of the ILD solenoid[17].

coil is to be constructed in five sections (although all sections of the coil are to be electrically and mechanically connected in the final machine). Additional currents are to be induced in selected sections of the coil so that the main solenoid can also act as its own correcting magnets, hence ensuring that the field produced is uniform within the detector[17].

GLD

The GLD detector would have included a uniform 3T field within the detector. This field was to have been generated by a superconducting solenoid situated outside the momentum trackers and calorimeters. The main coil was to have been integrated with smaller correcting coils at the ends of the coil in order to maintain a uniform field within the detector. The surrounding iron yoke is shown in figure 2.6 and would have been used as the absorber in the muon tracker mentioned above[15].

LDC

The LDC Solenoid was intended to produce a uniform 4T field within the detector. The design selected for the LDC solenoid was similar to the solenoid currently used by the CMS detector at the LHC. The LDC solenoid would have consisted of the barrel yoke (constructed in three sections), the endcap yokes (each constructed in two sections) and the superconducting coil (constructed in five sections). Additional currents were to be induced in particular sections of the coil to act as correcting coils to maintain a uniform magenetic field within the detector[15].

SiD

The solenoid of the SiD detector is expected to produce a uniform 5T magnetic field within the detector. This unusually strong field is intended to compensate for the relatively small size of the detectors momentum trackers (a design feature which was in turn motivated by the high cost of the raw materials for the detector). The fringe fields created by this solenoid should be limited by an iron flux return yoke. This yoke is intended to have an octagonal central barrel and flat plate endcaps, all of these components will consist of 11 layers of steel each (multiple layers are required because this yoke is intended to serve as part of the muon tracker system)[25]. The location of this system relative to other components is shown in figure 2.8.

4th

In the 4th detector concept two powerful solenoid magnets will bracket the muon tracker. The inner solenoid provides the 3.5T magnetic field that curves the tracks of charged particles in the TPC, while the outer solenoid produces a weaker field in the opposite direction to provide flux return. The field produced by the solenoids should be contained by a 'wall of coils', effectively removing the need for an iron flux return yoke, the structure of this system and the magnetic field lines within it are shown in figure 2.19[15][26].
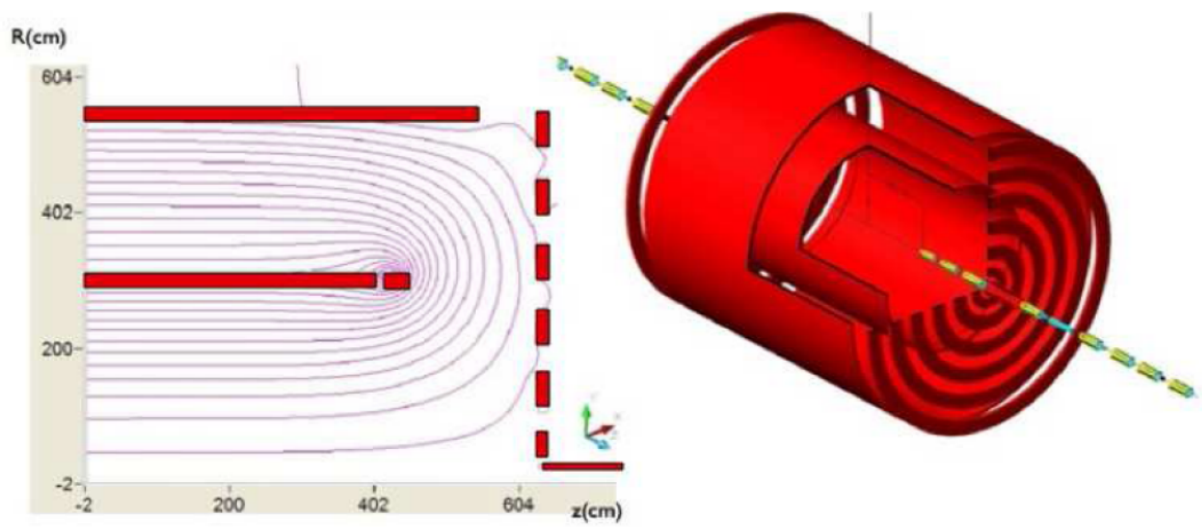
Figure 2.19: A diagram of the Dual Solenoid of the 4th concept detector, and the 'wall of coils' which contain the field. The magnetic field produced is a uniform 3.5T within the inner solenoid, and a uniform -1.5T between the inner and outer solenoids[15].

Chapter 3

MAPS

3.1 Introduction

Monolithic Active Pixel Sensors (MAPS) are an option for sensitive components of
an ILC ECAL. MAPS is currently under development for potential use in either
the SiD or ILD detector[17][25]. This chapter is intended to provide an overview of
how MAPS would work, what distinguishes them from the contemporary analogue
silicon sensors they might replace, and the current state of the MAPS TPAC (Tera-
Pixel APS for Calorimetry, where APS stands for Active Pixel Sensor) test sensors
under development.

3.1.1 Calorimetry Requirements

Naturally the motivation for the development of MAPS is rooted in the initial
calorimetry requirements for ILC detectors. As mentioned in chapter 2 an ILC
detector will need to be able to reconstruct the energies of hadronic jets with a
precision of $\sigma_E/E < 30\%/\sqrt{E}$[15]. This performance is well beyond what is possible
with any detector currently in existence and will require a combination of new sensor
development and Particle Flow Algorithms (PFAs). PFAs analyse the information
from all detector components together to reconstruct the energy of the initial parti-
cles. This can significantly improve the performance of a detector. However in order

for this to work it must be possible to bring together all the evidence a particle left in the detector, even if that particle was part of a complex event containing many other particle showers leaving traces in multiple detector components. This latter requirement creates a need for a detector which permits the possibility of reconstructing how particle showers develop within each detector component. The end result of these factors is a requirement that all components within a detector using PFAs have excellent granularity, with the highest granularity required for components closest to the interaction region[15]. This does not require significant modifications to the designs of the vertex detectors or tracking systems because those components are by necessity already optimised for high spatial resolution, however achieving a high spatial resolution in the ECAL is a new requirement which would otherwise not be applied to this system.

In practice high spatial resolution in an ECAL means a large number of sensitive layers with small pixels. However the large number of layers in turn adds another new requirement; the sensitive components of the ECAL must be reasonably inexpensive per unit area to produce since multiple layers quickly creates a very large surface area to cover. Given that an ILC ECAL can be expected to have about 30 sensitive layers, a length of around 4m and a typical radius of around 1.6m, such a machine would require approximately 2000m^2 of sensors. Consequently even sensors which are relatively cheap on the small scale become highly expensive when scaled up for an ILC ECAL[28]. Additionally, particle flow calorimetry mandates one feature of calorimeters which was already a common convention; that the calorimeter should be entirely contained within the detector solenoid. While this characteristic is desirable under most circumstances, this positioning is vital for particle flow calorimetry due to the possibility of losing particle tracks as particles shower unobserved in the material of the solenoid coil[15]. Since a high magnetic field solenoid is typically one of the more expensive parts of a detector and its cost increases significantly with radius, this means that the calorimeters contained within it need to be compact[15]. This creates two new requirements: that the sensitive layers of an ECAL should be physically thin (which would also help to reduce its effective Moliere radius), and

70

that they should consume as little power as possible to minimise waste heat.

There are two notable features that would set a MAPS ECAL apart from a conventional analogue silicon calorimeter and which should make it much easier for a MAPS calorimeter to match the requirements described above. The first of these two features is a new method of using the ECAL to measure energies referred to as digital calorimetry. The basic principles of this technique are described below in section 3.1.2. This technique is significant because it permits the second novel feature of MAPS sensors, namely the differences in the structure and production of the sensor detailed in section 3.3, which should allow a MAPS ECAL to fulfill the previously mentioned requirements[27].

3.1.2   Digital Calorimetry

The basic concept behind digital calorimetry (in contrast with the analogue calorimetry used by most current detectors) is that it is not necessary to directly measure the amount of energy deposited on the sensitive layers of a calorimeter. Instead it is assumed that the vast majority of particles passing through a calorimeter layer will deposit the same amount of energy per particle on the sensitive regions of that layer. Therefore, if the transverse pixel size in a calorimeter is small enough to register independently every particle passing through, then every hit in that calorimeter would represent the same amount of energy deposited. This would mean that the energy deposited on each layer of the calorimeter would be directly proportional to the number of hits recorded on that layer as shown in figure 3.1. This in turn would mean that the total energy deposited on the whole calorimeter (i.e. the sum of the energy deposited on all the layers of the calorimeter) would be proportional to the total number of hits registered on the whole calorimeter, negating the need to actually measure the energy deposited by each hit. Therefore energy measurements could be made using pixels which only record whether or not they are hit, i.e. pixels with binary responses, hence digital calorimetry[29].

It is predicted that the highest particle shower density within the an ILC ECAL
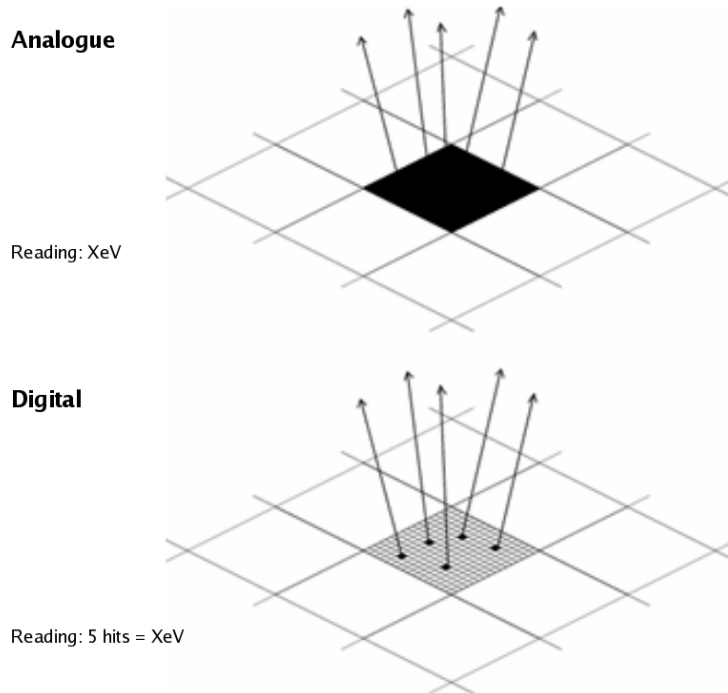
Figure 3.1: A comparison of energy measurement in analogue and digital electromagnetic calorimeter sensors[30].

will be roughly 100 MIPs/mm^2. This means that in order to individually record every particle passing through (and therefore function as a digital calorimeter) an ILC ECAL its pixels must be smaller than $100\mu m \times 100\mu m$. The current design for a MAPS ECAL calls for pixels which are $50\mu m \times 50\mu m$[27]. Assuming a Poisson distribution for the number of hits per pixel at the core of a shower, these pixels would have 2.6% probability of being hit more that once even at the centre of an EM shower[28].

3.2 Practical Concerns

3.2.1 An Overview of MAPS

At present MAPS is being considered as an option for use in the SiD and ILD detector concepts, and a MAPS ECAL would in many ways be identical to the analogue silicon ECALs detailed in chapter 2 for these detectors. This is an intentional

design feature intended to ensure that a MAPS ECAL would not have compatability issues with detector components that have been designed to work alongside an analogue silicon ECAL. In each case the MAPS ECAL would share the same absorber placement and overall structure as its analogue counterpart with the only difference being in the composition of the sensitive layers. In the analogue silicon designs the sensitive layers of the ECAL would be made up of high resistivity silicon pixels usually around 25mm^2 in area per pixel. However digital calorimetry at the ILC requires pixels that are smaller than 0.01mm^2 and in the case of a MAPS ECAL the pixels will typically be around 0.0025mm^2 per pixel[17][25]. Additionally the sensitive layers of MAPS ECAL are likely to be physically thinner than their analogue counterparts whilst being cheaper and easier to produce[27]. Some of the advantages and disadvantages of these changes are discussed in sections 3.2.2 and 3.2.3.

3.2.2 Advantages

The principal advantages of a MAPS ECAL relative to analogue designs can be divided into two categories; performance and production (including cost). In terms of performance, a MAPS ECAL would have a much higher spatial resolution than an otherwise comparable analogue ECAL[27]. This is due to the digital nature of the ECAL, which requires small pixels to work whilst simultaneously making small pixels more practical to produce[27]. While higher spatial resolution is of limited use when the ECAL is viewed as an independent detector component, improvements in spatial resolution do allow the ECAL to work better as part of a unified detector[15]. As noted previously analysis of results at the ILC using PFAs is likely to involve the reconstruction of hadronic jets, which will require the tracking of single MIPs through the ECAL[27] in order to distinguish the tracks caused by charged hadrons from other deposits in the ECAL. In this case the position resolution of the ECAL would be primarily based on the size of the pixels used within it, which would give a MAPS ECAL an advantage over a more conventional analogue equivalent[25][17][27].

Due to the close packed structure of potential ILC ECALs, cooling is likely to be a problem for the sensitive components of those ECALs[28][15]. It is expected that a MAPS ECAL will be easier to cool than a conventional analogue ECAL due to more evenly spread readout electronics which would give a more even temperature distribution[27][28]. This might allow a MAPS ECAL to use the tungsten absorber layers of the ECAL as heat sinks for the sensitive layers which would make it possible to cool the detector during convenient points in its cycle[28]. It is hoped that this advantage will outweigh the greater initial heat load which MAPS sensors would produce relative to their analogue counterparts.

On the production side, one of the primary motivating factors in developing MAPS ECALs is that they are expected to be significantly simpler and less expensive to produce than a comparable analogue ECAL. Analogue ECALs can be expensive to produce because their performance is highly dependent on the thickness of the high resistivity sensitive silicon used in the sensor. The amount of energy deposited by particles passing through an analogue silicon ECAL is proportional to the thickness of sensitive silicon used, while the noise rate for the ECAL is proportional to the capacitance (and therefore the surface area) of the sensitive layers[31]. Therefore the signal to noise ratio of an analogue silicon ECAL can be improved by increasing the sensitive silicon thickness. The result of this is that the construction of a high performance analogue ECAL typically requires a large quantity of highly processed silicon and the cost of this silicon can form a large part of the cost of the ECAL. The cost of a silicon ECAL, currently estimated to be a quarter of the cost of an ILC detector, can be large enough to strongly influence detector design, affecting the performance of the whole detector[17][25]. The pixels in a MAPS ECAL would have a significantly lower capacitance per pixel than a comparable analogue design resulting in a lower noise rate per pixel[32][31]. This means that ECAL designs using MAPS pixels can deliver signal to noise ratios comparable to contemporary analogue ECALs with less energy deposited on the sensor. The result of this is that a MAPS ECAL requires significantly thinner layers of silicon than an analogue ECAL to get the same signal to noise ratio, resulting in a less expensive sensor[17].

Additionally the fact that CMOS sensors like MAPS have seen considerable use in other fields means that there is significant pre-existing manufacturing capacity which could be used to produce a MAPS ECAL[32]. While the production of a large analogue ECAL for the ILC might be dependent on a small number potential suppliers, components of a MAPS ECAL could be produced by many different companies, allowing production to be moved as needed. It is hoped that these factors will make manufacturing a MAPS ECAL both cheaper and more reliable than the construction of a comparable analogue machine[17][28].

3.2.3 Disadvantages

Perhaps the most significant disadvantage of a MAPS ECAL is that the large number of pixels contained within such a sensor (estimated to be of the order of 10^{11} pixels[28]) can produce huge amounts of raw data[27]. At $5mm$ by $5mm$ per pixel the analogue pixels proposed for the ILD ECAL are a hundred times the size of a $50\mu m$ by $50\mu m$ MAPS pixel[17]. This means that even though a MAPS pixel only produces one bit of data per time stamp to record whether or not it has been hit, an analogue pixel would have to record the energy deposited upon it as a 10000 bit number for an analogue ECAL to produce as much data as the MAPS ECAL. Therefore, unless each analogue pixel requires more than 10^{301} values to describe the energy deposited, a digital ECAL is likely to produce more data than an analogue ECAL. This can be countered by using zero suppression to limit the amount of data read out, by making the pixel readout as energy efficient as possible, and by reducing the number of readouts per bunch crossing as much as possible[27]. One study investigating this last factor is shown in chapter 4.

The level of data reduction that is possible via zero suppression in a MAPS ECAL is obviously dependent on the rate at which such a detector would register hits during normal operations. This rate is likely to be dominated by noise which in turn makes noise reduction a priority for MAPS development. Noise in this case refers to any "hit" within the sensor which is not caused by the passage of a charged

particle. Currently it is assumed that MAPS pixels will have a noise rate of 10^{-6} hits per pixel per beam bunch crossing[17]. Combined with the large number of pixels required for a MAPS ECAL (approximately 8×10^{11} pixels for the whole detector[28]) this translates to an impressive number of hits, of the order of 8×10^5 hits per bunch crossing. For comparison it is predicted that during normal detector operations the dominant source of hits caused by actual charged particles is electron positron pair created by beam-beam interactions[33]. According to simulation studies detailed in chapter 4 during a typical bunch crossing a MAPS ECAL would record fewer than 3×10^5 hits per bunch crossing from these electron positron pairs. This means that that the readout from a MAPS ECAL would be heavily dominated by noise, and that there will be a large amount of data to read out from the ECAL regardless of external influences. This effect can be minimized (reducing the amount of noise data read out) by fine tuning the minimum hit energy threshold of the sensor, ideally this threshold should be high enough to discount most noise hits whilst not being so high that it also discounts genuine hits. A more detailed description of how this threshold is defined and controlled is included below in section 3.3.2, and one of the studies aimed at finding the ideal operating threshold for a MAPS ECAL is included in chapter 7.

Another challenge created by the small pixel size used by MAPS is that it is possible for a hit on one pixel to cause nearby pixels to fire. Mostly this is caused by charge diffusion through the silicon epitaxial layer spreading the charge carriers from a hit across multiple pixels, or by interference between individual pixel read-out channels[28]. This is a potential problem because as noted previously digital calorimetry relies on accurately recording how many particles pass through each ECAL layer. However this issue can be circumvented, or even turned into an asset, provided the number of pixels recording hits due to the passage of a single particle remains both small and consistent.

Finally, one of the most persistent issues creating a viable MAPS ECAL is ensuring uniform behaviour across large number of pixels that such a system would require. The principal manifestation of this problem in current test sensors is non

uniformity in pixel threshold. One of the studies intended to address this problem is discussed in chapter 5.

3.3   TPAC

In order to properly test and refine MAPS pixels it was necessary to produce a number of test sensors for a characterisation of their response. With this in mind TPAC sensors were developed to study the viability of MAPS pixels whilst simultaneously demonstrating innovations in the underlying design of the pixels. At the heart of each TPAC sensor is a small square of working MAPS pixels suitable for testing under a variety of conditions. This square consists of 28224 pixels which can be characterised by a range of complementary methods[32]. Typical tests for TPAC sensors include gain measurement using ^{55}Fe, pixel uniformity scans using lasers, MIP response using charged particle test beams and noise runs to fine tune the response of the pixels without external input. TPAC sensors have been used in several experiments (some of which are detailed in chapters 5 and 7) to gauge the behaviour of MAPS pixel variants and to refine the performance of TPAC sensors.

Some of these experiments have led to refinements in the TPAC sensor design and TPAC sensors are currently in their third iteration (TPAC 1.2). The first iteration (TPAC 1.0) incorporated four pixel designs on to a single sensor in order to test their relative performance described below in section 3.3.2[32]. Later iterations (TPAC 1.1 and 1.2) only used the best of these designs as determined by earlier testing[34][35]. Further discussion of these variants is contained in sections 3.3.3 and 3.3.4.

3.3.1   TPAC PCBs

While the TPAC sensors went through several modifications during development, the overall design of the Printed Circuit Boards (PCBs) remained fairly consistent throughout all the TPAC variants, a picture of one of these PCBs is shown in figure 3.2. The TPAC PCBs are 205mm×105mm in surface area (of which 9.15mm×8.45mm is taken up by the TPAC sensor) and is composed of eight layers
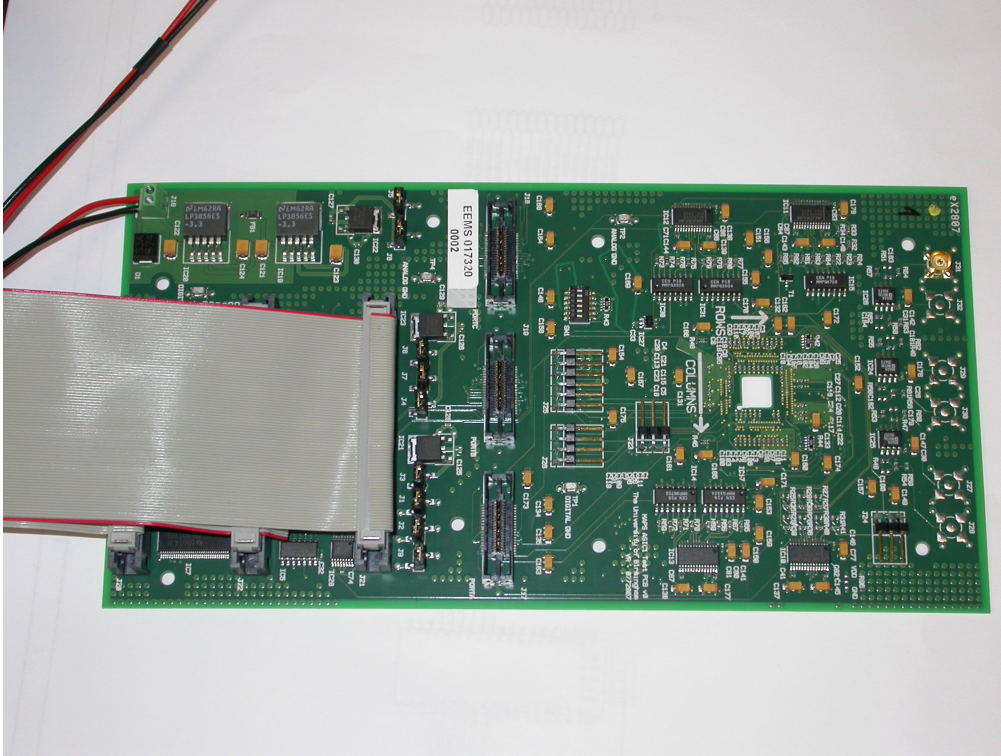
Figure 3.2: A picture of a TPAC Printed Circuit Board (PCB).

(four layers for signal routing, four layers for power and ground planes). A TPAC
PCB has 68 LVDS inputs and 48 LVDS outputs in addition to one loopback input
and one loopback output. Of the 68 LVDS inputs, 61 are sensor inputs and seven
inputs to an SPI bus which has a temperature sensor and four DACs (which control
various aspects of sensor operation) attached. The 48 LVDS outputs consist of 41
sensor outputs, six outputs which give the board an identifying number from 0 to
63, and one output from the SPI bus. Each TPAC PCB requires a 6-7.5W (4-5V,
1.5A) power supply[36][37][38].

3.3.2 TPAC Pixels

The sensitive component of a TPAC test sensor is composed of a CMOS (Compli-
mentary Metal Oxide Semiconductor) wafer divided up into $50\mu m \times 50\mu m$ pixels,
the vertical structure of the wafers used is shown in figure 3.5. The basic principle
upon which a MAPS pixel operates is that when an ionising particle passes through
the P-epitaxial layer of the CMOS wafer, it will leave behind a trail of electron-hole

pairs. These charge carriers will then disperse through the P-epitaxial layer and the minority charge carriers are then collected at a diode. The resulting current can be then amplified and analysed to establish whether or not the pixel associated with that diode should record a hit. If a conventional CMOS wafer (such as the design shown on the left of figure 3.5) were used this analysis would be problematic due to difficulties in incorporating PMOS (P-type Metal Oxide Semionductor) transistors into the sensor. PMOS transistors are necessary for complex processing of signals however they need N-Wells which can compete with the collection diodes for charge carriers. This reduces the amount of charge collected at the diodes meaning the pixel has a smaller signal to read out[32].

To prevent this competition without removing PMOS transistors from the sensor, the CMOS wafers used in TPAC sensors include implants in the P-epitaxial layer which create "Deep P-Wells" (DPWs). These implants are positioned between the bulk of the epitaxial layer and the N-wells created by the PMOS transistors as shown in figure 3.5. Because these DPWs are p-wells relative to the rest of the P-epitaxial layer, they prevent positive charge carriers from entering the N-wells created by the PMOS transistors, effectively isolating the PMOS transistors from the epitaxial layer[32].

Once the minority charge carriers within a pixel have been collected at that pixel's diodes the resulting signal is analysed and amplified by one of two structures. These structures are the Pre-Shape structure and and the Pre-Sample structure, both shown in figure 3.4. Which structure is used for each pixel depends on the design iteration of the sensor and the location of that pixel within that sensor as described in sections 3.3.3 and 3.3.4 below. The 'local hit decision' which determines whether or not a given pixel records a hit is influenced by the global threshold set for the sensor and a trim adjustment set for each pixel. Both these factors are introduced in the two stage comparator shown in figure 3.4[32]. The number of bits which store the trim for each pixel (and hence determine both how large and how granular that trim can be) varies between different sensor designs[39][34][35].

The end result of modifying the global threshold and trims for a sensor is a

change in the minimum charge collected in a pixel to register a hit, the higher the threshold the more charge will be required for an individual pixel to register a hit. Setting this threshold too low would result in the sensor registering an excessive number of noise hits, while setting it too high could cause the sensor to discard genuine hits (as shown in chapters 5 and 7). As shown in figure 3.3 both phenomena can compromise the energy resolution of the ECAL, making it desirable to modify the thresholds set for each pixel for optimal resolution. Unfortunately the memory required to store both the global threshold for each sensor, and the 'trim' which fine tunes the threshold for each pixel takes up physical space on the sensor which can compromise its performance[32]. To minimise this problem the number of memory bits used are reduced as much as possible.

In order to decide the number of bits used to store the global threshold for each sensor, the range and precision over which the threshold might need to be modified were considered. Figure 3.3 shows that in order to achieve optimal energy resolution the threshold of the sensor would need to be fine tuned to within an approximately 0.5 keV range. This means that the exact threshold of each sensor needs to be tuneable in roughly 0.1 keV increments since the exact location of this 'sweet spot' will be slightly different for each sensor. It is expected that on average a MIP passing through the epitaxial layer of a TPAC sensor will produce roughly 80 electron-hole pairs per micron path length. Since the epitaxial layer of a TPAC pixel is typically 12μm thick, and assuming the MIPs hit the pixel head-on, this translates to 960 electron-hole pairs per MIP[32]. Given the low probability of multiple hits in a single pixel discussed previously[28], 960 electron-hole pairs can be considered as a reasonable upper limit for practical consideration, this would correspond to approximately 3.6 keV registered by the pixel[32]. Combining this upper limit with the previously mentioned requirement to modify the threshold in 0.1 keV increments implies 36 separate threshold settings. This would in turn require a minimum of six bits to store this threshold on each sensor. In practice each sensor has 1250 different threshold settings with the highest threshold eliminating all hits below roughly 36 keV and the lowest threshold permitting all hits above roughly -9 keV[40].
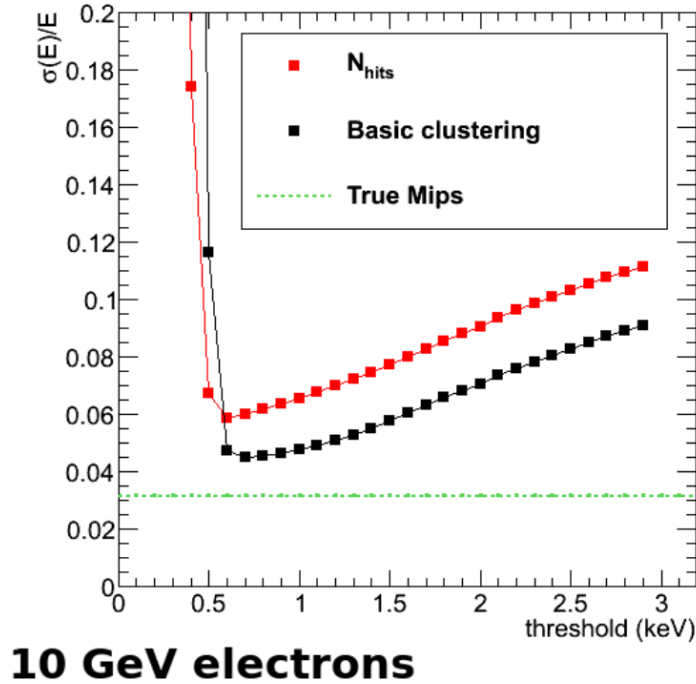
Figure 3.3: Predicted variations in ECAL energy resolution with varying sensor threshold based on simulations. The line labelled N_{hits} represents the energy resolution based on simply counting the number of hits found within the sensor for an energy measurement while the line labelled Basic Clustering counted only hits found within clusters. Similarly the line labelled "True MIPs" represents the energy resolution based on counting the number of MIPs simulated[39][29].

Trim bits are added to modify the thresholds set for individual pixels due to pixel non-uniformity which can make the effective threshold set for each pixel vary slightly from the global threshold set for the sensor. Trim bits are intended to modify the thresholds of all the pixels in a sensor back to a single value and therefore the number of trim bits required is set by the variation between pixels in the same sensor[32]. Since the extent of this variation could not be accurately predicted in advance, the number of trim bits per pixel changed between different iterations of TPAC sensors as new data was gathered, this is discussed in more detail in chapter 5[39][35][34].

3.3.3 TPAC 1.0

The sensitive region of a TPAC 1.0 sensor consists of a 9.15mm × 8.45mm area containing 28224 pixels arranged into 168 rows and 168 columns. Each row is divided
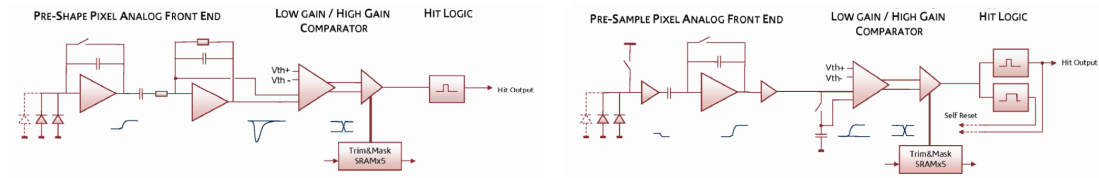
Figure 3.4: A block diagram showing the path from analogue input to digital output in Pre-Shape pixels(left), and Pre-Sample pixels(right)[32]. TPAC pixels using the structure on the left are often referred to as 'shaper pixels' while pixels using the structure on the right are referred to as 'sampler pixels'[32]. Note: for the TPAC 1.0 sensor four variants of pixels were used, two shaper variant distinguished by the capacitors incorporated into their circuits, and two sampler variants, likewise distinguished by the capacitors used[32].
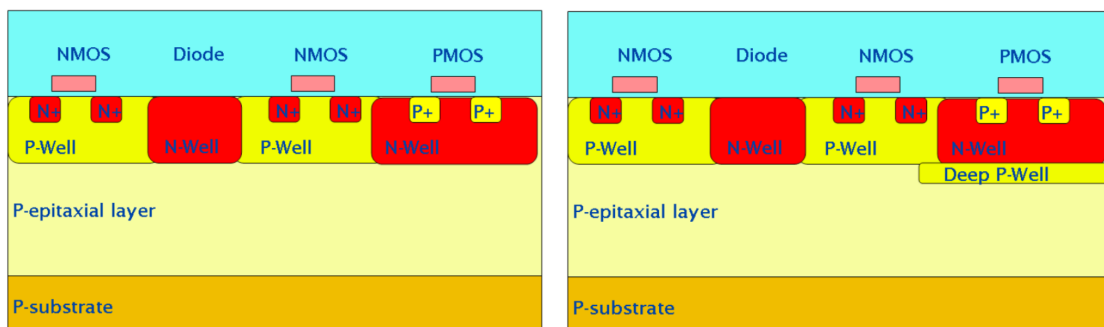
Figure 3.5: Vertical section of a standard CMOS wafer (distances not to scale), unmodified (left), and modified to include Deep P-Wells (DPW) to mask PMOS transistors(right)[32].
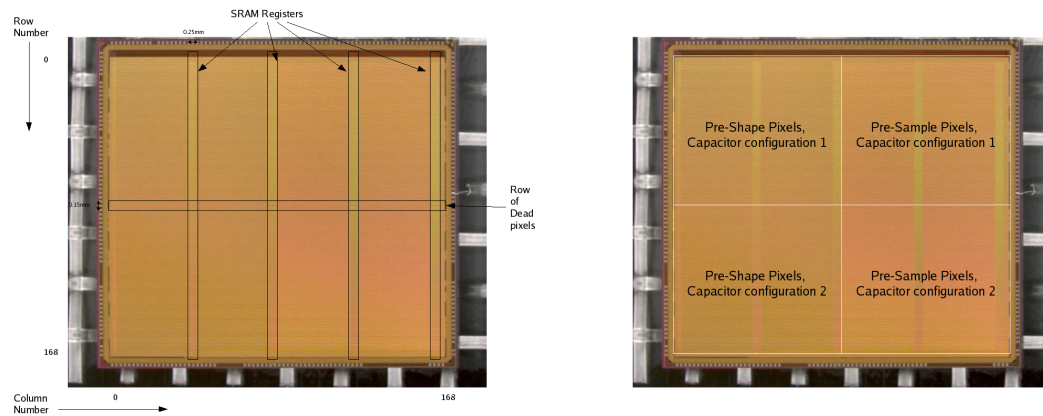
Figure 3.6: A picture of a TPAC 1.0 sensor showing the dead areas present in the sensitive region(left), and the relative positions of different pixel types(right)[32].

into four sets of 42 pixels which share logic containing SRAM(Static RAM) registers. Each SRAM register can store up to 19 hits before being read out, if a set of 42 pixels records more than 19 hits before readout these pixels become saturated and only the first 19 hits will be recorded (this is one of two forms of saturation that can occur in MAPS sensors, saturation caused by the binary readout of the pixels is discussed in chapter 4). These SRAM registers take up space on the sensor, dividing each set of 42 pixels from the next by 250μm of inactive area, put together these form columns of dead areas splitting up the sensor into four regions shown in figure 3.6. Combined with a row of dead pixels across the centre of the sensor to re-buffer control signals, and to distribute bias and reference voltages, a total of 11.1% of the sensor is insensitive[32].

In addition to these divisions, the sensitive region of the TPAC 1.0 sensor is divided into quadrants, each quadrant containing pixels of a slightly different design as shown in figure 3.6. Two quadrants of the sensor contained Pre-Shape pixels using analysis circuits shown in figure 3.4 (the pixels in different quarters are distinct from each other due to different capacitors in their analysis circuits). The remaining two quadrants contained Pre-Sampler pixels using analysis circuits also shown in figure 3.4 (likewise distinguished by the capacitors used)[32]. All TPAC 1.0 pixels contained four trim bits for threshold fine tuning[39].

83

3.3.4   TPAC 1.2

The design of TPAC 1.2 sensors differed from TPAC 1.0 in only two important respects: the pixel variants used, and the trim bits available. During the testing of TPAC 1.0 it was established that Pre-Shape pixels provide more uniform performance than Pre-Sample pixels and for this reason TPAC 1.2 used only Pre-Shape pixels in all regions of the sensor. Additionally, the study described in chapter 5 showed that for the pixels to produce acceptably uniform behaviour, more trim bits would be required for each pixel. Therefore the number of trim bits per pixel was increased from four bits in TPAC 1.0 to six bits in TPAC 1.2. These modifications were included in the intermediate TPAC 1.1 sensors, however problems with pixel addresses created a need for a new revision of sensors which was labelled TPAC 1.2[35][34].

Chapter 4

Simulated Pixel Saturation Study

4.1   Introduction

According to current designs a MAPS ECAL would make use of digital pixels[27], and because of this it could prove vulnerable to a phenomenon referred as 'pixel saturation'. The problem arises from the fact that the digital pixels which would be used for such an ECAL record only whether energy has been deposited on them, not how many particles have passed through. This means that if a pixel in the ECAL had energy deposited on it by multiple particles, before that pixel was read out there would be no evidence of the second or subsequent particles. For the ECAL to function properly, it should as far as possible record all the electromagnetically interacting particles that are found in each layer of the ECAL while the detector is active. While this pixel saturation is unlikely to occur from hits caused by 'physics events', background processes could produce significant numbers of hits in the ECAL during normal detector operations[28][33].

The obvious solution to this problem is to reduce the time between pixel readouts so that there is a negligible chance of any given pixel being hit by two or more charged particles before it is read out. Therefore to ensure that a MAPS ECAL functions properly without losing any data its pixels should be read out as often as possible. Reducing the interval between pixel readouts as far as possible is also desirable for another reason; the longer the interval between pixel readouts the larger the amount

of memory required on the sensor to buffer all the hits. A shorter readout time would mean a smaller memory requirement per sensor which would mean a smaller surface area taken up by that memory, resulting in fewer insensitive (or 'dead') areas on the sensor[32]. Conversely, practical concerns, namely the power required to read out all the pixels of an ECAL (which is predicted to have approximately 10^{11} pixels), mean that especially frequent pixel readouts are undesirable for a practical and smoothly functioning MAPS ECAL. The natural compromise between these requirements would be to read out the pixels in a MAPS ECAL just often enough so that the probability of data loss is kept within acceptable limits, without performing any pixel readouts which would be superfluous to this goal (provided this readout time would result in an acceptable amount of dead area on the sensor).

For most regions of the ECAL this compromise is dictated by the balance between pixel saturation due to noise hits recorded in the ECAL and the power required to read out the ECAL pixels[28][17]. However, it is likely that beam-beam interactions (as described in section 4.2.1) would cause large numbers of hits in regions of the ECAL close to the beam axis. These hits would likely dominate the hits recorded in these regions, meaning that the ideal pixel readout time in these regions would be dictated by the balance between the power required to read out the ECAL pixels and pixel saturation caused by beam-beam interactions[33].

With this in mind the study detailed in this chapter was performed in order to provide information about the probability of data loss due to pixel saturation within a MAPS ECAL caused by beam-beam interactions, as a function of time between pixel readouts. This information could then be used to identify the time period between pixel readouts that would provide the best compromise for minimising data loss and operating an ECAL with practical power requirements.

This study is divided into two sections, the first is an initial investigation to find out whether or not significant numbers of the electron-positron pairs produced through beam-beam interactions would interact with LDC detector components near to the beam axis. This investigation was intended to discover if these electron-positron pairs could be a potential source of pixel saturation before any in depth

86

simulations were started. This initial investigation is described in section 4.4. Having concluded from the results of the initial investigation that beam-beam interactions could be a potential source of pixel saturation, the second section of this study is a more in depth and quantitative investigation of the predicted interactions between particles produced via beam-beam interactions and a simulated LDC detector. This study is detailed in section 4.5.

4.2   Simulation Software

4.2.1   GuineaPig

GuineaPig is C++ program which served as the event generator for the initial investigation described in section 4.4 as well as the full detector simulation described in section 4.5. GuineaPig simulates the production of low energy electrons and positrons from the interactions of electron and positron beams as described below and shown in figure 4.1[41].

Almost all the processes which GuineaPig simulates are related to a phenomena known as the 'pinch effect'. This refers to the tendency for converging beams of electrons and positrons to focus each other due to electromagnetic attraction between the electrons in the electron beam and the positrons in the positron beam. This attraction tends to create smaller effective beam cross sections, enhancing the luminosity of the beams. However it also results in the emission of bremsstrahlung photons due to changes in the velocities of the beam electrons and positrons[42].

Photons produced in this way often have sufficient energy to produce electron-positron pairs. This occurs either through a photon forming a virtual electron-positron loop in the strong electromagnetic fields within the detector (coherent pair production), or through the collision of bremsstrahlung photons with either another real photon (the Breit-Wheeler process), or with a virtual photon produced by one of the beam particles (the Bethe-Heitler process). In addition to the electron-positron pairs produced by the interactions of bremsstrahlung photons, electron-positron

pairs can also be produced through collisions of virtual photons produced from beam particles (the Landau-Lifshitz process, the only one of these four processes which could potentially occur without the pinch effect)[42]. All four of these processes can create electrons and positrons which can create background hits in the detector. Additionally, beam particles which lose large amounts of energy to bremsstrahlung photons can cease to be part of a coherent beam and can show up as background in the detector. The Feynman diagrams for all of these processes are shown in figure 4.1.

When supplied with appropriate beam parameters GuineaPig can be used to simulate all five of these low energy particle production processes for a single bunch crossing in any electron-positron collider. Once the simulation has been completed, information about the resulting electrons and positrons is stored in a single ascii text file. This text file can then be used as input for an analysis program (as in section 4.4), or used as an event generator for the detector simulation program Mokka (as in section 4.5)[41].

4.2.2   Geant4

Geant4 is at the core of all simulations performed during this study. It is a toolkit designed to simulate the passage of fundamental particles through matter, tracking the paths of the particles along with their interactions with the structures they pass through. Using Geant4 it is possible to construct a model of virtually any structure (including the composition of components, the response of any component designated as 'sensitive', and any existing electromagnetic fields), simulate the behaviour of virtually any particle within that structure, and record the results[43].

Models in Geant4 are created by defining components of a structure first as logical, then as physical volumes. The logical volume of a component defines all the characteristics of that component that are independent of the component's position in the detector. Such information typically includes the shape, size, sensitivity, composition, and information about other volumes contained within the component.
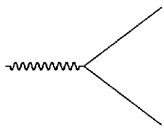
Coherent Pair Production　　　　**Breit-Wheeler Process**
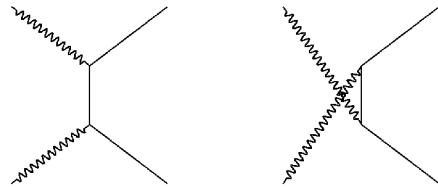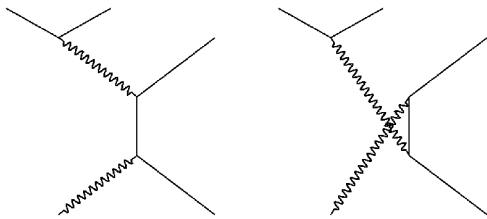
Bethe-Heitler Process　　　　**Landau-Lifshitz Process**
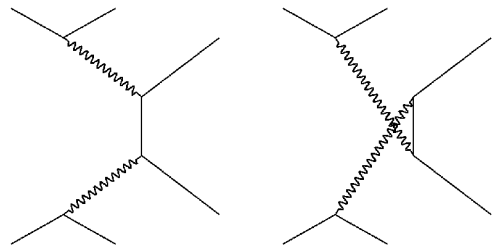
Bremsstrahlung Emission
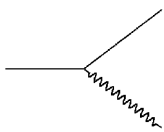
Figure 4.1: Feynman diagrams for all beam-beam interaction processes which produce low energy electrons and positrons.

The physical volume of a component defines its position within the logical volume which contains that component[43].

Typically in Geant4 a detector model will be created by first defining a single 'mother' volume which encompasses the whole detector. Within that mother volume other volumes are defined describing the different large scale systems of the detector. These volumes in turn contain volumes which describe the components of those detector systems which in turn contain volumes describing subcomponents. This process continues, potentially right down to defining volumes for individual pixels and wires, creating a highly detailed detector model[43].

Once a detector model has been created it can then be exposed to simulated particles in order gauge its performance. These particles can either come from relatively simple event generators included in Geant4, or can be generated by external event generators. Once particles are simulated within a detector Geant4 is capable of extrapolating their movements and interactions (including the production of additional particles) using a wide range of physics processes. These processes include (but are not limited to)[43]:

- Compton Scattering
- Coulomb Scattering
- Gamma Conversion
- Positron Anihilation
- the Photoelectric effect
- Cherenkov emission
- Scintillation
- Synchrotron Radiation

4.2.3 Mokka

Mokka is an application developed within the ILC collaboration based on the Geant4 toolkit. It is used to construct and run simulations with pre-set detector models us-

ing the Geant4 toolkit to construct the models and handle the resulting simulations. Mokka provides a user interface built on the Geant4 UI allowing the user to specify the detector model used, the initial conditions for a simulation, and various parameters for the simulation. Since it is based on the Geant4 toolkit, Mokka has access to a several built in event generators, and can accept particle inputs from several external event generators. These generators include Pythia (using HEPEvt and stdhep formats) and GuineaPig (using the 'pairs' format)[44].

4.3   Analysis Software

The software used to analyse results for the second half of this study is called Marlin, it is a modular software framework designed to extract and analyse files in LCIO (Linear Collider Input/Output) format such as those produced by Mokka. Marlin is based around a range of processors each of which performs a separate task[45]. During this study the only processor used was a processor called Mapsana which was developed within the MAPS collaboration specifically for the task of analysing data from simulated ECALs. Mapsana was used to search through LCIO files, extract specified hit collections (in this case collections containing hits from the ECAL), analyse them, and write the results to a file. Almost all of the analysis described in section 4.5.3 was performed using Marlin, and as a result a modified version of Mapsana was produced to create the histograms required for those analysis techniques.

4.4   Initial Investigation

4.4.1   Theory

As noted in chapter 2 the LDC detector will include a large electromagnet intended to produce a uniform 4T magnetic field within the detector parallel to the beam axis. A simple depiction of this setup is shown in figure 4.2. Any charged particle within this field (such as an electron or positron produced via beam-beam interactions) will
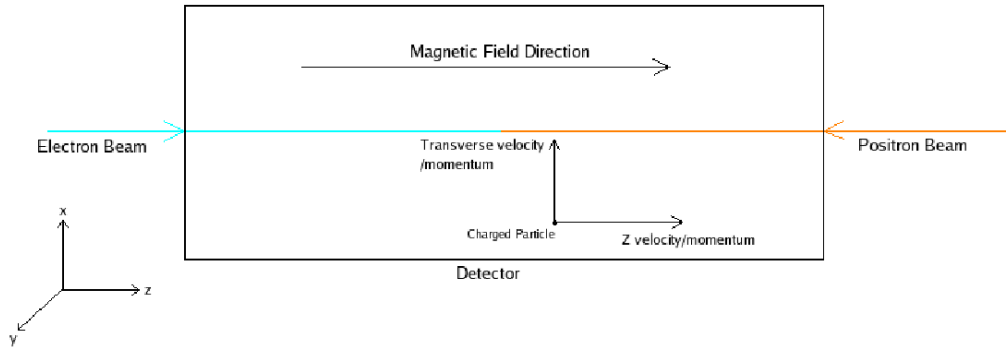
Figure 4.2: A basic schematic layout of the interaction region showing the coordinate system used in this chapter when referencing the detector. A diagram showing the detector geometry of the LDC detector used for the studies shown in this chapter is shown in figure 2.7.

move in a helix with the axis of the helix parallel to the magnetic field lines (and therefore parallel to the beam axis). The radius of such a helix is given by[13]:

$$r = \frac{P_T}{0.3B} \qquad (4.1)$$

where : P_T is the transverse momentum of the charged particle

B is the magnetic field in Tesla, and

r is the radius of the helix in metres

The period of rotation about this helix is given by:

$$T = \frac{2\pi r}{V_T} \qquad (4.2)$$

where : T is the period of rotation of the charged particle

r is the radius of the helix, and

V_T is the speed of the charged particle perpendicular to the magnetic field

92

When the charged particle is within the
detector long enough to complete half a
rotation around its spiral:

When the charged particle is **not** within
the detector long enough to complete
half a rotation around its spiral:

$\theta = \frac{\pi \cdot t}{T}$

● Beam Axis
→ Path of Charged Particle
↔ Maximum separation between particle and beam axis
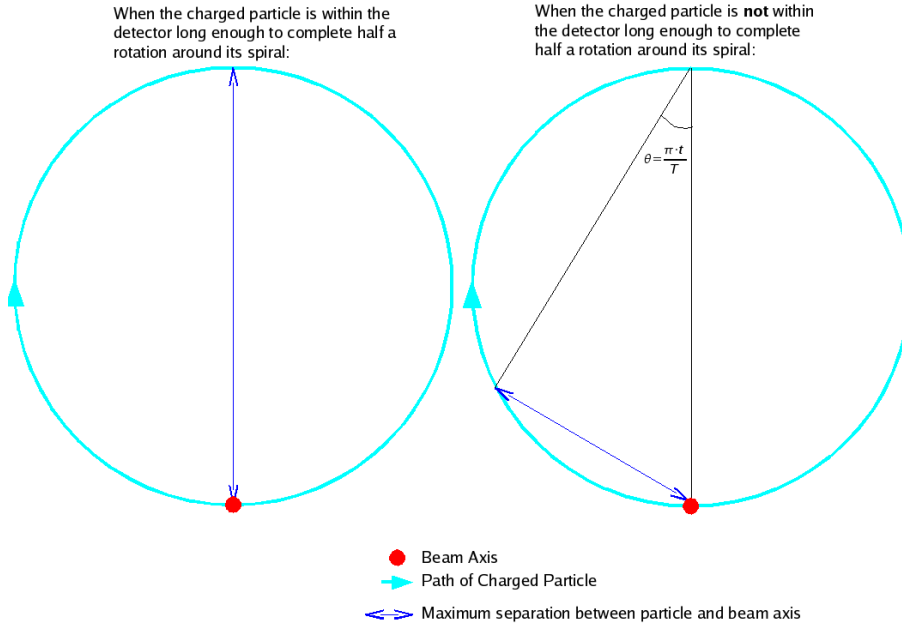
Figure 4.3: The maximum distance between a charged particle within the detector barrel and the beam axis, given that there is a uniform magnetic field parallel to the beam axis.

(and therefore perpendicular to the beam axis).

Since particles produced by beam-beam interactions will naturally begin their motion on the beam axis, the point at which such a particle is furthest from the beam axis is half way through its rotation around its helix as shown in figure 4.3. At this point the particle should be separated from the beam axis by a distance D which should be equal to twice the radius of the helix, i.e. the maximum distance from the beam axis is given by:

$$D = \frac{2P_T}{0.3B} \tag{4.3}$$

Therefore it is a reasonable initial assumption that if D for a particular particle is found to be greater than the minimum distance separating any detector component from the beam axis, then it is possible that particle will interact with that detector component. However it is possible for particles with a large momentum in the z-direction, compared to their transverse momentum to leave through one of the ends

93

of the detector barrel before they reach their maximum distance from the beam axis. For these cases it is necessary to judge the chances of the particle interacting with detector components on the basis of the maximum distance separating the particle from the beam axis while the particle is still within the detector (in terms of distance along the beam axis). For a given time after production t the distance between the particle and the beam l is given by:

$$l = 2r \sin \frac{\pi t}{T} = 2r \sin \frac{tV_T}{2r} \tag{4.4}$$

The maximum distance between a charged particle and the beam axis (within the detector barrel) when the charged particle does not have time to complete half a revolution about its helix is shown in figure 4.3. In cases where the particle would leave the detector before reaching its maximum transverse separation from the beam axis (D), the value of l can be used to determine whether or not that particle would interact with the detector. Specifically, if the value of l exceeds the minimum separation between detector components and the beam axis, then the particle could still interact with detector components (and therefore could affect the performance of the ECAL) before leaving the detector.

4.4.2 Procedure

The GuineaPig program takes as its input a small subset of the beam parameters under investigation in order to predict how the two beams will interact. For this study GuineaPig was run with each of the ten possible beam parameter sets proposed for the ILC (as of March 2007), see tables 2.1 and 2.2 for details[20]. In this case the GuineaPig program was used to simulate the creation of electron-positron pairs as described in section 4.2.1. For each of these ten scenarios information about these simulated particles was stored in a text file where it could be analysed directly or used in a full detector simulation. For this stage of the study, these files were analysed as described in section 4.4.3 in order to estimate how many particles would interact with the detector for each of the described scenarios.

4.4.3 Analysis

The overall aim of this analysis was to estimate how many electrons and positrons produced via beam-beam interactions could be expected to interact with the detector for each proposed beam parameter set. Determining whether or not a particle had a chance to interact with the detector consisted of a two stage test which was administered to each particle. The second stage of this test was to determine a value for the maximum separation between the particle and the beam axis within the detector (hereafter refered to as k). The first stage of the test was to decide which calculations would be needed to determine k.

The first stage used the amount of time the particle spent in the detector to determine how k would be calculated, if the particle remained within the detector for long enough to complete half a revolution around its helix, it would reach its maximum potential separation from the beam axis (D as defined in equation 4.3). For the sake of simplicity in these cases k would then be considered to be equal to D. If however the particle would not spend enough time in the detector to complete a half a revolution around its helix, the maximum separation between the particle and the beam axis within the detector would be determined by how far around the first loop of its helix the particle would go, requiring a different calculation. Therefore the first stage of the test for each particle is essentially a comparison between the time required for that particle to complete half a revolution round its helix, and the time that particle would spend within the detector.

The time the particle spends in the detector (t_d) is given by:

$$t_d = \frac{d}{V_Z} \tag{4.5}$$

where : d is the distance along the beam axis between the interaction point and the end of the detector, and V_Z is the speed of the charged particle parallel to the beam axis.

While the time required for a particle to complete a half rotation ($T_{1/2}$) is given

by:

$$T_{1/2} = \frac{T}{2} = \frac{\pi r}{V_T} \tag{4.6}$$

If $t_d > T_{1/2}$ then the particle should have time to reach its maximum transverse distance from the beam axis and k was considered to be equal to D. In this case the second stage testing was to calculate the value of D (see equation 4.3) and set $k = D$. Then if $k < r_{min}$ (where r_{min} is a radius determined by the separation between various detector components and the beam axis as described below) the particle would be flagged to be discarded. Conversely, if $t_d < T_{1/2}$ then the second stage of testing would be to calculate l (see equation 4.4) when $t = t_d$ and set $k = l$, if $k < r_{min}$ then the particle would be flagged to be discarded.

These tests were performed using the output files for all the beam parameter sets shown in tables 2.1 and 2.2. For each set the tests were performed several times using different definitions of r_{min}, namely:

• $r_{min} = 400$mm (the distance between the LDC01 ECAL and the beam axis, shown in figure 2.7)

• $r_{min} = 13$mm (the distance between the LDC01 beamCal and the beam axis, shown in figure 2.7)

• $r_{min} = 6$mm (half the distance between the LDC01 beamCal and the beam axis, shown in figure 2.7)

In each case, each particle would be tested in turn, and if it was flagged by the tests, it would be discarded. Particles which were not discarded in this way would then be written out into a new text file specific to the simulation that created them and the value of r_{min} used (i.e. there was one final output text file per GuineaPig run, per value of r_{min}, and therefore three final output files for each possible set of beam parameters). The results of these tests (based on the number of particles found in these output files) are shown in table 4.1.

For each set of beam parameters the number of particles in the output file using $r_{min} = 400$mm represents the number of beam-beam interaction particles which could directly interact with the ECAL for that parameter set. Similarly the number

96

Beam Parameter Set	Number (%) of particles interacting with detector/b.c.		
(c.o.m. energy)	$R_{min} = 6mm$	$R_{min} = 13mm$	$R_{min} = 400mm$
High Lum(500 GeV)	120395(43.5)	73297(26.5)	0(0)
High Lum(1 TeV)	271336(46.2)	166756(28.4)	$2(3.4 \times 10^{-4})$
Large γ(500 GeV)	31105(31.0)	17846(17.8)	0(0)
Large γ(1 TeV)	69109(33.5)	42559(20.6)	0(0)
Nominal(500 GeV)	34981(34.2)	18931(18.5)	0(0)
Nominal(1 TeV)	60639(37.6)	18932(11.8)	0(0)
Low P(500 GeV)	97103(41.0)	58071(24.5)	0(0)
Low P(1 TeV)	191569(43.2)	115524(26.0)	$1(2.3 \times 10^{-4})$
Low Q(500 GeV)	12847(31.1)	6363(15.4)	0(0)
Low Q(1 TeV)	25073(34.6)	13395(18.5)	0(0)

Table 4.1: A table showing the particles interacting with the LDC01 detector created by beam-beam interactions from a single bunch crossing.

of particles in the output file using $r_{min} = 13$mm would represent the number of beam-beam interaction particles which could directly interact with the beamCal. The number of particles in the output file using $r_{min} = 6$mm would represent the number of beam-beam interaction particles which could reach that radius away from the beam axis, since no detector components were that close to the beam axis in the LDC01 design, this test was included primarily as a safety check.

These distances were based around the ECAL and beamCal because the ECAL was the detector component which had the most direct significance for the rest of this study, and the beamCal was the closest component of the LDC01 detector to the beam axis (as shown in figure 2.7). The tests using $r_{min} = 6$mm were included so that the results of this investigation could still provide qualitative predictions, even if future changes to the detector design result in a smaller separation between the detector and the beam axis.

4.4.4 Conclusions

The results shown in table 4.1 indicate that the majority of pairs produced by beam-beam interactions will leave the detector without ever interacting with it. This is true for all proposed ILC beam parameters as of March 2007. Additionally the number of beam-beam background particles directly striking the ECAL is shown to be

very small compared to the number of these particles produced. However this simulation and analysis shows that there are still significant numbers of particles that may strike detector components closer to the beam axis (such as the beamCAL). This is particularly significant for the High Luminosity and Low P parameter sets. This is important because once a particle has directly interacted with any detector component its behaviour becomes much harder to predict, meaning that other components could be affected. Therefore, at this level of investigation, if a particle strikes any detector component, some effect on the ECAL cannot be ruled out. On this basis further investigation was judged necessary to see what effect beam-beam background would have on the detector. This motivated the investigation described below in section 4.5.

4.5 Full Detector Simulation

4.5.1 Theory

Due to the large amount of time typically necessary to run a Mokka simulation of the beam-beam interactions from a single bunch crossing, practical concerns required that the number of pixels occupied in the ECAL over multiple bunch crossings must be extrapolated from a small number of GuineaPig/Mokka simulations.

It was therefore necessary to extrapolate the number of hits in the ECAL (or part thereof) after an arbitrary number of bunch crossings n, from the number of hits recorded after a single bunch crossing. Assuming that all background particles entering the detector are incident on separate pixels (maximising the possible effect on detector operation), the number of pixels hit in the ECAL (or region thereof) after n bunch crossings p is given by:

$$p = n \times q \tag{4.7}$$

where : q is the number of hits registered in the ECAL (or region thereof) in a single bunch crossing

If there are N bunch crossings before the ECAL is read out and the pixels are reset, then if the time separating bunch trains is discounted (as it can be if the calculation only considers the reaction of an ECAL during a single bunch train) N can be approximated as:

$$N = \frac{t_R}{t_b} \quad (4.8)$$

where : t_b is the time between bunch crossings within a single bunch train

t_R is the time between pixel resets

Therefore the number of pixels inactive immediately before read out/reset (p_R) approximates to:

$$p_R = N \times q = \frac{t_R}{t_b} \times q \quad (4.9)$$

Since beam-beam background is highly anisotropic [18] the density of hits simulated by GuineaPig and Mokka in the ECAL should vary considerably with location in the detector. Because of this it is quite possible for the chance of losing 'physics events' due to beam-beam background to be small in the whole detector while still being high in specific regions. It is therefore possible for a relatively small number of hits to pose a potential problem. With this in mind it was necessary to analyse regions of the ECAL separately to show the chance of losing physics events in each region. For a given value of t_R the value of p_R in each region can be calculated. The value of p_R in a given region can then be compared with the number of pixels in the same region (n_R) to find out what percentage of those pixels will be inactive due to background hits immediately before reset (f_R) i.e. f_R is given by:

$$f_R = \frac{p_R}{n_R} \times 100 = \frac{t_R}{t_b} \times \frac{q}{n_R} \times 100 \quad (4.10)$$

Logically the percentage of 'physics event' hits lost in any given region of the ECAL should be equal to f_R calculated for that region.

4.5.2 Procedure

GuineaPig was used simulate beam-beam interactions for a single bunch crossing using each of the beam parameter sets described in tables 2.1 and 2.2 in turn. Each simulation resulted in the production of an ascii text file containing information about the low energy electrons and positrons produced as a result of beam-beam interactions in each case. These text files were used (after appropriate re-labelling) as event generators for Mokka using the LDC01 detector model (a diagram of the LDC detector is shown in figure 2.7). Mokka was then used to simulate the interactions between the low energy particles and the LDC01 detector for each beam parameter set, resulting in ten LCIO files (one file for each beam parameter set). These LCIO files were then analysed as described in section 4.5.3 below.

4.5.3 Analysis

At the point when this study was performed it was unclear what beam characteristics would eventually be used for the ILC, therefore any ECAL operating parameters decided at this stage would need to be workable for any reasonable set of beam characteristics. With this in mind the first stage of this analysis was to identify which of the proposed (as of March 2007) beam parameter sets was the 'worst case scenario' in terms of pixel saturation. Provided the distribution of hits in the ECAL was comparable for all parameter sets, the hit number would be the only characteristic which would control the extent of pixel saturation in any region of the ECAL. Figures 4.4, 4.5, 4.6 and 4.7 show that it is reasonable to assume that all parameter sets result in roughly the same distribution of hits, therefore the worst case scenario was selected on the basis of which set resulted in the largest number of hits in the ECAL. On this basis the simulation using the 1TeV High Luminosity parameter set was chosen as the 'worst case scenario' (as shown in table 4.2) and all further analysis was performed using the results from that simulation.

Once the 1TeV high luminosity parameter set had been selected, the next step in this analysis was to create a new 3D histogram to show the distribution of hits

recorded by the ECAL during the simulation using that parameter set. This histogram was filled by simply examining each hit recorded by the ECAL in turn, finding its x, y and z positions, and using those values to fill bins in the histogram. Since this investigation is focused on ECAL regions near to the beam axis (the electrons and positrons produced via beam-beam interactions usually remain close to the beam axis), only hits found in the ECAL endcaps were used to fill this histogram. The resulting histogram is shown in figure 4.8.

From this hit map it is possible to see that the density of hits recorded is highly dependent on distance from the beam axis. Since equation 4.10 implies that the probability of data loss due to pixel saturation should depend on hit density, this means that the probability of data loss in the ECAL should vary with the distance from the beam axis.

On this basis the ECAL endcaps were divided into annular regions according to distance from the beam axis as shown in figure 4.9 (note: regions of the ECAL endcaps that are the same distance from the beam axis but on separate endcaps are considered to be a single region for analysis). The number of hits found in each region was then recorded in a new 1D histogram (shown in figure 4.4), hits with energies less than 3 KeV were not included in this histogram to represent the limitations of a real ECAL. Once this histogram had been filled it could then be used as a reference to find out the number of hits registered in each region of the ECAL. These values could then be compared with the number of pixels present in each region (calculated from the total ECAL surface area from all layers present in the region and the size of individual MAPS pixels) to find the percentage of pixels in each region which had recorded hits during the simulation. The percentages found in the different regions of the ECAL were then used to fill a new 1D histogram which is shown in figure 4.10.

The percentages stored in this histogram should each be equal to the percentage probability of losing hits due to pixel saturation in the corresponding region of the ECAL after a single bunch crossing. This means that these values can be substituted into equation 4.10 as $\frac{q}{n_R} \times 100$ to predict the probability of losing hits due to pixel

101

Parameter set	Number of hits recorded in the ECAL
1 TeV High Lum	28791
1 TeV Large γ	158
1 TeV Nominal	226
1 TeV Low P	11985
1 TeV Low Q	122
500 GeV High Lum	11796
500 GeV Large γ	58
500 GeV Nominal	161
500 GeV Low P	5549
500 GeV Low Q	26

Table 4.2: The number of simulated hits on the LDC01 detector created by beam-beam interactions from a single bunch crossing, using different beam parameter sets.

saturation in their corresponding regions for any pixel reset time. This substitution was used to extrapolate the probabilities of losing ECAL hits to pixel saturation for a wide range of potential pixel reset times for several of the ECAL regions close to the beam axis. The results are shown in figures 4.11 and 4.12.

4.5.4 Conclusions

This study implies that electron-positron pair production from beam-beam interactions is likely to be a major source of background hits in the ECAL close to the beam. For long pixel reset times (around one reset per bunch train) a significant percentage of pixels are likely to be inactive shortly before they are reset due to background hits. However for the pixel reset times currently being considered (generally in the $1\mu s$ range) the percentage of pixels inactive in any region of the detector and at any time between resets remain below acceptable limits.

While these results indicate that the operation of a MAPS ECAL should not be significantly impaired by the presence of beam-beam background hits, nevertheless these hits do constitute a major source of non-signed hits (i.e. hits which do not come from any interesting physics events) in the ECAL. This background may be
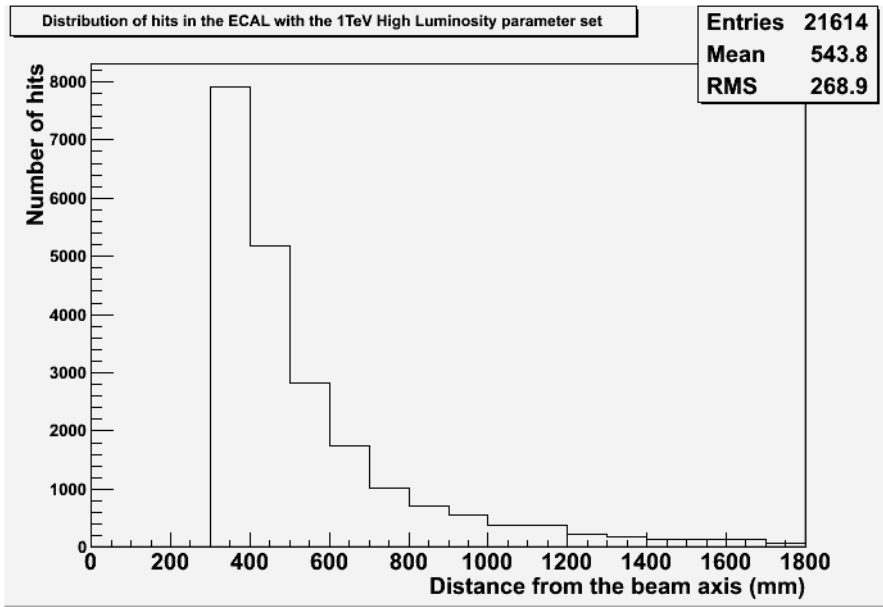
Figure 4.4: A sample histogram showing the distribution of hits in the LDC01 ECAL endcap relative to the beam axis recorded after a single bunch crossing using the 1TeV High Luminosity parameter set. Note: this distribution does have a minimum hit energy cutoff of 3×10^{-6} GeV.
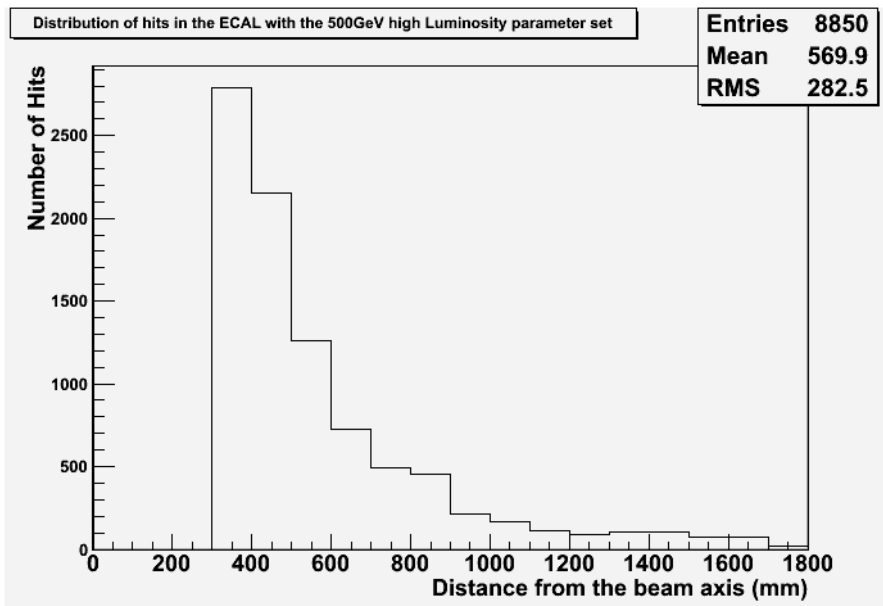
Figure 4.5: A sample histogram showing the distribution of hits in the LDC01 ECAL endcap relative to the beam axis recorded after a single bunch crossing using the 500 GeV High Luminosity parameter set. Note: this distribution does have a minimum hit energy cutoff of 3×10^{-6} GeV.
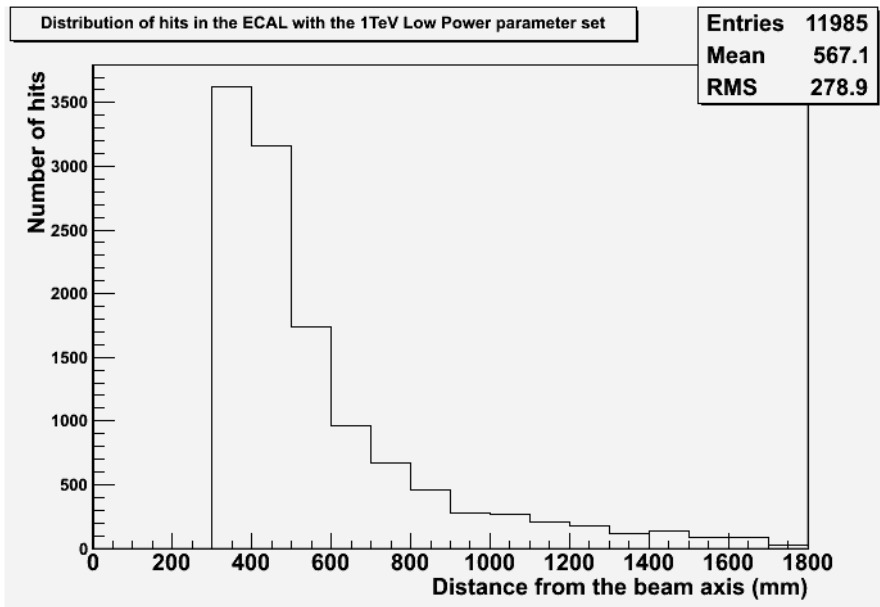
Figure 4.6: A sample histogram showing the distribution of hits in the LDC01 ECAL endcap relative to the beam axis recorded after a single bunch crossing using the 1TeV Low Power parameter set.
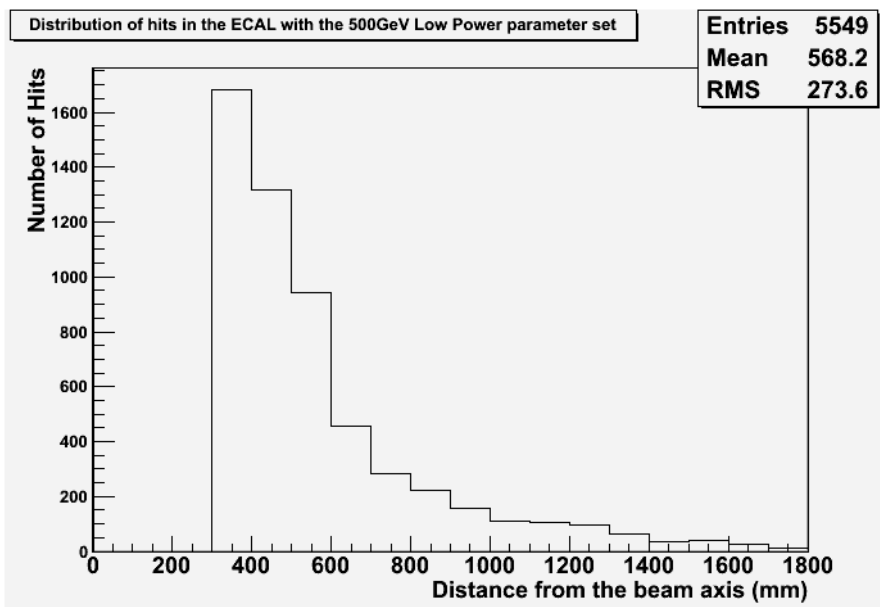
Figure 4.7: A sample histogram showing the distribution of hits in the LDC01 ECAL endcap relative to the beam axis recorded after a single bunch crossing using the 500 GeV Low Power parameter set.
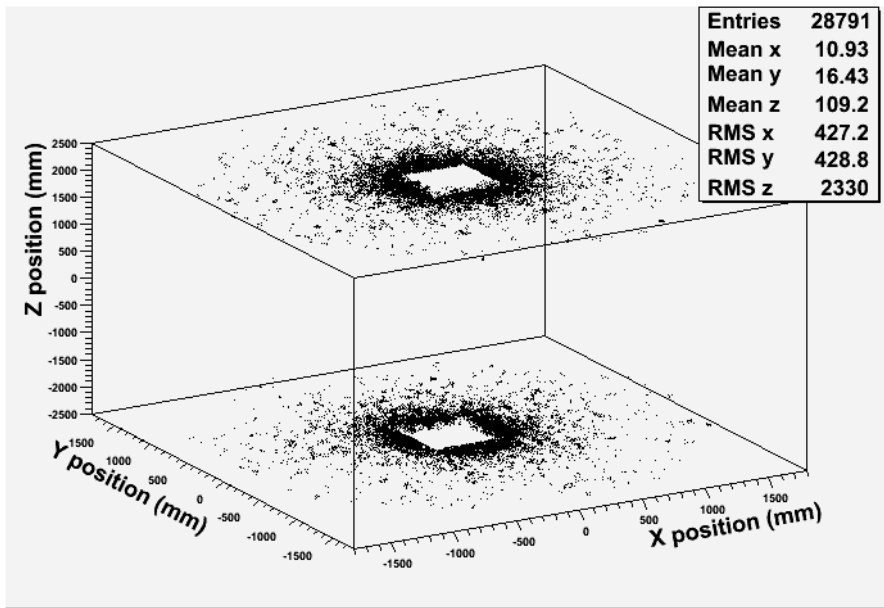
Figure 4.8: A sample histogram showing the positions of all hits in the LDC01 ECAL endcap recorded after a single bunch crossing using the 1TeV High Luminosity parameter set.
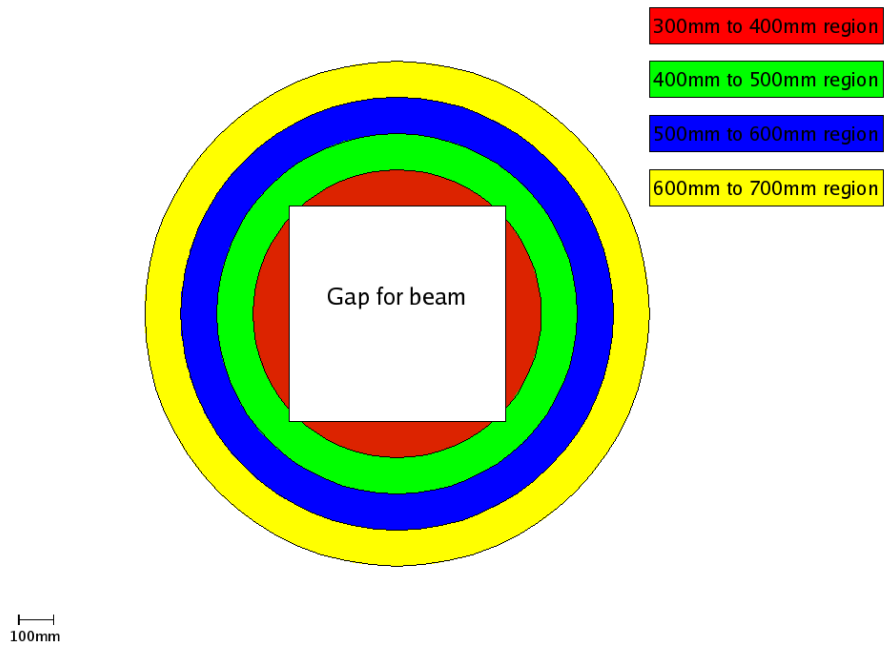
Figure 4.9: A diagram showing some of the regions the ECAL endcaps were divided into close to the beam axis.
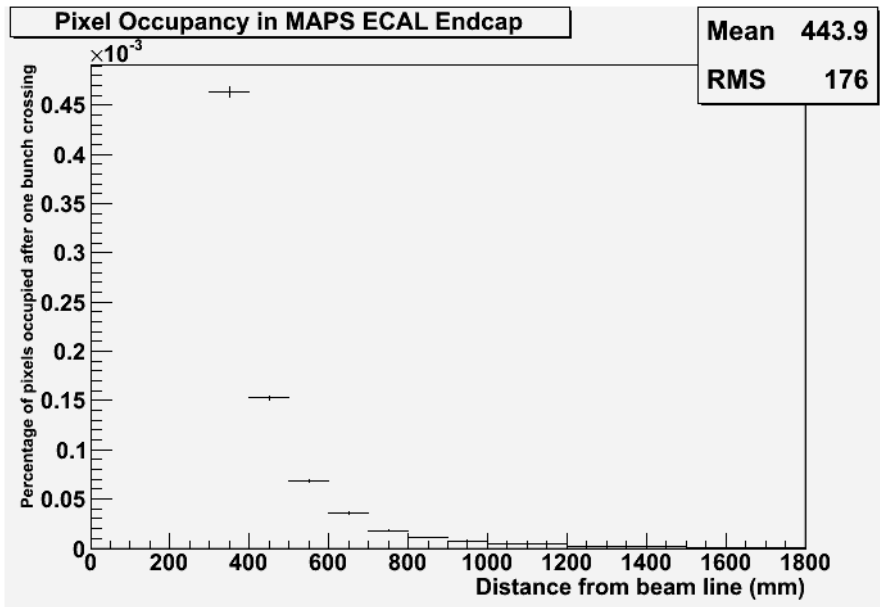
Figure 4.10: The percentage of pixels inactive in the ECAL endcap after a single bunch crossing with 1TeV c.o.m. energy and High Luminosity beam settings
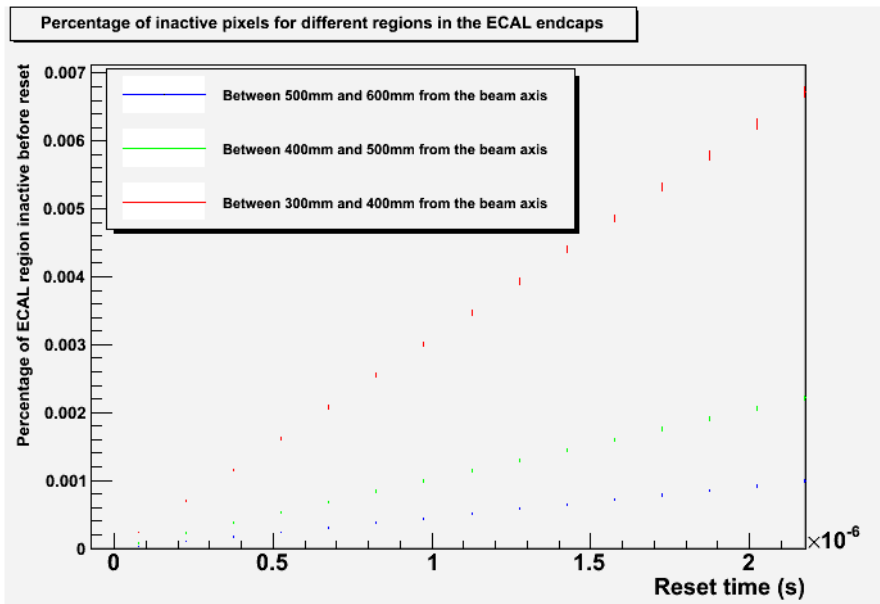
Figure 4.11: Variation in percentage of pixels inactive in ECAL endcap with reset time and location relative to the beam. The maximum reset/readout interval shown is 2000ns, approximately equal to the pixel reset times under consideration for a MAPS during this study.

106
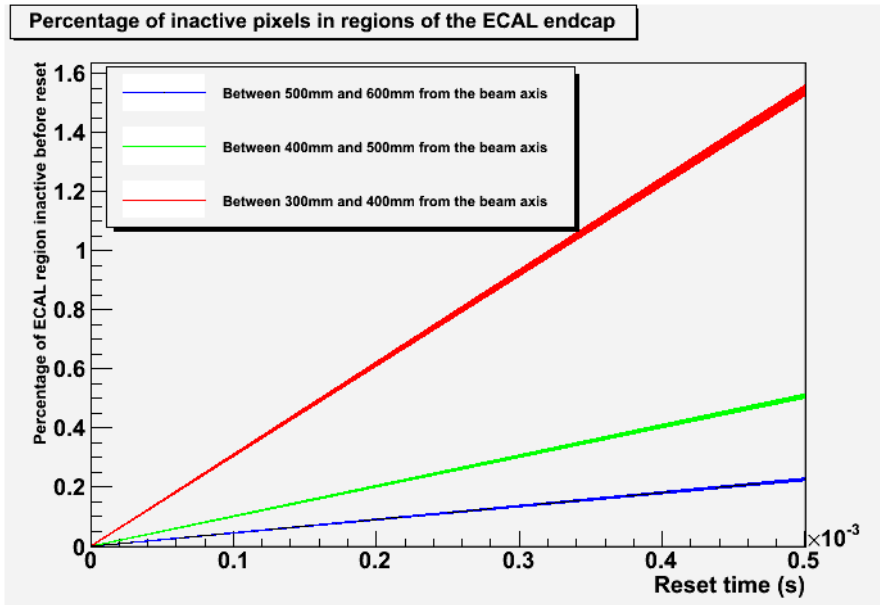
Figure 4.12: Variation in percentage of pixels inactive in ECAL endcap with reset time and location relative to the beam. The maximum reset/readout interval shown is the same order of magnitude as the time taken for a single bunch train passing through the detector[14].

significant in future physics event simulations, it may also prove significant when combined with other sources of noise. Work on both these potential issues is ongoing.

The single most obvious avenue for improvement in this study is the inclusion of more data on which to base the final results. At present the predictions made in this study about the number of pixels which would have recorded hits from beam-beam interactions after a given number of bunch crossings, are all based on the simulation of a single bunch crossing. Ideally predictions should be based on simulations of multiple bunch crossings since this would make those predictions less dependent on statistical fluctuations within the simulations used. In the study described above predictions were based on a single simulated bunch crossing due to the time required to simulate them, given sufficient time and/or computing power this constraint could be bypassed.

A potential extension for the study described in this chapter would be to repeat it using different detector models. Such extensions would be especially relevant to any further research on detector design since this study used the LDC01 detector model. The LDC concept has since been merged with the GLD concept to produce

107

the ILD detector model. This means that the LDC is essentially no longer under consideration for use in the ILC[17]. Therefore the obvious detector models to use in follow up studies would be recent versions of the three remaining potential ILC detector models; ILD, SiD and the 4th detector concept. Studies using SiD and ILD models are more likely to be useful than studies using 4th detector models since the design of the 4th detector does not include a MAPS ECAL.

Another potential extension to the study described in this chapter would be to extend it to encompass other forms of noise found in a MAPS ECAL. Regardless of its source, noise in the ECAL (i.e. any hits recorded in the ECAL which do not come from 'physics events') can render areas of the ECAL insensitive due to pixel saturation. While the study detailed in this chapter does deal with one of the largest sources of noise in the ECAL, a more comprehensive study incorporating multiple sources of noise could still prove useful.

Chapter 5

Pixel Threshold Uniformity in TPAC 1.0 Sensors

5.1 Introduction

In creating any detector based around a significant number of pixels, one of the principal requirements of the sensor is pixel uniformity. Every pixel in the detector should as far as possible behave like every other pixel in the detector. If the pixels in a sensor are not uniform then this can seriously jeopardise any attempts to calibrate the sensor or otherwise analyse information from it. Given that a completed MAPS ECAL would contain of the order of 10^{11} pixels[28], ensuring pixel uniformity has been an area of significant interest during sensor development. In addition to compromising the utility of a finished sensor, pixel non-uniformity also causes problems in attempting to characterise the behaviour of prototype sensors. Without uniform pixels the performance of a new sensor cannot be properly studied and therefore cannot be constructively altered or improved. This makes establishing pixel uniformity a high priority when new prototypes are produced because many measurements of sensor behaviour must be put on hold until the pixels can either be made uniform, or their variation can at least be well characterised. For the test sensors described in this study, one of the primary concerns for pixel uniformity was uniformity in pixel threshold.

In order to explain this concern, and hence the objective of this study, it is first necessary to explain what is meant by threshold in this context. Threshold is a value set for a sensor which controls the minimum amount of charge which must be accumulated in total for all diodes in the pixel for that pixel to register a hit. Setting the threshold of a sensor too low results in the sensor rapidly becoming saturated and unusable because pixels fire due to noise. At the other end of the spectrum, setting the threshold of a sensor too high results in a sensor which is inefficient because particles passing through the sensor might not deposit enough charge to cause pixels to fire.

Given these facts it is clear that being able to set the right threshold for a sensor is important for successfully operating and testing that sensor. Naturally, correctly setting the threshold for a sensor is hampered by a non-uniform response from the pixels in that sensor. Unless the global threshold set is the actual threshold used by all the pixels within a sensor, it is impossible to predict how sensors will behave when a given global threshold is set.

These problems are exacerbated by the fact that pixels with the wrong threshold can do more than just compromise their own reliability. Pixels in TPAC sensors are grouped into sets of 42 pixels sharing 'on sensor' memory as described in section 3.3.3. When this memory fills up, as it does after a certain number of hits (specifically 19 hits) are recorded in total on the corresponding 42 pixels, no further hits on those 42 pixels are recorded until the on sensor memory is read out[32]. A pixel with its threshold set too low can fill up the on sensor memory almost immediately after becoming active, effectively blinding the whole 42 pixel group until the sensor is read out (read out occurs at the end of each bunch train).

The principal method through which this problem could be solved is known as pixel 'trimming'. The 'trim' of a TPAC 1.0 pixel is an adjustment to the threshold which is used by that pixel. The higher the trim value set, the higher the threshold for the pixel in question. Pixel trims cannot increase the threshold of a pixel, only decrease them, however, by tailoring the decreases in thresholds set for different pixels it is possible to use trims to perform small corrections to reduce pixel non-

uniformity.

This study dealt with identifying the correct trims for each pixel in a TPAC 1.0 test sensor through passive threshold scans (altering the threshold of the test sensor without an external particle source i.e. noise scans).

5.2   Apparatus

The principal equipment for this experiment was the TPAC 1.0 sensor PCBs described in section 3.3.1. As with later sensor PCBs, the sensitive section of a TPAC 1.0 sensor consisted of a 9.15mm by 8.45mm rectangle containing 28224 MAPS/TPAC pixels which are described in section 3.3.2.

5.3   Overview

This study was carried out as a series of iterative experiments, analysis of each experiment either motivating the next experiment, or providing the information necessary to begin the next experiment. The experiments were divided as follows: the 'initial tests' where information on the unmodified behaviour of the test sensor was recorded described in section 5.4, the 'first trimmed runs' described in section 5.5 where the test sensor was run with preliminary trims based on the behaviour of the sensor in the initial tests, and the 'final trims' described in section 5.6 where the sensor was run with trims produced after observing both the unmodified behaviour of the test sensor and its response to the preliminary trims.

5.4   Initial Tests

5.4.1   Procedure

The basic tool for all of the experiments detailed in this study was subjecting the sensor to threshold scan run sets. A threshold scan run set consisted of 42 separate threshold scan runs, runs in which the sensor was active with no external stimuli

and with a range of different thresholds set so that the behaviour of the sensor could be observed.

Ideally the test sensor should only need to be scanned once with all the pixels active, however 42 separate runs were required due to the possibility of pixel 'cross-talk'. A complete description of, and investigation into the nature and causes of pixel cross-talk would require a full chapter on its own, and since cross-talk is not a major focus of this document only a brief summary of the characteristics of cross-talk in TPAC sensors and how it was dealt with in this study will be included here. Cross-talk is when a pixel registers a hit from any source and this causes other pixels to register hits[46]. The probability of a pixel recording a hit due to cross talk is largely dependent on the number of pixels active at the same time, the more pixels active, the more likely it is that pixels will experience cross-talk[47].

To limit the effects of pixel cross-talk, masks were applied to each sensor so that only one in every 42 pixels pixels would be active during each run, with the separation between those pixels maximised, hopefully reducing the effects of cross-talk. After each run was completed a revised mask would be applied to the sensor in which the unmasked pixels are 'moved along' slightly so that a different set of 672 pixels would be active during each run. Histograms showing the locations of active pixels during consecutive runs (showing both the pattern of active pixels and how that pattern changed over a run set) are shown in figure 5.1. After the full set of 42 runs, threshold scans would have been performed on every pixel within the sensor.

Each of these threshold scan runs was divided into 20000 bunch trains, where each bunch train was a 3.2ms period when the test sensor was active and recording data. These bunch trains were then further subdivided into 100 sets of 200 bunch trains. Each of these sets of bunch trains was defined by the global threshold set on the sensor while the sensor was active for these bunch trains. Specifically, the threshold applied for the first 200 bunch trains was 250 threshold units (a threshold of 1 threshold unit, referred to as a TU, is roughly equivalent to a minimum deposited energy of 36eV (therefore the energy deposited by one MIP should be equal to 100TU)[39]), for the next 200 bunch trains this threshold was reduced by 5TU to
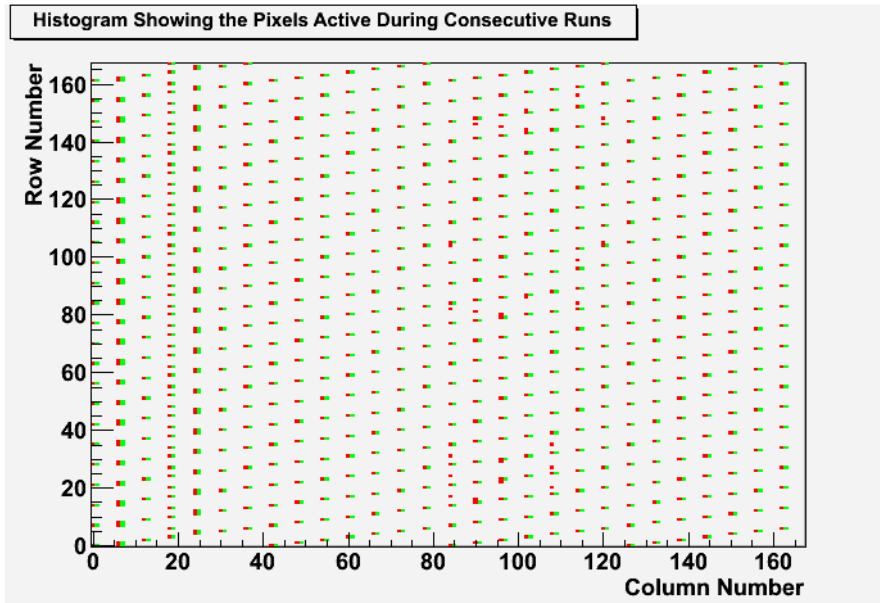
Figure 5.1: A diagram showing the locations of active pixels in the sensor during threshold scan run 450674 (in red), and threshold scan run 450675 (in green).

245TU. This reduction was repeated for each of the subsequent 200 bunch train groups until the global threshold set for the final 200 bunch trains was -250TU[40]. In this way the behaviour of the sensor could be observed at a range 100 different of thresholds. The data collected during these runs was then analysed to produce trim files as described below.

5.4.2 Analysis

Since threshold scan runs came in sets of 42 (each run with one pixel in 42 active), analysis of threshold scan runs effectively had two stages; the first stage dealing with processing the original 42 runs to get a single set of results, and a second stage consisting of analysing those unified results to find suitable trim setting for the pixels in the test sensor.

To describe the initial analysis of threshold scan runs, it is first necessary to detail the basic structure of data recorded during threshold scan runs. Like standard beam or cosmics runs, threshold scan runs are divided into a number of 'bunch trains' (lasting approximately 3.2ms), with all hits recorded during a run being assigned to their appropriate bunch train (in addition to recording the pixel location within the

sensor where the hit was recorded).

The initial analysis of a threshold scan run consisted of first producing one 1D histogram per pixel (for a total of 28224 histograms), referred to as the threshold scan histogram. These histograms were used to record the number of hits recorded on the pixel in question (y-axis) for each global threshold set (x-axis), see figures 5.5 and 5.6 for samples. To fill these histograms the bunch trains within the run were then divided according to the global threshold set during those bunch trains. As noted previously this resulted in 100 different threshold settings, each setting containing 200 bunch trains.

Each of these sets of bunch trains was then analysed individually. In each set the average number of hits recorded per bunch train was calculated for each pixel of the sensor. For each of these pixels the corresponding threshold scan histogram was then modified so that the bin corresponding to the current global threshold had a content equal to the average number of hits found in the pixel. Once all the bunch train sets had been analysed in this fashion, the end result would be a set of 28224 histograms, each one recording the variation in average number of hits recorded per bunch train for a single pixel as the sensor threshold was altered. These 28224 histograms were then saved in a root file for further analysis. Examples of completed threshold scan histograms for a sampler pixel and a shaper pixel are shown in figure 5.5 and 5.6 respectively. A sensor contains 14112 shaper pixels and an equal number of sampler pixels. Typically the threshold scans of the shaper pixels follow gaussian distributions similar to that showm in figure 5.5, while the threshold scans of shaper pixels commonly resemble the 'flat-top' gaussian distribution shown in figure 5.6 (the 'flat-top' is created by the pixel becoming saturated after recording 19 hits).

Once all 42 runs had been analysed in this fashion they were ready to be merged into a single data set. This was accomplished by using the original masking instructions used to set up the run set to identify which pixels were active during each run. Each run was then analysed using this data and the pixels that had been active during that run were identified. Once the active pixels had been identified for a run, the root file created by that run was opened and the threshold scan histograms cor-

114

responding to those pixels identified as active were copied to a new root file created to hold those histograms. This process was repeated for all 42 runs resulting in a single root file containing 28224 histograms (one for each pixel in the sensor, 672 taken from each run), each histogram showing the behaviour of a single pixel during a threshold scan when that pixel had been active. This unified data set was then the focus of later stages of analysis.

The second stage of analysis was to actually determine the trim settings suitable for the individual pixels in the test sensor. Ideally when all pixels are properly trimmed the individual threshold scan histograms should all be identical, in practice however all that is really possible with trimming is to decrease the effective threshold set, increasing the global threshold at which the pixel will saturate (i.e. the highest threshold at which an active pixel will on average record enough hits to fill up its associated memory buffer when not exposed to external stimuli during a bunch train). In terms of the threshold scan histogram produced this means that the effect of trimming is to simply move the whole distribution to a higher threshold value by decreasing the threshold set on the pixel in question, therefore the target of pixel trimming is simply to decide how much the the threshold applied to each pixel needs to be decreased to get the same behaviour from all pixels. Therefore it was necessary to identify at least one piece of information about each histogram which could be used as a descriptive statistic to characterise the overall location of the threshold scan distribution for that pixel.

Once a suitable statistic had been identified, the objective of pixel trimming could then be simplified to identifying the trim settings necessary to make the value of this descriptive statistic uniform for the whole sensor. Additionally, in later stages of this study the distribution of this descriptive characteristic for all pixels across the test sensor was used to measure pixel uniformity across the sensor (the smaller the RMS for this distribution, the more uniform the sensor). There were three values which were selected as being potentially suitable descriptive characteristics for this purpose:

1. The mean threshold of the threshold scan histogram

2. The peak threshold of the threshold scan histogram (i.e. the threshold where the number of hits recorded reaches a peak, or the lowest possible threshold meeting the criteria if the histogram reached a plateau)

3. The 50% drop-off threshold of the threshold scan histogram (the highest threshold where the number of hits recorded would exceed 50% of the peak number of hits recorded)

An example histogram with these values marked is shown in figure 5.7. Of these three descriptive statistics the 50% drop off threshold was judged to be the most useful because this value would most accurately predict the threshold at which a pixel would begin to saturate.

The 50% drop off threshold was found for all of the pixels in the test sensor by examining their individual threshold scan histograms. Specifically, for each pixel threshold scan, the highest threshold histogram bin where the mean number of hits recorded exceeded 50% of the maximum bin content was identified and its bin centre was recorded as the 50% drop off threshold. Each pixel threshold scan was analysed in this fashion and the 50% drop off thresholds found in this way were then recorded in an array for further analysis.

Initially all the pixels were to be trimmed so that their 50% drop off thresholds would be the same value, however, after some initial examination of the threshold scans it was decided that this would not be practical. Figure 5.2 shows a significant difference in the pixel threshold scans recorded for shaper pixels and the threshold scans for sampler pixels. For comparison, figure 5.3 shows that the behaviour shown in the pixel threshold scans is fairly consistent within shaper pixel regions, and similarly figure 5.4 shows that the same behaviour is fairly consistent within sampler pixel regions. With this difference in behaviour between the shaper and sampler pixels in mind, the objective in trimming the sensor became to find the trim setting so that the 50% drop off thresholds for all sampler pixels would be one value, while the 50% drop off thresholds for all shaper pixels would be another value.

Therefore the next challenge was to identify the 50% drop off threshold which the shaper pixels should be trimmed to, while also finding the 50% drop off threshold

which the sampler pixels should be trimmed to. This is achieved by establishing a wide range of potential target values for the 50% drop off threshold encompassing all feasible target values and separated by regular intervals. The 50% drop off threshold of each pixel histogram was then compared to each of the potential target values to see whether or not the pixel could be successfully trimmed to that value. If the pixel 50% drop off threshold was less than the potential target, and was separated from the target by a threshold difference less than the estimated change created by applying the maximum trim (initially thought to be 100 threshold units), then the pixel could be trimmed to that value, otherwise an accurate trim would be impossible. For each potential target value, the number of shaper pixels which could be trimmed to that value was recorded, as was the number of sampler pixels.

Once all the potential target values had been tested in this fashion, two target values were selected: one target threshold for the shaper pixels, selected as the target threshold where the greatest number of shaper pixels could be trimmed to that threshold. The second target threshold was for the sampler pixels, and was selected as the target threshold where the greatest number of sampler pixels could be trimmed to that threshold.

Once these target thresholds had been identified, the next task was to identify the trim settings needed for the 50% drop off point on each pixel threshold scan to meet its appropriate target threshold. In order to identify these trim settings it was first necessary to know the change in pixel threshold created by altering the trim value by one. Since all trim values were integers, this value would be equal to the precision of the trims (i.e. the smallest possible change in threshold created by altering the trim setting). At this point in the experiment the maximum number of threshold units the threshold of a pixel could be reduced by due to applying a trim (referred to as the trim range), and the number of trim settings available, were both thought to be well known. These values were used to calculate the precision of the trims by dividing the maximum trim setting by the trim range. The initial estimate for the trim range was 100TU and there were 16 trim settings ranging from 0 to 15, meaning that the precision of the trim applied was estimated to be $6\frac{2}{3}$TU.

Once the precision of the trim had been calculated, the target 50% drop off threshold for shaper pixels was then compared with the 50% drop off threshold values previously identified for each individual shaper pixel. For each pixel the trim setting necessary to make the 50% drop off threshold match the target threshold was calculated, rounded to the nearest integer (only integer trims can be set), and stored in a text file. If the trim required to make the 50% drop off threshold of a pixel equal the target threshold was found to be greater than the maximum trim (15), then the maximum trim would be entered into the text file for that pixel instead of the calculated value, similarly if the trim required was less than zero (the minumum possible trim), then a trim of zero would be recorded in the text file for that pixel. This procedure was then repeated comparing the target 50% drop off threshold for sampler pixels to the 50% drop off thresholds found for sampler pixels in the sensor, using the same text file as output.

The end result of this was a text file containing one trim value for every pixel in the test sensor (alongside information noting which pixel each trim value should be used for). Correctly formatted, this text file could be used to configure the trims of all the pixels in a sensor at the start of a run.

5.5 First Trimmed Runs

5.5.1 Procedure

The trims calculated as described in section 5.4.2 were applied to the test sensor and a new threshold scan run set (as described in section 5.4.1) was performed. The results from this run set were then analysed (along with further analysis of the initial run set) as described below.

5.5.2 Analysis

Unlike the analysis of the initial test runs, there were two separate objectives in the analysis of the first trim runs. These objectives were; first, to judge how well the
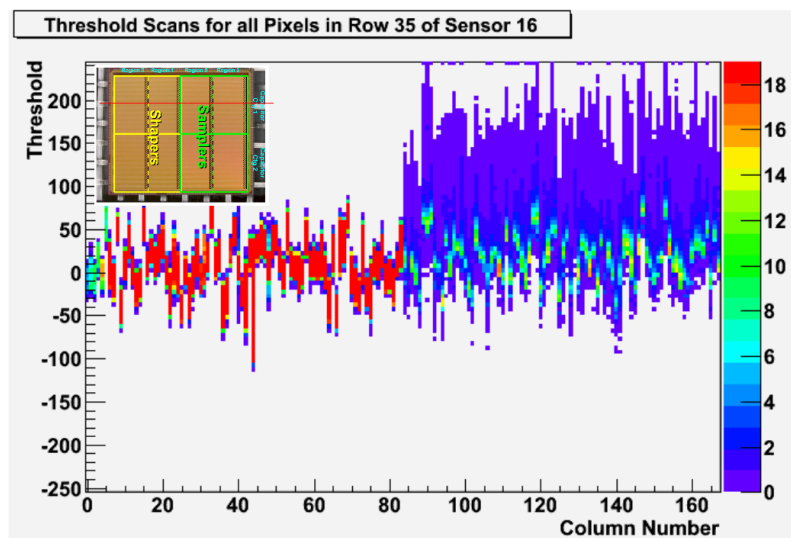
Figure 5.2: A sample 2D histogram showing the profiles of the threshold scan histograms for all pixels in row 35 of the test sensor when those pixels were active. In order to acquire all the threshold scans depicted, 42 threshold scan runs (with one in every 42 pixels active in each case) were merged together with the inactive pixels in each run being discarded. The small picture in the top left hand corner of the histogram is a picture of the test sensor with the location of row 35 marked by a red line. All threshold measurements are in TU.

trim had worked, ideally by allowing a direct comparison between the behaviour of the sensor with and without trims applied, and second, to observe the exact effects of applying a given trim to a pixel.

Up to a certain point the runs produced with the previously identified trims were analysed in the same fashion as the untrimmed runs described in section 5.4.2. Each of the 42 runs making up the threshold scan run set was analysed to produce threshold scans for all of the pixels in the sensor, and once all these runs had been analysed this way, the threshold scan histograms from all the active pixels in these runs were collected in a single 'merged' root file. Each of the threshold scan histograms in this merged file were then analysed to find the 50% drop-off thresholds (i.e the highest threshold at which the mean number of hits would exceed 50% of the maximum) for each of the individual pixel threshold scans. After this point the analysis applied to this new data began to diverge from the previously described procedures.

119
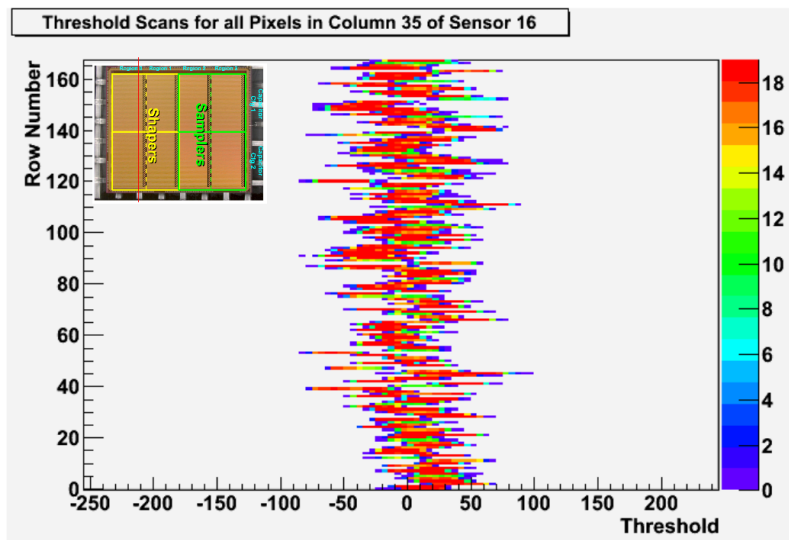
Figure 5.3: A sample 2D histogram showing the profiles of the threshold scan histograms of all pixels in column 35 of the test sensor when those pixels were active. Since columns 0 to 83 inclusive are composed of shaper pixels, all of the threshold scans in this histogram are from shaper pixels. In order to acquire all the threshold scans depicted, 42 threshold scan runs (with one in every 42 pixels active in each case) were merged together with the inactive pixels in each run being discarded. The small picture in the top left hand corner of the histogram is a picture of the test sensor with the location of column 35 marked by a red line. All threshold measurements are in TU.
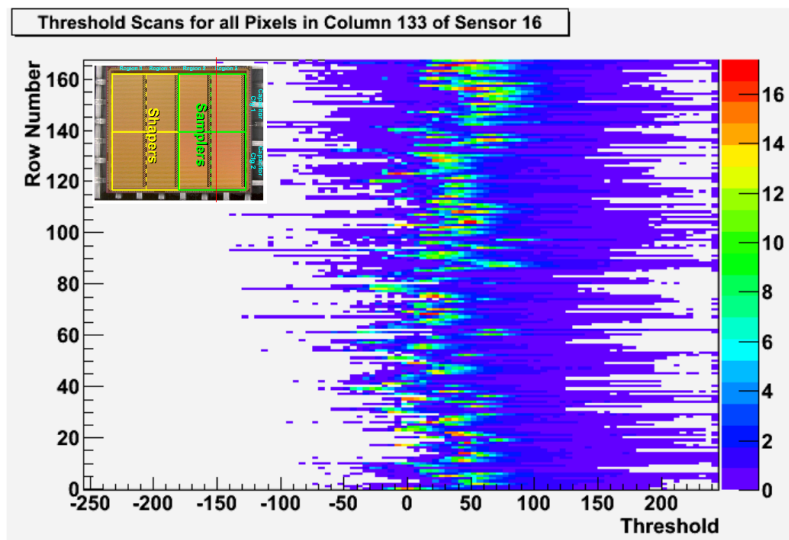
Figure 5.4: A sample 2D histogram showing the threshold scans of all pixels in column 133 of the test sensor when those pixels were active. Since columns 84 to 167 inclusive are composed of sampler pixels, all of the threshold scans in this histogram are from sampler pixels. In order to acquire all the threshold scans depicted, 42 threshold scan runs (with one in every 42 pixels active in each case) were merged together with the inactive pixels in each run being discarded. The small picture in the top left hand corner of the histogram is a picture of the test sensor with the location of column 133 marked by a red line. All threshold measurements are in TU.

121
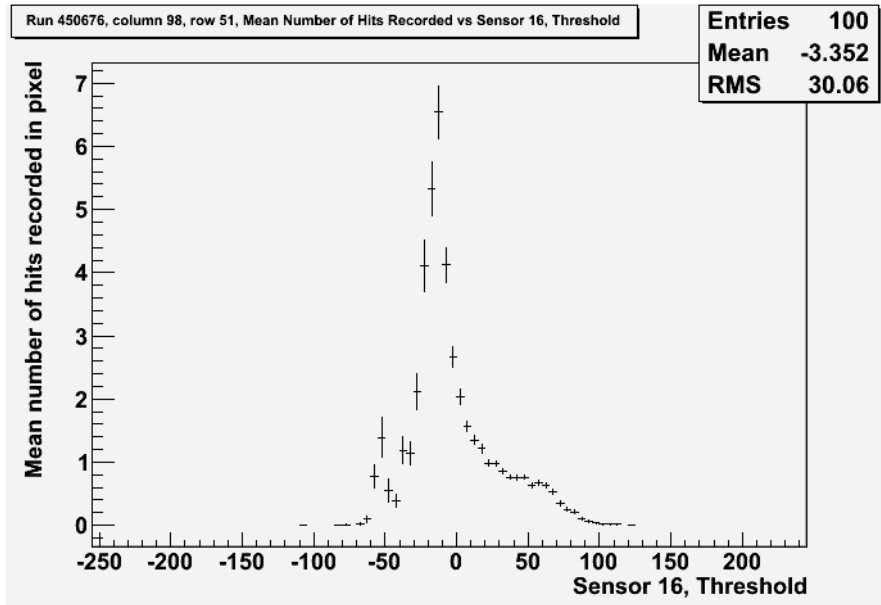
Figure 5.5: A sample threshold scan histogram for an active pixel in the sampler region of the sensor. For every threshold scan run 28224 pixel threshold scan histograms were produced of which 672 were scans of active pixels, and 336 of those active pixels were sampler pixels. In the whole sensor there were 14112 sampler pixels and they commonly displayed the gaussian distribution shown in the threshold scan above. All threshold measurements are in TU.
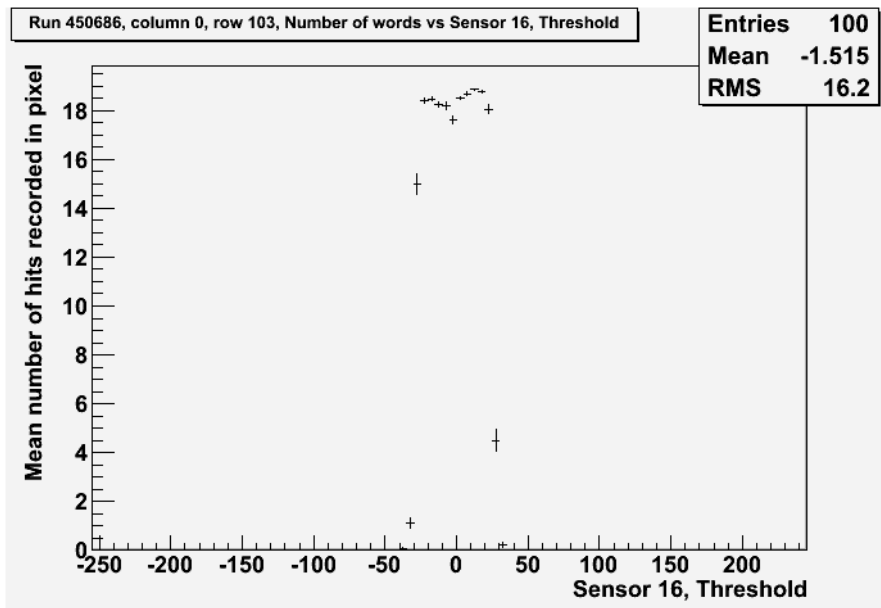
Figure 5.6: A sample threshold scan histogram for an active pixel in the shaper region of the sensor. For every threshold scan run 28224 pixel threshold scan histograms were produced of which 672 were scans of active pixels and 336 of those active pixels were shaper pixels. In the whole sensor there were 14112 shaper pixels and they commonly displayed the 'flat-top' distribution shown in the threshold scan above. It is likely that this distribution is in fact a gaussian distribution similar to the one shown in figure 5.5 with the 'flat-top' created by the pixel becoming saturated at 19 hits. All threshold measurements are in TU.

122
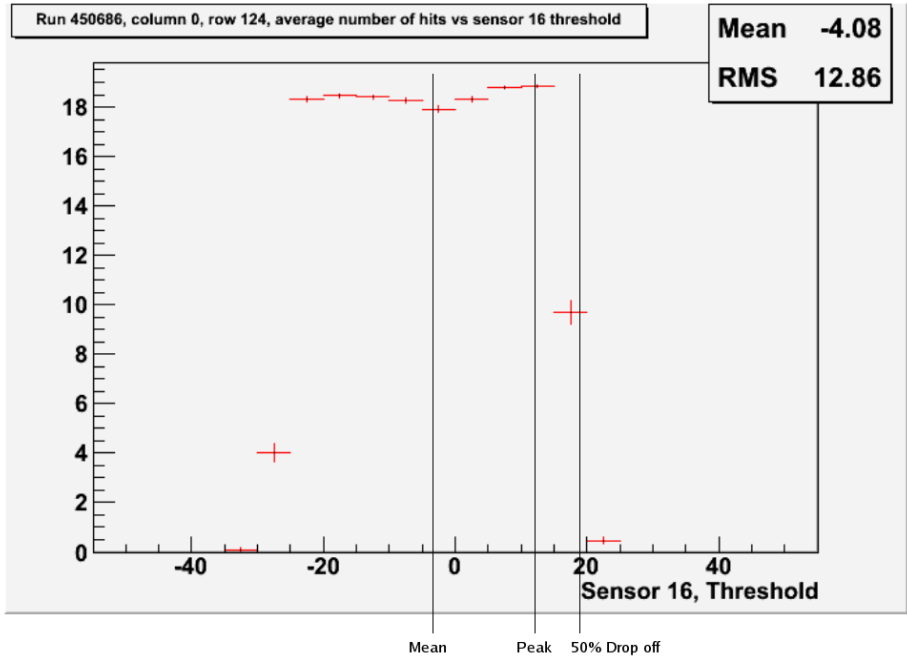
Figure 5.7: A sample threshold scan histogram for an active pixel showing the positions of the mean, peak and 50% drop off threshold for this pixel. The threshold scan shown came from a shaper pixel, all threshold measurements are in TU.

The 50% drop-off thresholds found were recorded in three new 1D histograms, one recording the distribution of 50% drop-off thresholds for all the pixels in the test sensor, one recording the distribution of 50% drop-off thresholds for all shaper pixels in the test sensor, and one recording the distribution of 50% drop-off thresholds for all sampler pixels in the test sensor. These three histograms are shown in figures 5.9, 5.11 and 5.13 respectively.

At this point in the analysis it became useful to begin directly comparing results from the preliminary tests (described in section 5.4) with the newly collected results from the preliminary trim run set. Therefore the merged file produced by the initial test runs was analysed in the same way, producing three additional 1D histograms showing the distributions of 50% drop off thresholds (one for all the pixels in the sensor, one for all the shaper pixels in the sensor, and one for all the sampler pixels in the sensor) when no trims were applied. These histograms are shown in figures 5.8, 5.10 and 5.12 respectively. Comparing these three histograms with their

counterparts from the preliminary trims run set shows a consistent decrease in the rms of the distributions when the preliminary trims are applied indicating more uniform pixel behaviour in the test sensor.

The second component of the comparison was to find the shift in the 50% drop off threshold for the same pixel when a trim was applied. The first step in this process was to establish a new 2D histogram to record the relation between the trim applied to a pixel and the resulting shift in the 50% drop off threshold. In this histogram the trim set was recorded on the x-axis and the resulting shift was recorded on the y-axis.

Once this 2D histogram had been established the trimmed and untrimmed threshold scan histograms for each pixel in the test sensor were openned in turn. For each pixel the trimmed and untrimmed 50% drop off thresholds for that pixel were identified from the histograms and the untrimmed drop off threshold was subtracted from the trimmed drop off threshold to find the shift in this threshold. The trim value applied to that pixel was then extracted from the text file used to store these values and together the trim and threshold shift values for the pixel in question were used to fill the 2D histogram.

Once all the pixels in the test sensor had been analysed in this fashion and the 2D histogram had been filled (the completed histogram is shown in figure 5.14), the trim range for the test sensor (i.e. the maximum shift in the effective threshold of a pixel achievable by altering its trim value) was calculated. Specifically an estimate of this value was calculated by finding the mean threshold shift of pixels which had a trim of zero applied (no trim), and subtracting it from the mean threshold shift of pixels which had a trim of fifteen (the maximum available trim) applied.

The result of this calculation was that the trim range was estimated to be (50.8±0.5)TU. When this calculation was repeated using only results from shaper pixels, the trim range was found to be (49.8±0.3)TU. The same calculation only using results from sampler pixels found a trim range of (52.4±0.5)TU. Since the errors created by the precision with which the trims applied affected the threshold of pixels would be significantly greater than any created by small inaccuracies in
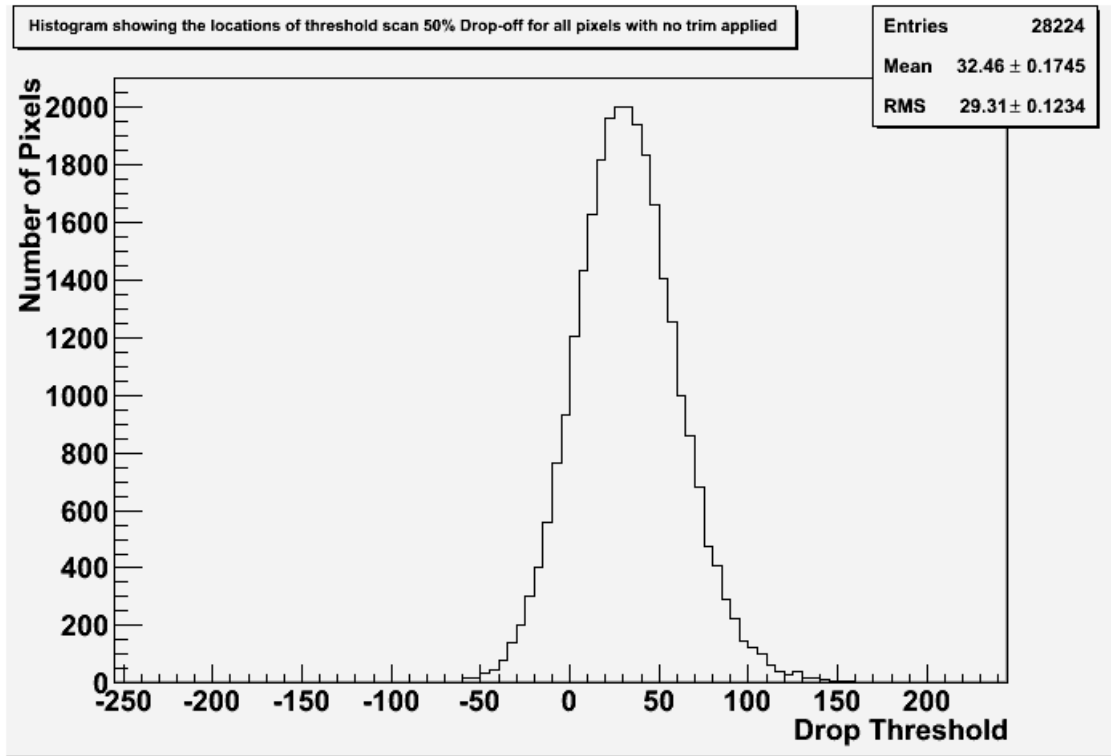
Figure 5.8: A plot showing the distributions of 50% drop-off points of all pixels in sensor 16 with no trim applied. All threshold measurements are in TU.

the trim range, this value was simply rounded to a trim range of 50 for the sake of simplicity.

Since the trim range found in this fashion is significantly different to the range originally estimated for the test sensor, it was then necessary to produce a new set of pixel trims using this range. These trims were calculated in the same fashion as described earlier in section 5.4.2 (using the results from the preliminary tests when the sensor was untrimmed), substituting the newly identified trim range for the estimate used to produce the preliminary trims.

5.6 Final Trims

5.6.1 Procedure

A new set of 42 runs was performed after the revised trims calculated with the trim range found in section 5.5 applied to the sensor. These runs were identical to the

Figure 5.9: A plot showing the distributions of 50% drop-off points of all pixels in sensor 16 with a preliminary trim applied to pixels in the sensor. All threshold measurements are in TU.
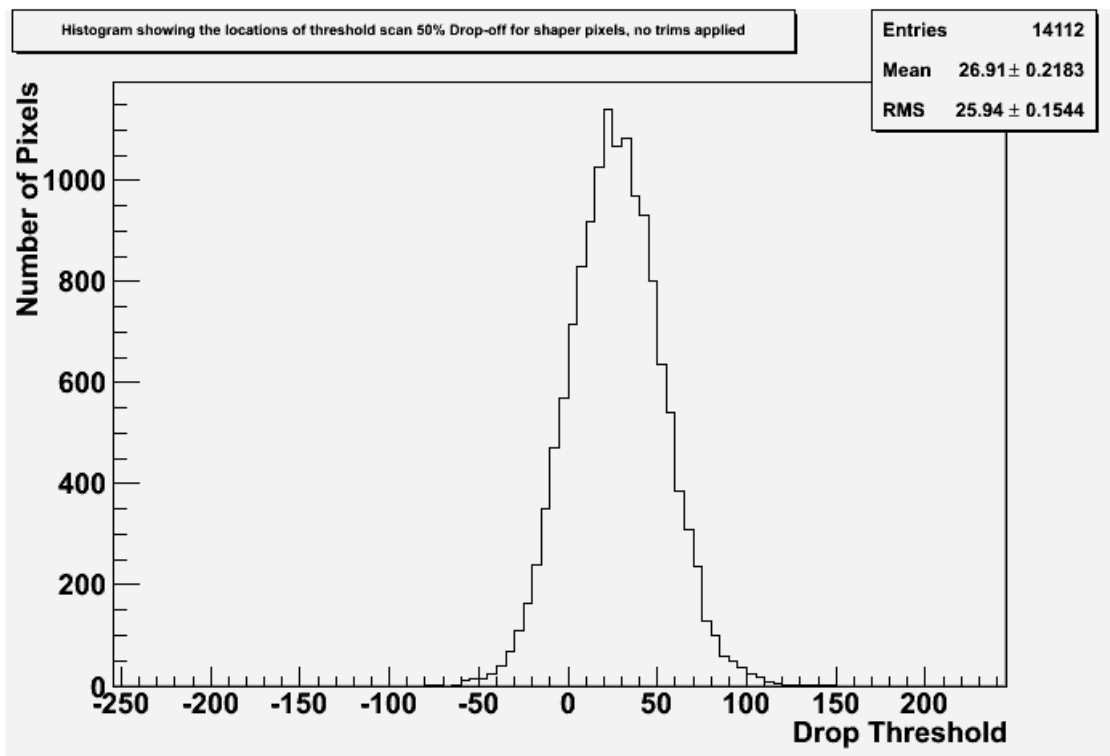
Figure 5.10: A plot showing the distributions of 50% drop-off points of shaper pixels in sensor 16 with no trim applied. All threshold measurements are in TU.

Figure 5.11: A plot showing the distributions of 50% drop-off points of shaper pixels in sensor 16 with a preliminary trim applied to pixels in the sensor. All threshold measurements are in TU.

Figure 5.12: A plot showing the distributions of 50% drop-off points of sampler pixels in sensor 16 with no trim applied. All threshold measurements are in TU.

127

Figure 5.13: A plot showing the distributions of 50% drop-off points of sampler pixels in sensor 16 with a preliminary trim applied to pixels in the sensor. All threshold measurements are in TU.

Figure 5.14: A plot showing the shifts in pixel 50% drop off points in sensor 16 caused by applying different trim settings. This data was collected by comparing run set 450674 to 450715 (untrimmed) to run set 452056 to 452097 (trim based on 50% drop off point, separate targets for shapers and samplers, trim range assumed to be 100 threshold units). Equivalent histograms showing only results from either shaper or sampler pixels are shown in figures 5.15 and 5.16 respectively. All threshold measurements are in TU.

Figure 5.15: A plot showing the shifts in pixel 50% drop off points in shaper pixels in sensor 16 caused by applying different trim settings. This data was collected by comparing run set 450674 to 450715 (untrimmed) to run set 452056 to 452097 (trim based on 50% drop off point, separate targets for shapers and samplers, trim range assumed to be 100TU). All threshold measurements are in TU.

Figure 5.16: A plot showing the shifts in pixel 50% drop off points in sampler pixels in sensor 16 caused by applying different trim settings. This data was collected by comparing run set 450674 to 450715 (untrimmed) to run set 452056 to 452097 (trim based on 50% drop off point, separate targets for shapers and samplers, trim range assumed to be 100TU). All threshold measurements are in TU.

threshold scan runs used in previous sections of the experiment, with one important exception, each run in previous sections consisted of 100 sets of 200 bunch trains, each set with a different global threshold set (ranging from 250TU to -250TU) for a total of 20000 bunch trains. The runs used in this section were instead divided into 500 sets of 200 bunch trains, each set with a different global threshold set (also ranging from 250 to -250) for a total of 100000 bunch trains. In principle these changes should not affect results. The results from these runs were analysed as described below.

5.6.2 Analysis

This set of 42 runs was then analysed in the same fashion as the preliminary trims run set as described in section 5.5.2, with the exceptions that there were 500 different global threshold settings during the run rather than 100, and it was of course not necessary to produce the 50% drop off distribution histograms for the original untrimmed run set a second time. The end result of this analysis is a set of three 1D histograms showing the distribution of 50% drop off thresholds when the new trims had been applied to the test sensor (one for all of the pixels in the test sensor, one for all of the sampler pixels in the test sensor, and one for all of the shaper pixels in the test sensor). These histograms are shown in figures 5.17, 5.18 and 5.19. These distributions could then be compared with the equivalent distributions for the untrimmed test sensor and the test sensor with preliminary trims applied already created as a result of the analysis described in section 5.5.2 to observe the effects of applying the new trims. Comparing figures 5.17, 5.18 and 5.19 with figures 5.9, 5.11 and 5.13, and with figures 5.8, 5.10 and 5.12 shows that the variation in pixel drop off thresholds is consistently lower for the run set using the revised trims than for either of the two preceding run sets (where the sensor was either untrimmed or had the preliminary trims applied). This indicates that pixel behaviour in the sensor did become more uniform once the revised trim was applied.

As in the analysis of the preliminary run set a 2D histogram was produced
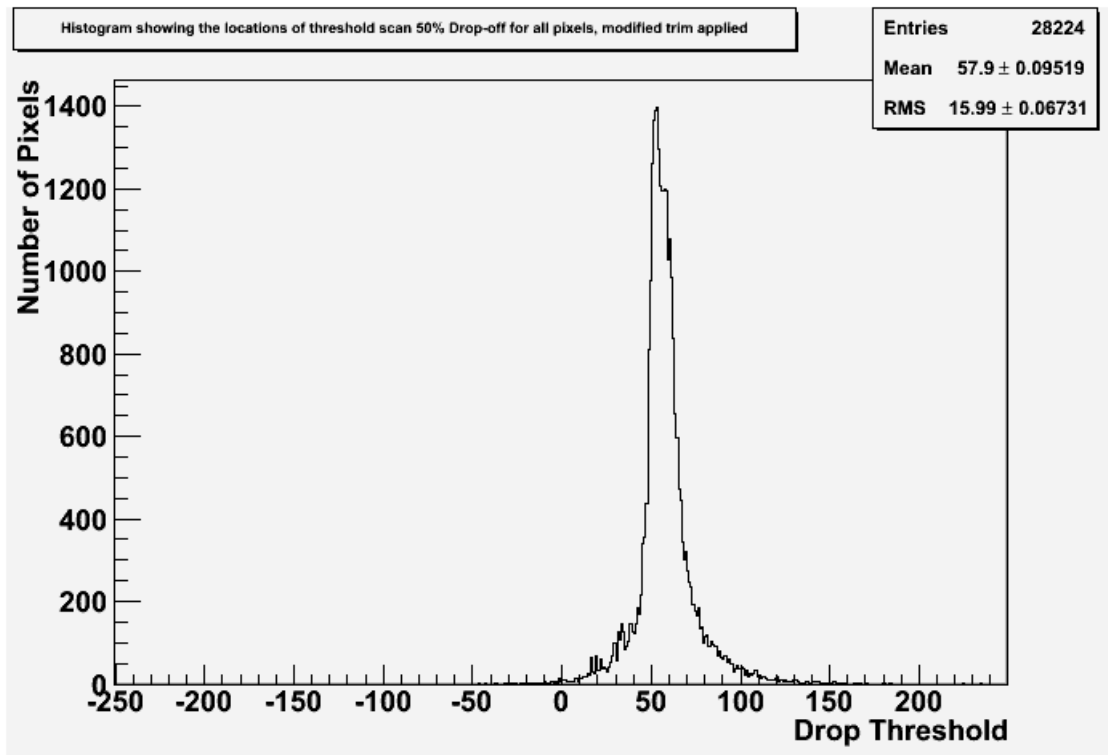
Figure 5.17: A plot showing the distributions of drop-off points of all pixels in sensor 16 with the final trims applied to pixels in the sensor. All threshold measurements are in TU.

showing the how the shift in 50% drop off thresholds for pixels related to the trim applied to those pixels, this histogram is shown in figure 5.20. This histogram acted as a useful safety check, ensuring that the trim range remained consistent with the range found from the preliminary trims, (50.8 ± 0.5)TU, even after a new set of trims had been applied. The trim range estimated from comparing the revised trim run set with the untrimmed run set (found by subtracting the average shift in pixel drop off threshold with zero trim applied from the average shift in pixel drop off threshold with maximum trim applied) was (51.4 ± 0.2)TU. The one σ error margins for this trim range overlap with the one σ error margin for the trim range calculated from the preliminary trim, confirming that the trim range is consistent between the run sets using the prelimary trim and the revised trim. This figure does show gaps in the range of trims applied implying that some trim values were never used. These gaps are artifacts of rounding values to integer trims caused by the smaller trim range used to produce the final trims.
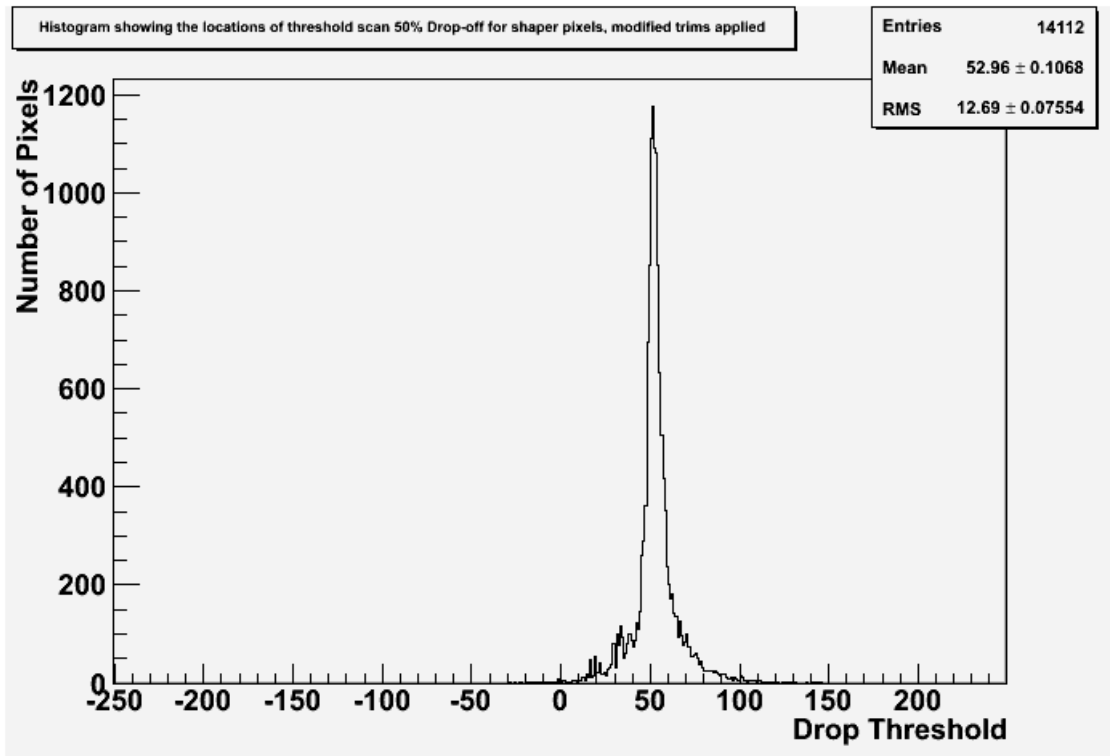
Figure 5.18: A plot showing the distributions of drop-off points of shaper pixels in sensor 16 with the final trims applied to pixels in the sensor. All threshold measurements are in TU.
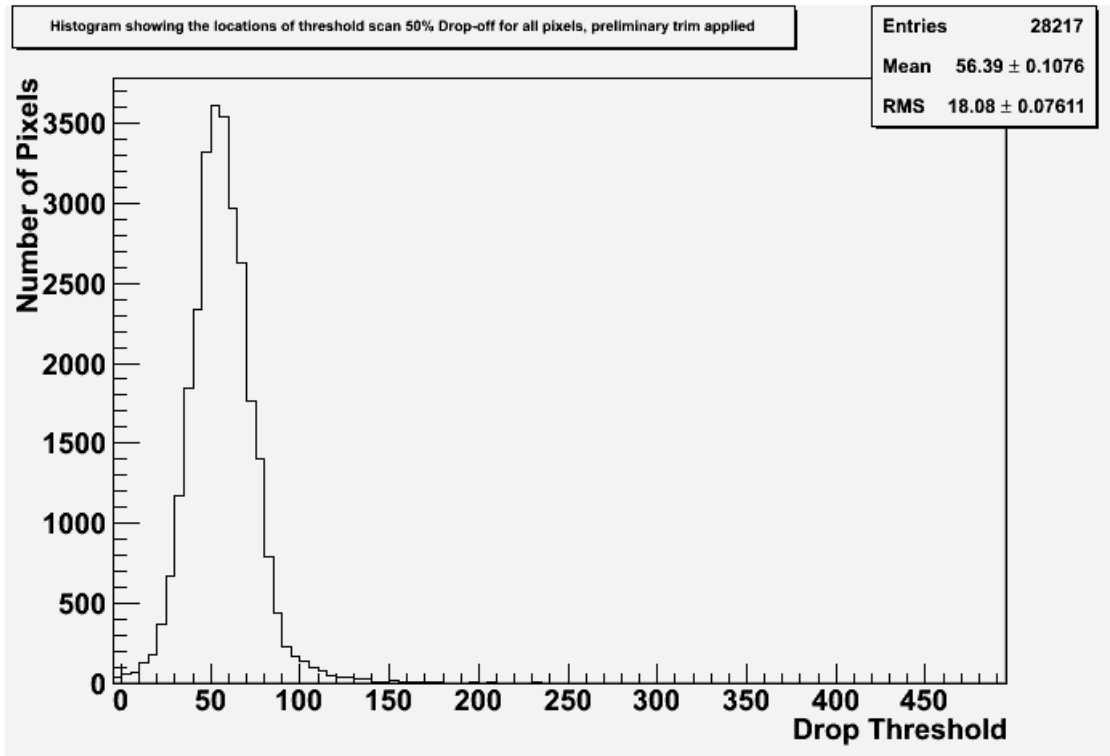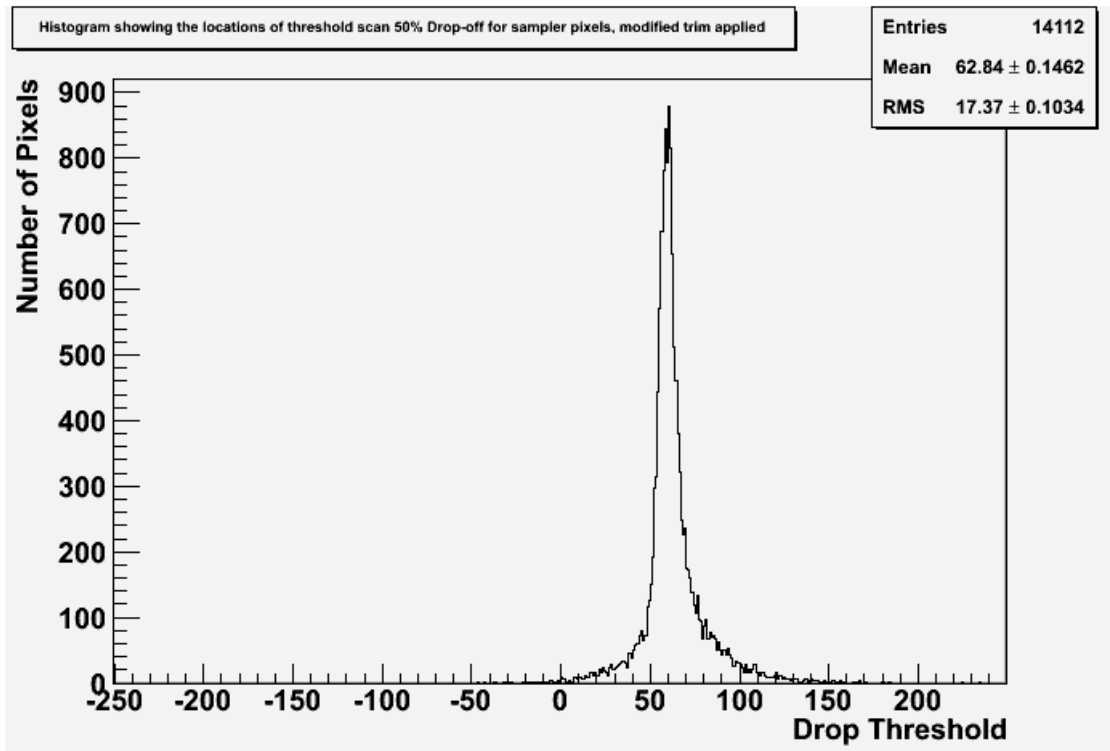

Figure 5.19: A plot showing the distributions of drop-off points of sampler pixels in sensor 16 with the final trims applied to pixels in the sensor. All threshold measurements are in TU.
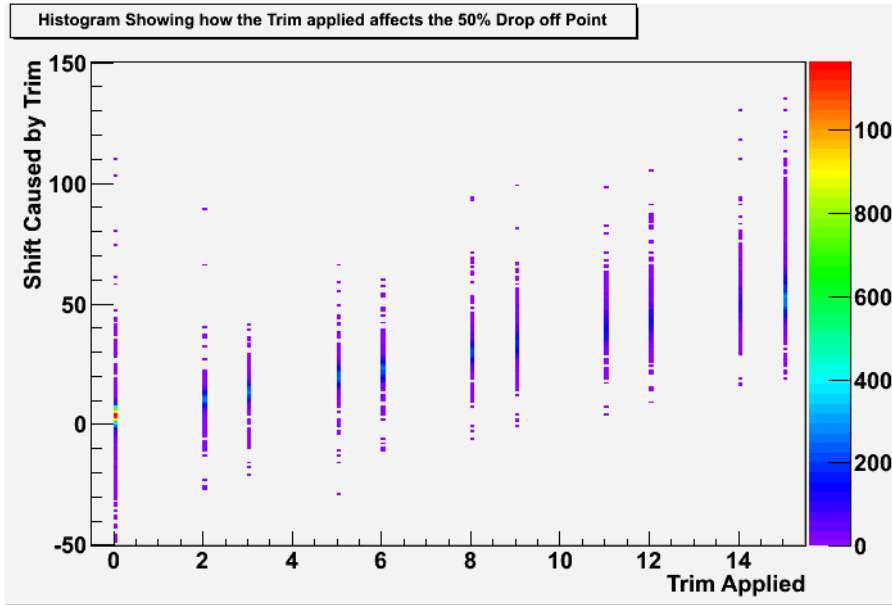
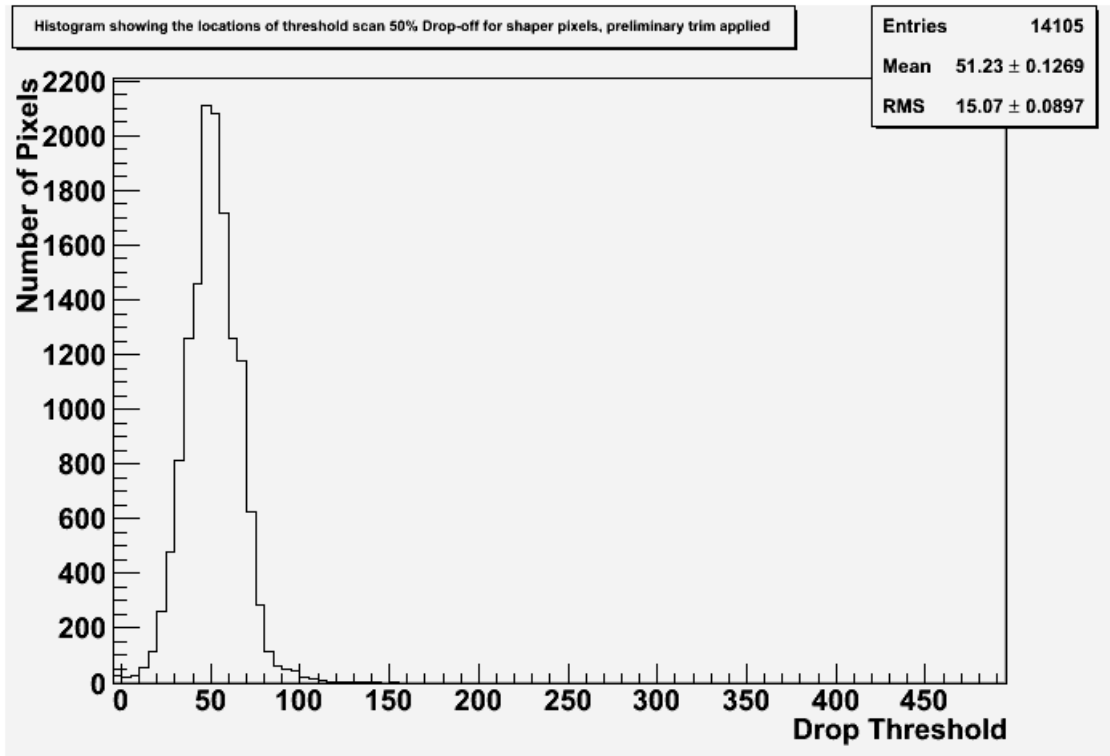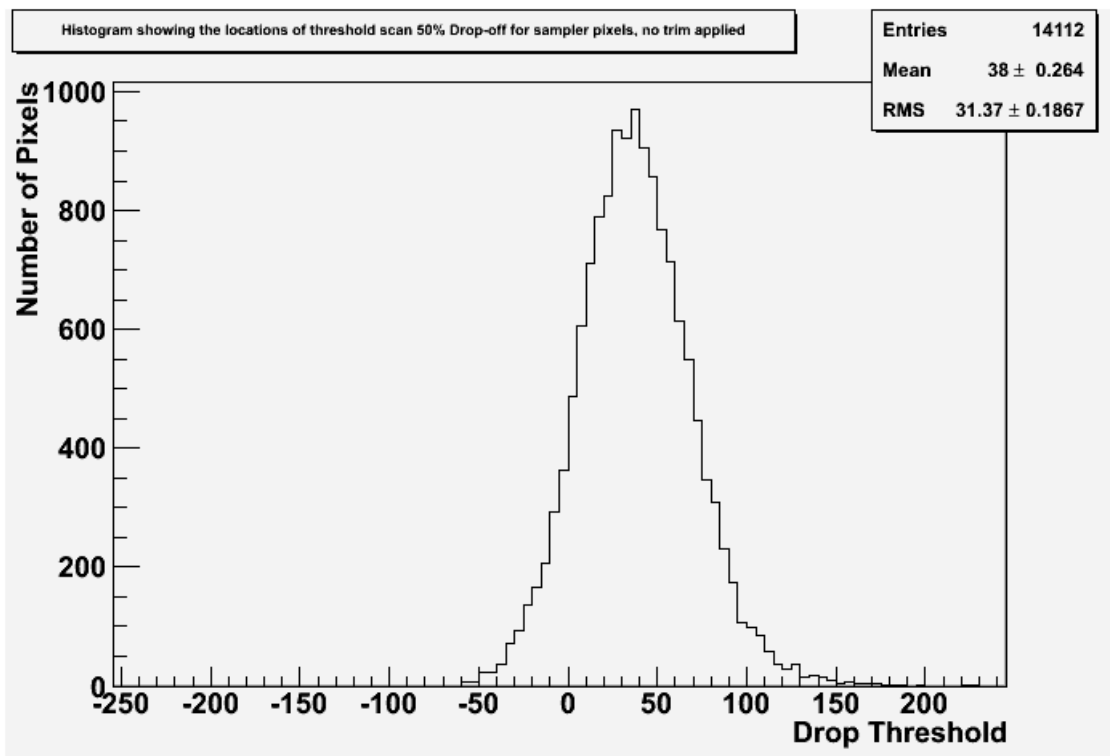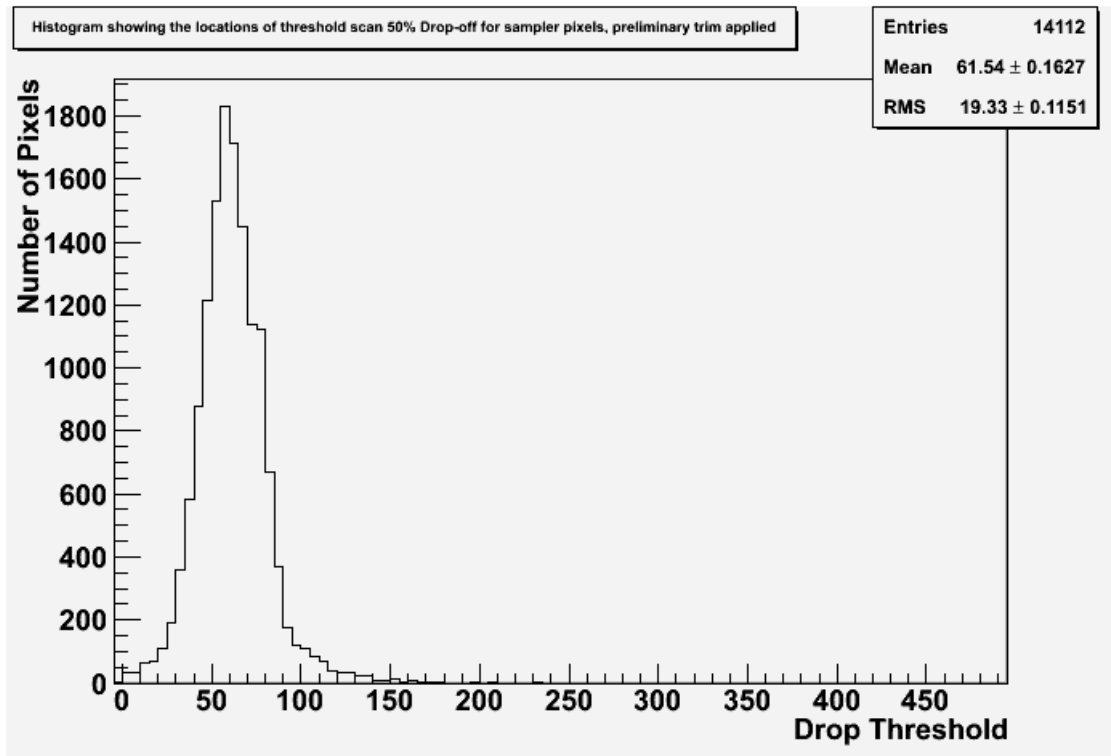Figure 5.20: A plot showing the shifts in pixel drop off points in sensor 16 caused by applying different trim settings. This data was collected by comparing run set 450674 to 450715 (untrimmed) to run set 452267 to 452308 (trim based on 50% drop off point, separate targets for shapers and samplers, trim range assumed to be 50 threshold units). Equivalent histograms showing only results from either shaper or sampler pixels are shown in figures 5.21 and 5.22 respectively. All threshold measurements are in TU.
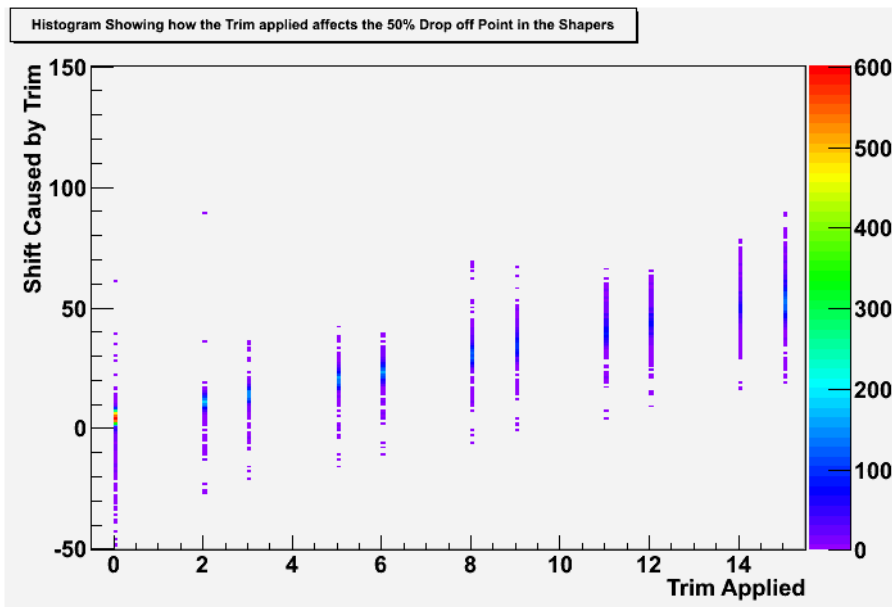
Figure 5.21: A plot showing the shifts in pixel drop off points in shaper pixels in sensor 16 caused by applying different trim settings. This data was collected by comparing run set 450674 to 450715 (untrimmed) to run set 452267 to 452308 (trim based on 50% drop off point, separate targets for shapers and samplers, trim range assumed to be 50 threshold units). All threshold measurements are in TU.
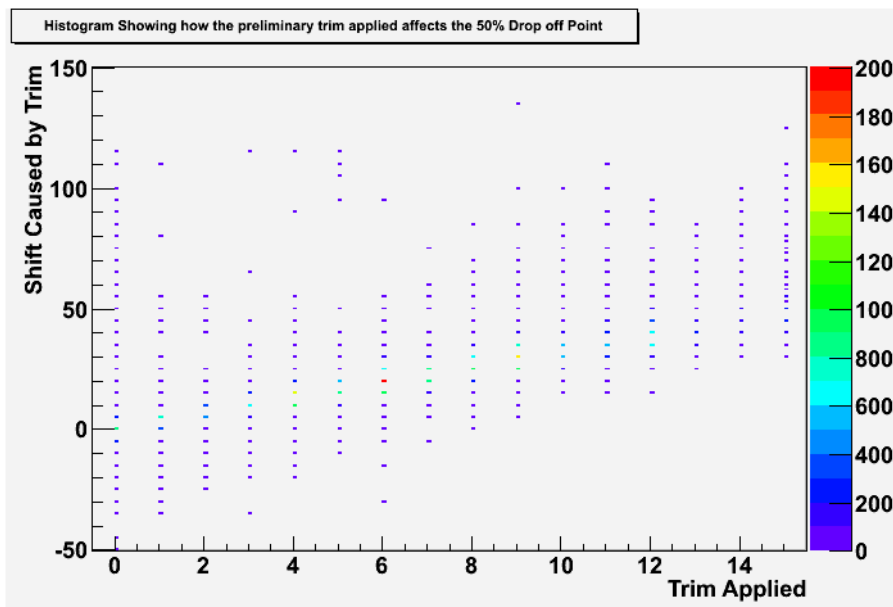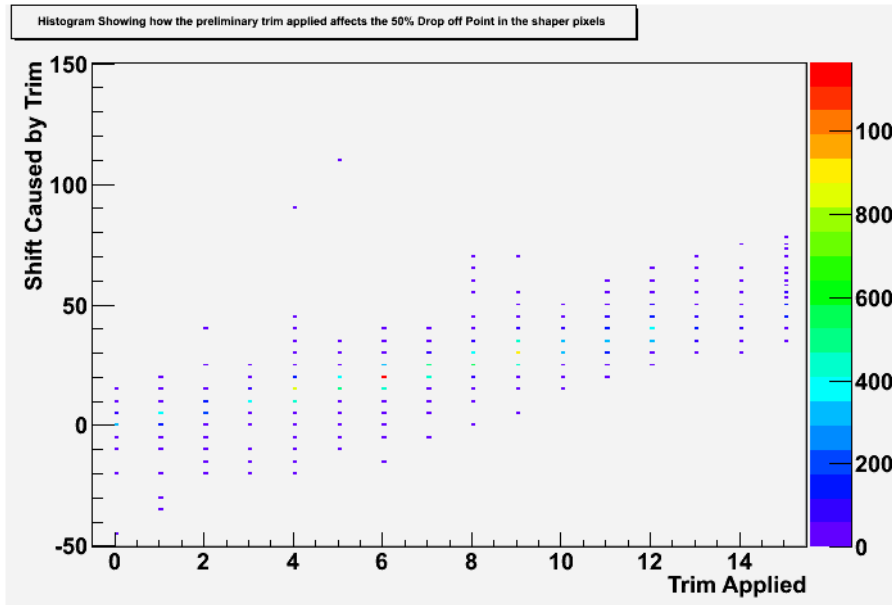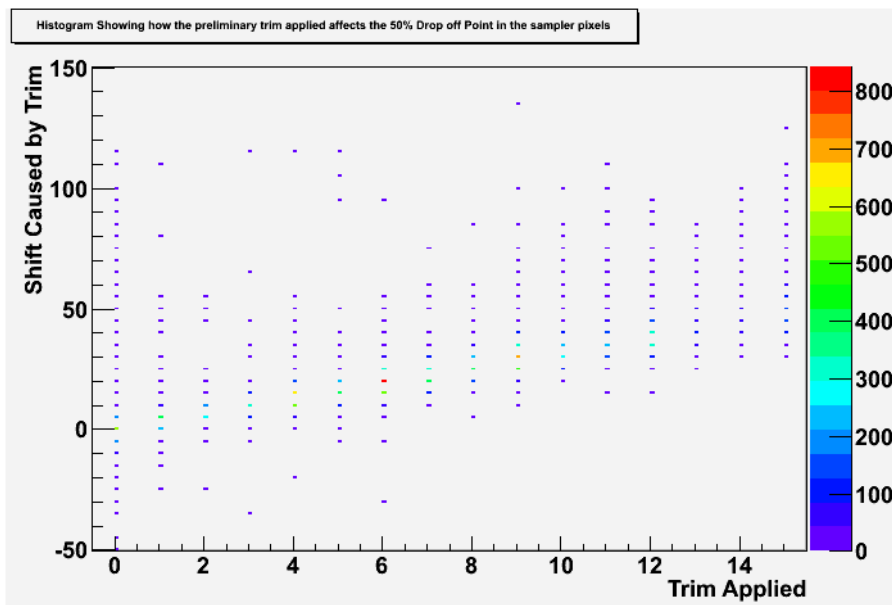
133
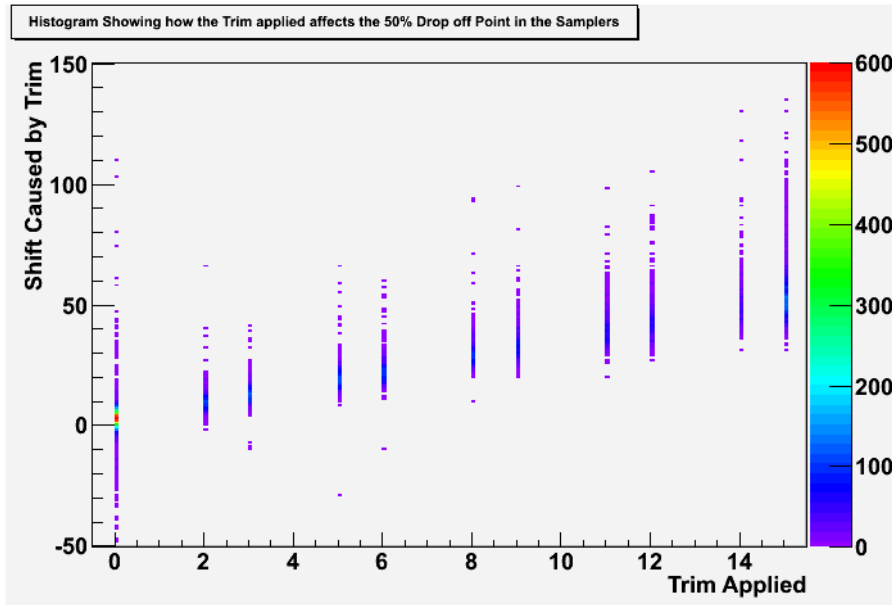
Figure 5.22: A plot showing the shifts in pixel drop off points in sampler pixels in sensor 16 caused by applying different trim settings. This data was collected by comparing run set 450674 to 450715 (untrimmed) to run set 452267 to 452308 (trim based on 50% drop off point, separate targets for shapers and samplers, trim range assumed to be 50 threshold units). All threshold measurements are in TU.

5.7 Discussion

The first and most obvious conclusion from this study is that TPAC 1.0 pixels were not uniform without amendment which can be seen in the untrimmed distributions of threshold scan 50% drop off thresholds shown in figures 5.8, 5.10 and 5.12. While this was an expected result, comfirmation is still significant in that it confirms the need for trimming in later prototype sensors.

Additionally, this study showed that this non uniformity could be reduced (but not eliminated) by applying the proper trims to pixels in the test sensor. This is shown by the differences between figure 5.10 and figure 5.18, and between figure 5.12 and figure 5.19. Specifically these figures show the distribution of the 50% drop off thresholds for all shaper pixels on the sensor (figures 5.10 and 5.18), and for all sampler pixels on the sensor (figures 5.12 and 5.19) with and without trims applied. Since the 50% drop off threshold of a pixel threshold scan is a good indicator of that pixels overall behaviour as the global threshold of the test sensor is changed, the shape of these distributions is useful in quantifying the pixel non uniformity

of the test sensor, the higher the RMS of the distribution, the less uniform the sensor. Comparing figures 5.10 and 5.18 shows that applying the final trims to the shaper pixels reduced the RMS of the distribution from (25.94 ± 0.15)TU to (12.69 ± 0.08)TU, while comparing figures 5.12 and 5.19 shows that applying the final trims to the sampler pixels reduced the RMS of these distributions from (31.37 ± 0.19)TU to (17.37 ± 0.10)TU, in both cases a significant improvement.

The results from this study and others were used to determine the design of TPAC 1.1 sensors, specifically TPAC 1.1 sensors allowed for a larger trim range with more potential trim settings (meaning fewer pixels would fall outside the viable trim range), and TPAC 1.1 sensors only included shaper pixels since these were found to have more uniform behaviour[35]. While TPAC 1.1 was quickly superseded by TPAC 1.2 due to problems with hit position reporting, TPAC 1.2 maintained these modifications[34].

One of the most obvious improvements to this experiment would be in the technique of identifying the 50% drop off threshold for a pixel. In the analysis described in section 5.5.2, this threshold was identified by finding the highest threshold where the mean number of hits exceeded 50% of the maximum and recording the centre of the corresponding histogram bin. This technique could be altered so that the 50% drop off threshold could be found from a suitable line fitted to the whole threshold scan, this should make the threshold found less susceptible to small scale variations in pixel behaviour and should make the 50% drop off threshold identfied more accurate. This more reliable technique was not used during this study because there were difficulties fitting a line to the 'flat top' shape of the threshold scan histograms shown in figure 5.6[48].

An additional improvement to the analysis described in section 5.5.2 would be to fit a straight line to the mean shift in 50% drop off thresholds caused by applying trims (i.e. plot the trims applied on the x-axis, plot the resulting mean shifts on the y-axis and fit a straight line to the resulting plot). This fitted line could then be used as a more accurate method of finding the trim range of the sensor, since this method would make use of more information than the current method. This

method was not used in this study because the granularity of the trims applied, and the limited trim range, were likely to be the limiting factors in the effectiveness of the trims applied, rather than the accuracy of the exact value of the trim range.

The most obvious extension to this study would be to repeat it using a more recent sensor design. As of the time of writing (spring 2010) the most recent MAPS TPAC sensor is TPAC 1.2 which as noted above should be more uniform in its initial behaviour (due to only using shaper pixels) while also accepting a wider range of trims. These two factors should create a much higher pixel uniformity after trimming than was shown by TPAC 1.0. A study performed on TPAC 1.2 would allow quantification of this improvement and might show other potential avenues of investigation.

During this study it was found that some pixels had behaviour too different from the behaviour of other pixels in the same sensor for trimming to plausibly bring them into line. These 'untrimmable' pixels pose potential problems for future attempts to use these sensors because during the normal operation of the test sensor they must be masked out to prevent their unpredictable behaviour from skewing results. This in turn results in sections of the sensor being unusable because the pixels there have been masked. This problem can potentially be dealt with in two ways; the first of which would be to impose higher quality standards on the sensors used, discarding sensors which had a large number of poorly behaved pixels, however this would tend to increase the cost per usable sensor. The other viable solution (which was used to improve the performance of TPAC 1.2 sensors) is to increase the number of trim bits available on the sensor, increasing the range of pixel behaviours which can be made uniform via trimming, unfortunately this also tends to decrease the percentage of the sensor that is sensitive. With this in mind it may be useful to know exactly how many trim bits would be necessary to make an acceptable proportion of the sensor usable. This could be achieved by attempting to trim sensors with artificially truncated trim ranges (i.e. deliberately using only a fraction of the trim range available) and measuring the fraction of pixels that remain unusable after these trims have been applied. These results could then be used to predict the

fraction of the sensor that is usable as a function of trim range, which (for a given acceptable proportion) could be used to predict the trim range necessary to ensure an acceptable proportion of the sensor is active. Such a study could be based on existing data, negating the need for any further experiments in this area.

Along similar lines TPAC sensors could be examined to check for other forms of pixel non-uniformity. Other forms of non-uniformity could include response to temperature variation. While at present it would be more difficult to deal with such non-uniformities than with simple threshold non-uniformity, this information could still prove useful in designing later sensors and in setting the thresholds and masks of existing sensors. A potentially troublesome form of pixel non-uniformity could be a non uniform response to trimming. As is shown in figure 5.20 the exact change in the 50% drop off point for pixel threshold scans is not completely uniform, to the extent that some pixels appeared to experienced negative shifts as a result of trimming (i.e. the threshold of the pixel seems to have been increased rather than decreased by applying a trim). This behaviour might be due to variations in pixel behaviour over time, or environmental changes during the threshold scans the test sensor was subjected to, but it is also possible that this variation in the apparent effects of trimming represents non uniformity in the response of different pixels. While the variation shown is fairly small, it could still be useful to examine a sensor using different trim values set uniformly across the whole sensor to find out if there is any consistent variation in the effects of trims on different pixels. Any variation in trim response found could then be incorporated into a new trimming method to produce more reliable trims by using the individual trim response of each pixel rather than assuming a single uniform trim response for the entire sensor. This would presumably produce more uniform sensors after trimming since variations due to non-uniform trimming response would be eliminated.

If however these experiments implied that trim response was essentially uniform across the test sensor, then this would imply that the variation in behaviour observed was due to either variations in pixel behaviour over time or environmental effects. Variations due to these causes could be further investigated by repeating threshold

scan run sets without changing the trims (or any other settings) applied to the tests sensor. If the behaviour of an individual pixel changed between these duplicate runs, then that variation could be attributed to either changes in pixel behaviour over time, or environmental variations, with repeated runs making it possible to identify any consistent trends in these variations. Such repeated runs were not incorporated into the study described in this chapter because it was judged that variations in pixel behaviour due to small environmental changes would be both inevitable, and impossible to remove.

Chapter 6

MAPS ECAL Simulation: Single Particle Energy Resolution

6.1   Introduction

The current objective in creating MAPS sensors for particle physics is the creation of a working MAPS ECAL. Because such a device is not trivial to produce, it is essential to understand the expected performance of a MAPS ECAL long before such a device is actually built and used.

For this reason the study detailed in this chapter was performed to attempt to predict some important characteristics of a MAPS ECAL. Specifically the principal characteristic investigated in the study described here was the single particle energy resolution of the ECAL over an energy range relevant to the ILC. The objective of this study was to characterise the variation of MAPS ECAL resolution with particle energy, and to compare this variation with the behaviour of a comparable analogue ECAL in the same circumstances. This was an important test for a MAPS ECAL because the single particle energy resolution is one of the two principal requirements for an ILC ECAL laid down in the ILC RDR[15].

In addition to establishing the suitability of a MAPS ECAL for use in the ILC and comparing its performance relative to a comparable analogue ECAL, there were two secondary motivations for this study. First a prediction of the single particle

energy resolution of a MAPS ECAL may prove useful in future studies. Any studies with a real prototype ECAL are likely to make at least some use of single particles due to the difficulty in producing a jet for testing purposes, and restricting it to the relatively small surface area of a prototype. This study can be regarded as preparation for such future testing, by providing parameters for the setup of such tests, and by providing predictions for comparison with results.

Second, this experiment can be seen as preparation for a potential future study intended to find the jet energy resolution of a detector using a MAPS ECAL. The experimental setup and analysis techniques used in this study are essentially simplified versions of the techniques which would eventually be used in a jet energy resolution study. Simulations using single particles were simpler to set up than jet simulations because they could be set up using a relatively simple event generator built into the simulation program (see section 6.2) where jet simulations would require the addition of an independent event generator. Similarly, analysis of single particle simulations is simplified compared to the analysis of jet simulations because, given that there was only one particle per event, there were no hits within an event which were not caused by that particle, essentially providing perfect clustering. By comparison, analysis of results found in the jet study would require the addition of new analysis packages to form hits into clusters according to which jet particle they were associated with. This would not only add another layer to the analysis, but also would also add the risk that results might be dependent on the clustering algorithms used. Therefore by performing a single particle energy resolution study first, it was possible to develop a 'simplified' version of the simulation and analysis techniques which could later be used for a jet energy resolution study whilst simultaneously collecting valuable (and clustering method independent) data.

6.2 Simulation Model

6.2.1 Simulation Software

This study used Mokka, an application based on the geant4 toolkit, to construct and run simulations using pre-set detector models described below. Both Mokka and Geant4 have been covered previously in sections 4.2.3 and 4.2.2 respectively.

6.2.2 Detector Models

This study required two detector models, one using the pixel parameters for a standard analogue ECAL, and another using the pixel parameters for a MAPS ECAL. To make a useful comparison between the two ECAL designs, it was necessary for both detectors to be identical apart from the ECAL pixels. To maximise the usefulness of this study the two detector models were based on a major planned detector where MAPS pixels could become part of the design. The models used had only minimal modifications relative to the default design since the effects of particle interactions with other components would be included within the simulations.

This study used a version of the proposed ILD detector (specifically ILD00) which already existed within the Mokka database, a diagram of this detector model is shown in figure 6.1. The ILD00 model was selected because it was the only model of the relatively new ILD detector which existed in the Mokka database when this study was carried out. Notably ILD00 included thicker layers of tungsten absorbers in the outer ECAL as described in the ILD letter of intent[17], the significance of this characteristic is discussed in section 6.3. Along with the SiD design, the ILD detector is one of the main potential users for a MAPS ECAL making studies using this detector highly useful[25][17]. The default ILD00 model had an ECAL design and pixel parameters consistent with an analogue silicon tungsten ECAL (such an ECAL is a likely component of the ILD design)[17]. Therefore the default ILD00 model was used entirely unmodified as the analogue ECAL model. Histograms produced to confirm the dimensions of the analogue ECAL and its pixels can be

seen in figures 6.6, 6.7, 6.8, and figure 6.10. Figures 6.7, 6.8 and 6.10 all show the distribution of hits in a small section of the analogue ECAL highlighted in figure 6.2. Figures 6.7 and 6.8 show the minimum separation between hits in the analogue ECAL in two directions parallel to the surface of the ECAL, in a single layer. This shows the transverse pixel size of the detector model in both directions (in this case approximately 5mm). Comparing the two figures seems to confirm that the pixels are square. Figure 6.10 shows the distance between separate sensitive layers in the analogue ECAL and therefore demonstrates the greater distance between sensitive layers on the outer ECAL relative to the inner ECAL due to increased tungsten absorber thickness in the outer ECAL. The histogram shown in figure 6.6 shows the full extent and the rough shape of the analogue ECAL by showing the locations of all the hits recorded in that ECAL.

In order to simulate the behaviour of a MAPS ECAL within the same detector a modified version of the ILD00 model was produced. In terms of the number and placement of sensitive ECAL layers and the associated absorber slabs, a MAPS ECAL does not need to differ noticeably from a comparable analogue ECAL, both designs broadly followed the ILD calorimeter design described in section 2.3.3. The main difference between the two designs is in the pixels used. When examined in detail MAPS pixels differ considerably from their analogue counterparts, however when considered purely in terms of how the pixels affect particles passing through, and how those particles potentially affect the pixels, MAPS pixels differ from analogue pixels in only three important features: their transverse size, the thickness of the sensitive silicon, and the information which the pixels record about particles passing through.

MAPS pixels have a significantly smaller transverse size than their analogue counterparts (to ensure that it is unlikely for more than one shower particle to pass through a single pixel at any given time), to represent this the MAPS model was modified to include a significantly smaller pixel size within the ECAL (50μm by 50μm rather than approximately 5mm by 5mm). Similarly the layer of sensitive silicon in a MAPS pixel is considerably thinner than in a typical analogue pixel.

To represent this the MAPS model was modified to include a considerably reduced sensitive silicon thickness (15μm rather than 0.5mm). Histograms produced to confirm the dimensions of the MAPS ECAL can be seen in figures 6.3, 6.4, 6.5, and figure 6.9. Like their analogue counterparts figures 6.4, 6.5 and 6.9 all show the distribution of hits in a small section of the MAPS ECAL highlighted in figure 6.2. Figures 6.4 and 6.5 show the minimum separation between hits in the MAPS ECAL in two directions parallel to the surface of the ECAL, in a single layer. This shows the transverse pixel size of the detector model in both directions (in this case 50μm). Comparing the two figures confirms that the pixels are square. Figure 6.9 shows the distance between separate sensitive layers in the MAPS ECAL and like the analogue ECAL, this demonstrates the greater distance between sensitive layers on the outer ECAL relative to the inner ECAL due to increased tungsten absorber thickness in the outer ECAL. Comparing figure 6.9 with figure 6.10 shows that the basic layer structure and positions remain the same in the analogue and MAPS ECAL models. The histogram shown in figure 6.3 shows the full extent and the rough shape of the MAPS ECAL by showing the locations of all the hits recorded in that ECAL. A comparison between figures 6.3 and 6.6 indicates that the overall size and shape of the ECAL is not changed between the two detector models.

The most significant difference between MAPS pixels and their analogue counterparts is that while analogue pixels record the energy deposited on them, MAPS pixels are digital, only recording whether or not a particle passed through. This difference was represented by differences in how data from MAPS and analogue ECALs was analysed as shown in section 6.5; no modifications in the detector model were necessary to represent this characteristic.

6.2.3 Test Particles

The particles used to test both ECALs in this study were photons at a range of different energies. Photons were selected because there is no risk of the magnetic field within the detector preventing low energy photons from reaching the ECAL, and

143
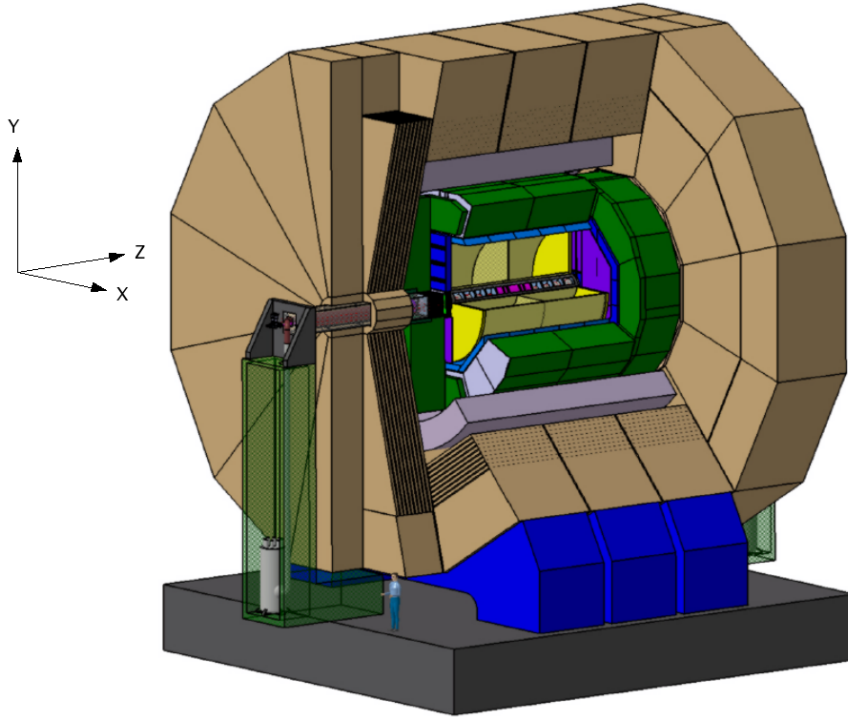
Figure 6.1: A diagram showing the overall layout of the ILD detector as well as the coordinates system used throughout this chapter. The zero point of all coordinate in this system is the interaction point at the centre of the detector.

because they cannot decay, ensuring that the study remains focused on the response of an ECAL to single particles. The starting point for the simulated photons was at the exact centre of the ECAL at the interaction point.

6.2.4 Analysis Software

This study used the program Marlin (described previously in section 4.3) to analyse results. A modified version of the Mapsana processor (also discussed in section 4.3) was produced to create the histograms required for the analysis techniques described in section 6.5 below.

6.3 Theory

As described above the simulations used in this study were intended to find both the single particle energy resolutions of the ECAL designs and how that value changed

144
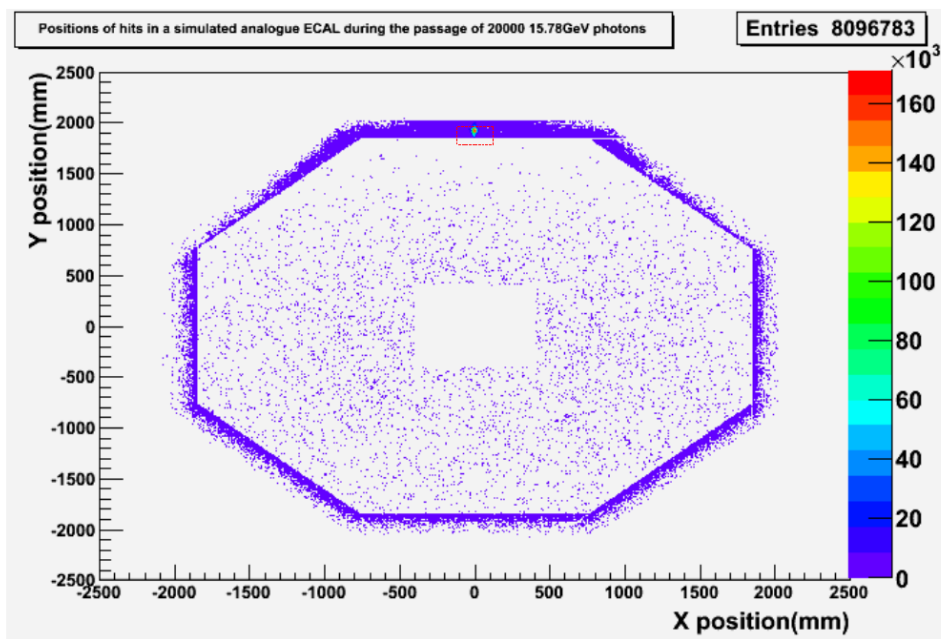
Figure 6.2: A diagram showing the distribution of simulated hits in an analogue ECAL during a test run using 15.78 GeV photons. Part of the highlighted area (specifically the innermost layers of the ECAL close to z=0mm) is shown in more detail in figures 6.7, 6.8 and 6.10. The same region in a MAPS ECAL is shown in figures 6.4, 6.5 and 6.9.
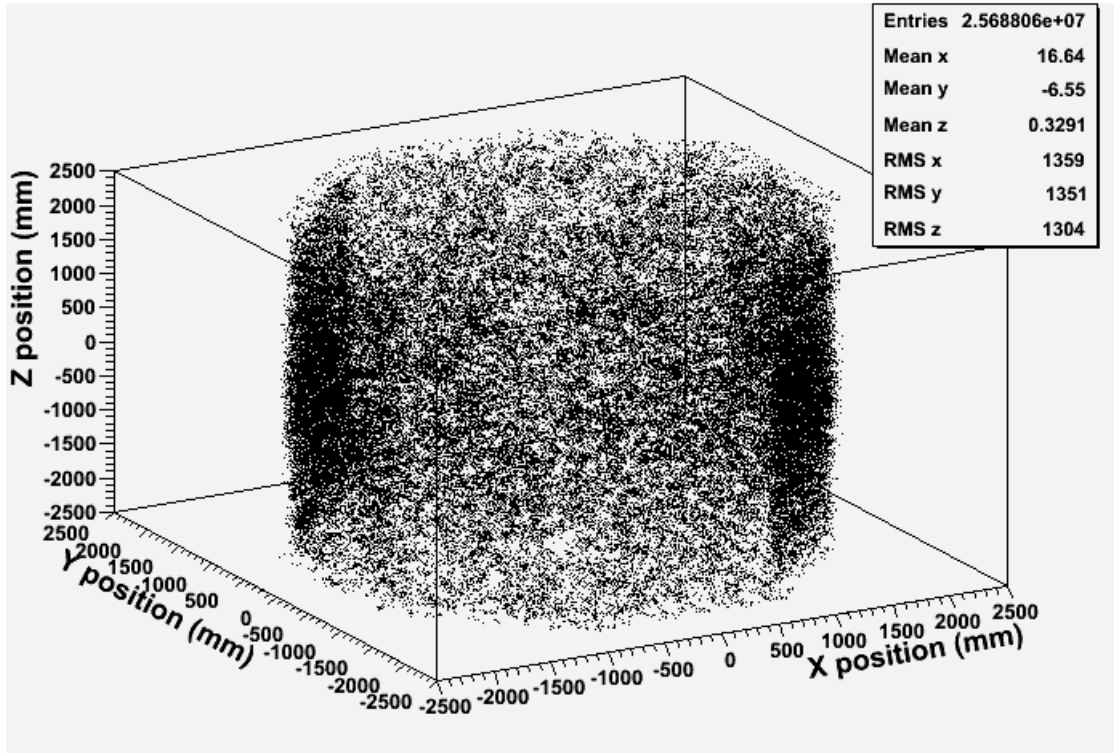
Figure 6.3: A sample 3D histogram showing the locations of all hits in a MAPS ECAL. The simulation used to produce this histogram used 15.78 GeV photons.
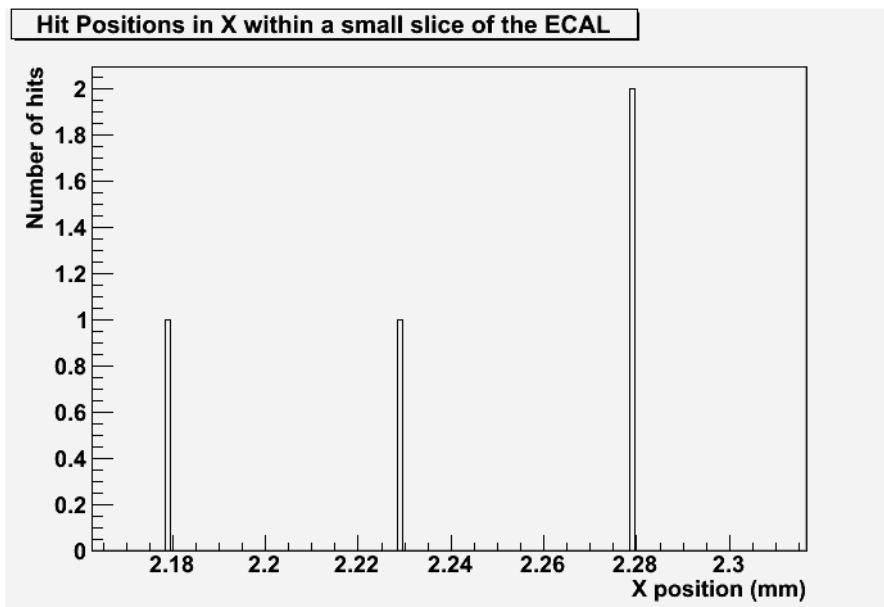
Figure 6.4: A sample histogram showing the transverse distance in the X direction between hits in a small segment of the MAPS ECAL in the extreme positive Y direction, in a single ECAL layer (see figure 6.2 for the region used). The simulations used to produce this histogram used 15.78 GeV photons.
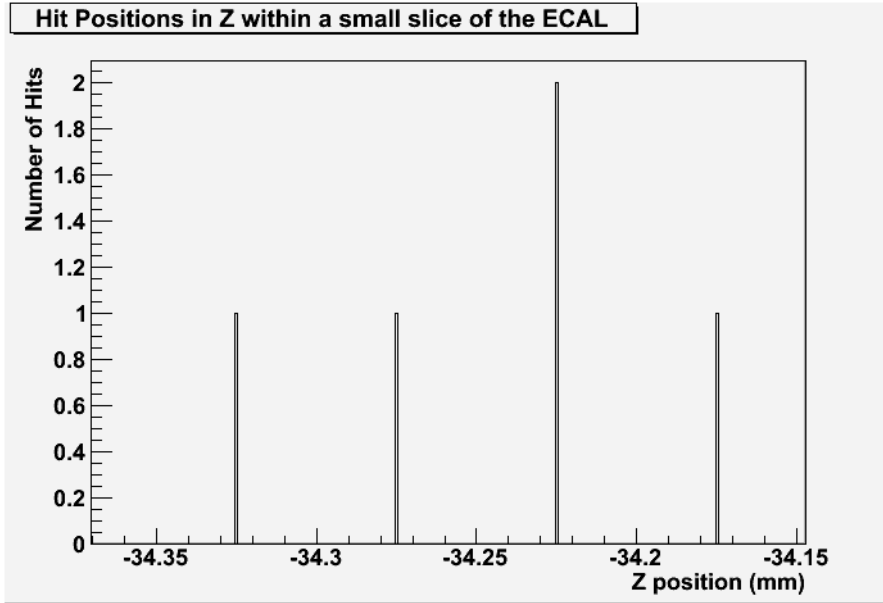
Figure 6.5: A sample histogram showing the transverse distance in the Z direction (along the beam line) between hits in a small segment of the MAPS ECAL in the extreme positive Y direction, in a single ECAL layer (see figure 6.2 for the region used). The simulations used to produce this histogram used 15.78 GeV photons.
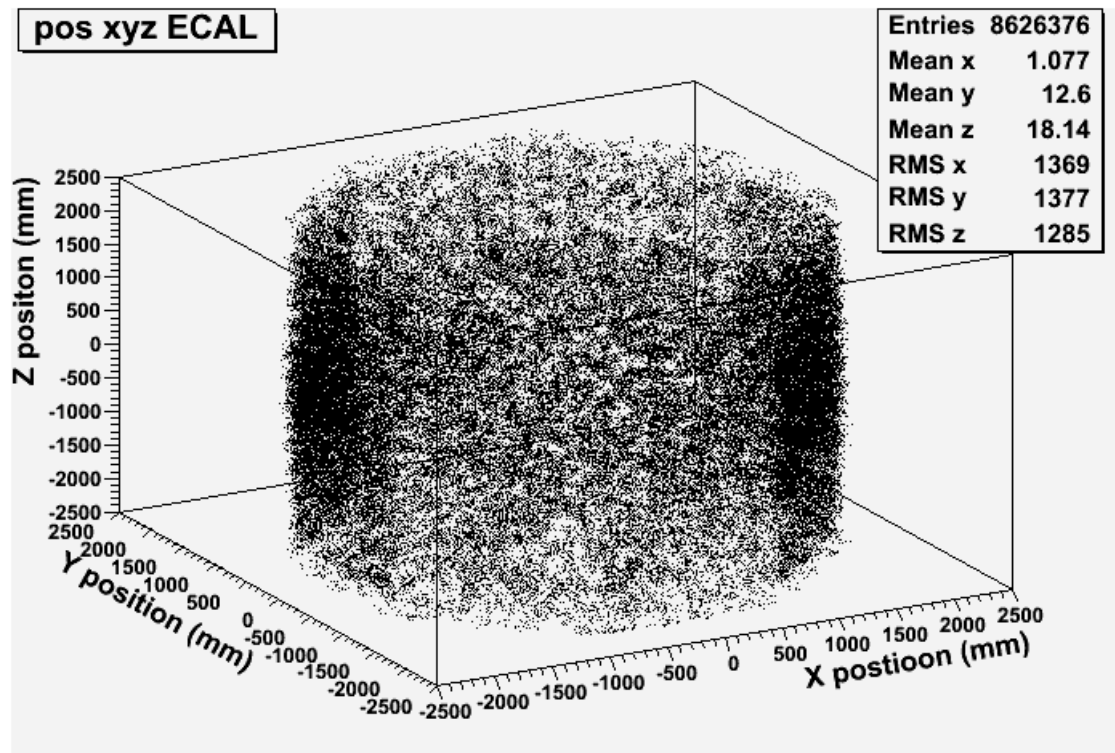
Figure 6.6: A sample 3D histogram showing the locations of all hits in an analogue ECAL. The simulation used to produce this histogram used 15.78 GeV photons.
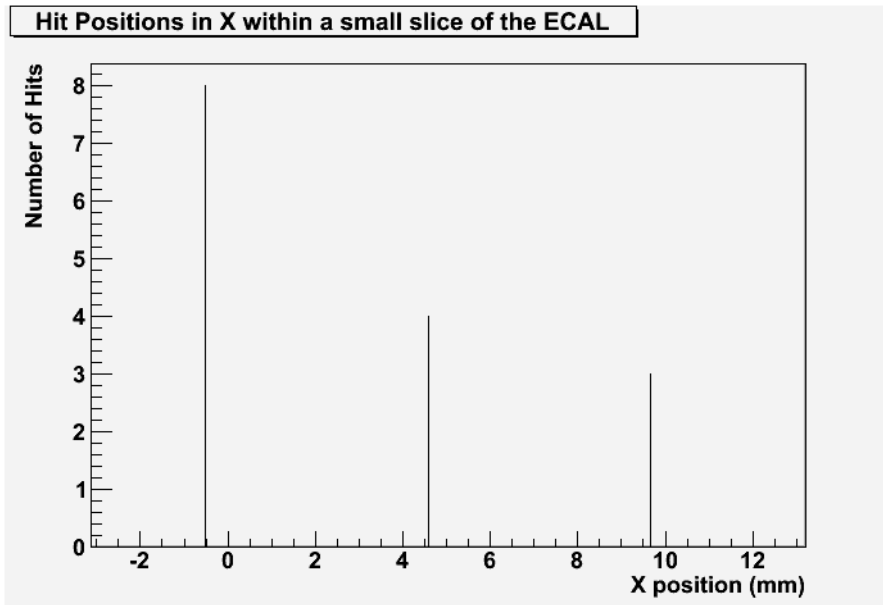
Figure 6.7: A sample histogram showing the transverse distance in the X direction between hits in a small segment of the analogue ECAL in the extreme positive Y direction, in a single ECAL layer (see figure 6.2 for the region used). The simulations used to produce this histogram used 15.78 GeV photons.
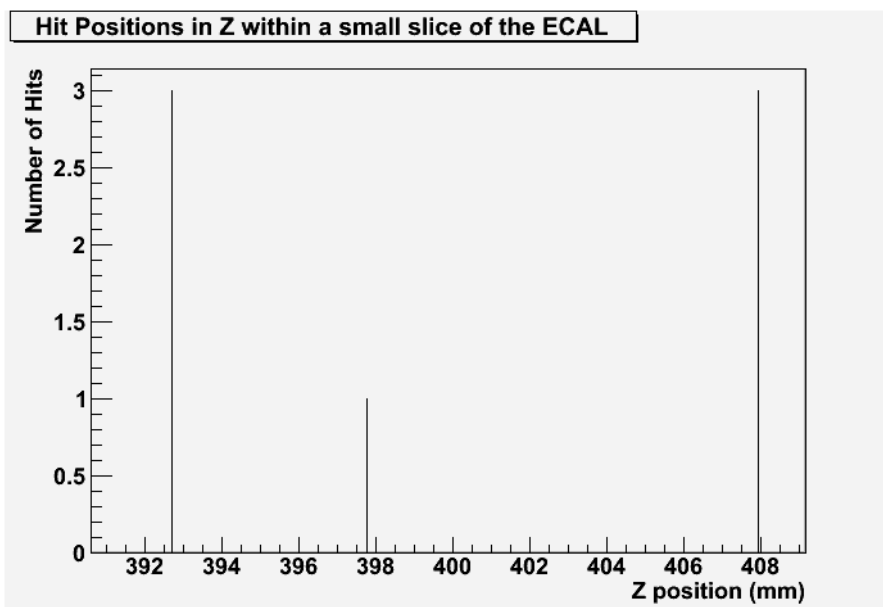
Figure 6.8: A sample histogram showing the transverse distance in the Z direction between hits in a small segment of the analogue ECAL in the extreme positive Y direction, in a single ECAL layer (see figure 6.2 for the region used). The simulations used to produce this histogram used 15.78 GeV photons.
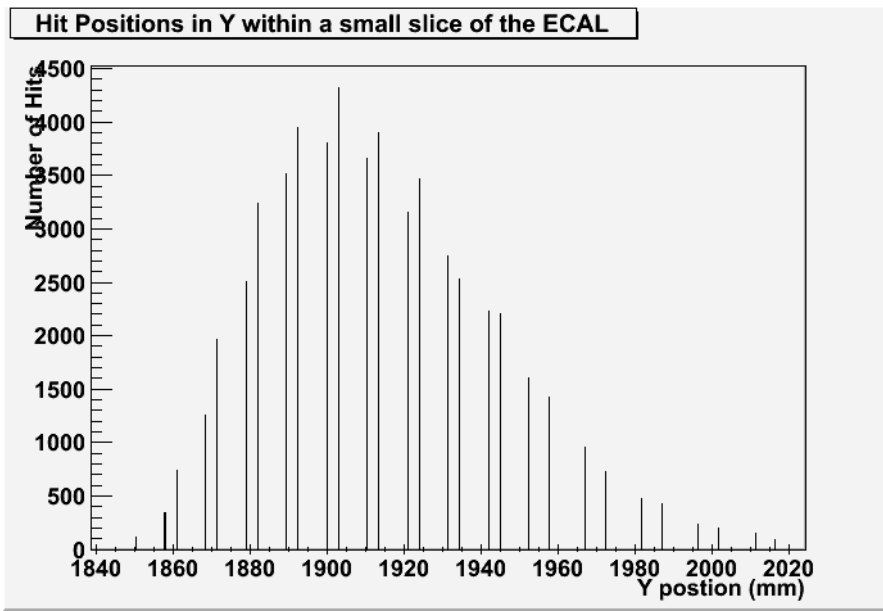
Figure 6.9: A sample histogram showing the distance in the Y direction between hits in a small segment of the MAPS ECAL in the extreme positive Y direction (see figure 6.2 for the region used). The simulations used to produce this histogram used 15.78 GeV photons.
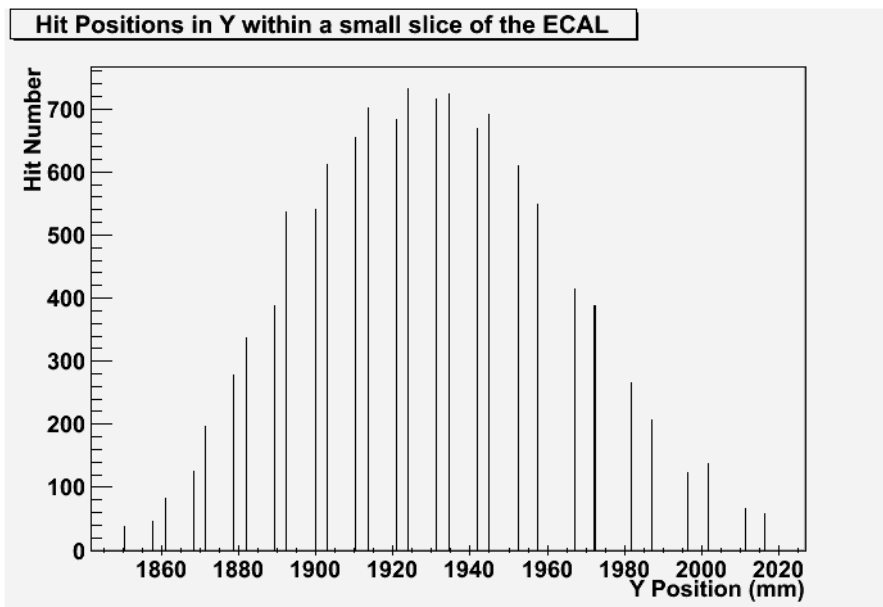
Figure 6.10: A sample histogram showing the distance in the Y direction between hits in a small segment of the analogue ECAL in the extreme positive Y direction (see figure 6.2 for the region used). This shows the distance between separate layers in the ECAL. The simulations used to produce this histogram used 15.78 GeV photons.

with the energy of the particle. Energy resolution for an ECAL is defined as $\frac{\sigma(E)}{E}$ (where E is the energy measured)[15]. In a working ECAL this value is typically split into three components as follows[49]:

$$\frac{\sigma(E)_{statistical}}{E} = \frac{p}{\sqrt{E}} \tag{6.1}$$

$$\frac{\sigma(E)_{instrumental}}{E} = \frac{q}{E} \tag{6.2}$$

$$\frac{\sigma(E)_{systematic}}{E} = r \tag{6.3}$$

Where: E is the energy of the particle

$\sigma(E)_{statistical}$ is the fraction of the energy standard deviation caused by fluctuations in shower formation.

$\sigma(E)_{instrumental}$ is the fraction of the energy standard deviation caused by instrumental effects such as pixel noise.

$\sigma(E)_{systematic}$ is the fraction of the energy standard deviation caused by miscalibrations and non-uniformities in instrument behavior.

p, q and r are constants.

The above equations can be combined to give the following:

$$\frac{\sigma(E)}{E} = \sqrt{\left(\frac{p}{\sqrt{E}}\right)^2 + \left(\frac{q}{E}\right)^2 + r^2} \tag{6.4}$$

Of the three terms of the above equation it is the $\frac{p}{\sqrt{E}}$ term which is of greatest interest for this study. This term is generally considered to be the most significant because it is typically the dominant term at most useful particle energies (the $\frac{q}{E}$ term becomes dominant at low energies, the r term becomes dominant at high energies)[49]. The $\frac{p}{\sqrt{E}}$ term is fairly easy to isolate in this case due to the nature of the simulations used for this study. Imperfections in real world equipment (such as noise) were not included in the simulations (eliminating the instrumental term), and likewise factors which might create systematic errors in the detector were not

included. This means that equation 6.4 can be simplified to:

$$\frac{\sigma(E)}{E} = \frac{p}{\sqrt{E}} \qquad (6.5)$$

This means that the constant p for a given ECAL, can be found by simply plotting values of $\frac{\sigma(E)}{E}$ against $\frac{1}{\sqrt{E}}$ and taking the gradient of the resulting graph. The value of p found can then be used to characterise the behaviour of the energy resolution for that ECAL, over likely energy ranges. Therefore the energy resolutions of the MAPS and analogue ECAL designs can be characterised by simply graphing the values of $\frac{\sigma(E)}{E}$ against $\frac{1}{\sqrt{E}}$ for these two designs and recording the gradients of the resulting graphs.

Ideally the information needed to produce such graphs would be found by simply running simulations and measuring the values of $\sigma(E)$ and E that are recorded by the simulated ECALs, however in practice this is not possible. While in theory ECALs are designed to measure the energies of suitable particles passing through them, real ECALs (and their simulated facsimiles) do not allow direct measurement of particle energies. Real ECALs (regardless of their design or operating principal) need to be calibrated before their readings can be translated into accurate energy measurements. Fortunately, because the objective of this study is to measure $\frac{\sigma(E)}{E}$ rather than $\sigma(E)$ or E, it is possible to bypass this calibration stage and simply substitute other values which equal $\frac{\sigma(E)}{E}$ using the methods described below.

It is important to note that like any other practical HEP calorimeter design neither of the ECAL designs used for this simulation was intended to function purely by observing the passage of a single particle through the ECAL. Instead the ECAL is designed so that the initial particle will repeatedly lose energy to its surrounding environment by producing a shower of particles through bremstrahlung and pair production. Eventually almost all the energy of the initial particle will be taken up producing these shower particles and the energy of the initial particle is then measured by measuring the energy of the shower.

With this in mind, it is possible to extract $\frac{\sigma(E)}{E}$ from the results recorded by

the ECAL via the following reasoning. Figures 6.11 to 6.16 support the idea that the particle shower is typically contained within the ECAL over the range of photon energies used in this study for both ECAL designs used. If a particle passing through an ECAL is stopped before that particle or any of the resulting shower particles can leave the ECAL (as implied by the previously mentioned figures), then the total energy deposited on that ECAL must be equal to the total energy of the particle (assuming the mass energy of the particle is negligible compared to its total energy).

Unfortunately it is not possible to measure the total energy deposited in a sampling ECAL. Instead the energy deposited on the sensitive silicon layers is measured while the energy deposited on the tungsten absorber layers remains unknown (at least via direct measurement). However if the thickness of the sensitive silicon layers relative to the tungsten absorber layers remains constant then the fraction of energy deposited on the silicon layers should be consistent, i.e.

$$E = k \times e \tag{6.6}$$

Where: E is the energy of the particle

e is the energy deposited on the sensitive silicon of the sensor

k is a constant

Therefore:

$$\frac{\sigma(E)}{E} = \frac{k \times \sigma(e)}{k \times e} = \frac{\sigma(e)}{e} \tag{6.7}$$

This means that when attempting to calculate $\frac{\sigma(E)}{E}$ the energy deposited on the sensitive layers of the ECAL can be substituted for the energy of the original particle without needing to know the relationship between the two.

This simple substitution is complicated by the fact that (as shown in figure 6.10) the tungsten absorber layers do not have a consistent thickness throughout the ECAL. Specifically the outer ten layers of the thirty layer ECAL are preceded by twice the tungsten thickness of the inner twenty layers[17]. This means that the relationship between the energy of a particle passing through the outer layers of the ECAL and the energy deposited in those layers, is different to the relationship

between the energy of a particle passing through the inner layers of the ECAL and the energy deposited in those layers, i.e. if, in the inner layers:

$$E_1 = k \times u_1 \tag{6.8}$$

Then in the outer layers:

$$E_2 = k_2 \times u_2 \tag{6.9}$$

Where: E_1 is the energy the particle loses when passing through the inner ECAL

E_2 is the remaining energy of the particle when it enters the outer layers of the ECAL

u_1 is the energy deposited on the sensitive silicon of the inner layers of the ECAL

u_2 is the energy deposited on the sensitive silicon of the outer layers of the ECAL

k and k_2 are constants

This can potentially be a problem since as shown by equation 6.7, the initial analysis model of an ECAL assumes only a single constant. This problem can be solved during analysis by considering that if the shower created by the initial particle is entirely contained within the ECAL then the following is true:

$$E = E_1 + E_2 = ku_1 + k_2u_2 = k(u_1 + \frac{k_2 \times u_2}{k}) = k(u_1 + u_3) \tag{6.10}$$

Where: E is the total energy of the particle

and $u_3 = \frac{k_2 \times u_2}{k}$

The hit maps shown in figure 6.11 and 6.12 indicate that it is not an unreasonable to assume that the particle shower will be contained within the ECAL for the detector designs and particle energies used in this study. Therefore it is possible for equation 6.7 to be valid provided the energy recorded in the outer layers of the ECAL is multiplied by $\frac{k_2}{k}$ before being added to the total energy detected.

With this in mind the only remaining question is: what is $\frac{k_2}{k}$ (since k is otherwise

eliminated from equation 6.7). Because the overwhelming majority of the energy of particles passing through the ECAL is deposited on the tungsten absorber plates, both k and k_2 are directly proportional to the thicknesses of the individual tungsten absorber plates in their regions of the ECAL, i.e.

$$\frac{k_2}{k} = \frac{L_2}{L} \tag{6.11}$$

Where: L is the thickness of a single tungsten absorber in the inner ECAL   and L_2 is the thickness of a single tungsten absorber in the outer ECAL

Because in this case L_2 is known to be twice L, $\frac{k_2}{k}$ is equal to two[17].

Taking these factors into account equation 6.10 becomes:

$$E = k \times (u_1 + 2u_2) \tag{6.12}$$

This means that:

$$\frac{\sigma(E)}{E} = \frac{\sigma(k \times (u_1 + 2u_2))}{k \times (u_1 + 2u_2)} = \frac{\sigma(u_1 + 2u_2)}{u_1 + 2u_2} \tag{6.13}$$

Therefore, with a few modifications (namely doubling the energy found in the outer layers of the ECAL), the energy deposited on the sensitive layers of the ECAL can still be substituted for the energy of the original particle without needing to know the relationship between the two.

In practice equation 6.13 is simplified to the following:

$$\frac{\sigma(E)}{E} = \frac{\sigma(U)}{U} \tag{6.14}$$

Where: $U = u_1 + 2u_2$, this number is referred to as the 'modified deposited energy'.

This final simplification is performed so that the value of U can be recorded for analysis without having to independently record u_1, and u_2.

Equation 6.14 alone is adequate for finding the value of $\frac{\sigma(E)}{E}$ recorded in an analogue ECAL, however for a digital ECAL there is another complication which
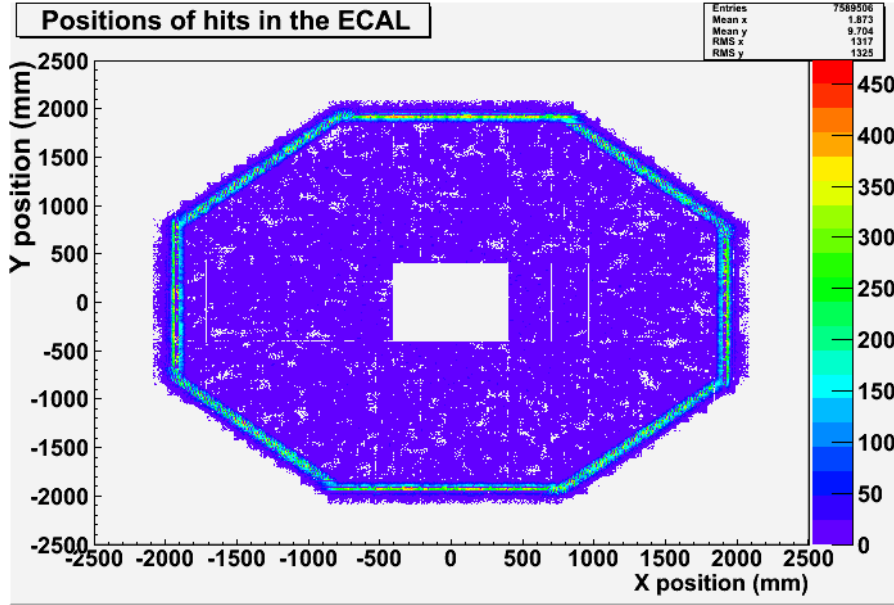
Figure 6.11: A sample hit map showing the distribution of all hits recorded in a simulated analogue ECAL during 20000 simulated 15.78 GeV photon events. This diagram shows the ECAL as it would be seen from further along the beam line (i.e. the beam is perpendicular to the page),X and Y are arbitrary directions perpendicular to the beam line and perpendicular to each other. The distribution of hits implies that the particle showers simulated were contained within the ECAL.
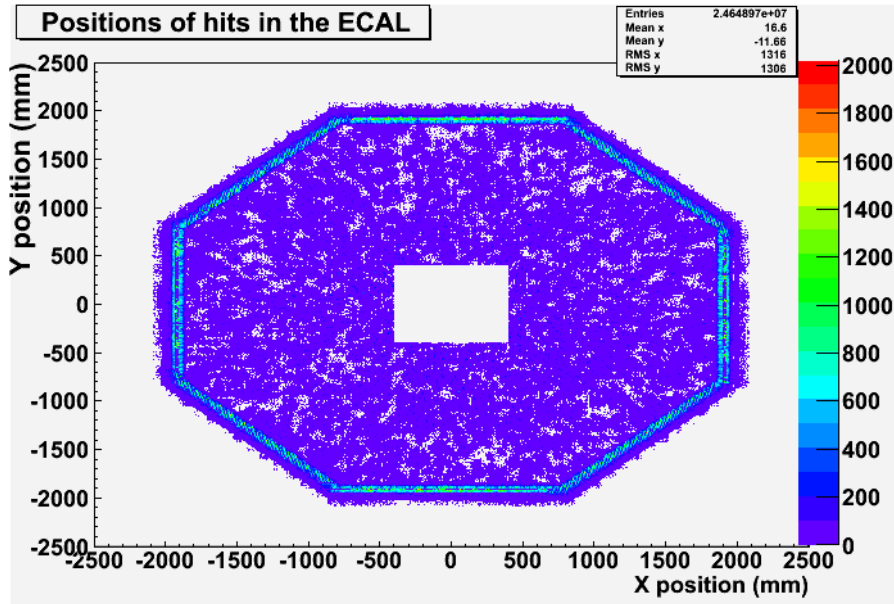
Figure 6.12: A sample hit map showing the distribution of all hits recorded in a simulated MAPS (digital) ECAL during 20000 simulated 15.78 GeV photon events. This diagram shows the ECAL as it would be seen from further along the beam line (i.e. the beam is perpendicular to the page),X and Y are arbitrary directions perpendicular to the beam line and perpendicular to each other. The distribution of hits implies that the particle showers simulated were contained within the ECAL.
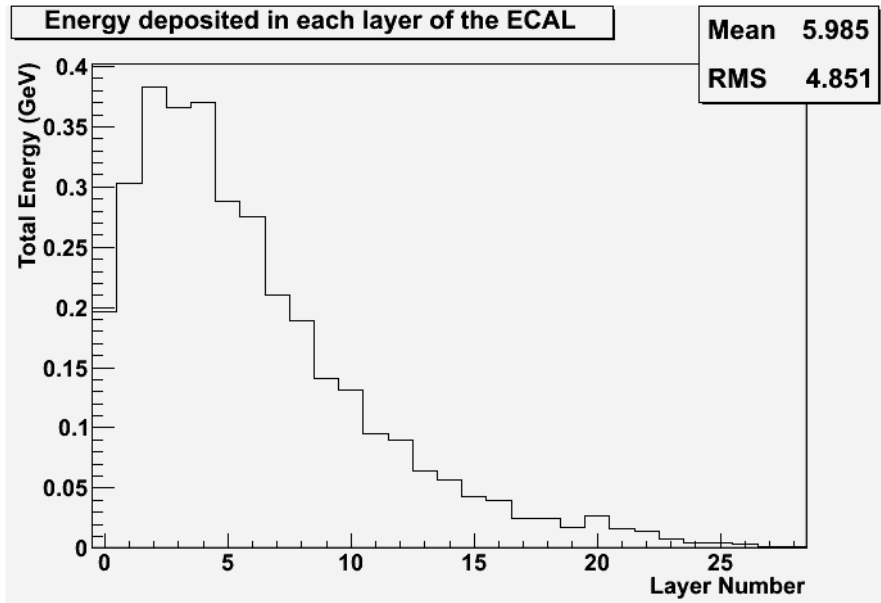
Figure 6.13: A sample histogram showing the distribution of energies deposited in different layers of the MAPS ECAL during 20000 simulated events using a 0.25 GeV photon. The relatively small energy deposited in the outer layers of the ECAL implies that the photon shower was typically well contained with the ECAL at this energy (0.25 GeV was the lowest particle energy used for this study). The energy deposited on the outermost 10 layers of the ECAL was doubled to represent the increased thickness of the absorber layers paired with these sensitive layers. This causes the energy recorded to increase at layer 20. Note: this histogram records the combined energies deposited on the ECAL during the entire simulation run, not the energies of individual events.

Figure 6.14: A sample histogram showing the distribution of energies deposited in different layers of the MAPS ECAL during 20000 simulated events using a 300 GeV photon. The relatively small energy deposited in the outer layers of the ECAL implies that the photon shower was typically well contained with the ECAL at this energy (300 GeV was the highest particle energy used for this study). The energy deposited on the outermost 10 layers of the ECAL was doubled to represent the increased thickness of the absorber layers paired with these sensitive layers. This causes the energy recorded to increase at layer 20. Note: this histogram records the combined energies deposited on the ECAL during the entire simulation run, not the energies of individual events.

Figure 6.15: A sample histogram showing the distribution of energies deposited in different layers of the analogue ECAL during 1000 simulated events using a 0.25 GeV photon. The relatively small energy deposited in the outer layers of the ECAL implies that the photon shower was typically well contained with the ECAL at this energy (0.25 GeV was the lowest particle energy used for this study). The energy deposited on the outermost 10 layers of the ECAL was doubled to represent the increased thickness of the absorber layers paired with these sensitive layers. This causes the energy recorded to increase at layer 20. Note: this histogram records the combined energies deposited on the ECAL during the entire simulation run, not the energies of individual events.

Figure 6.16: A sample histogram showing the distribution of energies deposited in different layers of the analogue ECAL during 1000 simulated events using a 300 GeV photon. The relatively small energy deposited in the outer layers of the ECAL implies that the photon shower was typically well contained with the ECAL at this energy (300 GeV was the highest particle energy used for this study). The energy deposited on the outermost 10 layers of the ECAL was doubled to represent the increased thickness of the absorber layers paired with these sensitive layers. This causes the energy recorded to increase at layer 20. Note: this histogram records the combined energies deposited on the ECAL during the entire simulation run, not the energies of individual events.

Figure 6.17: A sample histogram showing the distribution of hit energies in GeV in the MAPS ECAL (i.e. the energy associated with an individual hit) for different initial photon energies.

159
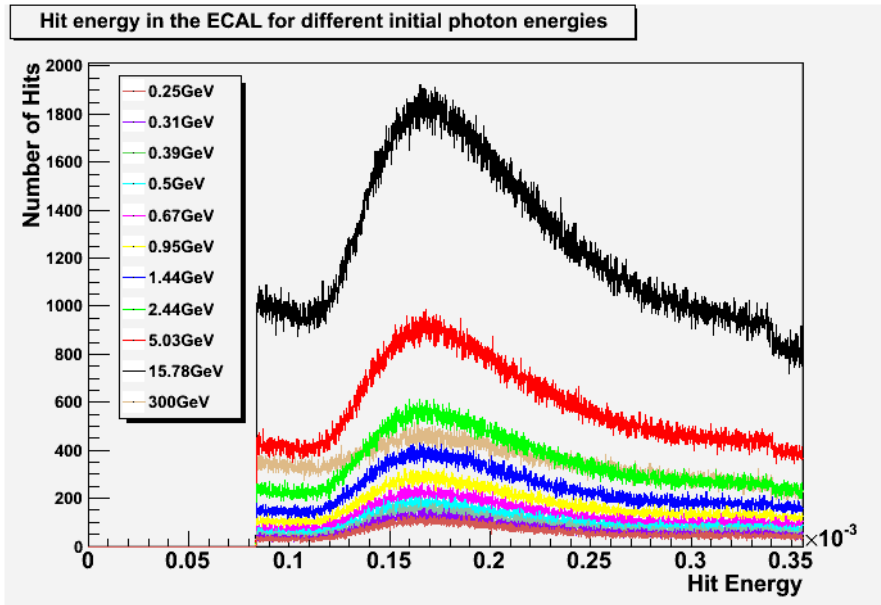
Figure 6.18: A sample histogram showing the distribution of hit energies in the analogue ECAL (i.e. the energy associated with an individual hits) for different initial photon energies. The peak of these distributions changes as the energy of the initial photon increases. This is due to an increased probability of multiple particles striking the same pixel leading to one high energy hit where a digital ECAL should measure several lower energy hits. This implies that the 5mm by 5mm pixels used in the analogue ECAL model would not be suitable for use in a digital ECAL.
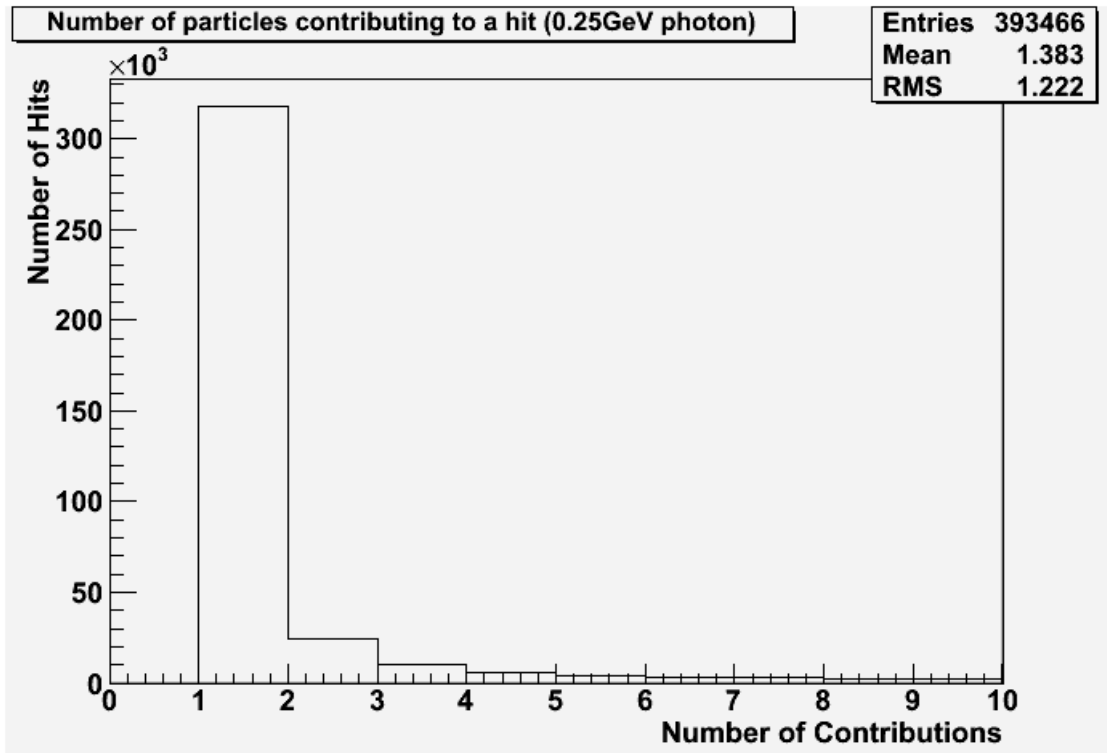
Figure 6.19: A sample histogram showing distribution of the number of particles contributing to each hit in a MAPS ECAL exposed to a 0.25 GeV photon.
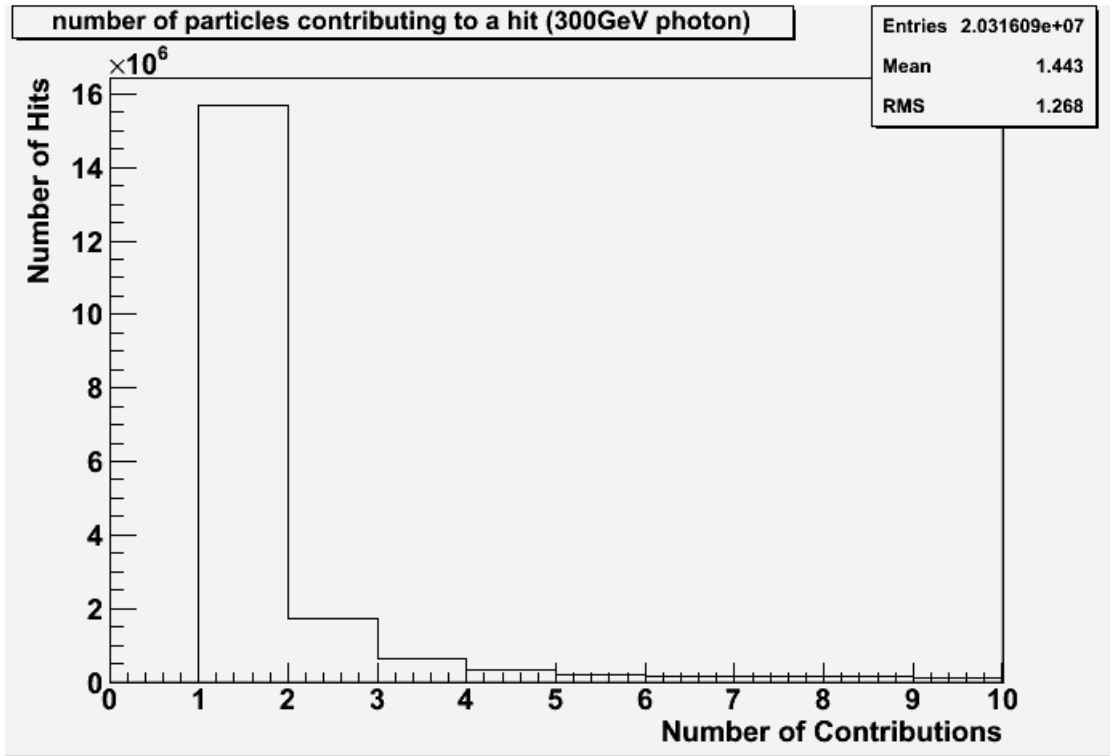
Figure 6.20: A sample histogram showing distribution of the number of particles contributing to each hit in a MAPS ECAL exposed to a 300 GeV photon.

makes equation 6.14 unsuitable in the digital case. Directly measuring the amount of energy deposited on the sensitive layers is not possible for a digital ECAL since a digital pixel can only detect the presence or absence of particles, not their energies. Because any reasonably high energy particle passing through a small thickness of sensitive silicon deposits roughly the same amount of energy on that silicon, for any single layer of an ECAL the energy deposited on that layer is proportional to the number of shower particles passing through that layer. This is supported by the plot shown in figure 6.17, the distributions of hit energies shown maintain a fairly constant peak energy as the energy of the initial photon increases, indicating hit energy is independent of photon energy. Assuming the pixels in an ECAL are small enough, the number of shower particles passing through an ECAL layer (and therefore the energy deposited on that layer) can be measured by simply counting the number of pixels that record hits within that layer. Figures 6.19 and 6.20 both indicate that over the energy range used in this study (0.25 GeV to 300 GeV) the 50μm by 50μm pixels used in the MAPS model are 'small enough' to accurately

record the number of shower particles passing through an ECAL layer. Therefore the number of hits in an ECAL layer should be approximately equal to the number of particles passing through that ECAL layer, and should therefore be proportional to the energy deposited on that layer. Since the total energy deposited on the sensitive silicon of an ECAL is just the sum of the energy deposited on each layer of sensitive silicon, the total energy deposited on the sensitive silicon should be proportional to the total number of hits recorded on the ECAL, i.e. if

$$e = e_1 + e_2 + e_3 + e_4 + ... \qquad (6.15)$$

$$n = n_1 + n_2 + n_3 + n_4 + ... \qquad (6.16)$$

and

$$e_i = a \times n_i \qquad (6.17)$$

then

$$e = an_1 + an_2 + an_3 + an_4 + ... = a(n_1 + n_2 + n_3 + n_4 + ...) = a \times n \qquad (6.18)$$

Where: n is the number of hits recorded by the ECAL

e is the energy deposited on the sensitive silicon of the ECAL

e_i is the energy deposited on the sensitive silicon of the ith layer of the ECAL

n_i is the number of hits recorded on the ith layer of the ECAL

and a is a constant

Since (as assumed previously) the energy deposited on the ECAL is proportional to the energy of the particle that entered the ECAL, the number of hits recorded on an ECAL with sufficiently small pixels must also be proportional to the energy of the particle that entered the ECAL. This means that the following is also true:

$$\frac{\sigma(E)}{E} = \frac{k \times \sigma(e)}{k \times e} = \frac{a \times k \times \sigma(n)}{a \times k \times n} = \frac{K \times \sigma(n)}{K \times n} = \frac{\sigma(n)}{n} \qquad (6.19)$$

162

Where: k and K are constants

Unfortunately this calculation is complicated by the fact that as stated previously the thickness of the tungsten absorbers in the outer ECAL is twice that of the inner ECAL[17]. This can be dealt with by considering that since the number of hits in a layer is proportional to the total energy of the layer (as shown in equation 6.17), the total energy deposited in the sensitive silicon of the inner ECAL is given by:

$$u_1 = an_a + an_b + an_c + ... = a \times (n_a + n_b + n_c + ...) = a \times m_1 \qquad (6.20)$$

and similarly:

$$u_2 = an_A + an_B + an_C + ... = a \times (n_A + n_B + n_C + ...) = a \times m_2 \qquad (6.21)$$

Where: m_1 is the number of hits recorded in the inner layers of the ECAL

m_2 is the number of hits recorded in the outer layers of the ECAL

u_1 is the energy deposited on the sensitive silicon of the inner layers of the ECAL

u_2 is the energy deposited on the sensitive silicon of the outer layers of the ECAL

n_a, n_b etc. are the number of hits recorded on individual layers in the inner ECAL

n_A, n_B etc. are the number of hits recorded on individual layers in the outer ECAL

and a is a constant

Substituting these equations for u_1 and u_2 into equation 6.13 produces the following:

$$\frac{\sigma(E)}{E} = \frac{\sigma(u_1 + 2u_2)}{u_1 + 2u_2} = \frac{\sigma(am_1 + 2am_2)}{am_1 + 2am_2} = \frac{a \times \sigma(m_1 + 2m_2)}{a \times (m_1 + 2m_2)} = \frac{\sigma(m_1 + 2m_2)}{m_1 + 2m_2}$$
$$(6.22)$$

Where: E is the total energy of the particle

163

In practice equation 6.22 is simplified to:

$$\frac{\sigma(E)}{E} = \frac{\sigma(M)}{M} \qquad (6.23)$$

Where: $M = m_1 + 2m_2$, this number is referred to as the 'modified hit number'.

This final simplification is performed so that the value M can be recorded for analysis without having to independently record m_1 and m_2.

Therefore, in the analogue ECAL model, equation 6.14 can be used to find values of $\frac{\sigma(E)}{E}$ to produce the graph implied by equation 6.5 and therefore find p for the analogue ECAL. Similarly in the MAPS ECAL model, equation 6.23 can be used to find values of $\frac{\sigma(E)}{E}$ to produce the graph implied by equation 6.5 and therefore find p for the MAPS ECAL.

6.4 Procedure

In order to simulate the behaviour of a digital MAPS ECAL in the proposed ILD detector design, a version of Mokka using a modified version of ILD00 was created using different values for ECAL pixel size and sensitive silicon thickness as described in section 6.2.2. The modified version of ILD00 was created by replacing references within Mokka files to the values for pixel size and sensitive silicon depth in the Mokka database, with locally specified values based on the dimensions of MAPS pixels. Once compiled the resulting modified version of Mokka automatically used the pixel specifications for a MAPS ECAL when the ILD00 detector model was used.

Once a modified version of Mokka had been compiled it was used to run a series of simulations using a particle gun event generator. The first simulation was used to simulate 20000 events within the modified ILD00 detector. For each event the particle gun event generator produced a single 0.25 GeV photon at the centre of the detector, travelling in a randomly determined direction. The results of all 20000 events including the movements of the photon and the response of the modified ILD00 detector were recorded in a single LCIO file for the run. This process was

repeated with photon energies of 0.31 GeV, 0.39 GeV, 0.5 GeV, 0.67 GeV, 0.95 GeV, 1.44 GeV, 2.44 GeV, 5.03 GeV, and 15.78 GeV. Additionally a run simulating 300 GeV photons was produced, however due to the large amount of time required to simulate and analyse 300 GeV photons, this run only contained 1000 events rather than the 20000 events used in other runs.

Additionally, in order to provide information to complete the analysis, a single run containing 20000 events simulating single 10 GeV muons passing through the detector was performed. This run was added to the other simulations because it would later become necessary to remove ECAL hits with energies that fell below half of the most probable value for MIP (minimal ionising particle) hit energies. A muon was selected as a reasonable approximation to a MIP because it would not significantly interact with the detector. An energy of 10 GeV was selected because this would ensure the muon reached the ECAL still travelling in a roughly straight line (equation 4.1 implies that an energy well in excess of 0.24 GeV would be required for a charged particle to reach the ECAL travelling in a rough straight line), while still being at a relatively low energy. Results from the photon runs were analysed using the methods described in section 6.5.3 and the calibration information provided by the muon run described in section 6.5.1.

Once these simulations had been completed a new version of Mokka was compiled without any of the modifications used to specify a MAPS ECAL, effectively reinstating the default ILD00 model. As noted in section 6.2.2 this produced a version of the ILD00 model which included an analogue ECAL. The simulation runs described above using the MAPS ILD00 model (including the 10 GeV muon simulation run) were then repeated using the default, analogue ECAL, ILD00 detector model. Results from these runs were analysed using the methods described in section 6.5.2.

6.5 Results and Analysis

To represent the differences between how digital ECALs and analogue ECALs work, runs using the two different detector models were analysed in different ways. Specifically runs simulating the behaviour of a conventional analogue ECAL (using an unmodified ILD00 model) were analysed to find values to substitute into equation 6.14, while runs simulating the behaviour of a MAPS ECAL (using a modified ILD00 model) were analysed to find values to substitute into equation 6.23. As detailed below, the analysis of both sets of runs was made more complex by the need to eliminate certain events and hits from the final results in order to more accurately simulate the behaviour of a real ECAL.

6.5.1 Analysis of Muon Runs

In order to more realistically emulate the behaviour of a real ECAL when analysing the results from the photon runs it was necessary to first have an estimate of the energy deposited by a MIP when it passed through the ECAL. The 10 GeV muon runs were performed to find this value.

This information was important because in a real functioning ECAL all hits below a certain energy would be discarded to reduce noise regardless of the origin of the hit. Typically this 'discard energy' (i.e. the energy below which hits would be discarded) would be half the hit energy of a MIP, therefore, to find a suitable discard energy for an ECAL design, it was necessary to find the most probable value for MIP hit energies in that ECAL design.

For both MAPS and analogue ECAL designs the analysis method used was essentially identical. In each case a single 1D histogram was created and filled with all the hit energies recorded in the entire muon run. A Landau function was then fitted to the resulting distribution and the most probable value of that Landau function was recorded as the most most probable value for MIP hit energies in the detector design used in the simulation in question. The resulting plots are shown in figures 6.21 and 6.22. The most probable MIP hit energy found in the MAPS
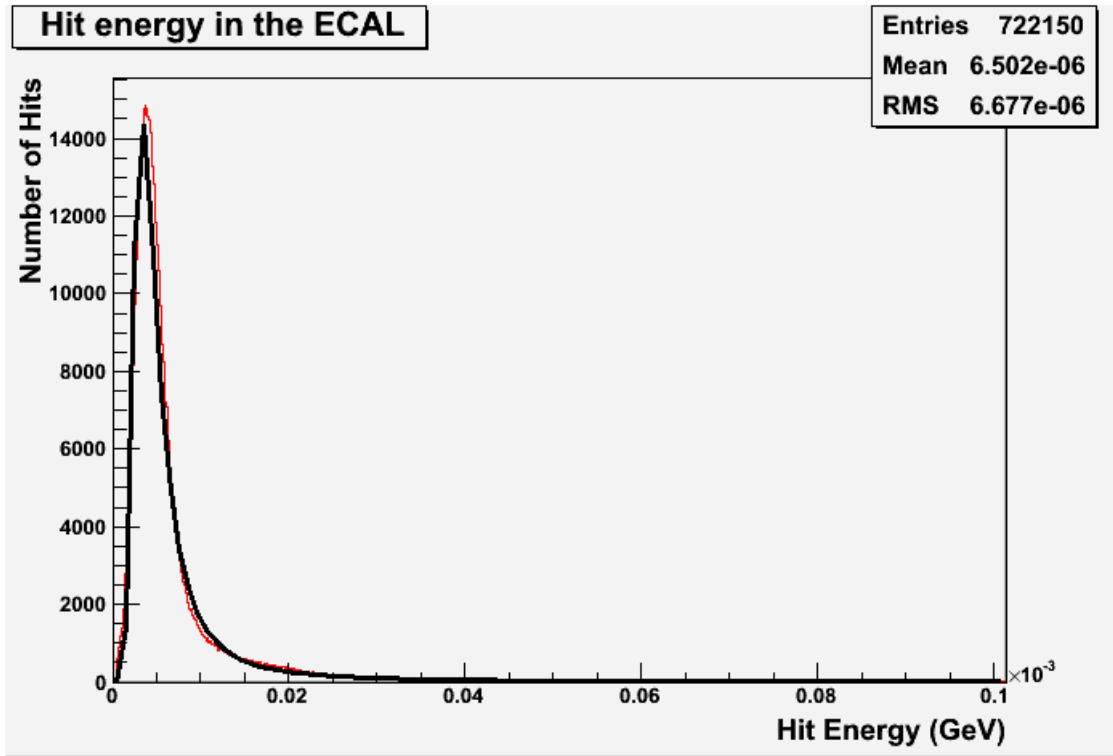
Figure 6.21: A histogram showing the distribution of hit energies recorded in the simulated MAPS ECAL when a 10 GeV muon passed through.

case was $(3.520 \pm 0.003) \times 10^{-6}$ GeV while the most probable hit energy found in the analogue case was $(1.6739 \pm 0.0006) \times 10^{-4}$ GeV. Therefore the discard energy used for analysing MAPS results was $(1.760 \pm 0.001) \times 10^{-6}$ GeV while the discard energy used for analysing analogue results was $(8.369 \pm 0.003) \times 10^{-5}$ GeV.

6.5.2   Analysis of Analogue Results

Each run using simulated photons was analysed individually to find the values of $\frac{\sigma(E)}{E}$ and $\frac{1}{\sqrt{E}}$ for the run. For a run simulating an analogue ECAL the first step of this analysis was to establish a pair of 1D histograms. The first of these histograms was created to record the distribution of modified deposited energies (see equation 6.14 for the definition of this value) on the ECAL during each event and was referred to as the 'raw energy histogram'. The second 1D histogram was created to record the same distribution of modified deposited energies , but with particularly low or high energy events removed, this histogram was referred to as the 'cut energy histogram'.

167
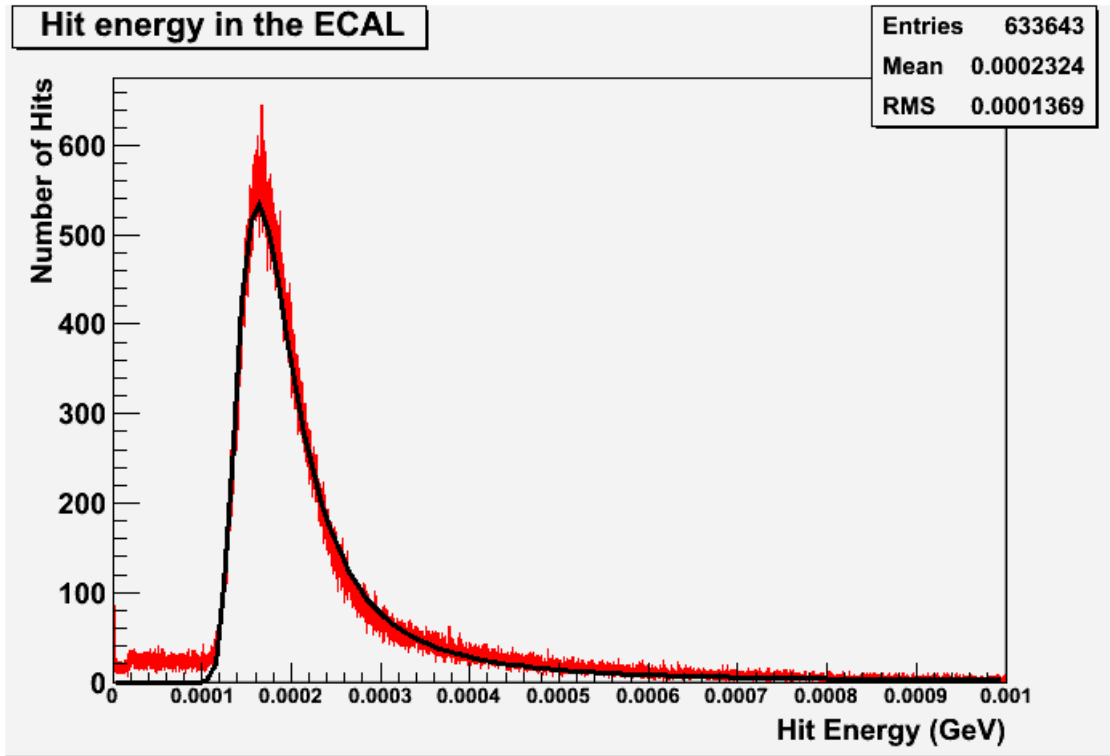
Figure 6.22: A histogram showing the distribution of hit energies recorded in the simulated analogue ECAL when a 10 GeV muon passed through.

Because 'particularly low or high energy events' are defined according to the the distribution of modified deposited energies recorded in the raw energy histogram, to fill both these histograms all the events in the run are essentially analysed twice, once to fill the raw energy histogram , and once (using the information from the previous analysis) to fill the cut energy histogram. The need for this 'two stage' analysis (one stage filling the raw energy histogram, the second filling the cut energy histogram) was created by the need to emulate the kind of analysis which would be used on results from a real ECAL in which ultra high or ultra low energy events would be discarded as noise. Therefore the analysis of the photon runs was modified so that particularly high or low energy events would also be eliminated from the final results gathered from the simulated runs.

During both analyses iterations each event was analysed individually. The first stage of each iteration was to discard any hits which had an energy less than the discard energy for the analogue ECAL (found in section 6.5.1). During this first analysis iteration the modified energy deposited (as defined by equation 6.14) was

measured by simply summing the energies of all hits recorded in the ECAL during a single event (with the energies of hits in the outer layers doubled), this value was then used to fill the raw energy histogram. An example of the resulting histogram is shown in figure 6.24. Once all the events in the run have been analysed in this fashion the mean and standard deviation of the raw energy histogram were measured and recorded.

Once this initial analysis had been completed all the events in the run were analysed a second time. In a similar fashion to the first stage of the analysis, the modified energy deposited in each event was found by summing the energies recorded for all the hits recorded by the simulated ECAL during that event, with the energies of hits in the outer layers doubled (note: in order to save processing time the modified energy deposited for every event was independently recorded when the raw energy histogram was filled to remove the need to completely re-analyse the data). If the modified energy deposited for an event was found to be less than the mean of the raw energy histogram plus two standard deviations, and if it was also more than the mean of the raw energy histogram minus one standard deviation, then that value would be used to fill the cut energy histogram. If the modified deposited energy measured did not meet these criteria, the event would be discarded from further study.

Once all the events in a run had been analysed for a second time and the cut energy histogram had been formed, its mean and standard deviation were substituted into equation 6.14 as U and $\sigma(U)$ respectively. The resulting value of $\frac{\sigma(E)}{E}$ for the run was then recorded. An example of such a histogram is shown in figure 6.26. The value of $\frac{1}{\sqrt{E}}$ was then calculated from the photon energy set when the Mokka simulation was initiated, this value was then recorded alongside the corresponding value of $\frac{\sigma(E)}{E}$.

This analysis process was repeated for each of the photon runs detailed in section 6.5.2 and the resulting values of $\frac{\sigma(E)}{E}$ found were plotted against the corresponding values of $\frac{1}{\sqrt{E}}$ to produce the graph shown in figure 6.28. The gradient of that graph was the value of p (as defined in equation 6.5) for the analogue ECAL model, this was

found to be (0.1190 ± 0.0004) GeV$^{\frac{1}{2}}$. This means that the relative energy resolution $\frac{\sigma(E)}{E}$ for the simulated analogue ECAL was found to be $\frac{(11.9 \pm 0.04)}{\sqrt{E}}$.

6.5.3 Analysis of MAPS Results

On a basic level the analysis of the MAPS runs using simulated photons is very similar to the analysis of their analogue counterparts. As with the photon runs using an analogue ECAL, each MAPS photon run was analysed separately to find the values of $\frac{\sigma(E)}{E}$ and $\frac{1}{\sqrt{E}}$ for that run.

For a run simulating a digital ECAL (i.e. those runs which had a version of ILD00 modified to include MAPS pixels), the first stage of analysis was to establish a pair of 1D histograms. The first histogram is designed to record the distribution of the modified hit numbers (as defined in equation 6.23) for each event, this is referred to as the 'raw hit number histogram'. The second histogram was designed to record the distribution of the modified hit numbers, after events with particularly low or high hit numbers were removed, this is referred to as the 'cut hit number histogram'.

Because like the analogue case the number of hits that is considered particularly high or low is defined by the mean and standard deviation of the raw hit number histogram, every event in a MAPS ECAL run is essentially analysed twice, once to fill the raw hit number histogram, and a second time to fill the cut hit number histogram. As with the analogue case this two stage analysis was intended to emulate some of the analysis techniques which would be potentially used to analyse results within a real MAPS ECAL. Specifically, like in an analogue ECAL, data from a real digital ECAL would be processed to remove especially high or low energy events to reduce noise. Therefore data from each run was initially screened to remove especially low or high energy events. This screening comprises the first analysis iteration for a MAPS photon run.

During the first analysis iteration, each event was analysed to measure the modified hit number by counting the number of hits registered on the ECAL (and counting the hits registered on the outer ECAL twice), once this value has been measured

170

it was used to fill the raw hit number histogram. As with the analogue case hits which were found to have energies below the discard energy for the MAPS design (found in section 6.5.1) were not counted towards this hit total. After all events in a run had been analysed in this fashion, the mean and standard deviation of the raw hit number histogram were measured and recorded. An example of the resulting histogram is shown in figure 6.23.

Once this initial analysis of a run was completed and the raw hit number histogram had been completely filled, all of the events in that run were analysed a second time. For each event the modified hit number was measured as described above, including the removal of hits with energies below the MAPS discard energy (note: in order to save processing time the modified hit number for every event was independently recorded when the raw hit number histogram was filled to remove the need to completely re-analyse the data). If the modified hit number for an event was found to be less than the mean of the raw hit number histogram plus two standard deviations, and if it was also more than the mean of the raw hit number histogram minus one standard deviation, then that value would be used to fill the cut hit number histogram. If the modified hit number measured did not meet these criteria, the event would be discarded from further study. An example of the resulting histogram is shown in figure 6.25.

As with the analogue runs, once every event had been completely processed and the resulting values had been input into the cut hit number histogram, the mean and standard deviation of that histogram were calculated and were substituted into equation 6.23 (as M and $\sigma(M)$ respectively), to find a value of $\frac{\sigma(E)}{E}$ for the run. The value of $\frac{1}{\sqrt{E}}$ was then calculated from the photon energy set when the Mokka simulation was initiated, and both $\frac{\sigma(E)}{E}$ and $\frac{1}{\sqrt{E}}$ for the run were recorded.

Once all the photon runs using the MAPS ECAL model had been analysed in this fashion, the collected values of $\frac{\sigma(E)}{E}$ were then plotted against the corresponding values of $\frac{1}{\sqrt{E}}$ to produce the graph shown in figure 6.27. A straight line was fitted to those data points and the gradient of the fitted line was extracted. The gradient of that fitted line was the value of p (as defined in equation 6.5) for the MAPS ECAL

171

Figure 6.23: A sample histogram showing the distribution of the number of hits recorded in a simulated MAPS (digital) ECAL in single events. These hit numbers are modified so that hits recorded in the outer ECAL are doubled. Each event in this distribution corresponds to a 15.78 GeV photon passing through the ECAL.

model, this was found to be (0.1147 ± 0.0004) GeV$^{\frac{1}{2}}$. This means that the relative energy resolution $\frac{\sigma(E)}{E}$ for the simulated MAPS ECAL was found to be $\frac{(11.50 \pm 0.04)}{\sqrt{E}}$.

6.6 Conclusions

For a single particle the performance of a digital MAPS ECAL seems to be highly comparable to the performance of an analogue ECAL. This indicates that MAPS is a viable alternative to conventional analogue ECAL designs. Combined with the reduced costs of a MAPS ECAL relative to an analogue design as discussed in section 3.2.2, this makes MAPS an attractive choice for an ECAL design.

Potentially this study could be altered in a number of ways without altering the overall objectives. Each of these alterations comes with associated advantages and disadvantages relative to the method used in this study. The first potential alteration would be to alter the analysis used to include a variety of clustering algorithms. As stated in the introduction to this study, one of the advantages of using a single particle (noiseless) simulation is that every hit detected on the ECAL
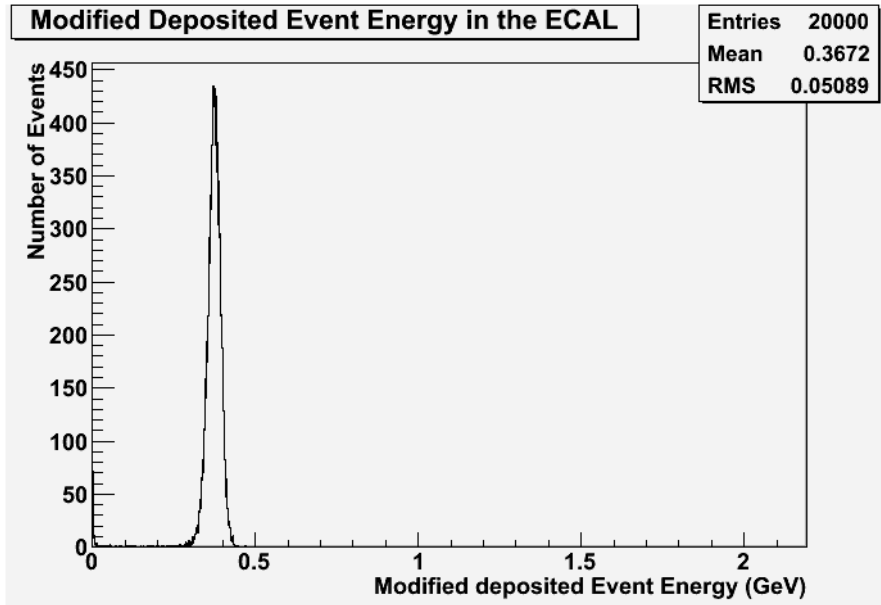
Figure 6.24: A sample histogram showing the distribution of the energy deposited in the sensitive silicon of a simulated analogue ECAL in single events. These energies have been modified so that the energies of hits recorded in the outer ECAL are doubled. Each event in this distribution corresponds to a 15.78 GeV photon passing through the ECAL.

is guaranteed to have been caused, either directly or indirectly, by that simulated particle. This means that the energy of that particle can be reconstructed without any concern about disentangling its results from the hits created by other particles, effectively predicting the performance of the ECAL if the analysis methods used were 'perfect'. While such 'analysis method independent' results are valuable, it is also important to acknowledge that in most cases there are additional factors which may alter results. In a real and active detector the situation is seldom so unambiguous as a single particle entering the ECAL, the need to disentangle the results from multiple different particles has created a range of different algorithms designed to form groups of hits into clusters, with each cluster (in theory) associated with a particular initial particle. With this in mind it could prove useful to attempt to analyse the results from this study using some commonly used contemporary algorithms. This could be used to find out how how big the difference would be between the results of a theoretically perfect analysis, and the results of a real and plausible analysis.
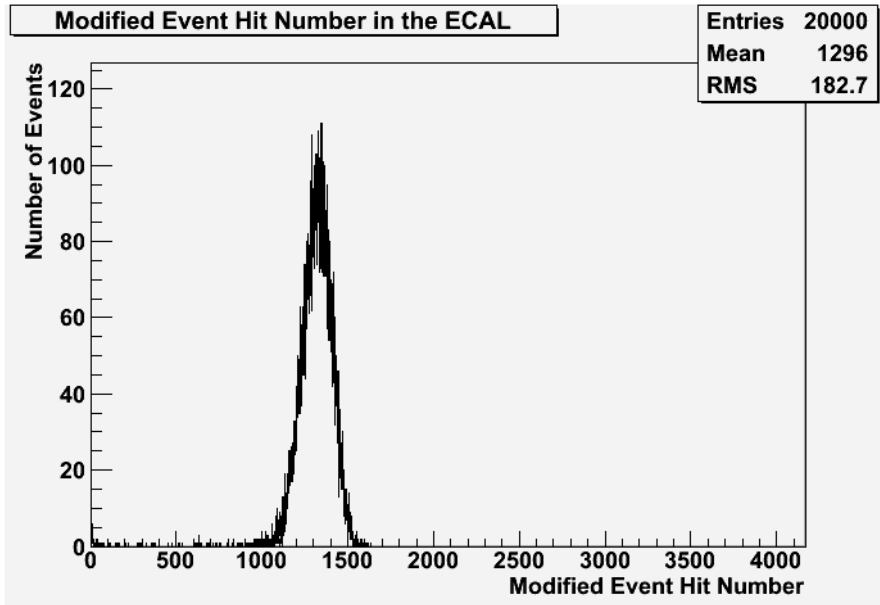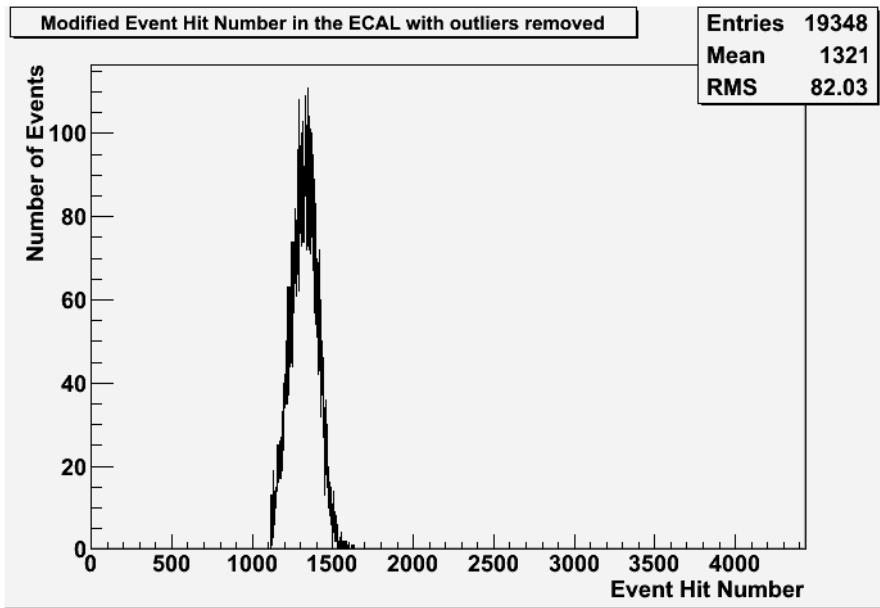
Figure 6.25: A sample histogram showing the distribution of the number of hits recorded in a simulated MAPS (digital) ECAL in single events. These hit numbers are modified so that hits recorded in the outer ECAL are doubled. Additionally the hit number distribution shown in this histogram has been modified to exclude all events where the number of hits recorded is more than the (unaltered) mean plus two (unaltered) standard deviations or less than the (unaltered) mean minus one (unaltered) standard deviation. The unmodified distribution used to produce this histogram is shown in figure 6.23. Each event in this distribution corresponds to a 15.78 GeV photon passing through the ECAL.

174
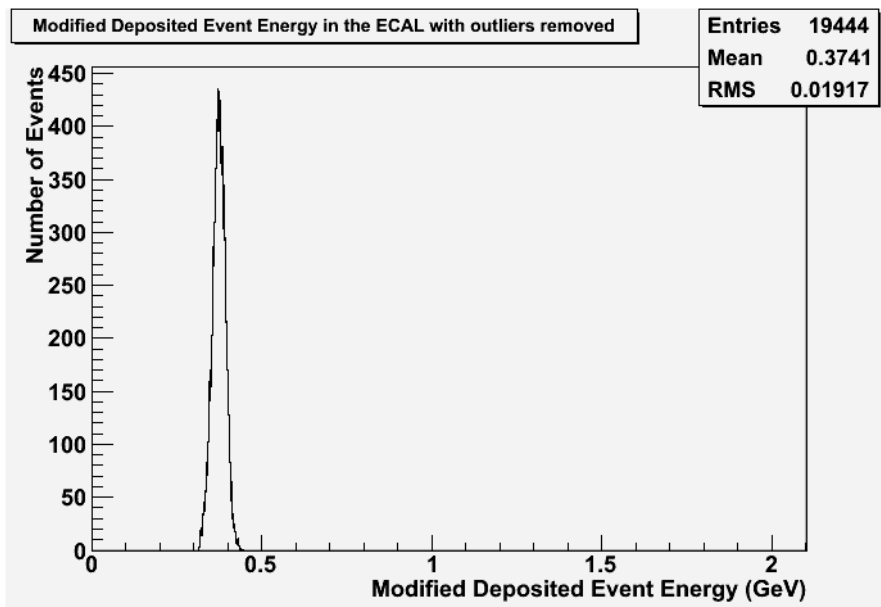
Figure 6.26: A sample histogram showing the distribution of the energy deposited in the sensitive silicon of a simulated analogue ECAL in single events. These energies have been modified so that the energies of hits recorded in the outer ECAL are doubled. Additionally the distribution of deposited energies shown in this histogram has been modified to exclude all events where the energy deposited was more than the (unaltered) mean plus two (unaltered) standard deviations or less than the (unaltered) mean minus one (unaltered) standard deviation. The unmodified distribution used to produce this histogram is shown in figure 6.24. Each event in this distribution corresponds to a 15.78 GeV photon passing through the ECAL.
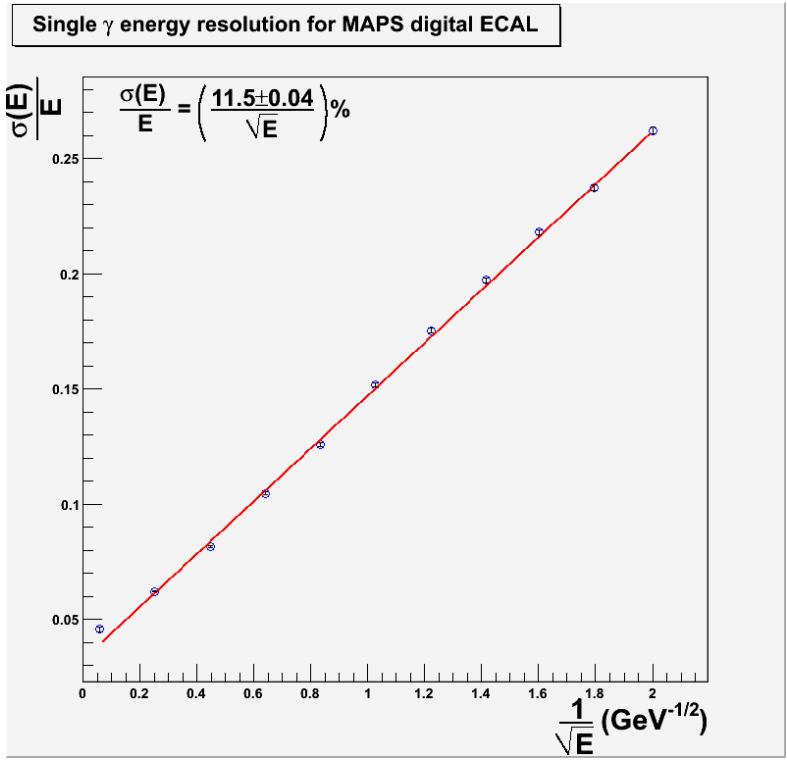
Figure 6.27: A graph showing the simulated variation in energy resolution with particle energy for a MAPS ECAL exposed to single photons within the ILD00 detector.
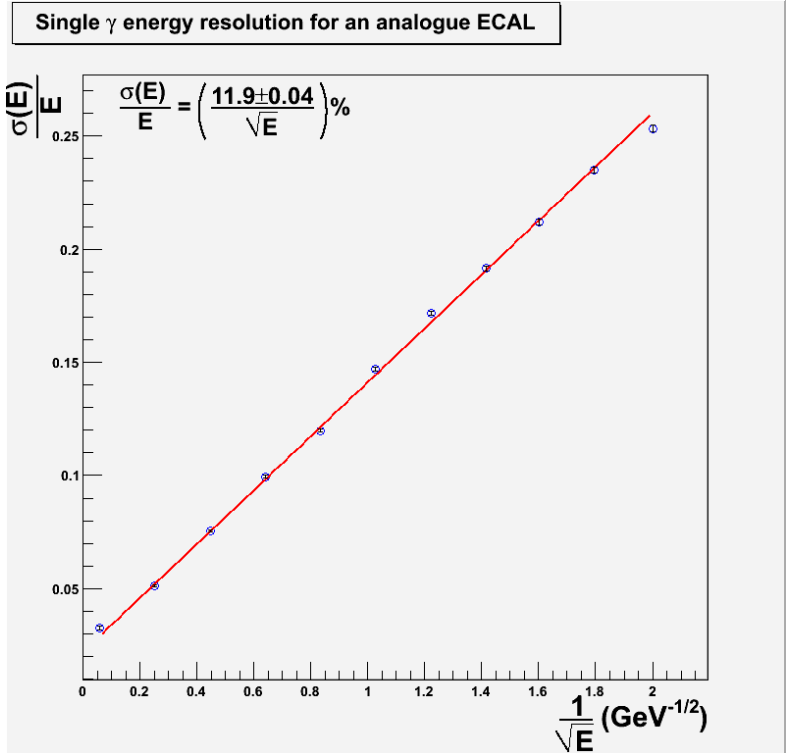
Figure 6.28: A graph showing the simulated variation in energy resolution with particle energy for an analogue ECAL exposed to single photons within the ILD00 detector.

In addition to finding the relative performance of MAPS and analogue ECAL designs using contemporary algorithms, information from this study could also be used to examine the effects of different clustering methods on the performance of the different ECAL designs. The results from this comparison could be used to determine which clustering method would work best with each ECAL design, and if modifying existing analysis algorithms could be beneficial to the performance of a digital (MAPS) ECAL. Specifically, if there is a considerable gap between ideal performance and practical performance for a digital ECAL which was not present for its analogue counterpart, then this would imply that it might be useful to produce a modified analysis algorithm optimized for use with digital ECALs. Overall this modification would give a more realistic impression of ECAL performance at the expense of potentially obscuring the relative strengths and weaknesses of the different ECAL designs behind variations in the suitability of the clustering techniques.

If the simulations used in the study were analysed using clustering algorithms then this would allow for a second alteration to the simulations: the simulations used in this study could be altered by adding modifying Mokka to simulate electronics noise in the detector. While such a modification would improve the realism of the simulation, it could also negate some of the advantages of using a single particle in the simulation (namely a relatively quick and simple setup and simulation, and effectively perfect clustering independent of any processor). Once full noise simulation had been perfected for simulations with a single initial particle, the study could then be extended to deal with multiple initial particles, taking advantage of the clustering algorithms to separate the particle showers.

The third and final potential alteration to this study would be to alter it to better prepare for any upcoming tests of a prototype ECAL. The most obvious modification to make along these lines would be to perform runs using the exact particles the prototype ECAL would be exposed to, in order to pinpoint the exact behaviour of the ECAL in these circumstances. A more demanding alteration would be to modify the barrel and endcaps structure of the simulated ECAL to a flat structure lacking any components other than the ECAL, closer to the likely shape and size of

a potential prototype ECAL. This would produce a model which could realistically simulate the effects of losing part of the particle shower due to the small solid angle likely covered by the prototype ECAL. A potential interim solution requiring a less radical redesign of the detector model would be to modify the analysis methods used to ignore all hits outside a small region of the ECAL centred on the point where particles enter the ECAL. While this compromise could provide a reasonable facsimile of the prototype ECAL while requiring significantly less time, it would however still permit the physical effects of the rest of the detector on the test particles (such as the passage of test particles through the momentum tracker causing them to lose energy), to alter results. Overall these modifications would make this study better suited to predicting the behaviour of a prototype ECAL at the expense of predicting finished ECAL behaviour in a full detector.

Additionally there are a range of potential extensions to this study which could be used to find additional related information about potential ECAL designs. First, it might be useful to extend the analysis of the data presented here to find (and therefore confirm the stability of) the calibration constants for the different ECAL designs. For the analogue ECAL this calibration constant would be the value that relates deposited energy to total energy and is marked as k in equation 6.12. Similarly, for the digital ECAL this calibration constant is the value that relates the number of hits recorded to the total particle energy. A record of this value could be useful for later studies and might prove to be a valuable guideline when attempting to set up a prototype ECAL.

Beyond modifying the analysis techniques used the most obvious progression from this study would be a similar study using a full jet (i.e. using initial particles that might decay before reaching the ECAL resulting in multi-particles events within the ECAL). This would be useful because jet energy resolution is one of the key benchmark behaviours for a detector and it can be affected by the performance of the ECAL[15].

Another potentially useful, and in principle fairly simple, extension to this study would be to modify it to use a variant of the SiD detector model rather than an

ILD variant. An ILD model was used for this study because it is a major proposed ILC detector which might make use of a MAPS ECAL, however the same can also be said of SiD (the 4th detector concept can be excluded from these simulations because there are currently no plans to include a silicon tungsten ECAL in that detector)[26][17][25]. Simulations using an SiD model could reveal how well a MAPS ECAL would function within SiD compared to the planned analogue silicon ECAL, and how sensitive MAPS ECAL performance is to the overall detector design outside the ECAL. Additionally, as both ILD and SiD detector designs continue to evolve over time, it might be useful to repeat this study with the latest detector designs to observe how the modifications made would affect ECAL performance. It would be best to perform such repeat analyses after major modifications are made either to the ECAL design or the overall structure of the detector. Additionally it might be useful to perform repeat studies immediately before any major events in the detector design process (such as the ILC TDR) even if no major modifications have been made recently. This would ensure that the latest results for detector performance match the latest detector model whenever those results are likely to see widespread use.

Another fairly simple additional study would be to use single photons to look for variations in energy resolution in different areas of the ECAL, or to find the optimal pixel size for a digital ECAL. The first of these two objectives could be achieved by repeating versions of the study described in this chapter altered so that the simulated photons were only fired into specific regions of the detector, and then comparing the results of all these studies. Similarly the second objective could be achieved by repeating the study detailed in this chapter using several slightly different ECAL designs and observing the results.

Similar studies using small numbers of simulated particles could also be used to predict the angular resolution of both MAPS and analogue ECALs. Such a study could be performed by simulating pairs of low energy particles passing through the ECAL with a small angle between them. The relative angles of these two particles could then be modified to find out at what angle standard analysis methods would not be able to separate the particle showers in the ECAL, this angle would then be

the angular resolution of the detector. This value is likely to change with particle energy, to deal with this the angular resolution could be calculated for a range of different particle energies. Also, it is likely that angular resolution will be partially dependent on the clustering algorithms used to separate the hits produced by the two particles. This extension could be used to investigate what impact different clustering methods have, how this changes with detector design, and how these methods could be fine tuned for the different detector designs.

Chapter 7

TPAC 1.2 Test beam study

7.1 Introduction

One of the most important characteristics for the sensitive components of a potential ILC ECAL is their efficiency in detecting single charged particles[15] because this directly affects the utility of the information produced by that sensor. Because MAPS pixels are entirely digital, efficiency for a MAPS is the probability that a pixel will fire when a detectable particle passes through it. In order to find the efficiency for a prototype MAPS several TPAC 1.2 sensors were exposed to a 120 GeV pion beam at CERN in August 2009.

7.2 Apparatus

Apparatus for this study can be divided into two groups; the test beam and sensor stack (the 'experiment apparatus'), and the attached data acquisition system (generally referred to as the DAQ).

7.2.1 The Test Beam and Sensor Stack

The test beam used for the experiments detailed was the H6 beam line at CERN, its characteristics are described in table 7.1. This test beam provided a 120 GeV pion beam which was fired through the sensor stack during the test runs. Figure

7.1 shows that the test beam was fired in a series of pulses while it was active. There is typically a 'spill signal' produced by the test beam whenever it fires one of these pulses which can be used to predict when to record data. Unfortunately, as mentioned below in section 7.4 the spill signal was not available during this study.

The sensor stack refers to the apparatus placed in the beam line. The sensor stack consisted of an anodised aluminium stand (shown in figures 7.2 and 7.3) containing three scintillators read out by photomultiplier tubes (PMTs), six printed circuit boards (PCBs) each containing a single TPAC 1.2 sensor and its support and control structures (see chapter 3 for details of the PCBs). The test stand held the sensors and PMTs in place (to a precision of less than 1mm) so that the six sensors and all three PMTs were lined up along the line of the test beam, and so that the plane of each sensor was perpendicular to the test beam. A diagram showing the layout of sensors and PMTs within the sensor stack is shown in figure 7.6 and a photograph of the completed sensor stack is shown in figure 7.5.

The role of the PMTs included in the sensor stack was to register exactly when a useable test beam particle passed through the stack. The PMTs inserted into the sensor stack had sensitive elements 10mm $\times$10mm in surface area and were positioned such that the array of six TPAC sensors were either directly in front of or directly behind the sensitive sections of the sensor PCBs (see figure 7.6 for details, and see figure 7.4 for information on how PMTs 0 and 1 were held in those positions, PMT2 was slotted into the test stand in the same manner as the sensors). This positioning was selected so that the PMTs would detect when there were beam particles potentially passing through the sensors. For the same reason the surface area of the PMTs was selected to be approximately the same size as the TPAC 1.2 sensors (which have a surface area of 9.15mm $\times$8.45mm each).

Prior to use in the sensor stack the PMTs were exposed to a ^{137}Cs source to test and refine their ability to detect beam particles. Ideally particles of the same type and energy as the test beam particles would have been used, however this was not practical due to the time and resources required to determine the threshold voltage of the PMTs in this manner. Since the ^{137}Cs source only produced signals

with at most half the energy deposited in the PMTs by test beam particles, once the PMTs had been modified to register the presence of the ^{137}Cs source they were quite capable of registering the test beam, however determining the threshold of the PMTs using lower energy signals almost certainly increased the noise rate of the PMTs in the test beam (figure 7.14 shows there were significant numbers of noise hits in the PMTs)[50].

The threshold voltage of the PMTs was determined by altering the voltage controlling the PMT gain and measuring the number of hits per unit time both with and without exposure to the ^{137}Cs source. The control voltage used (i.e. the voltage threshold) was then the lowest control voltage where the PMT registered considerable more hits when exposed to the ^{137}Cs source than it did without[50].

The behaviour of the PMTs is shown in figure 7.14 which shows the relative frequencies of different PMT signal types during a typical test beam run. Because the PMTs were linked together via a single USBDAQ board, a single signal recording the number of PMT hits registered at the same time is produced each time one or more PMTs registers a hit. The relatively large number of PMT signals which were just a single PMT registering a hit not recorded by any other PMT implies a non negligible noise rate in the PMTs. This becomes especially apparent when considering the relatively small numbers of PMT signals which consisted of exactly two PMTs registering hits at the same time compared to the much larger number of signals where all three PMTs register hits. The large number of signals recording only a single PMT hits might be due to low efficiency in the PMTs, however if this was the case there would be a similar drop in signal numbers between signals recording two hits and signals recording three hits. The fact that the number of signals recording three hits is much higher than the number recording two hits implies that the PMTs were highly efficient, which in turn implies that hits only recorded in a single PMT were likely to be spurious.

Of the six sensors used in this set up the outer four sensors were not the subject of the study (i.e. their efficiencies were not measured), instead they were used to identify exactly where test beam particles passed through the sensor (once the time

Momentum Range	5 to 205 GeV/c
Particles Produced	π^+ and π^-
Intensity for 10^{12} incident protons at 450 GeV/c	10^8 π^+ at 150 GeV/c or 10^7 π^- at 150 GeV/c

Table 7.1: The characteristics of the H6 beam line at CERN[51].

at which the particle passes through has been identified by the PMTs). These four sensors were referred to as the control sensors. The remaining two sensors at the centre of the sensor stack were the test sensors/devices under test (i.e. the sensors where the efficiency is measured). All the sensors could be swapped for comparable sensors if the sensor was found not to be functioning properly, or if (in the case of the test sensors) the sensor has been fully investigated and the slot is needed for a new test sensor. A diagram showing the positions of these sensors within the sensor stack is shown in figure 7.6.

The sensor threshold set, i.e. the amount of charge deposited at a diode necessary for a pixel to register a hit, was set to a single value for all six control sensors while the threshold set for the two test sensors was altered during the experiment to test their responses to different thresholds. As described in chapter 5, pixel non-uniformity (i.e. different pixels having thresholds that are effectively slightly higher or lower than the sensor threshold) can be a problem. This was solved by pixel trimming, where the threshold of each individual pixel within a sensor are altered slightly to ensure uniformity. The threshold set individually for each pixel could only be modified upwards. To deal with this in practice the overall threshold for a sensor was set slightly lower than the target value, and the threshold of each pixel was then increased slightly until all the pixels had the target threshold. Problematic pixels such as 'hot' (always firing), 'cold' (never firing) or unstable pixels were then masked, i.e. results from that pixel were not read out or recorded, effectively removing those pixels from the sensor.
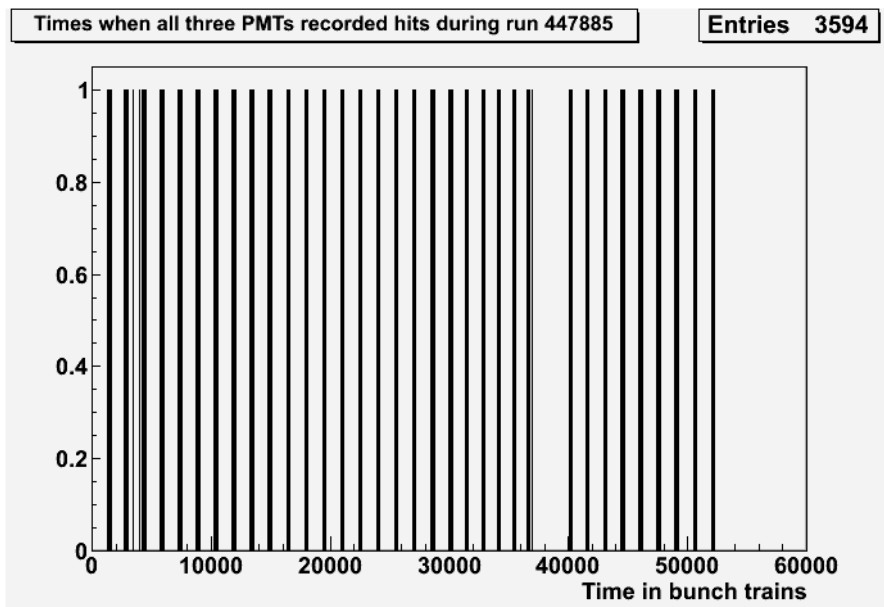
Figure 7.1: A histogram showing the distribution of test beam pulses during a single test run. On this histogram a 1 represents a point in time when all three photo-multiplier tubes attached to the sensor stack recorded simultaneous hits, implying that a beam particle had passed through the sensor stack. Naturally the zeros on this histogram represent times when there were no such hits implying that the test beam was absent. Times are listed in the number of bunch trains (discrete 3.2ms periods when the sensor stack recorded data, see section 7.5 for details) since the run started. The approximately 50000 bunch trains during run 477885 were evenly spread out over a period of 1800 seconds.
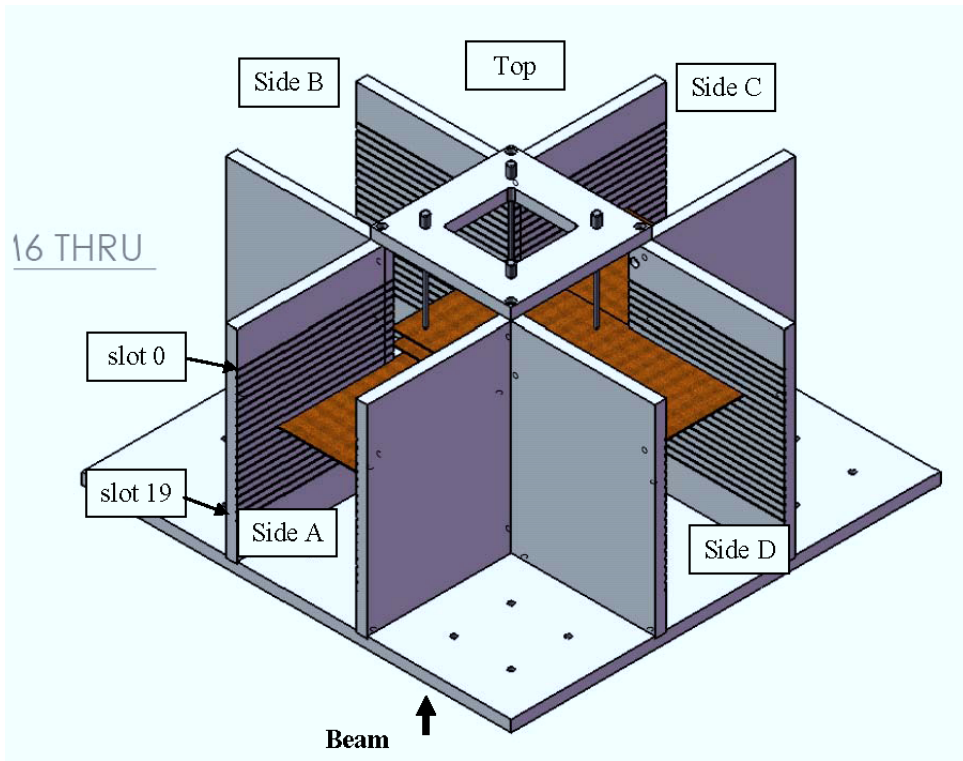
Figure 7.2: Test stand used for TPAC 1.2 test beam.
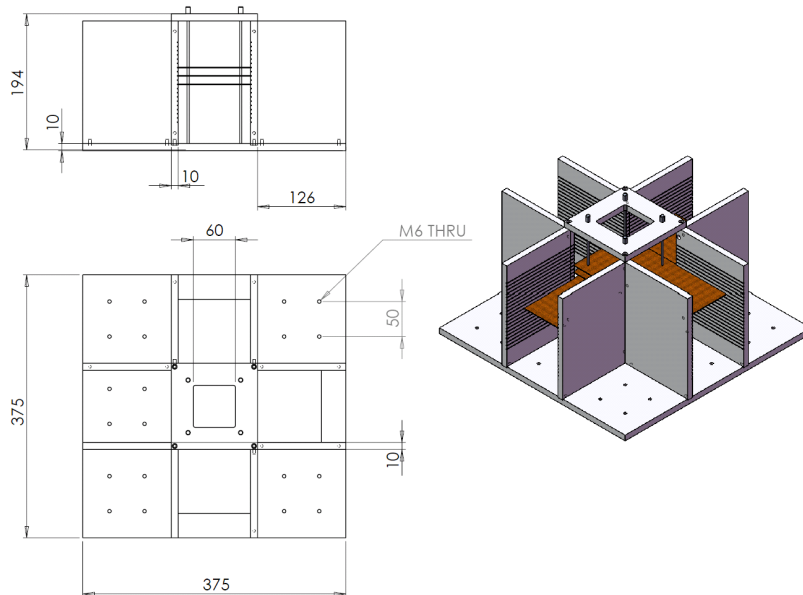
Figure 7.3: Schematics of the test stand used for TPAC 1.2 test beam, all measurements are in millimetres. The slots shown are 1mm deep and can hold sensor PCBs, PMTs (one of the three PMTs used was mounted in this fashion, the other two were mounted as shown in figure 7.4), or absorber slabs (not used in this experiment).
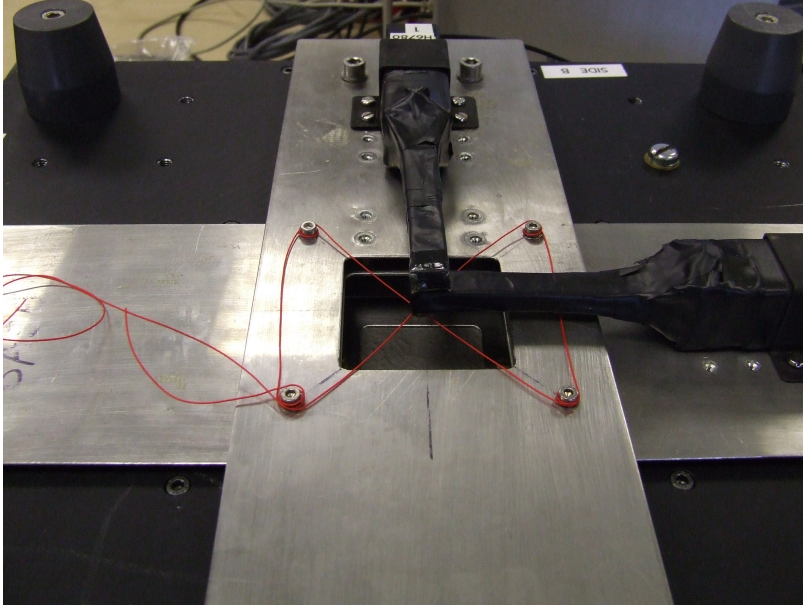
Figure 7.4: A pair of PMTs attached to the underside of the test stand used for the TPAC 1.2 test beam. Due to the alignment of the sensor stack in the test beam, these two PMTs were the first sensor stack component in the path of test beam particles.
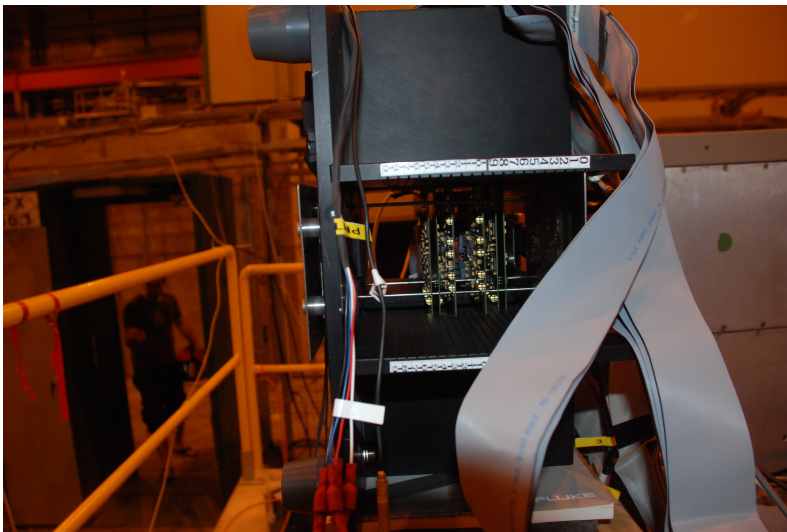
Figure 7.5: A picture of the completed TPAC 1.2 sensor stack. Once placed in the test beam the stack was positioned so that the base of the stack (on the left hand side of this picture) faced the test beam, with the beam passing through the centre of the stack. This picture shows that the sensor PCB which would be hit second and the sensor PCB which would be hit sixth by test beam particles are inverted relative to the other sensor PCBs. These two sensor PCBs were inverted so that they could be placed in slots adjacent to the sensors first and fifth in line for the test beam without interfering with their cabling. For the same reason the sensor PCBs third and forth in line for the test beam (the test sensors) are rotated ninety degrees relative to all the other sensor PCBs (the control sensors).
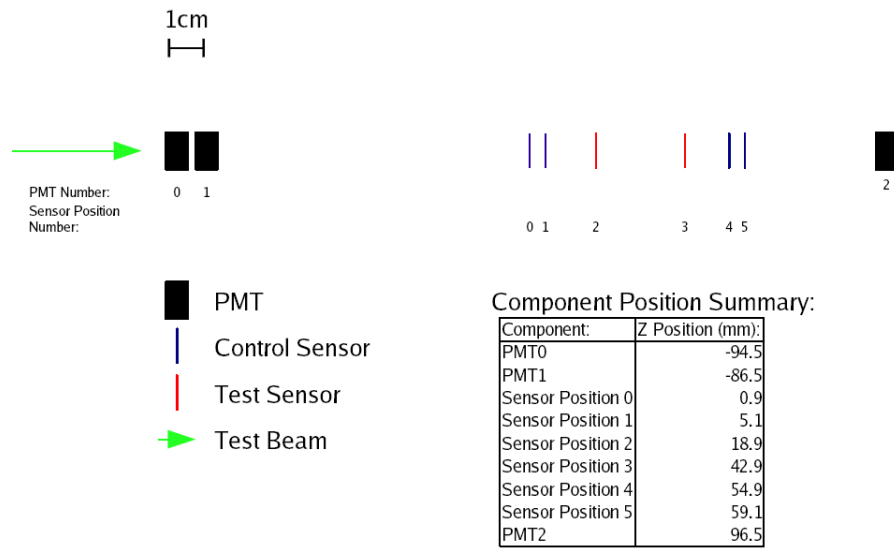
Figure 7.6: Layout of sensitive regions (both sensors and PMTs) within a completed sensor stack. Z position for each component is the distance (along the beam line) between the base plate of the sensor stack and the centre of the sensitive region of the component in question.

7.2.2 The Data Acquisition System

The data acquisition system (or DAQ) refers to the components of the experiment necessary to control the sensors and record data from them. The DAQ used for this study consisted of seven USBDAQ boards, one master PC, two slave PCs, the sensor PCBs themselves, three PMTs, an external amplifier/discriminator for the PMTs, and the associated cabling and power supplies for these items. Initially these components were connected as shown in figure 7.7, however this setup was changed to the design shown in figure 7.8 mid way through the experiment due to problems writing data recorded by the sensors and PMTs to file.

As shown in figures 7.7 and 7.8, in both designs used the DAQ was set up with one USBDAQ board per sensor PCB and the three PMTs sharing a single USBDAQ. The role of the USBDAQ boards was essentially to act as intermediaries between the slave PCs and the sensor PCBs. In the USBDAQ boards, commands transmitted from the slave PCs were translated into signals that would control the sensors attached to the PCBs, and readouts from the sensors were turned into signals that could be processed by the PC. While each USBDAQ boards is capable of working off its

188

own internal clock to provide timing information for readouts (ensuring that every hit recorded has an associated 400ns time stamp), it was useful to have all the USBDAQs working off a single clock so that the times were synchronised. With this in mind the USBDAQ boards were designed such that multiple boards could use share the clock of a single 'master' board. In this case the master board used was the USBDAQ board controlling the PMTs. A photograph showing the physical state of the USBDAQ boards, their cabling and their power supplies once set up for a test beam run is shown in figure 7.9.

In the earlier setup (see figure 7.7) where three PCs were used, one PC was the master while the other two 'slave' PCs controlled the sensors and the PMTs respectively. In this case the commands inputted via the master PC would be split up into separate commands to be executed by the slave PCs. Similarly the data from the sensors would initially be recorded separately from the PMT data (as the sensors were read back to one separate slave PC while the PMTs were read back to the other slave PC) and the two data streams would not be unified into a single record until both were recorded onto a central hard disk (attached to the master PC).

In the setup used for later runs there was only a single PC used which acted as both the master and slave PCs (see figure 7.8). Commands were transmitted directly from this PC to the USBDAQ boards, and information read from the sensors and PMTs was transmitted directly back to the PC (via the USBDAQ boards) and stored.

7.3   Theory

In principle, the efficiency of the pixels in a given sensor should be the number of beam particles that the sensor detects, divided by the number of beam particles independently registered as passing through the sensor i.e.

$$\text{efficiency} = \frac{N_D}{N} \tag{7.1}$$
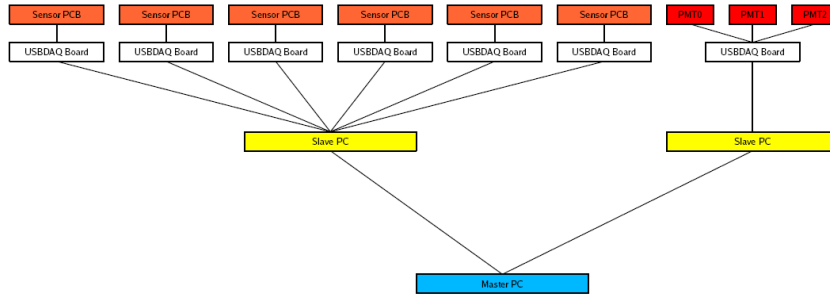
Figure 7.7: Block diagram of the original layout of DAQ apparatus used for the TPAC 1.2 test beam (used from 13/08/2009 to 21/08/2009). The black lines connecting components represent cables carrying data (in various formats) between the components.
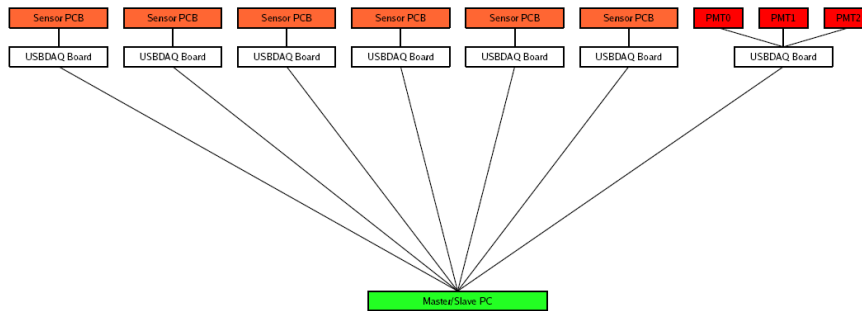
Figure 7.8: Block diagram of the second DAQ layout used for the TPAC 1.2 test beam (used from 21/08/2009 to 28/08/2009). The black lines connecting components represent cables carrying data (in various formats) between the components.
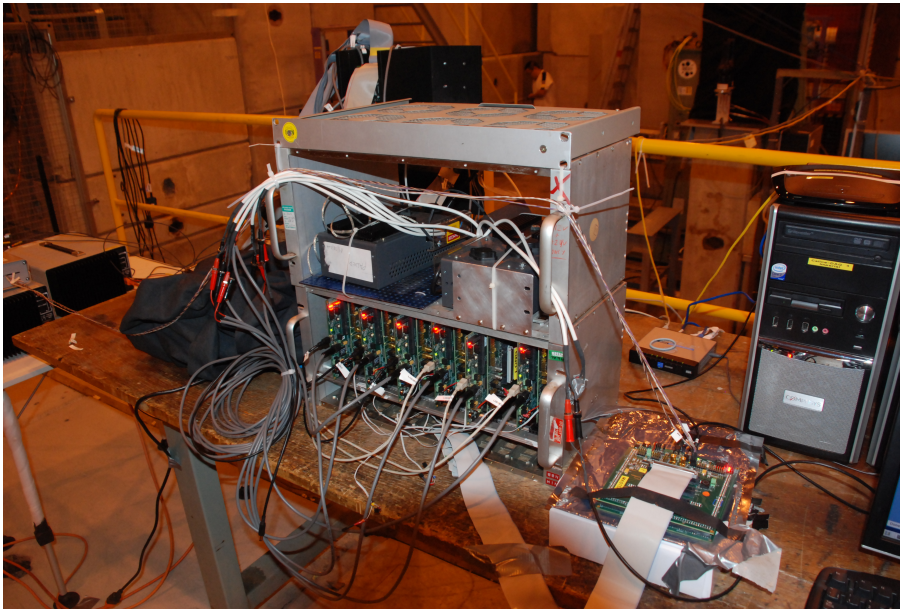
Figure 7.9: A picture of the DAQ crate containing six USBDAQ boards with the seventh board lying next to the crate in the foreground. The two cables attached at the front of each of the crated USBDAQ board are the data cables connecting the USBDAQ boards to one of the slave PCs (this is the USB cable), and a power lead connecting the USBDAQ boards to the power supplies on the upper level of the DAQ crate. The TPAC 1.2 test stand is visible at the back of the picture and the sensor PCBs and PMTs are connected to their respective USBDAQ boards via ribbon cables (the connection between the cables and the USBDAQ boards is obscured by the USBDAQ boards themselves and the DAQ crate).

Where: N_D is the number of particles detected passing through the test sensor

and N is the number of particles passing through the test sensor

Using equation 7.1 the analysis of the data from this experiment would seem to be a simple matter. The number of times a test sensor recorded a hit (indicating that the sensor had detected a particle) could be divided by the number of times all three PMTs fired, indicating that a particle passed through the sensor stack, to give the efficiency of the sensor and therefore the pixels within that sensor. However this approach has several problems, the first of which is that due to charge diffusion a test sensor can register multiple hits from a single particle. This means that the number of hits detected by a test sensor may not be identical to the number of particles detected by that test sensor, distorting the apparent value of N_D. There are several methods of dealing with this discrepancy which will be discussed later in sections 7.5.1, 7.5.2 and 7.5.3).

The second problem is more immediate; directly measuring N is not practical, the PMTs used for this study (described previously in section 7.2) are not perfectly efficient, meaning that data from the PMTs cannot be used to directly measure N. This inefficiency means that it is possible for a particle to go undetected by the PMTs but still be detected by the test sensor, artificially increasing the apparent efficiency. This problem may be exacerbated by the fact that particles passing through the sensor stack can be excluded from the study for other reasons (depending on the analysis method used, see sections 7.5.1, 7.5.2 and 7.5.3), but might still be detected by the test sensor. This problem can be solved by considering the following:

$$n = N \times p \tag{7.2}$$

Where: N is the number of particles passing through the test sensor

n is the number of useable particles passing through the test sensor

p is the proportion of particles that are useable

$$n_D = N \times \text{efficiency} \times p = N_D \times p \tag{7.3}$$

Where: n_D is the number of useable particles detected by the test sensor

N_D is the number of detected particles passing through the test sensor

Therefore:

$$\frac{n_D}{n} = \frac{N_D \times p}{N \times p} = \frac{N_D}{N} = \text{efficiency} \qquad (7.4)$$

Since the existence of any test particle not detected by all three PMTs was uncertain, only particles which were detected by all three PMTs were considered useable. Therefore the efficiency of a test sensor could be calculated by substituting the number of test beam particles detected by all three PMTs as n, and the number particles detected by that test sensor at approximately the same time as n_D. However as described in section 7.5 below there were additional factors which could make test particles unusable, further modifying n and n_D.

7.4   Procedure

Under normal circumstances the spill signal from the test beam (an electronic signal indicating when the test beam was firing) would have been integrated into the procedure to control when the sensor stack was recording data. Ideally the sensor stack would have been set up so that the sensor stack was only active and recording data while the test beam was firing. However the spill signal was not available when these experiments were carried out. To compensate for this, long continuous runs were used to ensure sufficient data could be collected. Without information from the spill signal, the PMTs alone were used to detect when beam particles passed through the sensor stack. In preliminary versions of this procedure the spill signal would have been used to find the approximate time when beam particles passed through the stack while the PMTs would have been used to identify the exact time. The procedure that follows is the procedure developed to compensate for the lack of a spill signal from the test beam.

The apparatus was set up as shown in figure 7.6 with sensors 26 and 32 (an 18μm

hi-res TPAC 1.2 sensor and a standard TPAC 1.2 sensor respectively) in the test sensor slots. The thresholds for the test sensors were set to 130TU (threshold units) while the thresholds for the control sensors were set to 150TU. The sensor stack was then placed in a 120 GeV pion beam for 30 minutes while data was collected continuously from all six sensors and the PMTs. The PMTs and control sensors were used to detect how many particles passed through the sensor, when this occurred, and where these particles passed through the test layers. Data from the test sensors (along with the times identified by the PMTs and control sensors) was then used to measure how many of these particles were detected by each test sensor.

Once these results had been outputted and stored the threshold for the test sensors was increased by 10TU to 140TU. The sensor stack was then exposed to the test beam for another thirty minutes with the number of particles passing through the stack, and the number of those particles detected by each test sensor, being recorded in the same manner. This process was repeated for test sensor thresholds of 150TU to 200TU in 10TU increments. This sequence was then repeated several times to collect more data and hence reduce the uncertainty in the final results.

Sensors 26 and 32 were then replaced by sensors 21 and 39 (a 12μm hi-res TPAC 1.2 sensor and a standard TPAC 1.2 sensor respectively). The procedure described above for sensors 26 and 32 was then repeated with these new test sensors (with the addition that the range of thresholds was increased so that runs at 205TU to 250TU in 5TU increments were added to the process).

For all of the runs detailed above the relative alignments and positions of the sensors were recorded, this information was later used along with data recorded from the control sensors and PMTs to form the particle tracks discussed in sections 7.5.1, 7.5.2 and 7.5.3. Once these runs had been completed the collected data was analysed using the techniques described below.

7.5 Analysis and Results

In order to understand how the data from the test runs was analysed it is first necessary to include some brief notes on how that data was structured: Each run was broken up into a large number (typically around fifty thousand) of 3.2ms periods called bunch trains (note: even during continuous running there is a gap between bunch trains while data from the sensor is read out). Events within each bunch train are given a timestamp (typically stretching from zero at the start of the bunch train to around eight thousand at the end of the bunch train). Each timestamp covers a 400ns period.

As mentioned in section 7.3, the efficiency of a test sensor can be calculated by measuring the number of particles recorded by all three PMTs, measuring the number of particles detected by that test sensor at approximately the same time, and dividing the latter by the former. However the problem of particles creating multiple sensor hits remains an issue for attempting to measure how many particles are recorded by a test sensor. Even if that problem was eliminated there is an additional problem with finding suitable input values for equation 7.4; the possibility of false positives and false negatives in the calculation of efficiency. In this case a false positive refers to any situation where a test sensor appeared to have detected a particle passing through, but in fact did not. Similarly, a false negative in this context is any situation where a test sensor appeared to not to register a particle passing through, when either the sensor did somehow detect the particle without this fact being recorded, or the particle did not in fact pass through sensitive material at all. The primary source of false positives is noise on the sensor, random pixel firings with no discernible external cause. This potentially creates a situation where the test sensor does not in fact detect a particle passing through, but appears to detect it due to the random firing of a pixel somewhere on the test sensor. Meanwhile false negatives are primarily caused by particles passing through sections of the sensor PCB which either contain no pixels, or where the pixels have been effectively shut down for some reason. Pixels can be unresponsive for two reasons, the first reason is

that if a sufficient number of hits are recorded in a set of forty two pixels (nineteen or more hits before being read out), their local memory is filled, meaning that any further hits will go unrecorded (i.e. this section of the sensor is 'saturated')[32], as described in section 3.3.3. During test beam runs sensors were read out after every bunch train, resetting the sensor memory and effectively removing any existing saturation on the sensor (new saturated regions were then created in the following bunch train). This regular readout schedule combined with sensor noise continuously creating new hits meant that the regions of the sensor which were saturated changed regularly throughout a test run. Pixels in this state were grouped together with insensitive areas of the sensor PCB for the purposes of analysis and were referred to as dead areas (an example showing dead areas in and around a sensor during a single bunch train is shown in figure 7.10). The second reason why areas of the sensor were unusable is that some pixels had to be shut down ('masked') before the sensor could be used. This was because these pixels did not respond correctly to the control mechanisms, resulting in pixels with unpredictable or otherwise counterproductive behaviour. These pixels are collectively referred to as 'bad pixels' and are typically identified and deactivated during preliminary sensor testing (an example showing the locations of bad pixels on a sensor is shown in figure 7.11). While this does remove most of the negative effects of these pixels, it does leave areas of the sensor insensitive. In cases where the particle passes through dead areas or bad pixels the sensor appears not to detect particles passing through it, when in fact those particles are not interacting with sensitive material at all. The need to deal with false positives, false negatives, and the discrepancy between the number of hits recorded and the number of particles detected was dealt with by the three techniques for analysing runs detailed in sections 7.5.1, 7.5.2 and 7.5.3.

7.5.1 The Counting Method

The counting method started with the creation of a pair of running totals for each test sensor for the entire run under analysis. By the end of the run, one of these totals
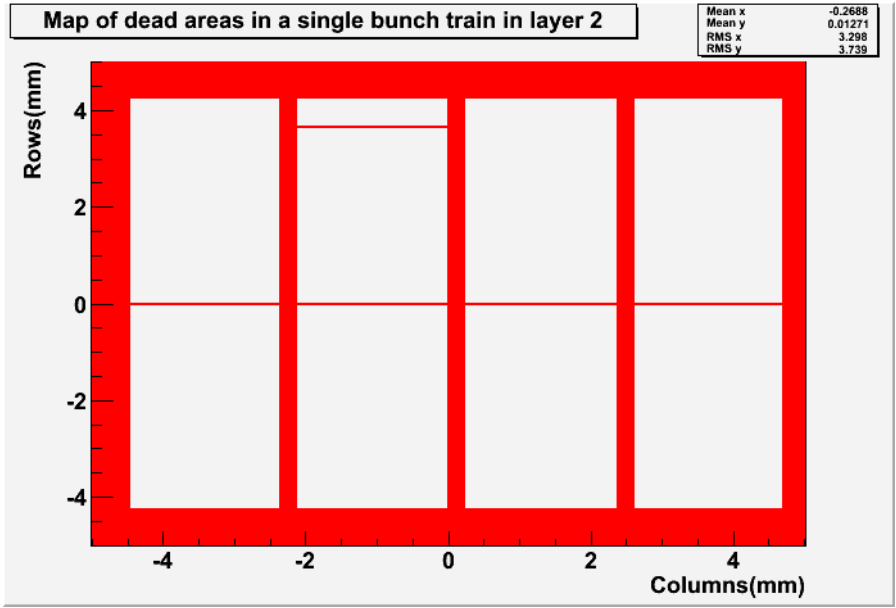
Figure 7.10: A map of the dead areas in and near sensor 39 during a single 3.2ms period (referred to as a bunch train). The red regions represent either areas which contain no pixels, or where the pixels were saturated during the bunch train in question, white regions represent functioning pixels. This map was recorded during a single bunch train in run 447885.

Figure 7.11: A map of the bad pixels on sensor 39. The red regions represent defective pixels while the white regions represent functioning pixels. The axes labels represent the column and row numbers of the pixels. This map was recorded during a single bunch train in run 447885. In this case the bad pixels represent approximately 8% of all the pixels on the sensor.

would record the number of useable particles that passed through that test sensor, and the other would record the number of useable particles that were detected by that test sensor.
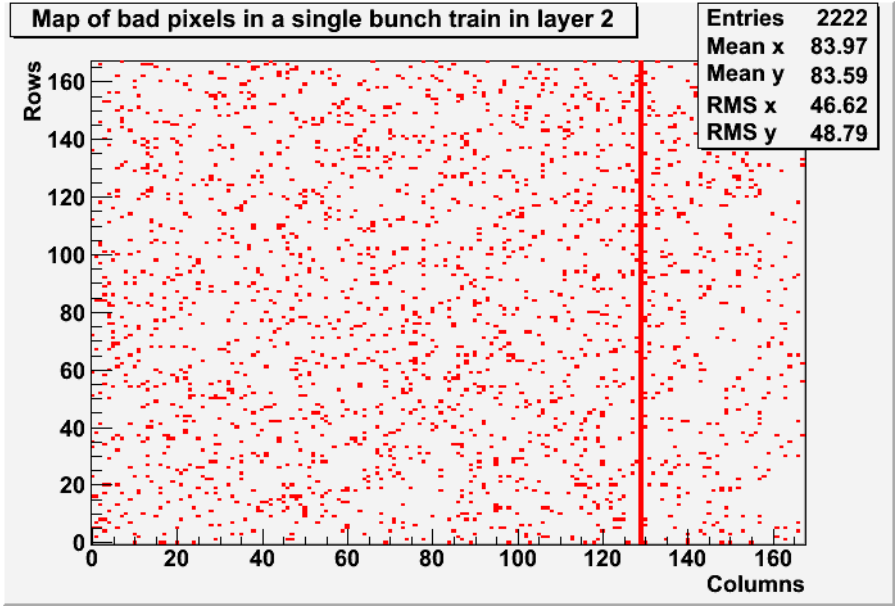
At the start of each bunch train the data recorded by the PMTs and control sensors was analysed to produce particle tracks in order to identify when and where particles passed through the test sensors. In this case a track was defined as a fit applied to three or four hits, arranged in an approximate straight line, found in separate control sensors within a single time stamp. This timestamp was separated by at most one timestamp from a timestamp in which a hit was detected in all three PMTs. It was necessary to use multiple PMTs for confirmation that a particle had passed through the sensor stack because (as shown in figure 7.14) a single PMT could be prone to registering noise hits). Naturally, if there were no timestamps where all three PMTs registered hits in a given bunch train, there would be no tracks in that bunch train.

Unfortunately due to the possibility of single particles creating multiple hits in the sensors it was possible to have multiple tracks associated with the same particle (figures 7.12 and 7.13 show that when a test particle passed through the test sensors it was quite common for the particle to create a cluster containing multiple hits). In order to prevent this, tracks recorded during the same bunch train were grouped together and the track with the highest χ^2 probability was selected. If that track had a χ^2 probability greater than 0.1 then it would be selected for further analysis whilst all other tracks from the same bunch train were discarded; if its χ^2 probability was less than 0.1 then all the tracks from that bunch train would be discarded. An example of the effects of this selection process on the χ^2 probability of the tracks used can be seen in figures 7.15 and 7.16.

The selected track was then extrapolated on to the test layers producing rectangular search areas on those test layers centered on the extrapolated position of the track with sides equal to twice the one, two or three σ uncertainty on that position (the data was re-analysed with each different search range resulting in three different counting efficiencies being recorded for each run). The search area was then
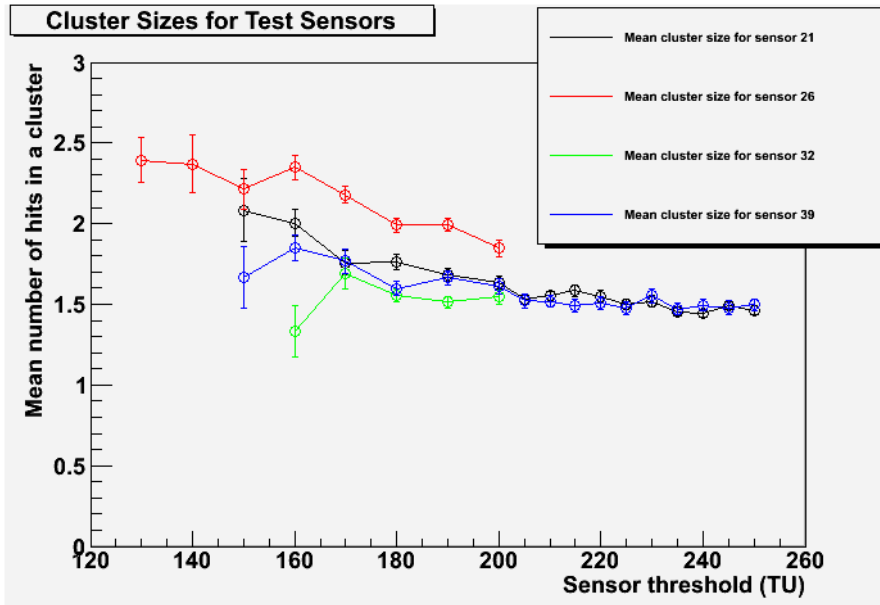
Figure 7.12: A graph showing how the sensor threshold set affected the mean number of hits found clustered together when test particles passed through the sensors. Sensor thresholds where there were insufficient statistics to estimate errors in the mean number of hits per cluster (i.e. where less than two clusters were detected for all results analysed) were ommitted from this graph. The plots for sensors 26 and 32 were based on results from runs 447526-447533, 447596-447603, 447667-447674, and 447683-447690. The plots for sensors 21 and 39 were based on results from runs 447783-447790, 447820-447827, 447883-447892, 447903-447912, and 447951-447960. An example of the distribution of cluster sizes during a single run is shown in figure 7.13.
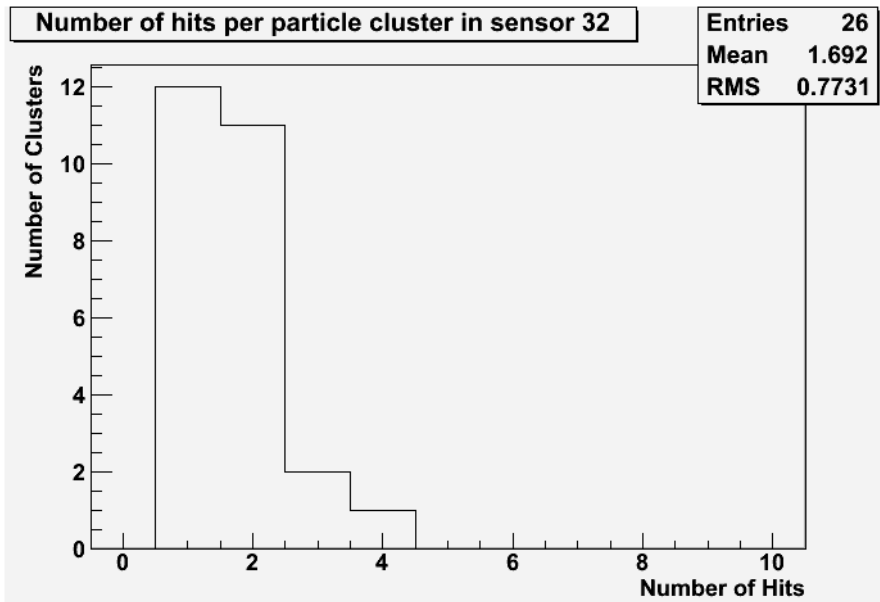

Figure 7.13: An example of the distribution of cluster sizes created by the passage of test particles through sensor 32 during run 447530 (the sensor threshold set during this run was 170TU).

199

expanded by a further 25μm in every direction to ensure that the centres of all pixels under investigation would be encompassed. These search areas were then examined to see if they contained any dead areas or bad pixels. If there were no dead areas or bad pixels in a search area then the track was considered evidence of a useable particle passing through the test sensor and the running total for the test sensor in question recording the number of useable particles passing through was increased by one. Additionally if there were no dead areas or bad pixels found in a search area then it would be scanned a second time to see if there were any hits recorded in that search area at the time the track predicted a particle passed through. If there were any suitable hits in the search area then this was considered evidence that a useable particle was detected by the test sensor and the running total for the test sensor in question recording the number of useable particles detected by the test sensor was increased by one.

At the end of each bunch train (where there had been at least some activity in the PMTs), the current values for the running totals for each test sensor were plotted on histograms. Examples of these histograms are shown in figures 7.17 and 7.18. Additionally, if there had been some activity in the PMTs (indicating that there might have been a useable particle passing through the sensor, and therefore that the running totals might have changed), the two running totals for each sensor were substituted into equation 7.4 to calculate the efficiency of that test sensor. This newly calculated efficiency was then plotted on a third histogram (an example of one of these histograms is shown in figure 7.19). Once all the bunch trains in a run had been analysed the sensor efficiency was the final efficiency recorded in this third histogram for that sensor (since this was the efficiency calculated from the total number of useable particles and the total number of useable detected particles in the run).

Although complete efficiency calculations were performed using one, two and three σ search ranges, the three σ search range was eventually selected as the default search range. This range was chosen so that the resulting search areas would contain the actual point where the test beam particle passed through in over 99% of cases.

200

Efficiency calculations using one and two σ search ranges were retained so that the effect of varying the search area could be observed in the resulting efficiencies.

Analysing the results in this fashion has several outcomes. First, false positives are substantially reduced by significantly reducing the area of the sensor scanned for hits (histograms showing typical search ranges are shown in figures 7.20 to 7.25) which reduced the probability of encountering a noise hit. Second, false negatives are eliminated by removing all results which might have been false negatives from the analysis (by discarding tracks that might have passed through 'dead areas and/or bad pixels'). Third, the discrepancy between the number of hits recorded and the number of particles detected was dealt with by simply recording whether or not there were hits in a search area (confirming or denying that the sensor had detected the passage of a particle) rather than recording how many hits there were.

However this method does have one flaw; it is possible for a particle to pass through a pixel without causing it to register a hit, while still causing surrounding pixels to fire due to charge diffusion. The counting method does not pinpoint the exact pixel where a particle passed through, and takes the presence of any hits in the search area as a successful detection. This means that the efficiency found by the counting method is the probability that the whole sensor will detect a particle, not the probability that an individual pixel will detect the same particle. In practice this value can be considered the upper limit for pixel efficiency.

7.5.2 The 2D method

The 2D method begins with processing each bunch train in the run under consideration to form and select tracks in the same manner as the counting method described above. As with the counting method, any track successfully created and selected was used to extrapolate positions in the test sensors. Once a track had been formed and extrapolated on to a test layer it was used to fill a pair of 2D histograms (per test sensor) established at the beginning of the run. The first histogram showed the location of each track relative to the centre of every good pixel in a 7 by 7 pixel
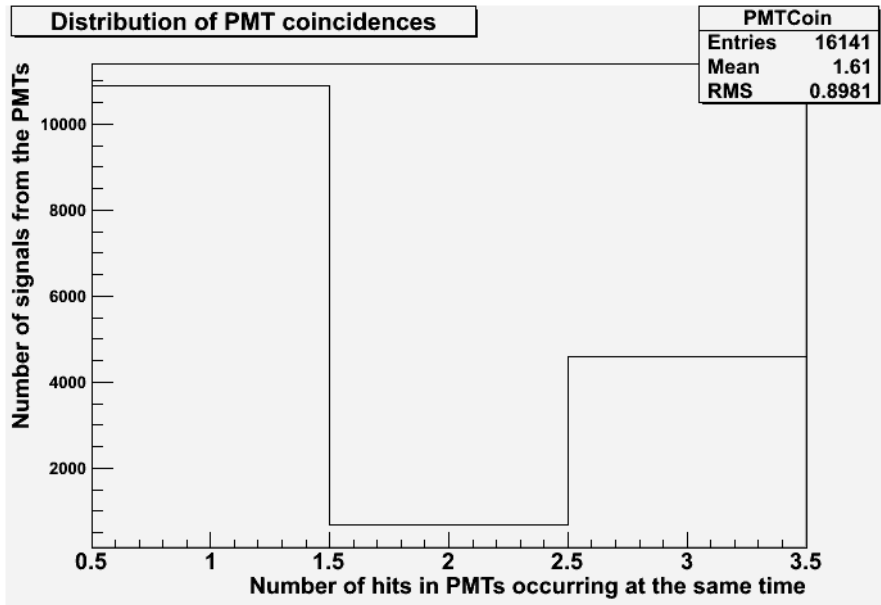
Figure 7.14: An example of the distribution of PMT signal types as recorded by the PMT USBDAQ board. A PMT signal in this case refers to the record of all PMT hits in the same timestamp (the shortest time difference measured by the USBDAQ boards, equal to 400ns), timestamps which did not include any PMT hits were not recorded in this fashion (although hits on the sensors were still recorded normally). This data was recorded during run 447885.

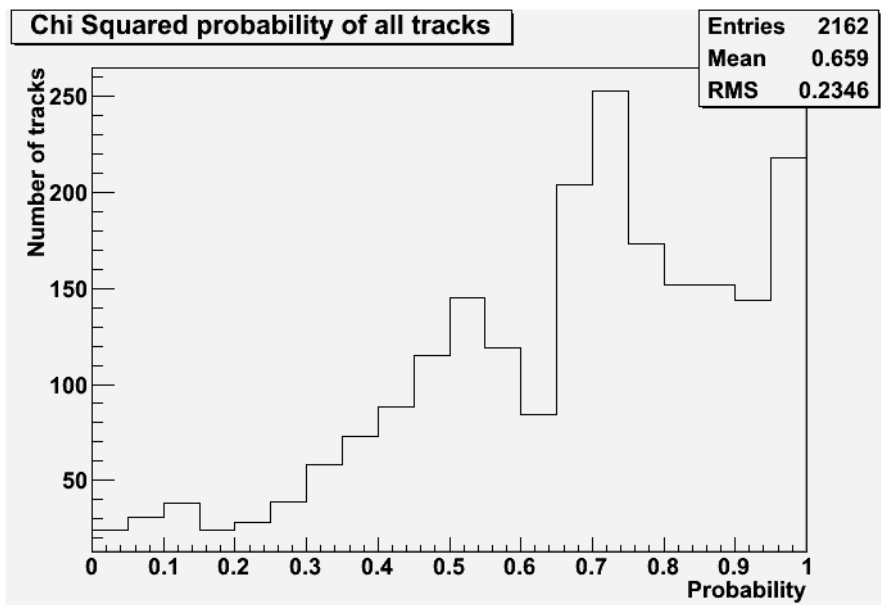Figure 7.15: An example of the distribution of χ^2 probabilities of all tracks reconstructed during a run. Due to cuts applied to the groups of hits used to reconstruct these tracks (specifically only groups of hits which were already found to form rough straight lines were used), there is already a predisposition towards high χ^2 probabilities at this stage. This data was recorded during run 447885.
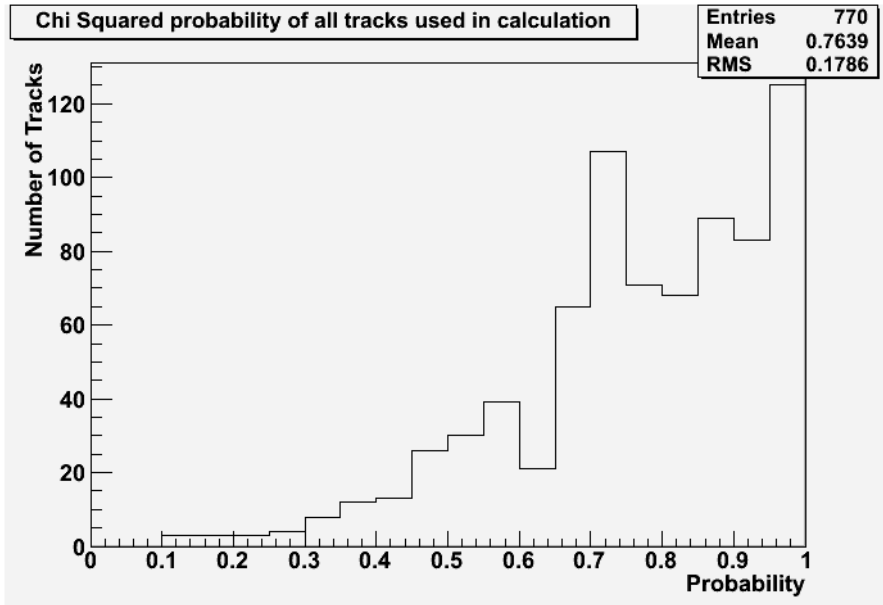
Figure 7.16: An example of the distribution of χ^2 probabilities of tracks selected for analysis during a run. Notable differences to the unfiltered distribution shown in figure 7.15 include a greater predisposition to high probabilities (due selecting the highest probability in a single bunch train), a complete lack of probabilities below 0.1 (those tracks were discarded), and an overall much smaller number of tracks (due to discarding all but one track when multiple tracks might have been caused by a single particle). This data was recorded during run 447885.

Figure 7.17: An example of how useable particles passing through a sensor are accumulated in a typical run. In this case useable are particles detected by all three PMTs and not having any dead areas or bad pixels in their projected search area)
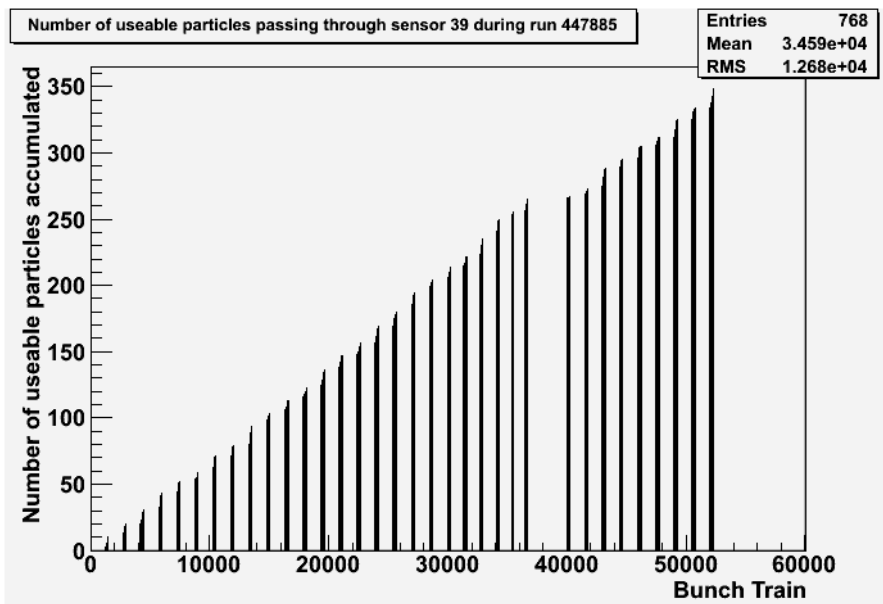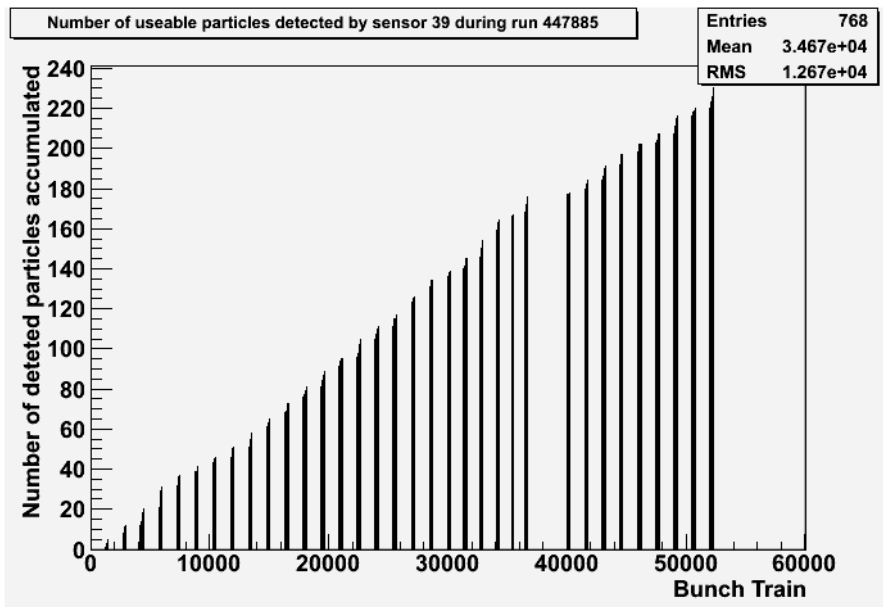
Figure 7.18: An example of how useable particles detected by a particular sensor are accumulated in a typical run. In this case useable particles are particles detected by all three PMTs and not having any dead areas or bad pixels in their projected search area.
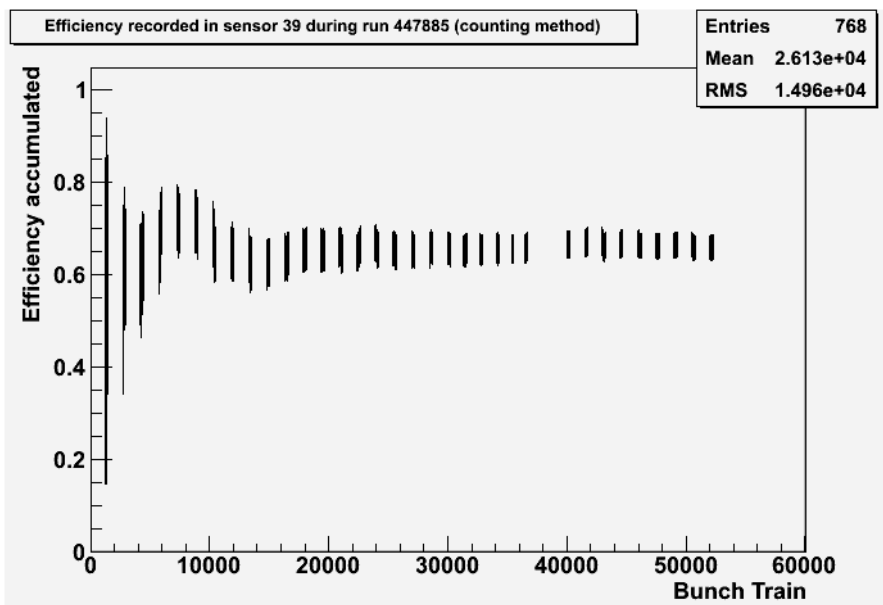

Figure 7.19: An example of how efficiency for a sensor is produced (using the counting method) during a typical run.

Figure 7.20: An example of one σ search ranges for the counting method, in columns, for sensor 39. This data was recorded during run 447885. Note: All search ranges were increased by 25μm to ensure that if the initial search range encompassed any part of a pixel, the search range eventually used would encompass the centre of that pixel (and therefore any hits recorded in that pixel). This histogram shows the final search ranges used.

Figure 7.21: An example of one σ search ranges for the counting method, in rows, for sensor 39. This data was recorded during run 447885. Note: All search ranges were increased by 25μm to ensure that if the initial search range encompassed any part of a pixel, the search range eventually used would encompass the centre of that pixel (and therefore any hits recorded in that pixel). This histogram shows the final search ranges used
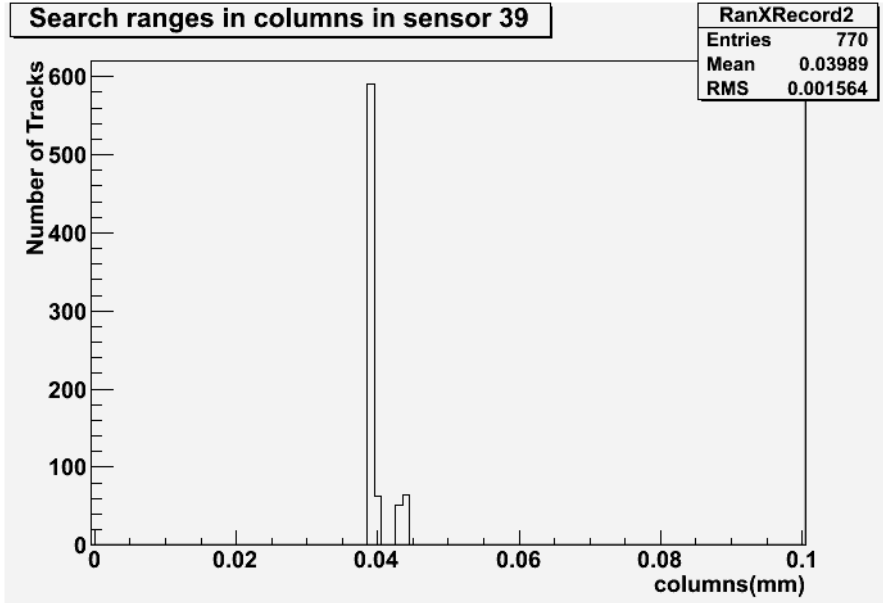
Figure 7.22: An example of two σ search ranges for the counting method, in columns, for sensor 39. This data was recorded during run 447885. Note: All search ranges were increased by 25μm to ensure that if the initial search range encompassed any part of a pixel, the search range eventually used would encompass the centre of that pixel (and therefore any hits recorded in that pixel). This histogram shows the final search ranges used
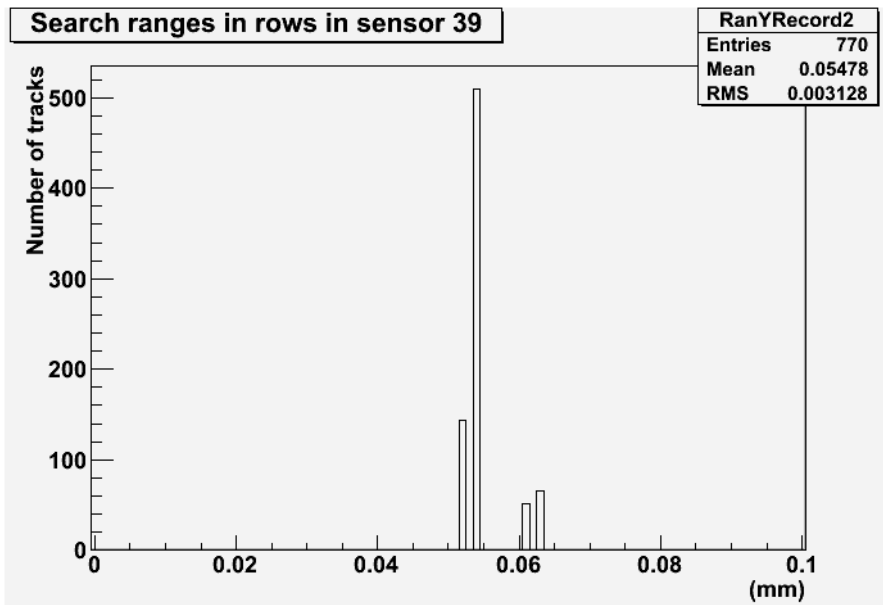
Figure 7.23: An example of two σ search ranges for the counting method, in rows, for sensor 39. This data was recorded during run 447885. Note: All search ranges were increased by 25μm to ensure that if the initial search range encompassed any part of a pixel, the search range eventually used would encompass the centre of that pixel (and therefore any hits recorded in that pixel). This histogram shows the final search ranges used
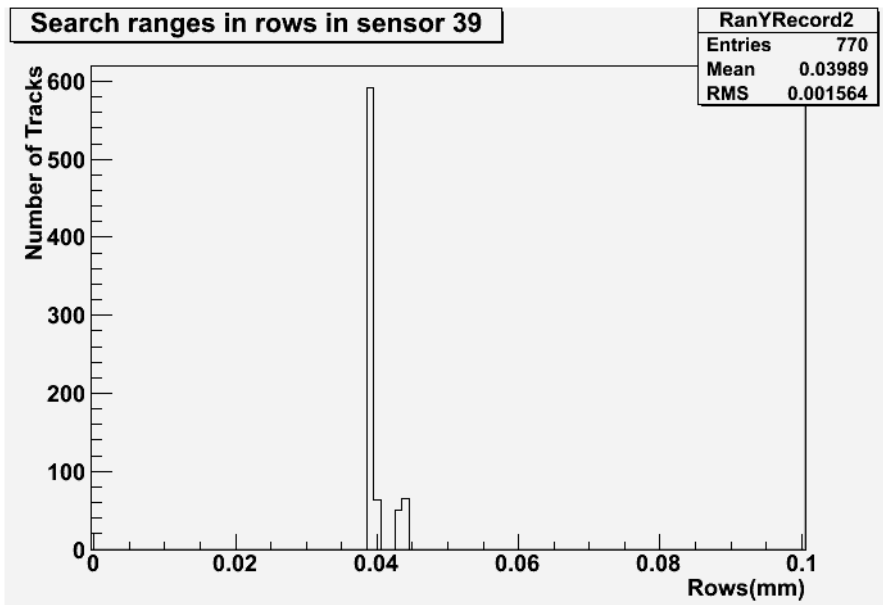
206
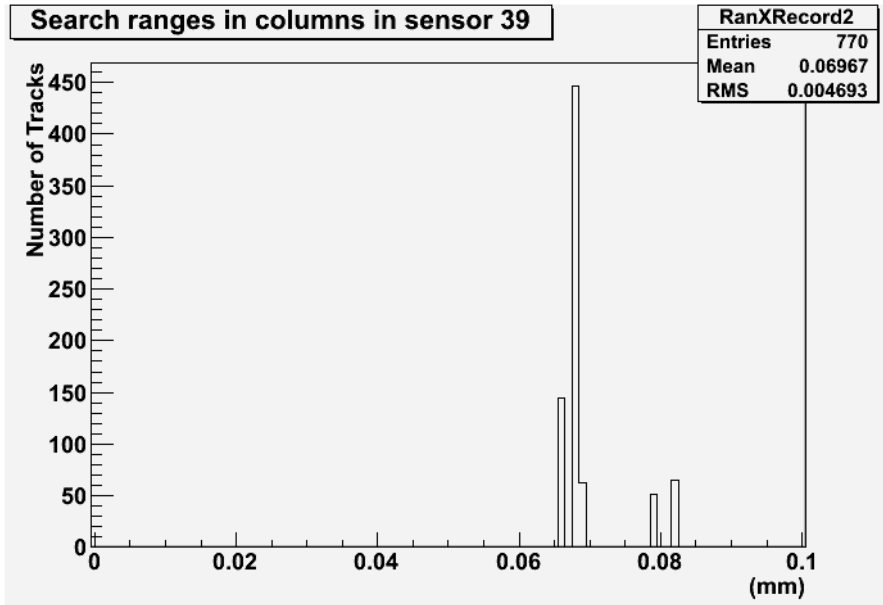
Figure 7.24: An example of three σ search ranges for the counting method, in columns, for sensor 39. This data was recorded during run 447885. Note: All search ranges were increased by 25μm to ensure that if the initial search range encompassed any part of a pixel, the search range eventually used would encompass the centre of that pixel (and therefore any hits recorded in that pixel). This histogram shows the final search ranges used
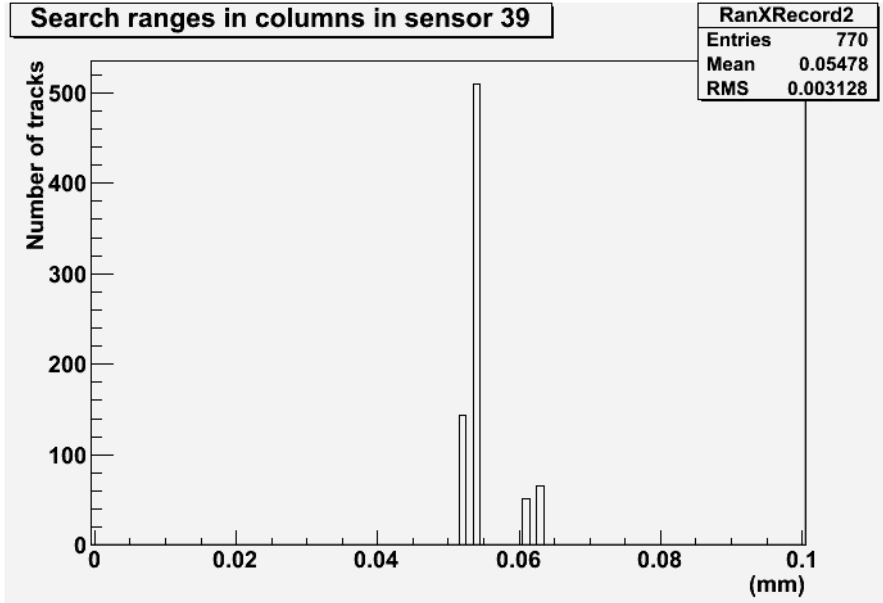

Figure 7.25: An example of three σ search ranges for the counting method, in rows, for sensor 39. This data was recorded during run 447885. Note: All search ranges were increased by 25μm to ensure that if the initial search range encompassed any part of a pixel, the search range eventually used would encompass the centre of that pixel (and therefore any hits recorded in that pixel). This histogram shows the final search ranges used.
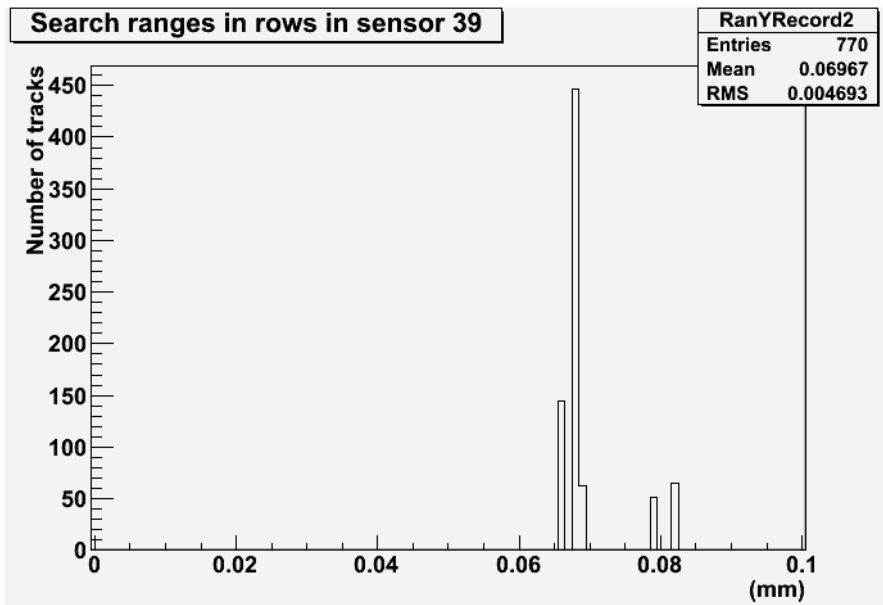
grid centered on the pixel the track passed through (assuming no error on the track location). The second histogram shows the location of each track relative to the centre of every good pixel (in the same 7 by 7 pixel grid) that recorded a hit in the same timestamp as the track (examples of these histograms are shown in figures 7.26 and 7.27 respectively).

At the end of the run a third histogram was then produced by dividing the second histogram by the first, producing a histogram showing the variation of pixel efficiency with distance from the track, with one bin per pixel in a 7 by 7 grid surrounding the track (an example of this third histogram is shown in figure 7.28).

Assuming there was no uncertainty on the track location then one bin in this third histogram, logically the bin containing the highest value, should contain the pixel efficiency (assuming the pixel a particle actually passes through is more likely to fire than other pixels nearby). Typically this bin will be the central bin, if it is not then that implies there was some consistent offset between the track prediction and the true location at which particles passed through the sensor, making these histograms a useful cross check.

Like the counting method, the 2D method is vulnerable to false negatives due to bad pixels and dead areas. In the 2D method this is dealt with by scanning the target pixel before filling either of the histograms, if the pixel is registered as bad, or is in a dead area, the distance between the pixel and the cenre of the track would not be included in either histogram, effectively removing its influence from the study.

While this method eliminates false positives (due to the extremely small effective sensor) area and conventional false negatives, it does have at least one flaw: It assumes that (negating any systematic offset) the pixel a track passed through was the same pixel that the associated test beam particle passed through. Since in reality it is not unreasonable for the test beam particle that created a track to be elsewhere within a one to three σ search range (which might encompass multiple pixels), this value is a lower limit for pixel efficiency.
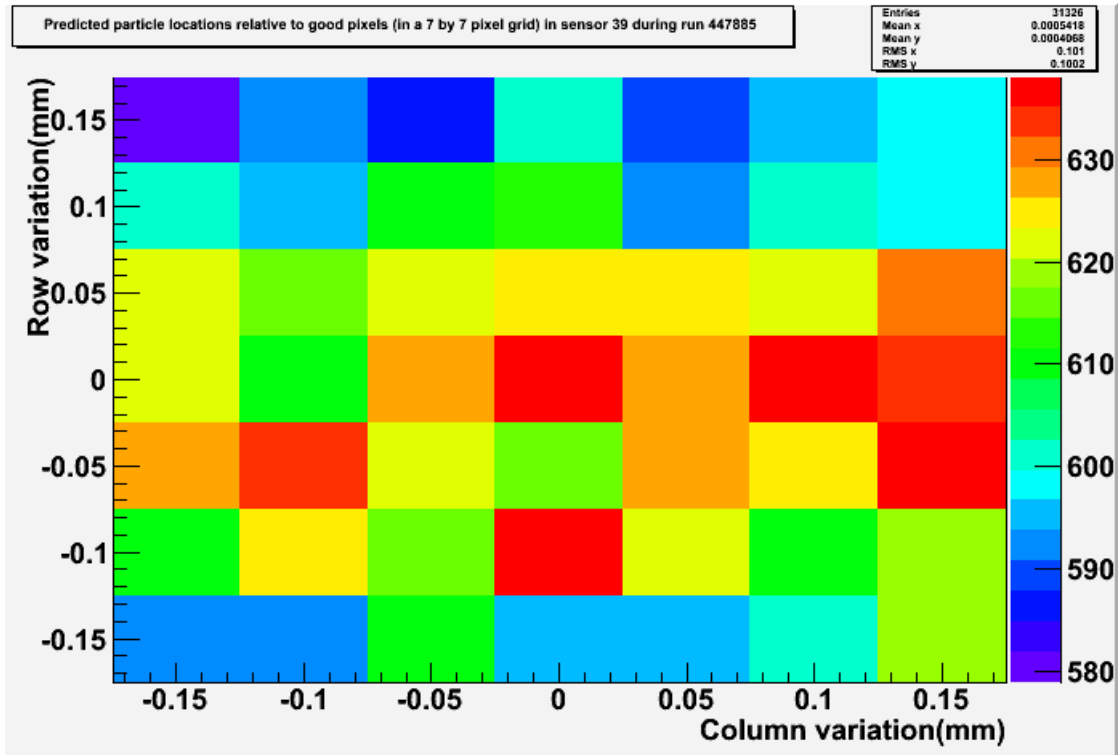
Figure 7.26: An example of the 2D histograms produced to record particle track postions relative to the centres of nearby pixels in a typical run (447885).
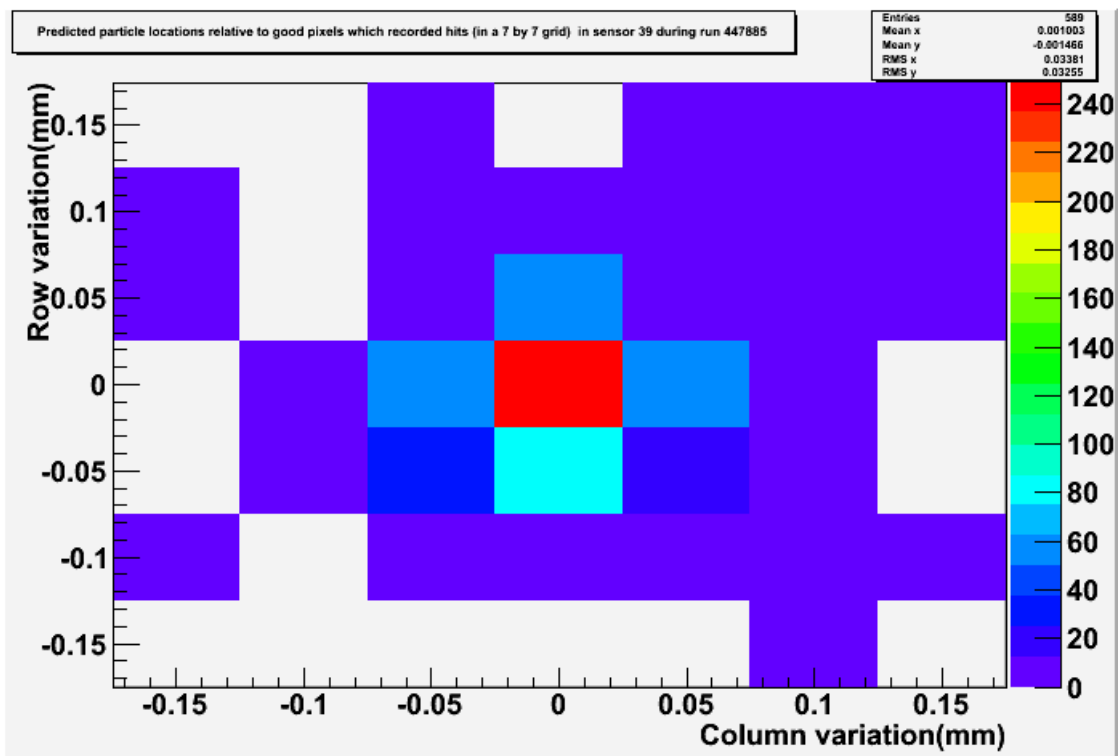
Figure 7.27: An example of the 2D histograms produced to record particle track positions relative to the centres of nearby pixels which recorded hits in a typical run (447885).
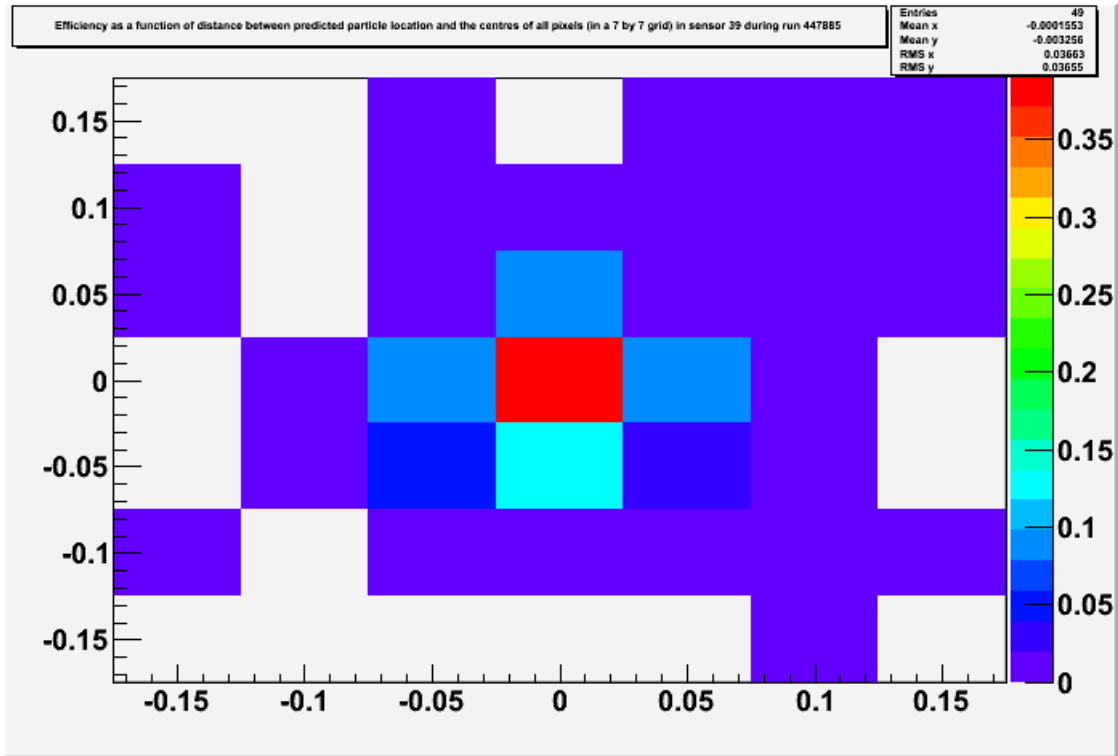
Figure 7.28: An example of the 2D histograms produced to record the variation in apparent pixel efficiency of pixels near to particle tracks in a typical run (447885).

7.5.3 The 1D Method

The 1D method works in the same fashion as the 2D method (see section 7.5.2) except each 2D histogram created by the 2D method was replaced by a pair of 1D histograms. Specifically where the 2D method required a 2D histogram plotting the distance between the track and the centre of every good pixel in a 7 by 7 pixel grid, the 1D method used a pair of 1D histograms: one 1D histogram showing the distance in rows between each track and every good pixel in a 7 row wide strip of pixels (centered on the relevant track), and another 1D histogram showing the distance in columns between each track and every good pixel in a 7 column wide strip of pixels (centered on the relevant track), an example of such a histogram is shown in figure 7.29. Similarly where the 2D method required a 2D histogram to plot the distance between each track and the centre of every good pixel which recorded a hit (in the right timestamp and in a 7 by 7 pixel grid), the 1D method required a pair of 1D histograms: one 1D histogram showing the distance in rows between each track

and every good pixel which recorded a hit in the right timestamp in a 7 row wide strip of pixels, centered on the relevant track, and another 1D histogram showing the distance in columns between each track and every good pixel which recorded a hit in the right timestamp and in a 7 column wide strip of pixels, centered on the relevant track. An example of such a histogram is shown in figure 7.30. These 1D histograms were created and filled in the same manner as the 2D histograms described in section 7.5.2. Each of the 1D histograms depicting the distance (in either rows or columns) between the track and good pixels with hits in a 7 pixel strip was divided by its counterpart recording the distance (in either rows or columns) between each track and all good pixels in the same strip. The result of this was a pair of histograms (for each test sensor), one depicting how pixel efficiency varied with the distance in rows from the predicted track location, and the other depicting how pixel efficiency varied with the distance in columns from the predicted track location (an example of such a histogram is shown in figure 7.31). As with the 2D method, the highest efficiency shown on each these histograms should be the lower limit of pixel efficiency (resulting in one efficiency reading from the row histograms, and another efficiency reading from the column histograms), however there is one more complication to consider:

As in the 2D method all pixels are scanned to check if they are 'bad pixels' or in dead areas before they were used in any of the histograms and were excluded from the study if they were found to have either of these problems. Additionally, in the 1D method any pixel where the centre of the pixel was more than 12.5μm from the track in the column direction (i.e. the direction which increases or decreases the column number) was excluded from being used in any of the row distance histograms, and any pixel where the centre of the pixel was more than 12.5μm from the track in the row direction was excluded from being used in any of the column distance histograms.

This means that both efficiencies found from the 1D efficiency histograms were efficiencies excluding all tracks that were not predicted to pass through a 25μm wide strip down the centre of a pixel. Figure 7.32 indicates that a MAPS sensor is much

Figure 7.29: An example of the 1D histograms produced to record the particle track positions relative to the centres of nearby pixels in a typical run.

more likely to detect charged particles passing through the centre of pixels with the areas around the diodes (visible as the four peaks of shown in figure 7.32) being particularly sensitive. Excluding tracks which were not predicted to pass through a 25μm wide strip down the centre of a pixel meant that the 1D method excluded most of the less sensitive areas of MAPS pixels shown in figure 7.32 from the efficiency measurement. Since the 1D method excludes some of the less sensitive areas of the pixel (but still suffers from the assumption that the location of a track is the loction of the particle that created that track), the 1D method finds the lower limit of pixel efficiency for an ideal pixel which does not have these relatively insensitive areas. This measurement is potentially valuable because it indicates the performance that could be expected from a MAPS sensor if the insensitive regions of the pixels could be eliminated.
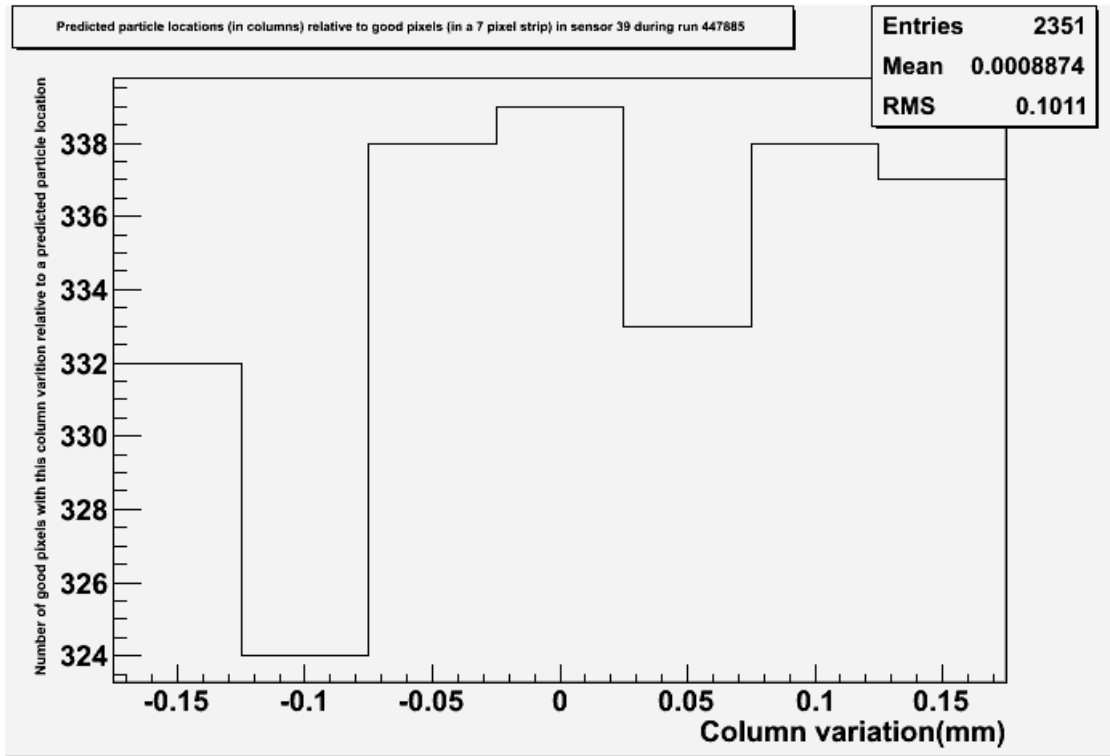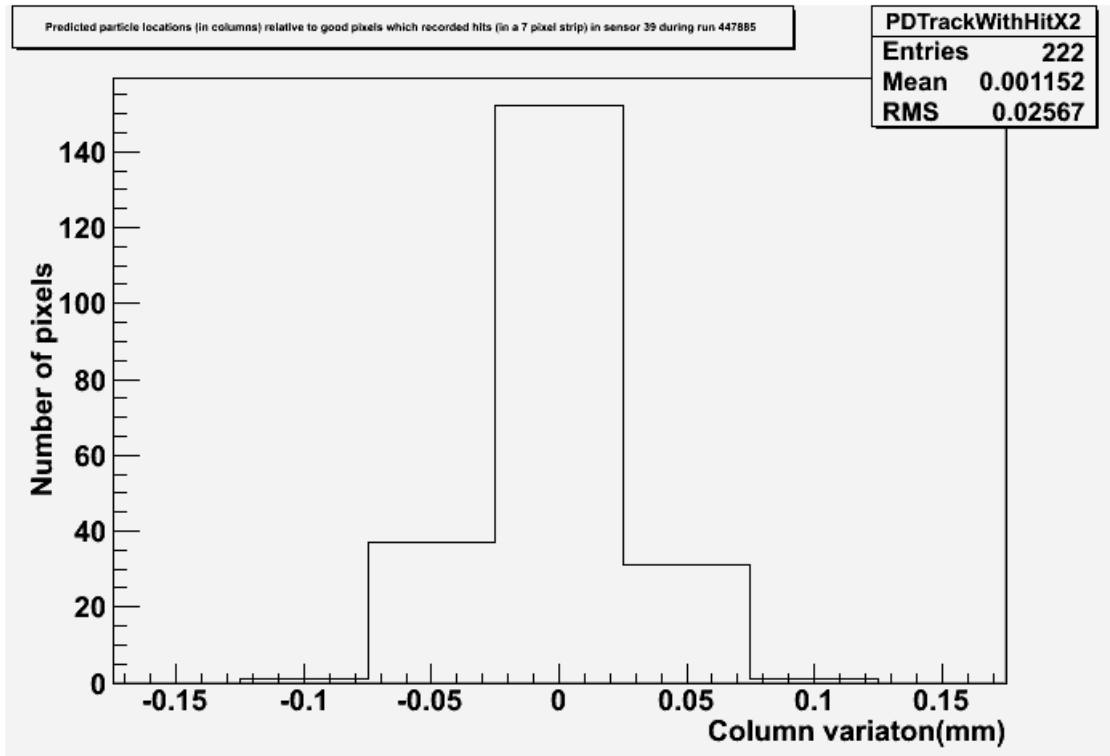
Figure 7.30: An example of the 1D histograms produced to record the particle track positions relative to the centres of nearby pixels which recorded hits in a typical run.
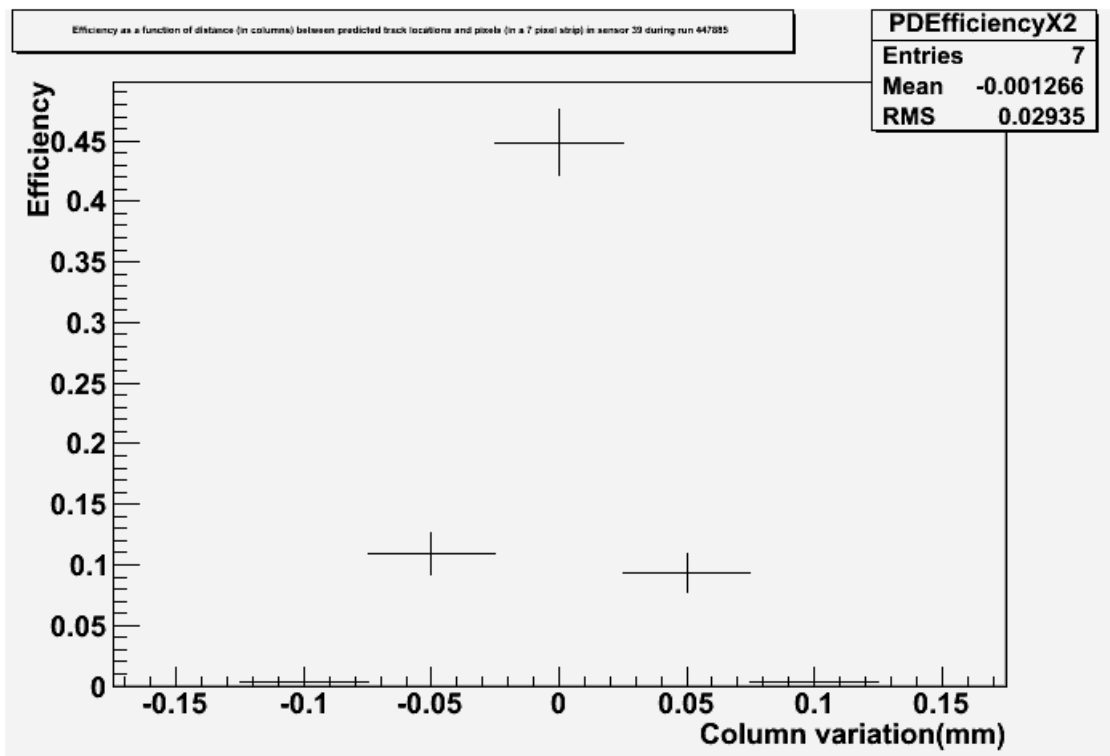
Figure 7.31: An example of the 1D histograms produced to record the variation in apparent pixel efficiency of pixels near to a particle track in a typical run.
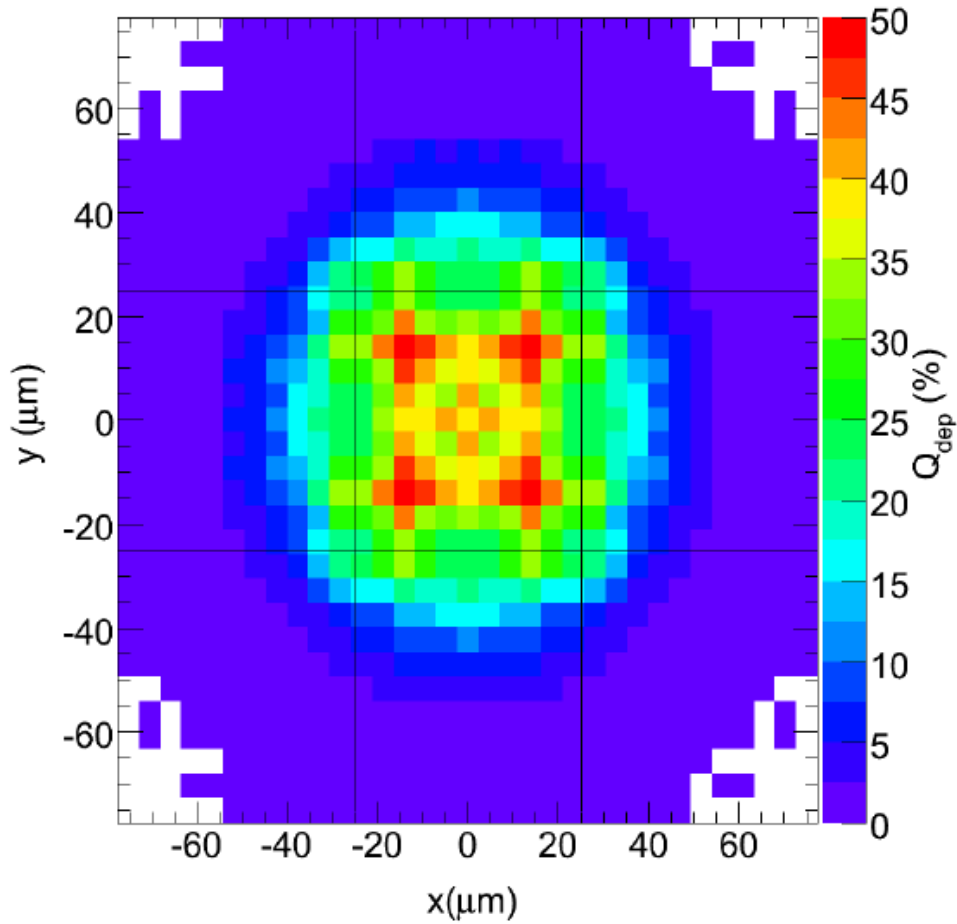
Figure 7.32: A plot showing what percentage the charge deposited by a laser is picked up by the diodes of a test pixel as the laser was moved across a 3×3 pixel grid centered on the test pixel. On this plot the areas defined by $25\mu m > X > -25\mu m$ and $25\mu m > Y > -25\mu m$ represent the charge detected when the laser was focused on the test pixel, with X=0μm and Y=0μm corresponding to the charge detected when the laser was focused on the centre of the test pixel. A small percentage (¡10%) of charge collected for a given set of X-Y coordinates would indicate that the pixel is relatively insensitive to particles in that region[39].

Figure 7.33: Counting method pixel efficiencies in test sensor 21, averaged from several runs in the test beam, using a range of different search areas.

Figure 7.34: Counting method pixel efficiencies in test sensor 26, averaged from several runs in the test beam, using a range of different search areas.

215

Figure 7.35: Counting method pixel efficiencies in test sensor 32, averaged from several runs in the test beam, using a range of different search areas. The efficiency calculated using the three σ search area has no results at a threshold of 160 because low statistics resulted in several results with efficiencies of either 0 or 1 at this threshold. This was a problem because the binomial error calculated from these values was zero, meaning that these results could not be included in a weighted mean. This combined with the low statistics of the remaining results, made it impractical to include a data point using the three σ search area at a threshold of 160.

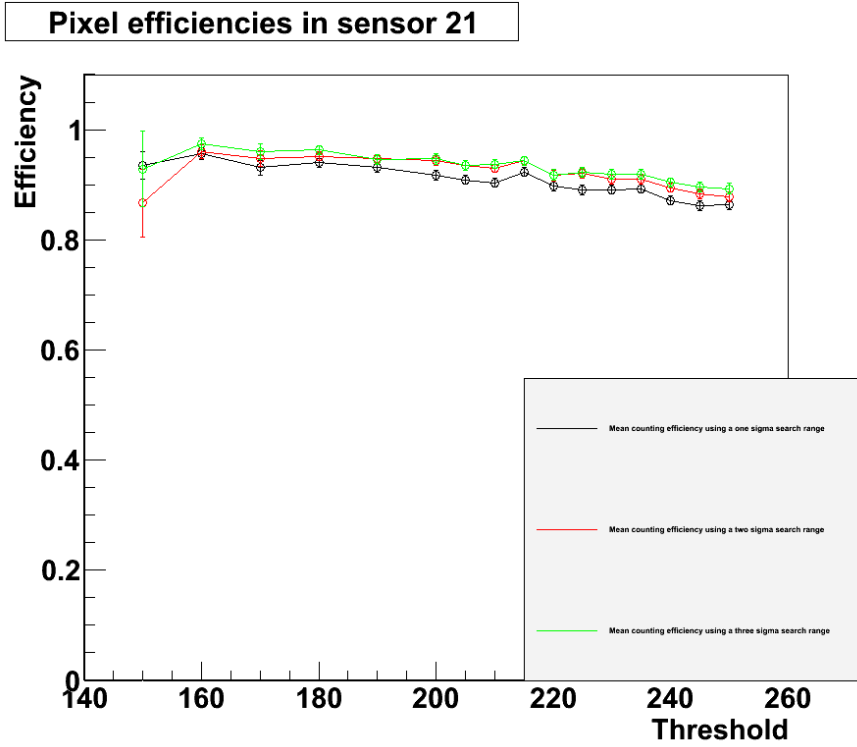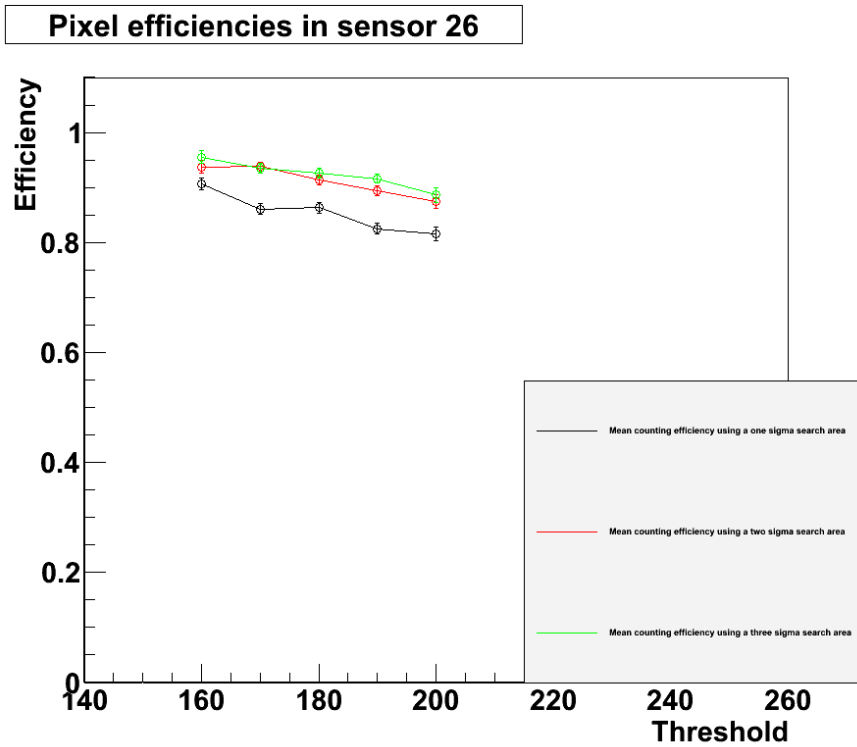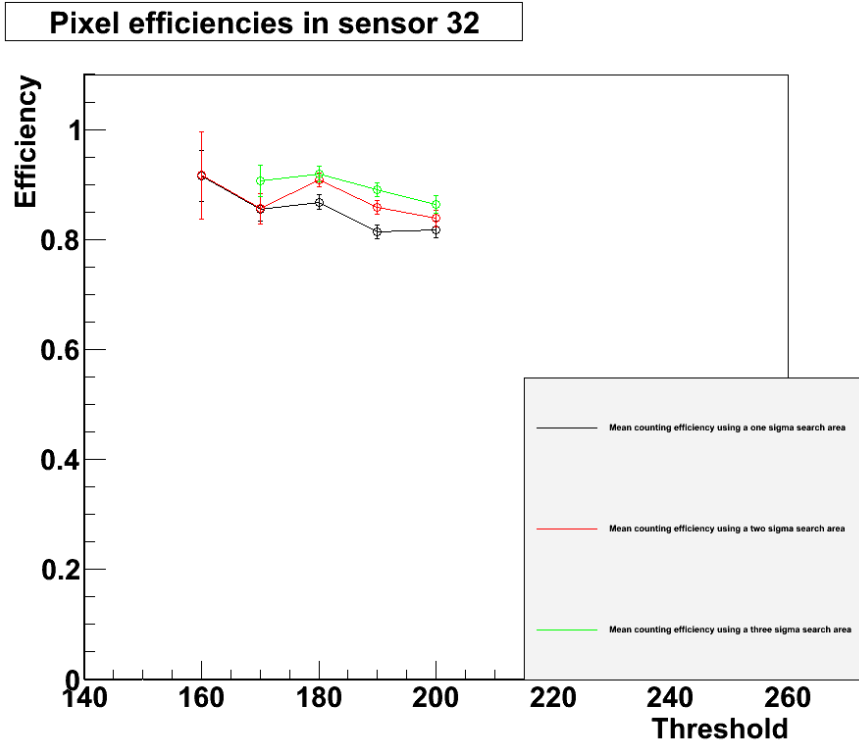Figure 7.36: Counting method pixel efficiencies in test sensor 39, averaged from several runs in the test beam, using a range of different search areas.

Figure 7.37: Pixel efficiencies in test sensor 21, averaged from several runs in the test beam. The counting method efficiencies were calculated using a three σ search range.
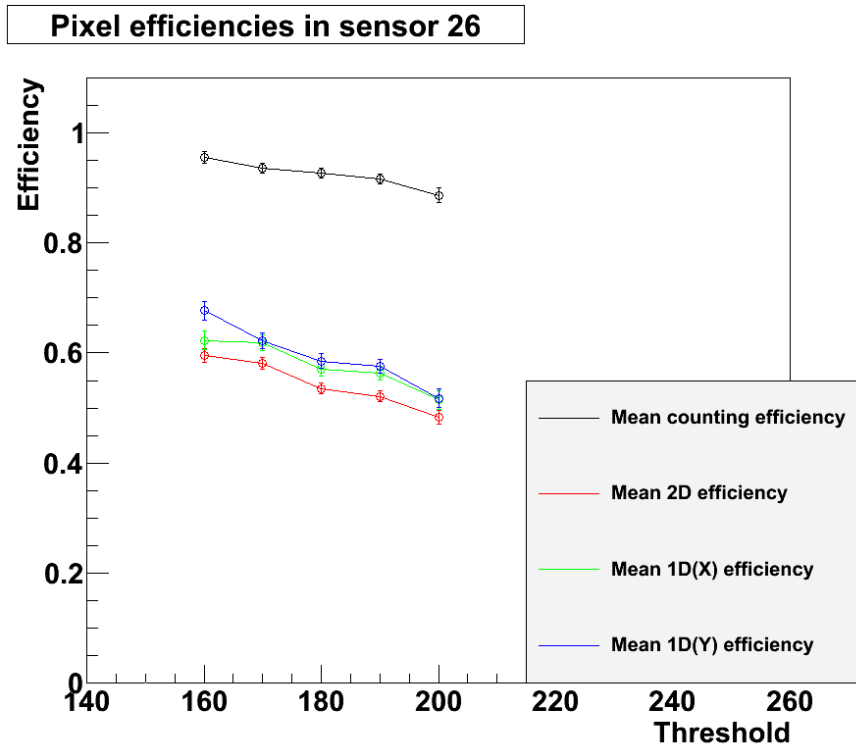
Figure 7.38: Pixel efficiencies in test sensor 26, averaged from several runs in the test beam. The counting method efficiencies were calculated using a three σ search range.

7.5.4 Final Results

Once all test runs had been processed using the methods described in subsections 7.5.1, 7.5.2 and 7.5.3, runs using the same sensors operating at the same threshold were grouped together. The efficiency results for each technique, and for each sensor, within each of these groups were then combined to produce a weighted mean (note: as mentioned previously in subsection 7.5.3, the 1D method produces two efficiency readings which are averaged separately). The results of this were: one mean counting method efficiency (using a three σ search range), one mean 2D method efficiency, one mean 1D(column) method efficiency and one mean 1D(row) method efficiency, per test sensor, per sensor threshold set. These mean efficiencies were then plotted against their associated sensor thresholds to produce figures 7.37 to 7.40. An example of some of the raw results (efficiencies calculated from individual runs) which were used to produce these mean efficiencies, is shown in figure 7.41.

In order to check for variations in efficiency with search area, mean counting

218
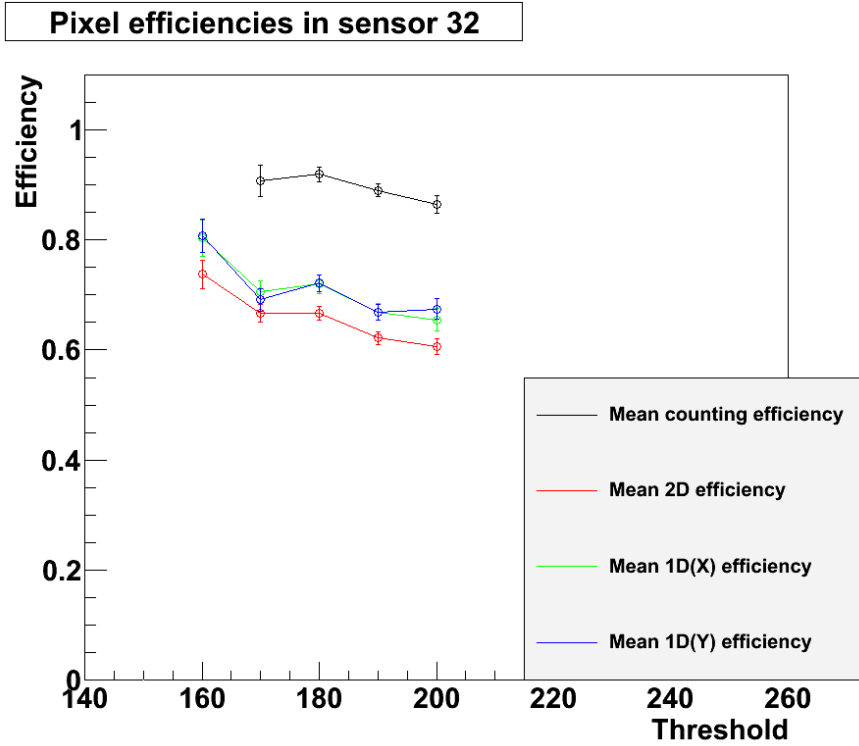
Figure 7.39: Pixel efficiencies in test sensor 32, averaged from several runs in the test beam. The counting method efficiencies were calculated using a three σ search range. The efficiency calculated using the counting method has no results at a threshold of 160 because low statistics resulted in several results with efficiencies of either 0 or 1 at this threshold. This was a problem because the binomial error calculated from these values was zero, meaning that these results could not be included in a weighted mean. This combined with the low statistics of the remaining results, made it impractical to include a data point using the counting method at a threshold of 160.
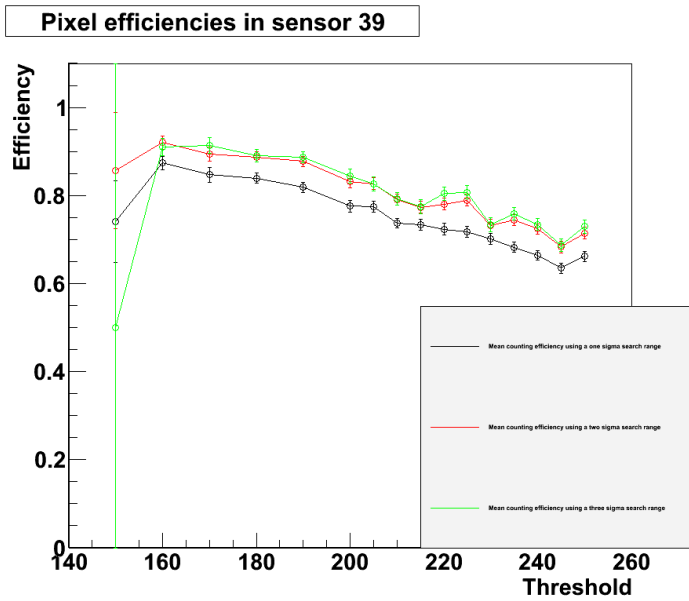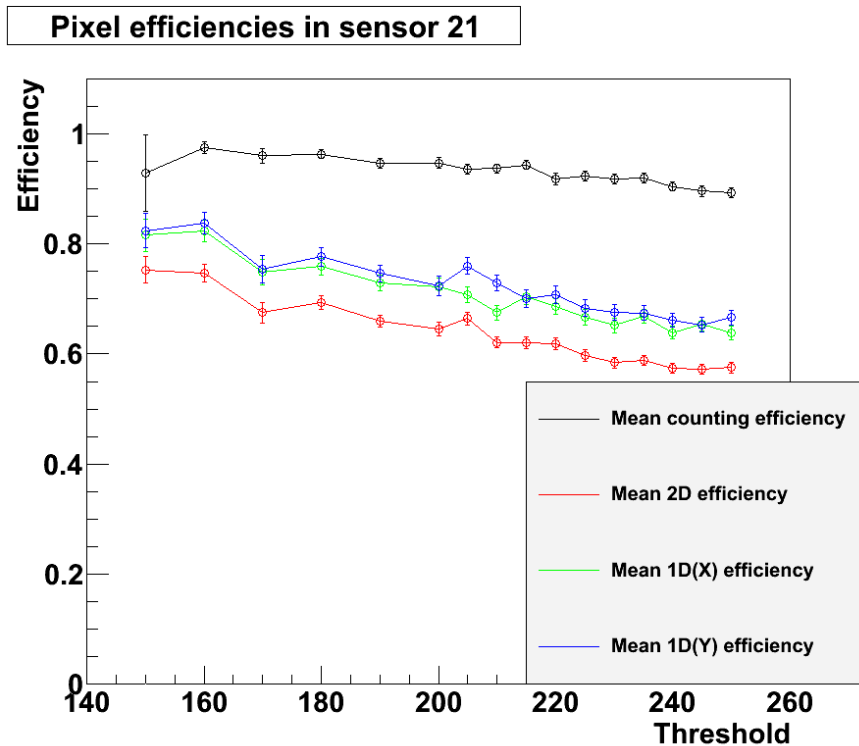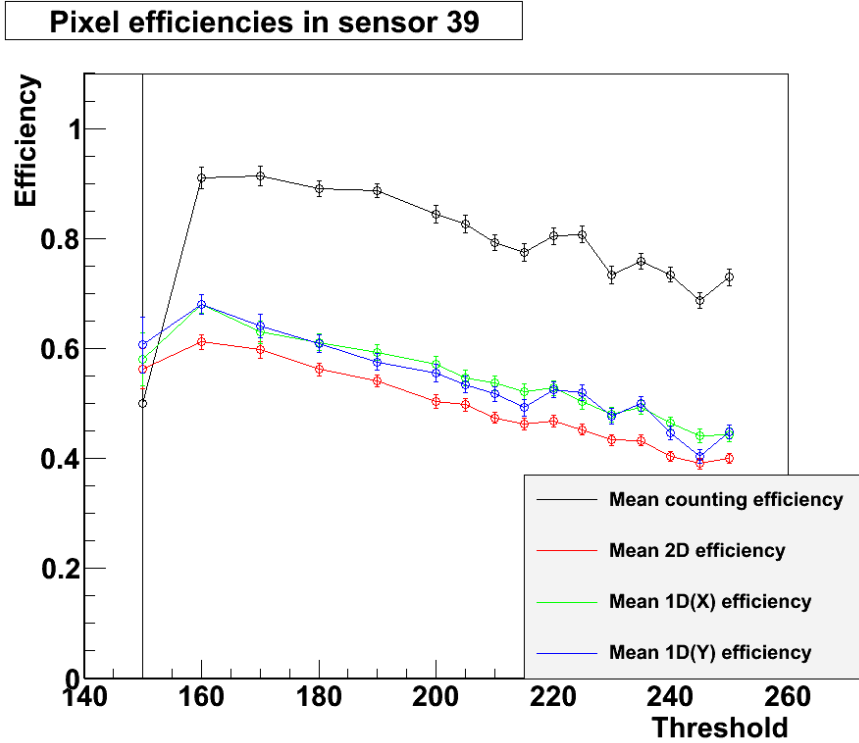
Figure 7.40: Pixel efficiencies in test sensor 39, averaged from several runs in the test beam. The counting method efficiencies were calculated using a three σ search range.

method efficiencies using one σ and two σ search areas were also produced. These results are shown in figures 7.33 to 7.36, the results using three σ search areas are reproduced in these histograms for comparison.

7.6 Conclusions

In ideal conditions pixel efficiency for TPAC 1.2 is found to be in the range 0.75 to 0.95 as illustrated by figures 7.33 to 7.40. This is a considerable improvement over comparable measurements for TPAC 1.0 taken in 2008[53]. Pixel efficiency appears to be dependent on the threshold set, specifically efficiency decreases with increasing threshold. This was an expected result since the threshold set for a sensor directly effects how much charge must be deposited at a diode before a pixel registers a hit, which affects how sensitive the pixels are[32]. The sudden drops in efficiency at low thresholds combined with significant increases in uncertainty implies that the
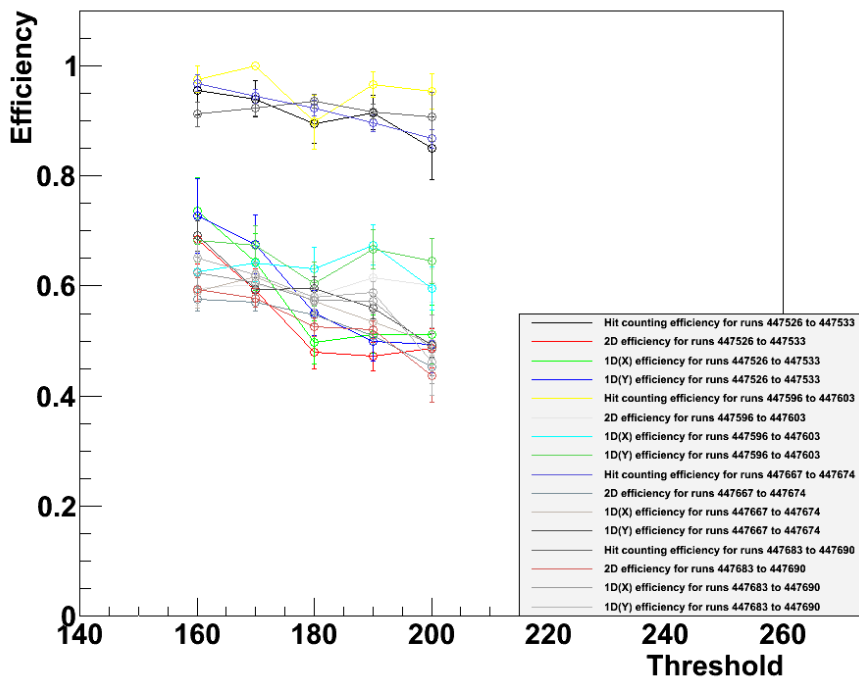
Figure 7.41: Pixel efficiencies in test sensor 26 calculated separately for each test beam run. As shown on this plot there were a small number of cases where the efficiency was calculated to be either exactly zero or exactly one. This was due to extremely low statistics in the runs in question (the small error bars in these cases are due to limitations in the error calculations at very high or very low efficiencies, not low uncertainty). Runs where this occurred were typically excluded from the mean efficiencies shown in figures 7.33 to 7.40. The counting method efficiencies shown here were calculated using a three σ search range.

sensors became increasingly unusable at low thresholds, probably due to domination by noise.

It is interesting to note that the results from the counting method change very little as the search area used is altered (typically less than 10%). Additionally the efficiencies recorded when one σ search areas were used are significantly higher than should be possible for this search range (efficiencies over 80% are shown in figures 7.33 to 7.36 for one σ search ranges while less than 50% test particles should have fallen inside this search area). Both these phenomena are likely to have been caused by overestimating the uncertainty on particle tracks (resulting in overestimates of search areas).

When examined over the same ranges of threshold values the behaviour of sensors 21 and 32 are almost identical, similarly when examined over the same threshold range the behaviour of sensor 26 matches the behaviour of sensor 39. This was an unexpected result because sensors 21 and 26 are both high resolution sensors (with silicon depths of 12μm and 18μm respectively), while sensors 32 and 39 are both standard 12μm silicon depth TPAC 1.2 sensors. Therefore it was expected that sensors 32 and 39 would behave in the same fashion while sensors 21 and 26 were expected to show behaviour that was both different to each other and to sensors 32 and 39. Adding to the confusion is the fact that during runs sensor 21 was paired with sensor 39 in the sensor stack and sensor 26 was paired with sensor 32 in the sensor stack. This meant that sensors 21 and 32 were not placed in the test beam at the same time, similarly sensors 26 and 39 were never simultaneously in the test beam. This meant that the similarities in behaviours of sensors 21 and 32, and the behaviours of 26 and 39, could not have been caused by a variation in the test beam between different sets of runs. Additionally, when the test sensors were swapped midway through the study the slot previously occupied by sensor 26 was filled by sensor 21, and the slot previously occupied by sensor 32 was filled by sensor 39. This means that the similarities in behaviour observed between sensor 21 and sensor 32, and between sensor 26 and sensor 39 could not have been caused by the positions of those sensors within the sensor stack.

A fairly minor improvement to this experiment would be to repeat it using the spill signal from the test beam to control when the sensor stack was active. As mentioned in section 7.4, without the spill signal the sensor stack had to be run continuously over a long period to collect the data needed to get reliable results. The result of this was that the files used to store test beam data were very large and unwieldy (often multiple gigabytes per run). This has made storage a problem and marginally increased the amount of time necessary to analyse the data. If the test beam spill signal had been used to control the sensor stack then the same amount of useful data could have been stored much more easily because there would be no records of periods during the test runs when there was no beam to detect.

As stated previously the analysis methods applied so far have narrowed down the pixel efficiency of TPAC 1.2 MAPS pixels to a relatively small range. While this is useful, finding the exact pixel efficiency is still desirable, therefore a potential extension to this study would be to add another analysis method to those described in section 7.5, in order to find the true pixel efficiency. One potential technique for finding the true efficiency would be a modified version of the counting method. In the conventional counting method the presence of one or more hits in the search area for a track is taken as confirmation that a particle has been registered by the pixel it passed through. In the modified counting method each time a 'relevant hit' (i.e. a hit ocuring at the same time as a test particle passed through the sensor) was recorded the probability that hit was not a false positive (i.e. it was not a noise hit and was not caused by charge spilling over from another pixel) would be calculated. Each time a particle passed through that sensor all the 'relevant hits' in the sensor associated with that test particle would be collected and the probabilities that each hit was not a false positive would be used to work out the probability that the test particle was detected by the pixel it passed through. That probability would then be added to a running total which (once all the test particles had been processed) could then be divided by the total number of useable test particles to find the true pixel efficiency of the sensor.

Alternatively, the problems encountered with the counting method and the 2D

223

method in attempting to estimate the true pixel efficiency could be solved by altering some of the hardware used in this experiment. In both methods problems arise because the uncertainty on where a test beam particle passes through a test sensor is not insignificant when compared to the size of a pixel as shown in figures 7.20 to 7.25. If the uncertainty in particle location was negligible then the search areas used in the counting method would only have to encompass a single pixel. If this were the case then there would be no risk of a false positive due to a particle passing through one pixel, but only causing hits in another (since no pixels other than the pixel the particle passed through would be checked for hits). This would cause the counting method to produce a genuine pixel efficiency, rather than an upper limit for this value. Similarly, if the uncertainty on particle location was negligible then the assumption made within the 2D method that the pixel that a track passed through was the same pixel the particle that created it passed through, would be valid. In this case the 2D method would produce a genuine pixel efficiency, rather than a lower limit for this value. Reducing the uncertainty on the positions of particles as they pass through the detector could be achieved in several ways. Using control sensors with significantly higher spatial resolution than the test sensors would reduce the uncertainty on particle positions, as would using a greater number of control sensors. Increasing the typical distances between the control sensors would also reduce uncertainty on test beam particle position within the test sensors (assuming that the positions of the control sensors relative to the test sensors would be known to a high precision).

Additionally the data collected for this study (or a comparable experiment) could be re-analysed to find out other information about the sensor. For example it might be useful to find out what the probability of the whole sensor registering the passage of a particle is. This information could be valuable in situations where the exact location of a particle less important (such as in the middle layers of an ECAL). This information could be acquired by using a modified version of the counting method. The counting method could be modified so that the search areas used are arbitrarily large (rather than being based on the uncertainty in the track location),

and where tracks are not discarded due to the presence of bad pixels and dead areas in the corresponding search area. If the typical noise hits within the sensor could be subtracted from the hits found, then the resulting efficiency measurement would be the probability that the sensor overall would register the passage of a MIP.

The trends shown in figures 7.33 to 7.40 suggest that a follow up study examining the limitations of operating TPAC sensors at low thresholds may be useful. A brief examination of results from this study (specifically the increase in error bars with decreasing threshold) implies that the principal limitation on decreasing the sensor threshold is a decreasing number of useable pixels. However a low threshold might be desirable due to the higher pixel efficiencies found at lower thresholds. Therefore a reasonable objective of such a follow up study would be to find what fraction of the sensor is useable at any given threshold. Results from such a study could then be used in combination with the efficiencies shown in figures 7.33 to 7.40 to identify the ideal operating threshold for these sensors, balancing efficiency with sensor viability.

Another potential extension to this study would be to investigate whether or not the pixel efficiency within a TPAC sensor is dependent on the location within that sensor. It is quite possible that the support structures within the sensor may affect pixel performance. Finding how efficiency changes across the sensor would reveal such non-uniformities which would in turn provide valuable information for any future sensor design. Such a study could be performed in the same manner as the study described above (albeit with longer run times, and less threshold variation), with each track and any associated hits being assigned to different efficiency calculations depending on the region of the sensor the track passed through. In this case efficiency (using all three techniques described) would be measured once for each region of the sensor, producing a map of efficiency variation across the sensor.

Chapter 8

Conclusions

8.1   Summary

The hardware based studies detailed in chapters 5 and 7 dealt with the development of MAPS pixels while the simulation based studies detailed in chapters 4 and 6 dealt with the properties of a MAPS ECAL in the LDC and ILD detectors respectively.

The study in chapter 5 showed that TPAC 1.0 pixels suffer from non-uniformity in their thresholds and that this non-uniformity could be reduced by applying trims to each pixel individually. The improvement in pixel uniformity from applying trims can be seen by comparing the distributions of '50% drop-off points' for the pixels in the sensor with and without trims (the 50% drop-off point for a pixel is a good indicator of the threshold at which that pixel will saturate due to noise). Applying trims reduced the standard deviation of the distribution of 50% drop-off points in the shaper pixels from (25.94 ± 0.15)TU to (12.69 ± 0.08)TU, shown in figures 5.10 and 5.18, and reduced the standard deviation of the distribution of 50% drop-off points in the sampler pixels from (31.37 ± 0.19)TU to (17.37 ± 0.10)TU, shown in figures 5.12 and 5.19.

The primary results of the study described in chapter 7 were a series of pixel efficiency measurements (shown in figures 7.33 to 7.40) which showed that pixel efficiencies for TPAC 1.2 pixels were in the range of 0.75 to 0.95. Additionally this study showed that replacing the standard silicon epitaxial layer in TPAC 1.2

226

sensors with high resistivity silicon did not seem to produce a significant difference in efficiency.

The study described in chapter 4 was an attempt to gauge the response of a MAPS ECAL to background particles produced by beam-beam interactions. It quantifed how frequently such an ECAL would need to be read out to prevent the background particles from saturating the detector. Figures 4.11 and 4.12 imply that saturation should not be an issue for the pixel reset/readout rates of around 1ms currently under consideration.

Chapter 6 describes a study using simulations of single photons passing through the ILD detector with and without a MAPS ECAL to compare the energy resolution $\frac{\sigma(E)}{E}$ of a MAPS ECAL with that of an analogue SiW ECAL. This value was found to be $\frac{(11.50 \pm 0.04)}{\sqrt{E}}\%$ for the simulated MAPS ECAL (as shown in figure 6.27), and $\frac{(11.9 \pm 0.04)}{\sqrt{E}}\%$ for the analogue ECAL (as shown in figure 6.28). Both these values are below the $\frac{15}{\sqrt{E}}\%$ required for an ILC ECAL[15].

8.2 Outlook

At present there are plans to establish the basic design of the ILC in 2012, at which time both the detectors used and their basic operating principles will be determined[54]. Naturally the collaboration working on MAPS pixels will make a case to include an ECAL using MAPS pixels in the SiD detector and/or the ILD detector at that time.

Unfortunately, like many other projects, MAPS has recently been cut from the STFC budget and is therefore at risk of shutting down. As of May 2010 the collaboration is running on a minimal budget in the hopes that further funding can be secured from other sources, or that the project will be re-evaluated by the STFC[30]. If in 2012 MAPS pixels are selected for use at the ILC (or a similar large project), future funding will become easier to secure. With this in mind, the MAPS collaboration needs only to find funding for two more years of operation so that the concept of a MAPS ECAL can be presented to the SiD and ILD collaborations in 2012.

If a MAPS ECAL is selected by a detector collaboration, research after that point is likely to focus on the development, testing, and construction of a full size MAPS ECAL. Current (as of 2010) MAPS ECAL designs are intended to produce an ECAL which will have the same external physical and thermal characteristics as contemporary analogue designs, ensuring that no other detector components will need to be redesigned to accomodate a MAPS ECAL[25][17].

In the event that a MAPS ECAL is not selected for any of the ILC detectors, (and if funding is available) the collaboration is likely to continue development of MAPS for use by other projects. There is already a program developing MAPS pixels for use in medical physics[55], and potential new projects might include development for other future HEP detectors, or detectors for use in X-ray astronomy[56].

8.3   Future Studies

Naturally the studies detailed in chapters 4 to 7 represent only a small subset of the studies which will be necessary to develop a working MAPS ECAL and there are several interesting studies planned for the future. Since tests using the TPAC 1.2 sensors (one of which is described in chapter 7) have been encouraging, future studies are likely to focus on developing this technology towards creating a fully functioning ECAL rather than pixel development as in previous studies.

Perhaps the most significant of the currently planned studies is the program to produce and test a prototype ECAL section based on TPAC 1.2. This Prototype would be at least 6cm×6cm in surface area and would consist of 30 alternating layers of sensors and tungsten absorber slabs[57]. Once produced, this prototype ECAL would be calibrated using particles with well established energies. Similarly the energy resolution of this prototype and its variation with energy could be measured by exposing it to a range of particles with different energies.

Additionally there is a study currently underway (as of Summer 2010) to test the current capability of existing TPAC 1.2 sensors to detect shower particles. Prior studies using TPAC 1.2 sensors have primarily focused on detecting relatively high

energy single particles, naturally if TPAC 1.2 pixels were used in a real ECAL they would need to deal with large numbers of relatively low energy electrons and photons produced by high energy particles passing through tungsten absorber plates. This situation is recreated by placing the sensor stack described in chapter 7 in a test beam behind several tungsten absorber sheets. This creates a particle shower 'downstream' of the tungsten absorbers. The resulting particle shower was simulated before performing this experiment in order to predict what the response of an 'ideal' the TPAC 1.2 sensor should be in these circumstances for comparison with the real results taken during the study. At present, the data taking for this study has been completed and the results are undergoing analysis[58].

Bibliography

[1] David Griffiths, *Introduction to Elementary Particles, Second, Revised Edition*, textbook, ISBN:978-3-527-40601-2, 2008

[2] K. Nakamura et al. (Particle Data Group), J. Phys. G 37, 075021 (2010), *2010 Review of Particle Physics: Quarks*, 2010

[3] K. Nakamura et al. (Particle Data Group), J. Phys. G 37, 075021 (2010), *2010 Review of Particle Physics: Leptons*, 2010

[4] K. Nakamura et al. (Particle Data Group), J. Phys. G 37, 075021 (2010), *2010 Review of Particle Physics: Neutrino Properties*, 2010

[5] Robert Eisberg, Robert Resnick, *Quantum Physics of Atoms, Molecules, Solids, Nuclei, and Particles, Second Edition*, textbook, ISBN:0-471-87373-X, 1985

[6] Ta-Pei Cheng, Ling-Fong Li, *Gauge theory of elementary particle physics*, textbook, ISBN: 0-19-851961-3, 1988

[7] K. Nakamura et al. (Particle Data Group), J. Phys. G 37, 075021 (2010), *2010 Review of Particle Physics: Electroweak Model and Constraints on New Physics*, 2010

[8] James Brau, Yasuhiro Okada, Nicholas Walker, et al, arXiv:0712.1950v1, *International Linear Collider Reference Design Report, Volume 2*, available at http://www.linearcollider.org/about/Publications/Reference-Design-Report, August 2007

[9] I.J.R. Aitchison, A.J.G. Hey, *Gauge Theories in Particle Physics, Second Edition*, textbook, ISBN:0261-7242, 1989

[10] Benjamin W. Lee, C. Quigg, H.B. Thacker, Phys. Rev. D 16, 1519·1531, *Weak Interactions At Very High Energies: The Role of the Higgs-Boson Mass*, April 1977

[11] C. Quigg, *The Standard Model (Electroweak Theory)*, European School of High-Energy Physics, August-September 2002

[12] Andreas Birkedal, Konstantin T. Matchev, hep-ph/0508185 ; UFIFT-HEP-2005-21, *Phenomenology of Higgsless Models at the LHC and the ILC*, 2005

[13] James Brau, Yasuhiro Okada, Nicholas Walker, et al, arXiv:0712.1950v1, *International Linear Collider Reference Design Report, Volume 1*, available at http://www.linearcollider.org/about/Publications/Reference-Design-Report, August 2007

[14] James Brau, Yasuhiro Okada, Nicholas Walker et al., arXiv:0712.1950v1, *International Linear Collider Reference Design Report, Volume 3*, available at http://www.linearcollider.org/about/Publications/Reference-Design-Report, August 2007

[15] James Brau, Yasuhiro Okada, Nicholas Walker, et al, arXiv:0712.1950v1 ,*International Linear Collider Reference Design Report, Volume 4*, available at http://www.linearcollider.org/about/Publications/Reference-Design-Report, August 2007

[16] ILC images and graphics available at http://www.linearcollider.org/about/Press/Images-and-graphics

[17] The ILD concept group, *The International Large Detector Letter of Intent*, ISBN:0418-9833, ISBN:978-3-935702-42-3, 2010

[18] Kaoru Yokoya and Pisin Chen,*Beam-Beam Phenomena in Linear Colliders*, Lecture Notes in Physics Vol. 400 (Springer-Verlag, Berlin, 1990), Rev. 11/1992

[19] Carsten Hensel, *Beam Induced Background at a Tesla detector*, January 2000, LC Note(TESLA):LC-DET-2000-001, 2000

[20] Tor Raubenheimer, *Suggested ILC Beam Parameter Range.*, ILC internal note available at http://www-project.slac.stanford.edu/ilc/acceldev/beamparameters.html, Rev. 28/2/2005

[21] Gerry Dugan,*Directors Corner:Cost Optimisation of Wigglers for the ILC Damping Rings*, ILC internal note available at http://www.linearcollider.org/cms/?pid=1000357, December 2006

[22] TESLA Collaboration, *TESLA Technical Design Report, Part 1*, available at http://lcdev.kek.jp/TESLA-TDR/, March 2001

[23] ILD Joint Steering Board, *Definition of the ILD Reference Detector*, internal note, available at http://www.ilcild.org/documents/ild-discussion-documents, 2008

[24] GLD concept study team, arXiv:physics/0607154 v1, *GLD Detector Outline Document version 1.2*, July 2006

[25] The SiD Concept Group, arXiv:0911.0006v1, *SiD Letter of Intent*, 31/03/2009

[26] 4th Detector Collaboration, *Letter of Intent from the Fourth Detector (4th) Collaboration at the International Linear Collider*, available at http://www.4thconcept.org/, March 2009

[27] P.D. Dauncey, *Discussion paper on the use of MAPS in a LC electromagnetic calorimeter*, available at http://www.hep.ph.ic.ac.uk/calice/, October 2004

[28] P.D. Dauncey, *Concept for a Si-W ECAL for the ILC based on MAPS*, available at http://www.hep.ph.ic.ac.uk/calice/, December 2004

[29] J.A. Ballin Et al, *Performance of a novel sampling electromagnetic calorimeter with binary readout*, PACS: 12.34, available at www.hep.ph.ic.ac.uk/calice/maps/papers/Nim/, June 2010

[30] P.D. Dauncey, Private Communication

[31] The CALICE collaboration et al, 2008 JINST 3 P08001, *Design and electronics commissioning of the physics prototype of a Si-W electromagnetic calorimeter for the International Linear Collider*, August 2008

[32] J. Ballin et al, Monolithic Active Pixel Sensors (MAPS) in a Quadruple Well Technology for Nearly 100% Fill Factor and Full CMOS Pixels. Sensors 2008, 8, 5336-5351, 2008

[33] TESLA Collaboration, *TESLA Technical Design Report, Part 4*, available at http://lcdev.kek.jp/TESLA-TDR/, March 2001

[34] Jamie Crooks, *TPAC 1.2 FDR*, internal presentation, available at http://www.hep.ph.ic.ac.uk/calice/maps/fdr3/fdr3.html, 27 Feb 2009

[35] Jamie Crooks, *Terapixel APS for Calice, ASIC 1.1 Technical Specification, Document Revision 1.1*, internal note, available at http://www.hep.ph.ic.ac.uk/calice/maps/pdr2/pdr2.html, 28 April 2008

[36] Jamie Crooks, Paul Dauncey, Vladimir Rajovic, Marcel Stanitzki, Konstantin Stefanov, Renato Turchetta, Giulio Villani, Nigel Watson, John Wilson, *MAPS Sensor PCB Schematics Review*, internal note, available at http://www.hep.ph.ic.ac.uk/calice/maps/daq/sensorpcb/reviews/notes070517.txt, 17 May 2007

[37] Jamie Crooks, Paul Dauncey, Matt Noy, Vladimir Rajovic, Konstantin Stefanov, Marcel Stanitzki, *MAPS Sensor PCB Layout Review*, internal note, available at http://www.hep.ph.ic.ac.uk/calice/maps/daq/sensorpcb/reviews/notes070626.txt, 26 June 2007

[38] Vladimir Rajovic, *MAPS Test PCB Schematics Review*, internal presentation, available at

http://www.hep.ph.ic.ac.uk/calice/maps/daq/sensorpcb/reviews/reviews.html, 17 May 2007

[39] J. Ballin et al., arXiv:0901.4457, *A Digital ECAL Based on MAPS* , proceedings of LCWS08, January 2009

[40] M. Stanitzki, Private Communication

[41] Daniel Schulte, Kathy Thompson, *GuineaPig Manual*, available at http://www-sldnt.slac.stanford.edu/nlc/programs/guinea_pig/gp_index.html, February 1999

[42] Daniel Schulte, *Study of Electromagnetic and Hadronic Background in the Interaction Region of the TESLA Collider, Chapter 4*, Thesis, available at http://flash.desy.de/sites/site_vuvfel/content/reports_publications /tesla_reports/tesla_reports_1997/, 1996

[43] Nuclear Instruments and Methods in Physics Research A 506 (2003) 250-303, and IEEE Transactions on Nuclear Science 53 No. 1 (2006) 270-278.

[44] Mokka Home Page, updated July 2006, http://polzope.in2p3.fr:8081/MOKKA/

[45] Marlin Ilcsoft Page, updated 16/03/2007, http://ilcsoft.desy.de/portal/software_packages/marlin/index_eng.html

[46] Paul Dauncey, Anne-Marie Magnan, Matt Noy, *Crosstalk and laser results*, internal presentation, available at http://www.hep.ph.ic.ac.uk/calice/mapsMeetings/meetings.html, 4 June 2008

[47] Paul Dauncey, *Various sensor test results*, internal presentation, available at http://www.hep.ph.ic.ac.uk/calice/mapsMeetings/meetings.html, 25 June 2008

[48] Owen Miller (with contributions from M. Stanitzki), *Status Report For Threshold Scans*, internal presentation, available at http://www.hep.ph.ic.ac.uk/calice/mapsMeetings/meetings.html, May 2008

[49] R.K. Bock, A. Vasilescu, *The Particle Detector BriefBook*, textbook, ISBN: 978-3-540-64120-9, 1999

[50] J. Wilson, *Scintillation counters for the test beam*, internal note, available at https://heplnm061.pp.rl.ac.uk/display/spider/Scintillators+and+PMTs, 6th August 2009

[51] Cern Beamlines - North Area, http://sl.web.cern.ch/sl/eagroup/beams.html#north

[52] J. Ballin et al., *Design and performance of a CMOS test sensor for a binary readout electromagnetic calorimeter*, available at www.hep.ph.ic.ac.uk/calice/maps/Tpac1Paper/paper.pdf, Sep 24, 2008

[53] J. Ballin, *MAPS-Beam Test: tracking efficiencies, Part III in a Saga Revised results-with dead areas implemented*, internal presentation, available at http://www.hep.ph.ic.ac.uk/calice/mapsMeetings/meetings.html, 18th March 2008

[54] B. Barish, *ILC/GDE Report*, presentation at TILC09, available at http://www.linearcollider.org/GDE/Selected-talks, 17 April 2009

[55] Wasi Faruqi, *MAPS and Medipix2: Two direct detectors for Cryo-Electron Microscopy*, presentation to IWORID 8 (Pisa), July 2006

[56] R. Turchetta, *CMOS Monolithic Active Pixel Sensors (MAPS) in RAL*, Presentation at Semiconductor Detectors and Applications Workshop, Rutherford Appleton Laboratory, 30 June 2009

[57] The SPiDeR Collaboration, *DESY PRC Report*, Submitted for DESY PRC 68, available at http://www.hep.ph.imperial.ac.uk/calice/official/091105prc/spider.pdf, Nov. 2009

[58] DESY   Testbeam   March   2010,   internal   records   available   at   https://heplnm061.pp.rl.ac.uk/display/spider/DESY+Testbeam+March+2010

"Th-th-th-th-that's all, folks!"

Porky Pig, recurring catchphrase.